Actuation for Rotating Stall Control of High Speed Axial Compressors

by

Roland Günter Berndt

B.Sc. Engineering, University of the Witwatersrand, 1990
M.Sc. Engineering, University of the Witwatersrand, 1992

Submitted to the Department of Aeronautics and Astronautics
in partial fulfillment of the requirements for the degree of

Master of Science

at the

MASSACHUSETTS INSTITUTE OF TECHNOLOGY

Feb 1995

Author .....
Department of Aeronautics and Astronautics
January 20, 1995

Certified by .....
Alan H. Epstein
Professor
Thesis Supervisor

Accepted by .....
Professor Harold Y. Wachman
Chairman, Department Graduate Committee

Actuation for Rotating Stall Control of High Speed Axial Compressors

by

Roland Günter Berndt

Submitted to the Department of Aeronautics and Astronautics
on January 20, 1995, in partial fulfillment of the
requirements for the degree of
Master of Science

Abstract

A high bandwidth jet actuator, commensurate with the control power and bandwidth requirements for active rotating stall control of high speed axial compressors, has been developed. Two candidate jet injection schemes were developed, namely a sheet injector with fluid dynamic influence limited radially to the outer 15% of the compressor annulus (affecting mainly the tip clearance region of the compressor), and a 3 hole injector with influence extending radially to the outer 40% of the span. The actuator has an overall -3dB bandwidth of 400 Hz with a phase lag of 185°.

The fluid dynamic response of the valve portion of the actuator was found to be linear with actuator command, the valve essentially acting as a mass flow modulator. The dynamics of the valve are governed entirely by the dynamics of the electromechanical servo motor driving the valve (400 Hz bandwidth with a phase lag of 100°).

The fluid dynamic response of the injector portion of the actuator was found to be characterized by a quasi-steady spatial distribution of momentum flux, modified temporally by a first order lag due to the internal fluid dynamics of the injector itself, as well as a pure time delay accounting for the convective lag of fluid traveling from the actuator to the compressor face. The spatial 'wiggling' of the injection pattern with varying amounts of injection was found not to be significant. The internal injector dynamics were modeled by a simple non-linear simulation, which was verified by experiment to capture the essential dynamics. The overall injector dynamics are not attenuated in magnitude in the measured frequency range (0 to 400 Hz), however, the combined first order and pure time delays account for 185° of phase lag.

As part of this research, a high bandwidth total pressure probe was developed. The probe has a pure time delay behavior (130° at 1 kHz), which was predicted by a simple acoustic model and verified by experiment.

Thesis Supervisor: Alan H. Epstein
Title: Professor

Acknowledgments

I would like to thank Professor Epstein for his enthusiasm and guidance, and for allowing me to do things my way 'every now and then'. The opportunity to make my own mistakes added much to my learning at MIT. Thankyou also to Professors Greitzer and Kerrebrock for all the insightful questions, and suggestions of new avenues to explore. Thanks to Professor Jim Paduano and Harald Weigl for all their contributions to the project, and for clearing up many of the 'control' aspects of the research.

On the practical front, I would like to thank Victor Dubrowsky, Bill Ames and Jimmy Letendre, who helped transform my drawings and sketches into real pieces of hardware. Thankyou also to Robin Courchesne, Holly Rathbun, Jean Anderson and Diana Park who kept tabs of the details so that I could do all the interesting stuff.

Then there are those people who kept me sane during my stay at 77 Mass Ave. Diego for listening, Sophie for helping me solve the problems of humanity, Chris for the South African connection, Sean for his insights into all things American, Emmanuel for many late night beers and Fred for taking me on some of the coldest hikes in my life.

Most of all, I am indebted to my wife, Frances, for her love, patience and support (and for proofreading my thesis). And to my parents and family who have, as always, supported me in all my endeavors.

This research was conducted under a grant from NASA, Grant Number NAG3-1457. Special thanks to Michelle Bright (project monitor), Tony Stazisar, Randy Chriss, Ken Suder and Duane Mattern from NASA LeRC, who all contributed to the project.

Contents

List of Figures

Nomenclature

a	Speed of sound $(m.s^{-1})$
A	Area (m^2)
C_d	Nozzle discharge coefficient
C_{mom}	Momentum flux ratio $(\rho U_j^2/\rho U_{fs}^2)$
C_{mass}	Mass flux ratio $(\rho U_j/\rho U_{fs})$
d	Diameter (m)
l	Length (m)
$\dot{m}$	Mass flow rate $(kg.s^{-1})$
M	Mach number
N	Spatial harmonic number
p	Static pressure (Pa)
P_t	Total pressure (Pa)
q_{oj}	Dynamic pressure of the jet at the nozzle exit (ρU_j^2)
q_{fs}	Dynamic pressure of the freestream (ρU_{fs}^2)
R	Gas constant $(J.kg^{-1}.K^{-1})$
T	Static temperature (K)
T_t	Total temperature (K)
U	Velocity $(m.s^{-1})$
V	Volume (m^3)
x	Circumferential length (m)
$\bar{x}$	Momentum weighted circumferential center of gravity (m)
y	Radial length (m)
$\bar{y}$	Momentum weighted radial center of gravity (m)

z	Axial length (m)
α	Non-dimensional valve opening $(A_1/A_{1,des})$
β	Meridional injection angle (rad)
γ	Ratio of specific heats
η	Efficiency
ρ	Fluid density $(kg.m^{-3})$
ω	Angular frequency $(rad.s^{-1})$
$\delta\phi$	Normalized variation in compressor flow coefficient
$\bar{\phi}$	Normalized mean compressor flow coefficient
$\delta\psi$	Normalized variation in compressor pressure rise coefficient
$\bar{\psi}$	Normalized mean compressor pressure rise coefficient

subscripts

For the actuator development

0	Valve upstream location
1	Valve orifice
2	Injector plenum
3	Injector nozzle exit
at	Atmosphere
des	Design
fs	Freestream
j	Jet
n	Time step counter for numerical simulation
nd	Non-dimensional

For the sensor development

0	Sense location
1	Sense tube end
2	Infinite tube entrance

3	Infinite tube end
4	Plenum tube entrance
5	Plenum tube end
6	Transducer location

superscripts

$\tilde{}$	Perturbation quantity
$\bar{}$	Mean value
$\cdot$	$\frac{d}{dt}$

Chapter 1

Introduction

1.1 Background

Turbomachinery compressors are generally limited at low mass flow rates by the onset of fluid dynamic instabilities. Figure 1-1 shows a typical pressure rise versus mass flow characteristic of a compressor operating at constant rotor rotational speed. Starting at the maximum mass flow, the pressure rise increases monotonically as the mass flow through the compressor is reduced. In practice this is usually effected by a downstream throttle or other restriction that increases the backpressure to the compressor. Continuing to decrease the mass flow rate, a point is reached at which axi-symmetric flow in the compressor can no longer be maintained. At this point, corresponding to point A on the constant speed compressor characteristic, the compressor flow field transitions from essentially steady axi-symmetric flow to some form of unsteady asymmetric flow, the overall (annulus averaged) pressure rise being dramatically reduced to point B. Depending on the size of volumes and duct lengths upstream and downstream of the compressor, the compression system (compressor and all other upstream and downstream components) exhibits either constant annulus averaged flow at this reduced pressure rise, or exhibits large amplitude annulus averaged fluctuations in mass flow and pressure rise. Returning the compressor to an axi-symmetric steady flow condition requires the mass flow to be increased to point C, the complete cycle into instability and then out again (A-B-C-A) involving some

hysteresis due to the different paths (combinations of pressure rise and mass flow) taken by the compressor from axi-symmetric flow to asymmetric flow and back again.

The nature of the fluid dynamic instability has been divided into two broad classes, namely surge and rotating stall, as described by Greitzer [1] in his landmark paper. Surge is an axi-symmetric one dimensional oscillation of the mass flow through the compressor, as shown by the right hand schematic in Figure 1-2. Surge is caused by the dynamic interaction of the compressor with the rest of the compression system (ducts and volumes upstream and downstream of the compressor), the flow oscillations being large and occurring at relatively low frequency (compared to the rotor rotational frequency). Rotating stall is a two- or three dimensional spatial disturbance of the mass flow field, which is characterized by the rotation of low or reversed flow regions (called stall cells) around the compressor annulus. The left hand schematic of Figure 1-2 shows conceptually this type of instability, indicating also that the natural frequencies associated with rotating stall are typically an order of magnitude higher than those of surge, and comparable to the rotor rotational frequency. Figure 1-3 shows schematically how small amplitude variations in axial velocity are circumferentially uniform in the case of surge (planar waves), but circumferentially varying in the case of rotating stall (rotating wave). Although rotating stall often leads to surge, strictly speaking there is no dynamic mean mass flow interaction between the compressor and the rest of the compression system during rotating stall, as is the case with surge. The constant speed operating point at which the compressor goes from essentially uniform and steady flow into either surge or rotating stall is called the surge point. The locus of these points for various rotor speeds is termed the surge line, as indicated by the bold line in Figure 1-4. On conventional compressors, steady operation to the left of the surge line is not possible since the compressor is dynamically unstable. Generally, the surge line occurs near the peak of the constant speed compressor characteristic. It is undesirable to operate too close to the surge line, since any small perturbation may push the compressor into the unstable operating regime, and thus into stall. To avoid this, the compression system is usually designed to operate somewhat to the right of the surge line. This safety margin, often

called the stall margin, while necessary, is undesirable since it forces the compressor to operate at a pressure rise less than maximum. It would therefore be desirable to operate closer to the surge line (or even to the left of it), if potential entry into either surge or rotating stall instability could be prevented.

1.2 Control of rotating stall

In 1989, Epstein, Ffowcs-Williams and Greitzer [2] proposed the idea of applying dynamic feedback control to turbomachinery compressors, with the aim of suppressing small amplitude compression system instabilities, and thus extending the stable operating range of the machine. Small perturbations in the compressor flow would be sensed, and using a suitable control law and actuation scheme, these perturbations would be driven to zero. Figure 1-4 shows how the compressor surge line would be moved to lower mass flows by the implementation of dynamic feedback control, therefore extending the stable operating envelope of the compressor. The effect of dynamic feedback control can be understood qualitatively, and in a quasi-steady sense, as follows. Consider a compressor operating at some point on the positively sloped (unstable) portion of the compressor characteristic, as shown in Figure 1-5. Without feedback, a decrease in axial velocity would result in a decrease in compressor pressure rise, since the compressor responds along the positively sloped compressor characteristic. The lower compressor pressure rise results in a further decrease in axial velocity, because the upstream and downstream pressure boundary conditions of the compressor remain the same. Since a small perturbation in axial velocity has been amplified, the compressor flow is unstable. If, however, a feedback scheme (comprising sensors, controller and actuators) is implemented that causes the compressor pressure rise to be increased when a velocity deficit is sensed, then the controlled system (combination of the compressor and the feedback control scheme) will respond along the negatively sloped (stable) effective unsteady compressor characteristic. The increased compressor pressure rise will result in an increase in axial velocity, therefore the compressor flow is stable. In this way, dynamic feedback control allows the

effective unsteady compressor slope to be negative (stable), even though the actual steady compressor slope is positive (unstable). Although the preceding qualitative description of feedback control has been applied to the annulus averaged mass flow and pressure rise of the compressor, it is possible to implement the same scheme in a circumferentially distributed fashion to stabilize circumferentially non-uniform axial velocity perturbations, as are found in the case of a compressor operating with rotating stall.

1.3 Previous work on rotating stall control

To apply active control to rotating stall, which is characterized by variations of flow quantities (usually axial velocity) circumferentially, requires sensing and actuation that can resolve and synthesize flow perturbations circumferentially. One approach to achieve this is to have distributed sensing around the annulus to resolve the circumferential flow variations. Similarly, a circumferential array of actuators allows circumferential control perturbations to be introduced into the flow. Figure 1-6 shows schematically the concept of distributed circumferential sensing and actuation (using variable inlet guide vanes in this specific example). If a suitable control law is implemented between sensors and actuators, it is possible to drive the circumferentially distributed perturbations in the system to zero (or very small amplitudes). Some past work using this concept, including the specific implementation of various rotating stall control strategies, will now be reviewed.

1.3.1 Dynamic control using tip injection

The first successful attempt to control rotating stall on an axial flow compressor using active control was by Day [3]. Sensing variations in axial velocity, and using pulsed fluid jets to actively perturb the flow, he was able to extend the stable operating range of a low speed machine by 6%. He showed that the dynamics of the compressor could be favorably altered by injection of momentum in the tip region of the compressor, allowing the stalling flow coefficient to be reduced. The control strategy employed by

Day was to track regions of low flow as they grew (in time) and rotated around the compressor annulus. Once the stall region had grown to a certain size, an injector at the appropriate circumferential location was activated to energize the low flow region. Since the actuators could only be switched on or off, and not modulated between these limits, the control strategy was not of the classical continuous type as suggested by Epstein et al [2], but rather a type of 'bang bang' control. Nevertheless, Day's control scheme could sense both long length scale modal disturbances (circumferential variations on the order of the annulus circumference), as well as short length scale disturbance called 'spikes' or 'pips' (circumferential variations on the order of a blade pitch), and was able to obtain a flow range extension for both types.

1.3.2 Dynamic control using variable inlet guide vanes

Paduano [4] used an array of 12 movable inlet guide vanes ('wiggly vanes') upstream of a single stage low speed axial compressor to increase the stable operating range of the machine. Using hot-wire sensors to measure the small amplitude circumferentially traveling axial velocity modal perturbations typical of this machine, the flow field could be represented as a summation of spatial Fourier harmonics. Using a micro-computer to compute a suitable linear control output, and then commanding the 'wiggly vane' actuators based on this output, Paduano was able to extend the stable compressor operating range by 23%. The controller implementation was based on the small perturbation rotating stall model originally developed by Moore [5] and Moore and Greitzer [6]. This research demonstrated not only that active control of rotating stall was indeed possible, but that the modal control approach (using spatial Fourier harmonics to represent the flow) was useful for machines that exhibited the long length scale type of disturbances. Haynes [7] extended the modal control scheme to a 3-stage low speed axial compressor. He demonstrated that the individual Fourier harmonics could be stabilized individually, and that the neutrally stable flow coefficient could be decreased if an increasing number of spatial harmonics were controlled.

1.3.3 Dynamic control using aeromechanical feedback

Gysling [8] used aeromechanical feedback to modulate the injection of mass and axial momentum into the face of a single stage low speed axial compressor. Reed valves, deflected by circumferential variations of static pressure in the upstream flow field, would modulate the quantity of injectant flow introduced into the compressor upstream flow field, tending to restore perturbations in the axial velocity flow field to zero. Using the small amplitude modal description of rotating stall by Moore [5], Gysling designed the local fluid dynamic feedback mechanism in such a way as to extend the stable operating range of the compressor. His experiment showed that the stalling flow coefficient of the compressor could be decreased by 10% using this locally reacting aeromechanical feedback system.

1.4 Motivation and objectives for this research

Having demonstrated the feasibility of using feedback control to extend the stable operating range of low speed axial compressors, a next logical step is to see whether the same feedback control approach can be used on high speed axial compressors. Since most modern machines are of the latter type, it would be useful to demonstrate the feasibility of applying feedback control to such machines. Due to the high axial and relative flow Mach numbers in these machines, it is expected that compressibility may play a role in the rotating stall dynamics of the compressor. Also, because the fluid power of these machines is much greater than an equivalently sized low speed machine, it is expected that the control power necessary to perturb the compressor will be commensurately larger. Lastly, the higher rotor rotation frequencies of high speed machines implies that the rotational speed of the rotating stall instability will be increased, all other things being equal. This would tax the bandwidth capabilities of the actuators (and sensors) used in the feedback control scheme. Several components of the existing feedback control systems for rotating stall control appear to be more critical when applied to high speed compressors, most notably the control power and bandwidth requirements of the actuation system. The objective of this research is

therefore to develop an actuation scheme that will allow rotating stall control to be implemented on a high speed axial compressor. Specifically, the goals of this research are to achieve the following:

- Develop an actuation scheme with sufficient control power to perturb the flow field of a high speed axial compressor.
- Develop an actuation scheme with sufficient spatial resolution to synthesize circumferential control perturbations for rotating stall control of a high speed axial compressor.
- Develop an actuation scheme with sufficient temporal bandwidth to synthesize circumferential control perturbations for rotating stall control of the high speed axial compressor.
- Develop an actuation scheme that can be practically implemented on an existing high speed axial compressor, and is rugged enough to operate in the harsh environments (vibration, temperature) typical of these machines.

1.5 Thesis overview

The thesis is organized along the following lines.

Chapter 1: Introduction

The problem of rotating stall is introduced, and the concept of active feedback control is discussed. Past work in the field is reviewed, and the motivation and objectives for the present research are given.

Chapter 2: Theoretical Elements of Actuator Design

The objectives of the actuator design are discussed, followed by a review of relevant work done by others concerning actuator design. The issues affecting actuation of high speed axial compressors are discussed, and the

conceptual design of a fluid jet actuator is proposed. Some performance limiting design criteria for the jet actuator concept are investigated, the detailed mechanical design of the fluid jet actuator being presented in Chapter 3, 4 and 5.

Chapter 3: Valve Development

The detailed mechanical design of the valve is discussed, with justification for the various design decisions taken. A description of the experimental equipment used to test the valve is given, followed by the presentation of performance data and their discussion. The development of a second generation valve is briefly outlined, after which a short summary of the overall valve development is given.

Chapter 4: Initial Injector Development

The detailed mechanical design of the injectors is outlined, with emphasis on the functional objectives of the designs. A description of the experimental facility developed to adequately test the injectors is given, as well as a description of some of the methods used to acquire and process the data. This chapter deals mainly with the learning process that was required to develop general design methodologies for injectors, Chapter 5 dealing with the final injector designs.

Chapter 5: Final Injector Development

The details of the final injector designs are outlined, after which the experimental data pertaining to these injectors are presented. The data are discussed, and a short summary of the injector development given. A summary of the overall actuator development and capabilities is given, followed by a brief discussion of the real-world applications for the actuator.

Chapter 6: Sensor Development

In addition to the actuator development, a high-bandwidth total pressure and wall static pressure probe were developed. The conceptual and mechanical design of the high frequency response pressure probes is outlined, and a description of the experimental test facility used to verify their performance given. A discussion of the experimental performance testing is presented, followed by a wrap up of the sensor development.

Chapter 7: Conclusions and Recommendations

The results and conclusions of the actuator and sensor development are summarized. Recommendations for future work on actuation and sensing are given.

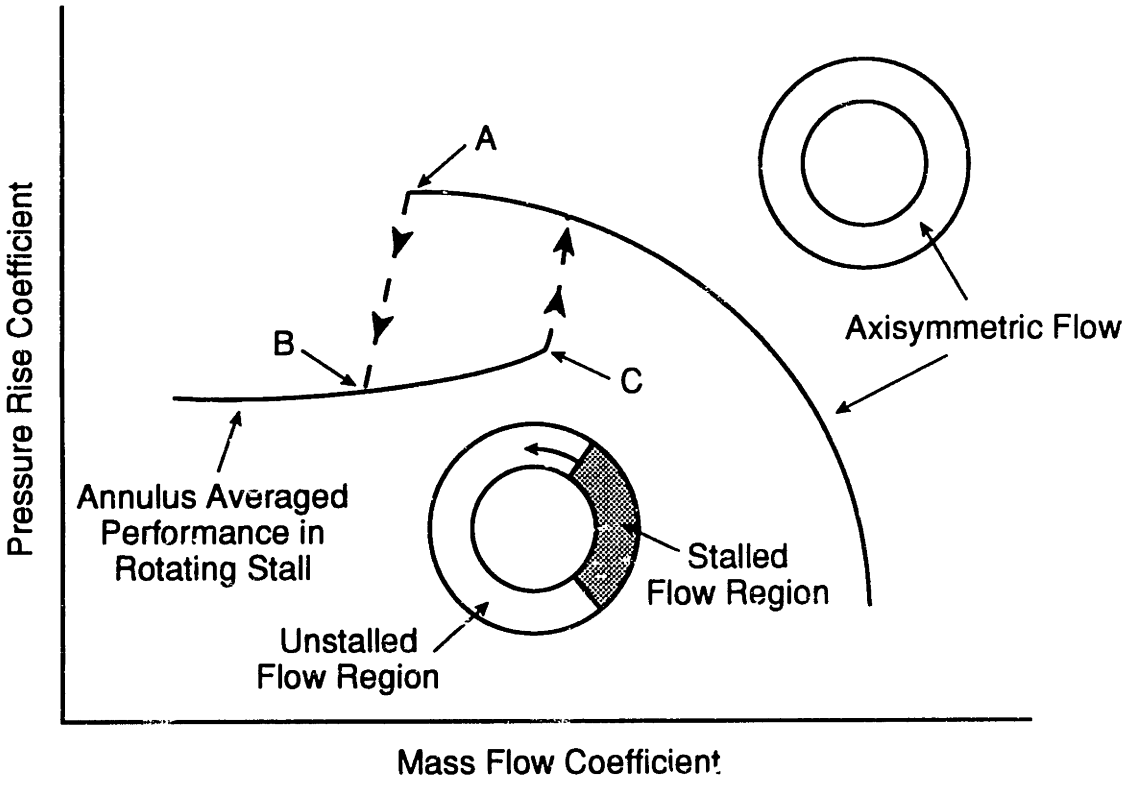

Figure 1-1: Compressor pressure rise versus mass flow characteristic, showing axisymmetric performance, and performance in rotating stall.

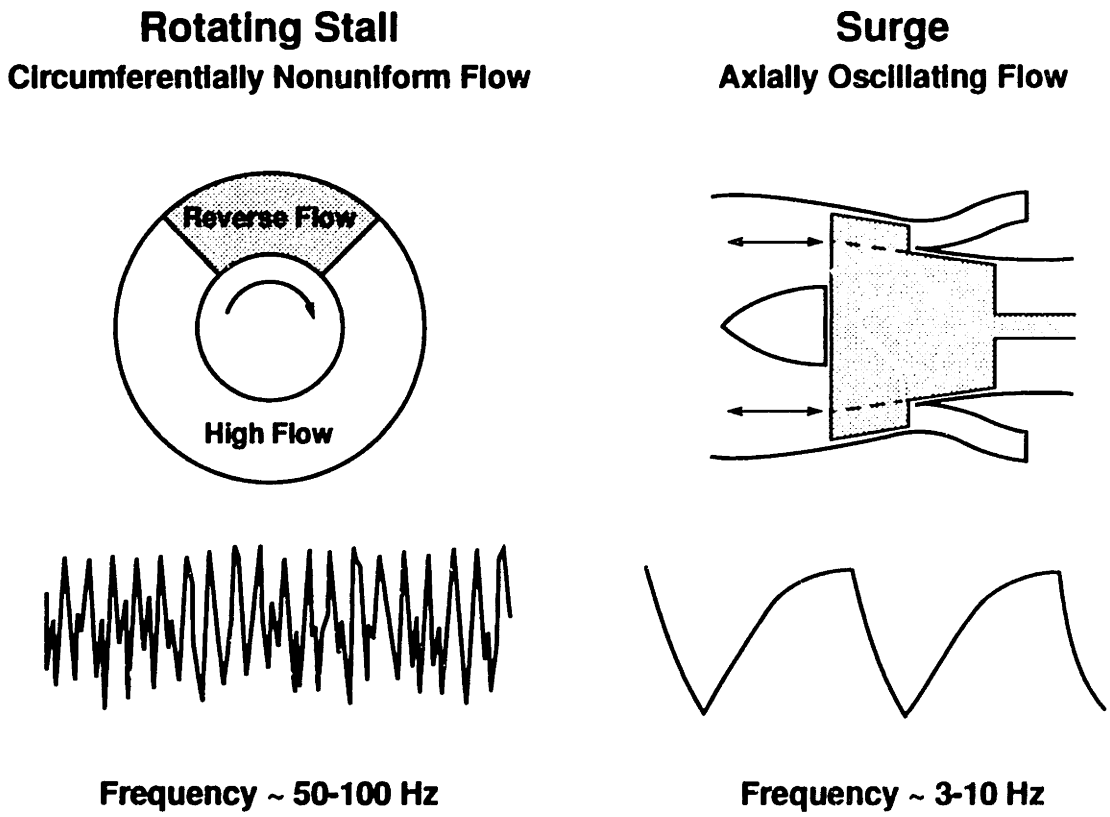

Figure 1-2: Schematic of rotating stall and surge in axial flow compressors.

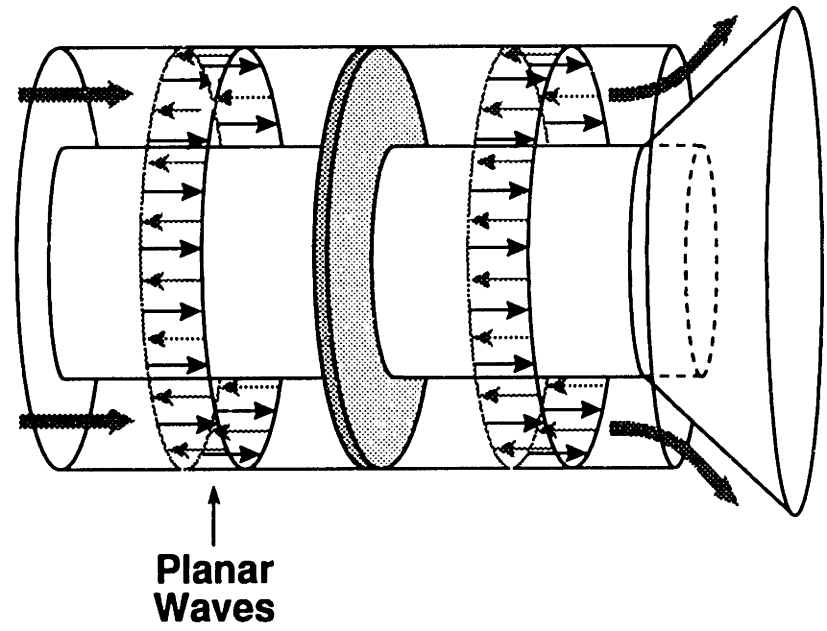

Surge

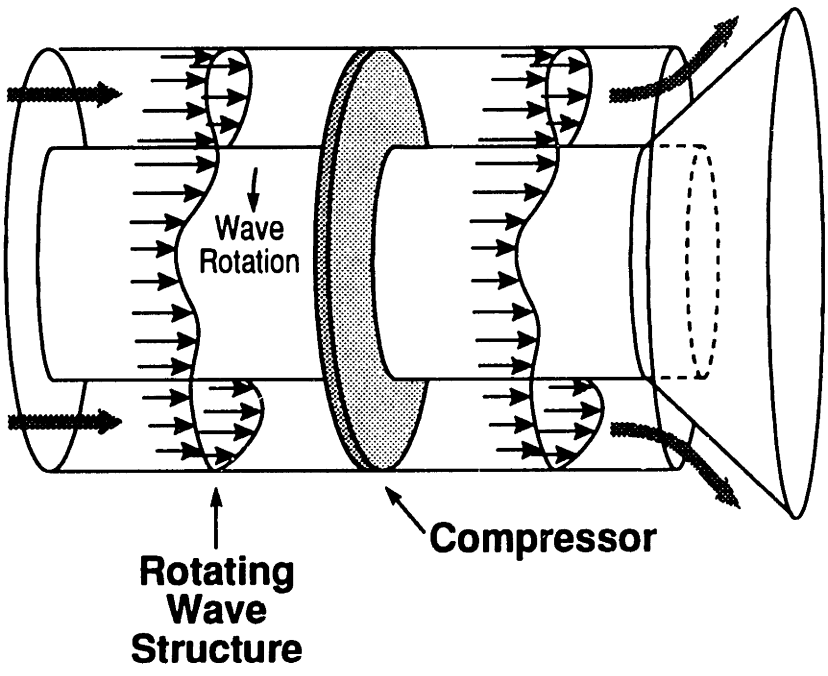

Rotating Stall

Figure 1-3: Comparison of axial velocity wave structure for surge and rotating stall.

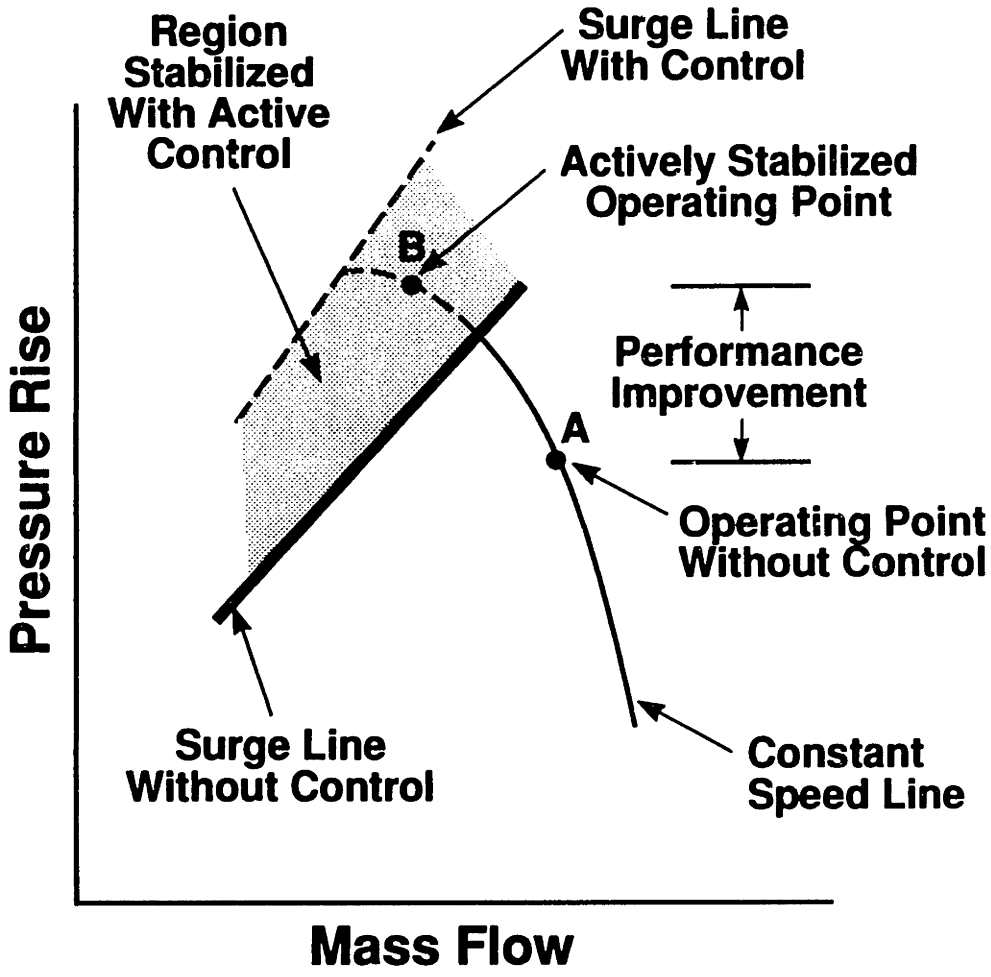

Figure 1-4: Extension of the compressor operating range using active feedback control.

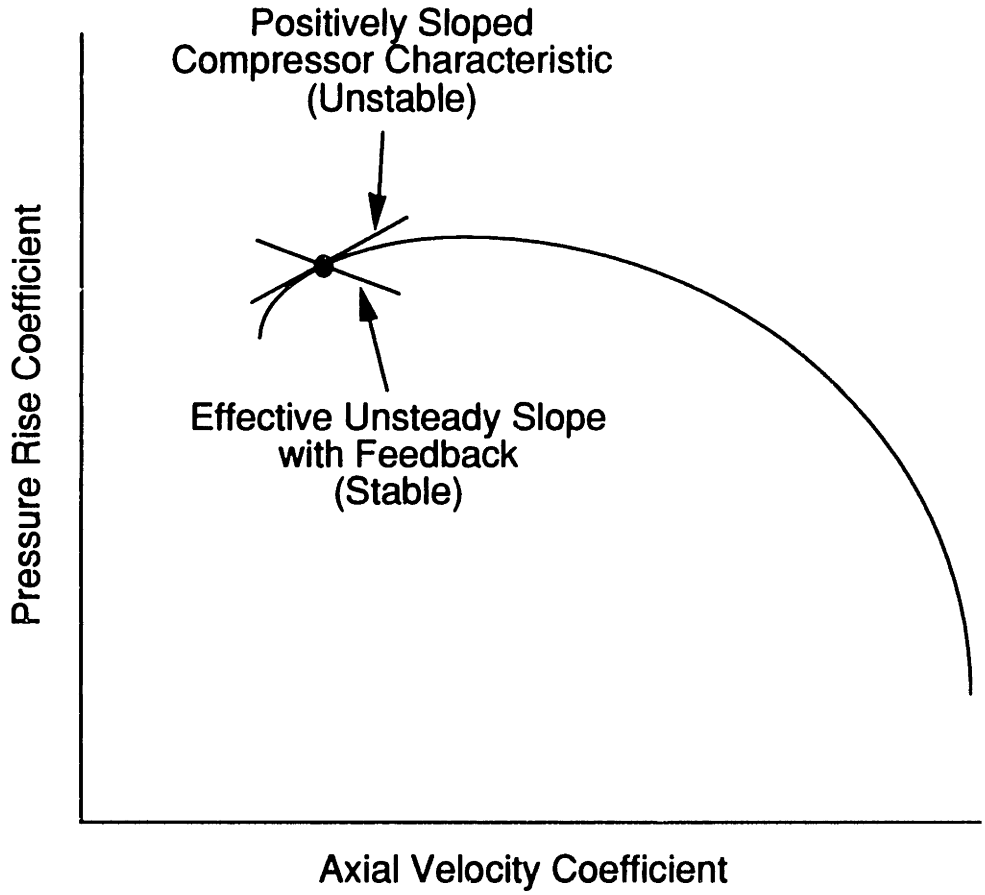

Figure 1-5: Dynamic feedback changes the effective compressor slope.

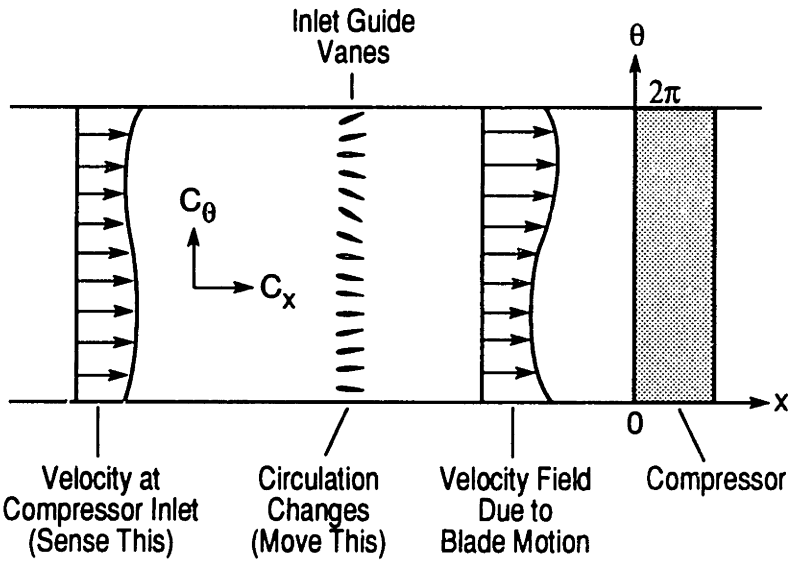

Figure 1-6: Distributed sensing and actuation for rotating stall control.

Chapter 2

Theoretical Elements of Actuator Design

2.1 Definition of actuation

Given the control system illustrated in Figure 2-1, the actuator is that component of the control loop which converts the low power controller output signal into a high power signal able to affect the plant. In the case of rotating stall, the compressor is the plant, and the input and output signals of the actuator can take various forms. Typically, for an electronically implemented controller, the controller output will be electrical, therefore the actuator input will also be electrical to be compatible with the controller. Since the variables that will modify the performance of the compressor (plant) are flow variables, the output of the actuator should be some form of flow variable. Practically, this will take the form of a device that can change the total pressure, static pressure, total temperature or vorticity of the flow (note: other combinations of four independent flow variables are possible, it is merely a matter of convenience to specify these four).

2.2 Types of actuation

Several different actuation schemes have been suggested to allow the pressure rise characteristic of an axial compressor to be (unsteadily) altered. These include variable inlet guide vanes (IGV's) and fluid jet injection upstream of the compressor, and bleed valves downstream of the compressor. To keep the analysis qualitatively simple, the effect of these actuation schemes on the compressor will be looked at in a quasi-steady sense. Dynamically, this may not be completely valid at higher frequencies, however, a quasi-steady analysis does illuminate some of the underlying principles of fluid actuation.

Variable IGV's change the swirl of the upstream flow field, without changing the upstream total pressure. The upstream swirl changes the amount of flow turning in the compressor, and hence the total pressure rise of the machine. Swirl in the direction of rotor rotation results in a decrease in compressor pressure rise for a given mass flow. Bleed valves extract mass flow from the downstream flow field of the compressor, causing a decrease in static pressure (relief) of the downstream flow. The pressure rise across the compressor for a given upstream mass flow is thus decreased.

Jet injection adds momentum and mass to the upstream compressor flow field. Depending on the azimuthal (in the axial/circumferential plane) injection angle, jet injection can also result in swirl upstream of the compressor. There are three primary mechanisms by which the jet actuator can alter the pressure rise characteristic of the compressor. The first mechanism is a change in mass flow through the compressor due to the addition of mass flow by the jet actuator. For a compressor operating on the negatively (stable) sloped portion of the characteristic, increased compressor mass flow will result in a decrease in compressor pressure rise. Conversely, for a compressor operating on the positively (unstable) sloped portion of the characteristic, the compressor pressure rise will increase with jet injection. The second mechanism is a change in upstream total pressure caused by the addition of axial momentum by the jet actuator. If the jet actuator and compressor are considered to be a single actuator disc, the pressure rise of the combination will increase with increased jet injection.

The third mechanism is a change in upstream swirl caused by the addition of tangential momentum by the actuator. Along the same lines as for the variable IGV's, swirl in the direction of rotor rotation results in a decrease in compressor pressure rise. It is clear from the above three mechanisms that the compressor pressure rise may not be altered at all if the 'correct' (but unfortunate) combination of mass, momentum and swirl addition is chosen that exactly counterbalance one another. Since the intended region of operation of the actuator is the positively sloped portion of the compressor characteristic (where the compressor is unstable and requires feedback control to operate in stable manner), both the addition of mass and axial momentum will lead to a pressure rise of the compressor. If the tangential momentum of the jet (azimuthal injection angle) is introduced in a direction opposite to the rotor rotation, all three pressure rise mechanisms of the jet actuator will result in increased compressor pressure rise.

2.3 Control power requirement

The destabilizing mechanism that occurs in compressors is one in which the compressor feeds energy into disturbances so as to increase the magnitude of these disturbances. This condition is achieved when the mass flow and pressure perturbations of the compressor are in phase, as is the case, in a quasi-steady sense, on all parts of the compressor characteristic with positive slope. If the compressor is viewed as contributing towards negative damping of the system, while the control system contributes towards positive damping, the greater the compressor's tendency towards instability, then the greater will be the control effort required to stabilize the entire system. A simple measure of the compressor's tendency towards instability is the magnitude of the positive compressor slope at which the compressor is operating. The greater the desired positive compressor slope (to achieve an extension of compressor flow range on the positively sloped portion of the characteristic), the greater the positive damping (or control power) required from the actuator to maintain system stability.

Hendricks and Gysling [10] quantified this effect to some extent in their analysis of various alternative actuation schemes (see also Section 2.6.1). Given that the controller gain relates the magnitudes of the actuator perturbations and the sensed compressor perturbations, Hendricks and Gysling showed that for a particular low speed machine, the controller gain was numerically similar to the slope of the compressor characteristic at the desired (unstable) operating point. As an example, a controller gain of 4 would introduce actuator mass flow perturbations four times larger than the measured compressor mass flow perturbations, and the compressor could be stabilized up to positive compressor slopes of about 4. Tryfonidis [9] analyzed experimental data of the pre-stall behavior of several high speed axial compressors. His investigation showed that the ambient pre-stall static pressure perturbations (and similarly mass flow perturbations) for high speed machines are typically on the order of 1%. Just to prevent these perturbations from growing at the stall point would require an actuator control power of 1%. If, however, the compressor is to be operated on the unstable portion of the compressor characteristic, more than this amount of control power is required. Assuming a controller gain of 5 to be reasonable (able to stabilize positive compressor slopes of about 5), the required actuator control power would be in the region of 5% of the total compressor mass flow. Although the quantitative details of the analysis by Hendricks and Gysling are bound to change with a different compressor, the qualitative arguments still hold. Thus, for a compressor operating under feedback control, increasing the unstable compressor slope by a certain factor will require greater control power approximately proportional to that factor.

In real control systems, actuators are subject to saturation which is caused by limiting physical processes within the actuation device (e.g. limited coil current capability). For a given actuator control power, there is a maximum system disturbance level that will cause the actuator to saturate, limiting how well the system can be controlled. Clearly, it is desirable to design the actuator to have greater control power than will be required to respond to typical disturbances. If a typical system disturbance is on the order of 1% (as suggested by Tryfonidis), and a controller gain of 5 is used, the actuator should have a control power equivalent to at least 5% of the

compressor mass flow.

Epstein et all [2] showed that the average (over a cycle) net mechanical power (ANMP) required to control compressor instability in surge is given by

$$\frac{ANMP_c}{mean\ compressor\ power} = \frac{\bar{\eta}_c}{2\pi}\int_0^{2\pi}(\frac{\delta\psi}{\bar{\psi}})(\frac{\delta\phi}{\bar{\phi}})dt \tag{2.1}$$

where $\bar{\eta}_c$, $\bar{\psi}$ and $\bar{\psi}$ are the mean compressor efficiency, pressure rise and flow coefficient. It can be seen that, depending on the perturbation size, the control power required to stabilize the compressor can be several orders of magnitude lower than the mean compressor power. Although the same derivation was not done for rotating stall, it can be argued that each circumferential element of a compressor operating in (small amplitude) rotating stall will obey the above relation, therefore the annulus averaged result will be identical. The important point here is that the ambient compressor perturbation level, and not only the overall power of the compressor, determine the size of the required actuator control power. Inlet distortion is a source of external compressor excitation, therefore it is expected that the control power requirements for a compressor with inlet distortion will be greater than that of the same machine operating with clean inlet flow. The actual control power required will depend on the specific perturbation level, as well as the magnitude of the positive compressor slope at which it is desired to operate the compressor.

2.4 Bandwidth requirement

In low speed axial flow compressors, the rotating stall cell angular frequency is typically around 50% of the rotor angular frequency. Theoretical studies by Hendricks et al [11], Bonnaure [12] and Feulner [13] showed that, for a high speed compressor, rotating stall modes exist with poles (natural frequencies) around 50% and 100% of the rotor rotational frequency, these being called the 'incompressible' and 'compressible' modes respectively. Since high speed axial compressors typically have blade tip Mach numbers much greater than low speed machines ($M_{tip} = 1$ as opposed to $M_{tip} = 0.3$),

but more or less the same diameter, the rotor rotation frequency is much greater for high speed machines than for low speed machines. Thus, all other things being equal, the bandwidth requirement for control of a high speed machine should be (3 times) higher than that of a low speed machine.

Considering first the 'incompressible' mode of a high speed machine, and assuming that a typical rotor frequency for such a machine (e.g. NASA Stage 35) is around 300 Hz, a rough estimate for the minimum bandwidth requirement of actuation can be obtained. Using a simple rule of thumb that the rotating stall cell speed is 50% of the rotor rotational frequency, a minimum actuator bandwidth of 150 Hz is required to control the first spatial Fourier harmonic (if modal control is implemented), and 300 Hz for the second harmonic.

Concerning the 'compressible' mode of a high speed machine, the theoretical predictions of Hendricks et al [11], Bonnaure [12] and Feulner [13] were confirmed by Tryfonidis [9], who investigated pre-stall experimental data from several different high speed compressors and found the 'compressible' mode to exist just prior to stall. Thus, assuming a rotor frequency of 300 Hz, this implies that the minimum actuator bandwidth requirement for control of the 'compressible' mode is 300 Hz.

If the rotating stall disturbance growth rate is much smaller than the disturbance frequency (i.e. the real part of the eigenvalue associated with the disturbance is much smaller than the imaginary part), then compressor stabilization requires an actuator bandwidth just greater than the disturbance frequency. If, however, the disturbance growth rate is comparable to the disturbance frequency, additional actuator bandwidth is required to stabilize the system (recall that the disturbance frequency is given by the modulus of the eigenvalue associated with the disturbance). There is also an inherent trade-off between actuator bandwidth and control power. If an actuator has a physical performance limitation (e.g. coil current), the bandwidth of the actuator is a function of the rise time to a specified level of actuation. If this required level of actuation (control power) is reduced, the rise time will also be reduced, thus increasing the bandwidth of the actuator. Thus, if the disturbance growth rate is small compared to the disturbance frequency (small negative damping), actuator

control power (which will translate into positive damping) can be traded for actuator bandwidth, to keep up with the disturbance to be controlled.

Taking the worst design case to be the control of a 'compressible' mode, a minimum actuator bandwidth of 300 Hz is required. Assuming that the compressor will exhibit slowly growing modal perturbations, any actuator bandwidth greater than 300 Hz should allow some degree of stabilization to be achieved. In practice, the actuator bandwidth is usually made greater than the highest (plant) frequency to be controlled, since some bandwidth margin is required to give the control system robustness against unmodelled dynamics, sensor noise and external disturbances. For lack of better design rules, a 'safety factor' of 1.5 yields an actuator bandwidth specification of around 450 Hz.

2.5 Circumferential distribution of actuation

As discussed in Section 1.3, it is desirable that the actuation for rotating stall control be able to perturb the compressor flow field in a circumferentially distributed fashion. One way of doing this would be to have a single actuator modifying the structure of the rotating stall cell as it passes by. Another approach, and the one taken up to this point, is to use multiple actuators distributed around the annulus, all able to simultaneously alter the compressor flow field in their immediate vicinity. This scheme has bandwidth advantages since it is not necessary to wait for the stall cell to come around to the actuator before a control perturbation is commanded. If a modal control scheme is implemented, a minimum number of actuators is required to synthesize a given spatial harmonic disturbance. The number of actuators N_A is given by the Nyquist criterion, namely $N_A = 2N + 1$, where N is the number of spatial harmonics. Thus, for example, to be able to control 3 harmonics, a minimum of 7 actuators is required. In practice, however, the number of actuators is chosen to be greater than this to take account of aspects such as harmonic distortion due to a finite number of actuators. The experiments done at the MIT GTL up to this point have used 12 actuators, this number allowing 3 spatial harmonics to be controlled

with some contingency.

2.6 Past work on actuation

Before proceeding with the development of a candidate actuation scheme, it is instructive to see what work has been done by others in the field of actuation for the active control of rotating stall in axial compressors. What is particularly relevant is a comparison of various actuation schemes with respect to control power and bandwidth capability.

2.6.1 Comparison of various actuation schemes

A theoretical study by Hendricks and Gysling [10] investigated the merits of several different actuation and sensing schemes in low speed compressors. The candidate actuators included variable IGV's (see also Figure 1-6), bleed valves and jet injection or intake ports, the latter two being illustrated schematically in Figure 2-2. Using the linearized small perturbation rotating stall model by Moore [5] to represent the plant (compressor), and a simple proportional feedback law for the controller (with variable gain and phase), they calculated the maximum positive (unstable) compressor slope that could be achieved for each actuation scheme. Figure 2-3 shows the maximum positive compressor slope that can be actively controlled (system neutral stability point) for various controller phase angles. Obviously, the larger the combination of positive (unstable) compressor slope and phase margin (i.e. the area within the neutral stability boundary), the more robust the control system will be. Clearly the upstream jet actuator is the superior actuation device here because it can achieve the highest positive compressor slope over a broad range of phase angles.

2.6.2 Dynamic control using tip injection

Day [3] used a dynamic control system employing fluid jet injection at the rotor tip, as was mentioned in Section 1.3.1. Figure 2-4 shows one of an array of 12

jets located less than a blade chord ahead of the rotor tip. The jets were switched on or off by opening and closing the trapdoor-style hinged valves. Although this on/off modulation of the actuation does not fit well into the existing linear continuous system modeling of rotating stall, Day was able to demonstrate how the tip injection scheme could extend the stable operating envelope of the compressor (a 6% increase in compressor flow range was achieved). Since the short length-scale disturbances that were most successfully controlled by the injection scheme originated in the tip region of the compressor, the scheme seems to work by altering the fluid mechanics in the tip (clearance vortex) region of the rotor. The injectors employed by Day could be rotated to vary the azimuthal injection angle, however, no mention of the result of this variation is made.

2.6.3 Jet injection using aeromechanical feedback

Gysling [8] used an aeromechanical feedback system to stabilize the flow in a low speed axial compressor, as was mentioned in Section 1.3.3. The reed valve mechanism used in this feedback system is shown in Figure 2-5. Static pressure perturbations acting on the surfaces of the reed valves cause them to deflect, thus allowing different amounts of injectant (and hence axial momentum) to be introduced into the compressor upstream flow field. The stabilizing effect can be understood qualitatively in a quasi-steady sense as follows. Flow in the upstream duct that has lower axial velocity will have a higher static pressure, since the far upstream total pressure is constant. The higher static pressure acting on the reed valve will cause it to deflect, thus injecting greater axial momentum into the upstream flow field. The increased momentum and mass flow result in a greater pressure rise of the compressor (at least in areas of the compressor map where the compressor slope is positive). The local increased compressor pressure rise causes the local axial flow to increase, since the far upstream total and far downstream static pressures have remained the same. The tendency of the injection system is thus to restore perturbations in axial velocity to zero. The aeromechanical feedback control system is limited in certain respects since the control law implemented by the feedback system is very much a function

of the specific hardware implementation, i.e. pressure sensing reed valves can only provide one type of control law or compensation. Furthermore, because the reed stiffness, damping and other physical parameters of the injection hardware are fixed, the design can only be optimized for one operating point of the compressor. Since changes in compressor wheel speed, as well as flow coefficient may require different optimum values for these parameters, the aeromechanical feedback control system is limited in its operating range. This may not be a problem in practice (especially if the optimum parameter values are not sensitive to changes in operating condition), however, it would seem to be more desirable (at least from a research point of view) to separate the role of actuator, sensor and control law, so that each can be optimized individually, and for different compressor operating conditions. In his theoretical optimization of the aeromechanical feedback control system, Gysling only stabilized the first two spatial harmonics due to the fact that the optimum parameters for each spatial harmonic differed somewhat. It would therefore appear desirable to have a control law that can be easily changed and optimized, the simplest way of doing this being a computer (digital) implementation of the controller, where changes in the control law and controller parameters can be made by altering the software.

2.7 Selection of a candidate actuator

From Section 2.6 it appears that the jet actuator offers the greatest advantage in terms of control power and robustness as an actuation system for the control of low speed axial compressors. The theoretical study of high speed compressor stability done by Hendricks et al [11] showed that there is both an 'incompressible' (rotating at about 50% of the rotor frequency) as well as 'compressible' (rotating at about the rotor frequency) mode in high speed machines. It is expected that the low speed actuator/sensor study by Hendricks and Gysling [10] would be applicable at least to the 'incompressible' mode of a high speed machine. Since this study clearly favors the jet actuator, and without having more information about the effect of different actuation schemes on the 'compressible' mode of a high speed machine, it would seem

wisest to proceed with the development of a jet actuator.

One of the key factors determining the frequency response of any mechanical system is the actual physical dimension of the system (this is because inertia scales with the cube of the length scale). A bleed valve actuation system is very attractive from the point of view of an aero-engine application, since an existing engine could conceivably be retro-fitted with the new actuation system. However, for this research the bleed valve system was not so attractive since the compressor on which the actuation scheme would be implemented was only a single stage machine. For a given actuator mass flow, the physical size of the actuator would have been large to account for the low supply pressure (compressor discharge pressure) to the actuator. This argument does not apply to multistage high pressure compressors which have high exit pressures, however in this case, the high temperatures associated with the high pressures at the exit of the compressor (adiabatic compression) make the implementation of a mechanical valve more complicated.

In the case of variable IGV's, rotating large airfoil sections through several degrees of angular rotation at high frequency will require substantial torque. This implies using a large motor, which may be bandwidth limited due to its physical size.

Based on the constraints mentioned above, it was felt that the jet actuator offered the route of least technical risk to meet the control power and bandwidth requirements of actuation for the control of a high speed single stage research compressor. Modulation of high pressure, yet low temperature, injectant can be achieved using a simple valve of small dimensions. The small physical size of the valve would allow a small servo motor to be used, and hence high bandwidths to be achieved. Concerning spatial distribution of actuation, all the alternative actuation schemes can be distributed circumferentially, therefore no particular limitation was presented by any of the actuation schemes in this regard. Because the design process is an iterative one, some of the issues discussed in the remainder of this chapter are as relevant to the decision to adopt the jet actuator as the arguments presented up to this point. It should also be noted that some of the analyses presented in subsequent sections use design data (flow rates, physical dimensions, etc.) from the final actuator design.

This is inevitable since the design process is iterative, and it is virtually impossible to present the design process in a chronological single-pass fashion. Therefore, for the sake of consistency, the final design is the relevant case in all subsequent analyses.

2.8 Implementation constraints for jet actuators

Having chosen the jet actuator as the candidate actuation scheme, it is necessary to investigate which factors will be critical to the successful development of the actuator. Some of the constraints imposed are fundamental, and cannot be overlooked, while others concern practical implementation issues which are subject to alteration as a result of design compromise. One of the primary considerations for the jet actuator design is how much radial or circumferential spreading of the jet is desirable, and how much can realistically be achieved. The effect of meridional and azimuthal injection angle of the jet is therefore investigated, to find its effect on the radial and circumferential spreading of the jet. Since jet spreading requires some axial distance in which to take place, time delays are introduced into the feedback control loop by the finite convection time taken for the injectant to travel from the actuator to the compressor. Lastly, there are additional practical constraints on the implementation of a jet actuator such as those caused by noise, blade vibration and blockage of the compressor flow path. A detailed discussion of the constraints imposed on jet actuation now follows.

2.8.1 Radial mixing of the jet

The theoretical models presented by Gysling [8], and Hendricks and Gysling [10] both assume that the injectant and upstream flows mix out before reaching the compressor face. In a real application, unless the actuators are situated very far upstream of the compressor, the injectant may not be mixed out radially when it reaches the compressor face. It is therefore instructive to see whether any benefits arise from an unmixed radial distribution of flow.

One of the reasons that the speed lines of a high speed compressor bend over near

the peak of the compressor characteristic is that the passage blockage is increased in the rotor tip region at low flow coefficients (increased blockage leads to higher rotor relative exit flow velocity at positive exit flow angles, resulting in less flow turning and hence less overall total pressure rise). The increased blockage is caused in part by the interaction of the tip clearance vortex with the adverse pressure gradient within the blade passage as elucidated by, amongst others, Crook [14] [15], Adamczyk et al [16] and Suder et al [17]. Especially if the adverse pressure gradient manifests itself as a passage shock in high speed machines, the rise in blockage at low flow coefficients (high loading) can be quite severe. Crook showed computationally that passage blockage could be relieved by the use of casing treatment, which exerts two main influences on the passage flow near the rotor tip. Firstly, because low total pressure fluid is sucked off at the rear of the passage, the blockage is reduced by getting rid of the fluid that is causing the blockage. Secondly, the tip leakage flow is energized by the injection of streamwise (in the blade direction) momentum by the casing treatment near the passage entrance. Concerning the design of the present jet actuator, it can be argued that injecting streamwise momentum near the tip region of a compressor would energize the tip leakage flow, reducing blockage by the same mechanism that is found to work with casing treatment. Especially in compressors that have been shown to benefit from casing treatment, this approach may be fruitful. If this is indeed the case, it would be advantageous to inject as much flow near the rotor tip as possible to reduce the tendency of the speed lines to change from a negative to a positive slope. This could be used to alter the shape of the overall steady compressor characteristic, or better still, by unsteady modulation of the injection, the effective unsteady compressor slope with feedback control could be made negative (stable), even though the steady compressor slope without feedback control is positive (unstable).

2.8.2 Circumferential mixing of the jet

It may be desirable to spread the injector flow as much as possible in the tangential direction, if the modal control approach is to be adopted. Since injectant flow that is

unmixed in the tangential direction will give rise to higher spatial harmonic content, which may be of similar magnitude to the desired commanded harmonic, the compressor response will not match that of the theoretical (linear) models used in the controller algorithm, if these assume no spatial harmonic distortion. Depending on how sensitive the compressor (plant) as well as the controller are to this harmonic distortion, there will be a decrease in the robustness of the control system. Furthermore, unmixed velocity peaks in the circumferential direction will lead to noise and blade vibration (and subsequent blade fatigue) due to the interaction of the moving blades with the varying total pressure regions around the annulus, this being undesirable from an operational point of view.

2.8.3 Convective time delays

Attempting to locate actuators far upstream of the compressor to ensure that the injectant flow is mixed out by the time it reaches the compressor face has some distinct disadvantages. Since it takes a finite time for the injectant to be convected to the compressor face, a time delay is introduced into any feedback control scheme that may be implemented. For open loop tests, i.e. no feedback, this is not critical since the time delay only introduces a constant phase shift between the actuator command signal and the compressor response signal. However, in the closed loop case, the time delays in the control loop will cause the system to go unstable if the system phase lag exceeds 180°. Assuming an axial flow Mach number of $M_{f_x} = 0.5$ upstream of the compressor, the convective time delay can be calculated for different actuator upstream locations, these time delays corresponding to different phase lags at various frequencies. Figure 2-6 shows that, if an actuator bandwidth of 500 Hz is assumed, convective phase lag exceeds 180° for upstream actuator locations of more than 300 mm. Since the compressor, sensor and controller combination will also have some phase lag (assume 60°), it can be reasoned that in order to maintain a reasonable system phase margin for robustness (probably on the order of 60°), the actuator convective phase delay should be less than 60°. At 500 Hz, this corresponds to an upstream location of the actuator of just more than 100 mm. It is clear that

there is a trade-off in actuator axial placement caused by the opposing requirements for flow uniformity and actuator frequency response.

2.8.4 Penetration of an oblique jet

Assuming that it is not possible to mix out the jet completely by the time it reaches the compressor face, a question that can be asked is how far the jet will penetrate radially (or circumferentially) into the freestream in a given axial distance. Since the axial actuator location upstream of the compressor will be set primarily by convective time delay considerations, it is interesting to see how this impacts on the radial (or circumferential) penetration of an unmixed jet. Figure 2-7 shows a meridional view of an inclined jet entering a freestream, calculated using an empirical relation given by Ivanov [18].

$$\frac{x}{d} = \left(\frac{q_{f_s}}{q_{oj}}\right)^{1.3} \left(\frac{y}{d}\right)^3 + \frac{y}{d}\cot\beta \tag{2.2}$$

where q_{f_s} is the freestream dynamic pressure, q_{oj} is the jet dynamic pressure at the jet nozzle exit, β is the meridional injection angle, and $\frac{y}{d}$ and $\frac{y}{d}$ are the jet centerline coordinates non-dimensionalized by the injecting nozzle diameter, d_o. Abramovich [18] approximates the cross-section of the jet by an ellipse with an aspect ratio of 5, and a major axis dimension that is given by

$$h = 2.25d_o + 0.22l \quad \text{where } l \text{ is the arclength along the jet centerline} \tag{2.3}$$

For the sake of simplicity, the freestream axial Mach number is assumed to be $M_{f_s} = 0.5$ (typical of high speed axial compressors), while the jet exit Mach number is assumed to be unity (convergent nozzle). The penetration of the jet into the freestream is governed by three main parameters, namely the ratio of jet to freestream momentum flux, the jet exit diameter, and the meridional injection angle. The momentum flux ratio is set by specifying the jet and freestream Mach numbers, while the jet exit diameter is set by the desired mass flow to be passed by the jet (18 mm in this case).

The only parameter left to be altered is the injection angle, the effect of this variation being shown in Figure 2-7. Increasing the meridional injection angle increases the relative radial penetration, especially at small axial distances from the actuator. Assuming the axial location of the actuator to be 100 mm upstream of the compressor face (to keep convective delays low), no more than 80 mm of penetration can be obtained. It should be noted at this stage that there are undesirable side-effects associated with high meridional injection angles. Since a perpendicularly injected jet has no axial momentum, it has to be 'bent' by the freestream to become parallel to the freestream. This creates a low momentum wake behind the jet in all regions where the jet is not yet parallel to the freestream. Even if the injection is not perpendicular to the freestream, there is always still a wake which manifests itself as a horseshoe vortex, similar to that shown in Figure 2-8. Only at very small injection angles (less than 30°) is this effect negligible. It must therefore be borne in mind that addition of mass and momentum at large radial depths will be accompanied by the formation of a wake at lesser depths.

2.8.5 Injector azimuthal flow angle

Since the jet actuator is injecting flow into a circumferentially moving blade row, the relative total pressure of injectant flow entering the blade row will vary depending on the azimuthal angle of injection. This is because the absolute tangential injection velocity increases significantly as the azimuthal injection angle is increased from zero (in the axial direction). Section 2.2 showed that the swirl imparted (in a direction opposite to the rotor rotation) to the upstream flow field of the compressor can be exploited to obtain an increase in compressor pressure rise, over and above that caused by the introduction of mass and axial momentum to the compressor upstream flow field. However, introducing injectant flow into the blade row at a flow angle other than the design flow angle, may lead to significant total pressure losses due to inlet flow misalignment with the blades (in the rotor relative frame). Especially at higher rotor relative inlet Mach numbers, where the total pressure loss buckets are very sensitive to inlet flow misalignment, the losses associated with a misaligned injectant

flow could be very large. The azimuthal injection angle should therefore be chosen such that it maximizes the overall compressor pressure rise for a given injection. This is best done experimentally, or by predicting the pressure rise characteristic of the compressor with injection using a CFD simulation.

2.8.6 Modulation of jet actuators

Since valves cannot be opened 'negatively', a mean injection rate, with modulation around this mean, is required to create both positive and negative perturbations in the compressor flow field. Positive and negative flow perturbations are required if continuous (or linear) control techniques are to be used to stabilize the machine. To obtain the greatest modulation for a given mean injection, it is desirable to make the mean injection half of the maximum injection, the modulation thus ranging between zero and the maximum.

2.8.7 Noise and blockage constraints

On high speed machines, especially the front fan of a bypass engine, having actuators that protrude into the flow upstream of the compressor will cause a wake interaction with the rotor, as well as flow blockage of the annulus. The wake interaction may be undesirable not only for acoustic reasons (siren effect of rotor blades chopping up a wake), but also because it may lead to blade vibration, fatigue and ultimate blade failure. Concerning flow blockage, because of the relatively high axial Mach numbers typical of high speed machines, the choking cross-sectional area of the machine is not very much smaller than the actual cross-sectional area. If the upstream flow path is blocked too much by the protruding actuators, the choking cross-sectional area could be reached, making it impossible to increase the flow through the compressor, and thus preventing the compressor from being 'started'.

2.9 Jet actuator conceptual design

To make the actuator development easier and more flexible, the actuator was divided into two distinct components, namely a valve and an injector. The function of the valve is to modulate the mass flow entering the injector, while that of the injector is to distribute the mass flow into the compressor in a suitable fashion. Figure 2-9 shows schematically how the valve and injector components are combined into the overall actuator. The valve modulates mass flow into the injector plenum, the flow then passing through the injector nozzle to the compressor flow field (not shown). The reason for this modular design approach is the following. Since the actuator not only modulates flow, but also has to introduce that flow into the compressor flow field, it is useful to separate the mechanical design of the actuator along the same boundaries as the functional design. Secondly, because the actuator development was quite empirical (especially the injector development), it was convenient to use a design that allowed various different injection schemes to be tested. Lastly, because it is usually easier to solve engineering problems one at a time, using a modular approach allowed the two main components of the actuator to be 'perfected' separately.

The valve orifice is designed to be a choked orifice, with an essentially linear relationship between mass flow and valve opening. The injector nozzle design is more subtle. If a convergent-divergent nozzle is used, as would be best to achieve the highest possible injector jet velocity and hence jet momentum, a complex shock structure will be present inside and outside the nozzle as the actuator is modulated from minimum to maximum flow. Having normal shocks popping in and out of the nozzle is bound to cause some form of non-linearity, therefore the injector nozzle was designed with only a convergent section to circumvent this problem. At maximum flow the nozzle exit area was chosen to just choke the nozzle , i.e. $M_3 = 1$, in order to get the maximum jet momentum without shock interactions. It will be shown later that the injector nozzle exit area is determined as much by dynamic frequency response considerations as by steady flow considerations.

2.9.1 Control power and bandwidth specification

Sizing the actuator in terms of mass flow capability was one of the first tasks of the actuator development. The number of actuators was chosen to be 12 since this was the number used on previous rotating stall experiments at the MIT GTL (able to control the first 5 spatial harmonics in theory). As it turns out, it would have been difficult to fit more actuators onto the casing of NASA Stage 35 or a similarly sized compressor, therefore this choice was justified.

Tryfonidis [9] found that the pre-stall perturbations of several high speed machines are typically in the region of 1%, while Gysling [8] observed the same perturbation level during his experiments on a low speed machine. Noting that the control power chosen by Gysling for his actuation system was 4% of the total compressor mass flow, it seems reasonable to assume the total mass flow of the proposed high speed compressor actuation scheme to be 5% of the total compressor mass flow (note that Day [3] only used a 1% control power and was still able to extend the operating range of a low speed compressor by 6%). The stalling compressor mass flow rate for NASA Stage 35 (high hub to tip ratio) is 20 $kg.s^{-1}$, while that for NASA Stage 67 (low hub to tip ratio) is 30 $kg.s^{-1}$. Assuming the mass flow rate for a typical high speed machine to be around 25 $kg.s^{-1}$, and that there are 12 individual actuators that have a cumulative mass flow of 5% of the total compressor mass flow, an individual actuator flow rate of about 0.1 $kg.s^{-1}$ is calculated.

Assuming the desired control case to be the 'compressible' mode of a high speed compressor with a rotor rotational frequency of 300 Hz, and using a 'safety factor' of 1.5, an actuator frequency of 450 Hz is required. As it turns out, the actuator bandwidth requirement was really hard to satisfy, therefore the initial approach was to do the best possible, and then to see if that was enough (the final actuator design has a bandwidth of 400 Hz).

2.9.2 Steady modeling of the jet actuator

Having assumed the valve orifice to act like a choked orifice (this being almost inevitable with the 700 kPa upstream pressure envisioned for this valve), the choked valve orifice area can be sized. Furthermore, assuming a convergent injector nozzle just choked at the maximum flow rate, the injector nozzle exit area can be calculated.

Valve orifice sizing

The mass flow through the valve orifice is given by

$$\dot{m}_1 = \frac{p_1}{RT_1} A_1 M_1 \sqrt{\gamma R T_1} \tag{2.4}$$

where

$$T_1 = \frac{T_{t1}}{(1 + 0.2M_1^2)}$$

and

$$p_1 = \frac{P_{t1}}{(1 + 0.2M_1^2)^{3.5}}$$

For a choked orifice with $M_1 = 1$, and upstream flow conditions of $T_{t1} = Tt_0 = 293K$ and $P_{t1} = P_{t0} = 8E5Pa$ (100 psig), the valve orifice area is $A_1 = 54mm^2$.

Injector nozzle sizing

The mass flow through the injector nozzle is given by

$$\dot{m}_3 = \frac{p_3}{RT_3} A_3 M_3 \sqrt{\gamma R T_3} \tag{2.5}$$

If the injector nozzle exit static pressure is taken to be that which exists in a freestream flowing at $M_{f_s} = 0.5$, then $p_3 = 85400Pa$. The total temperature of the flow passing through the actuator is constant since no work or heat transfer is done on the flow, thus $T_{t3} = T_{t1} = T_{t0} = 293K$. This yields

$$T_3 = \frac{T_{t3}}{(1 + 0.2M_3^2)}$$

The injector nozzle exit area is found to be $A_3 = 261mm^2$, or in the case of a circular hole nozzle, $d_3 = 18mm$.

2.9.3 Dynamic modeling of the jet actuator

The dynamics of the actuator are governed primarily by the dynamics of the injector and the servo motor driving the valve, and not by those of the valve itself. This is because the flow length scale of the valve orifice is very small (a few mm), while the characteristic velocity is fairly high (several hundred $m.s^{-1}$), thus essentially the valve acts in a quasi-steady fashion for the actuator frequencies of interest (0 - 500 Hz). Ignoring the frequency response of the valve servo motor for the moment, two limiting cases can be investigated when trying to determine the frequency response of the injector. The first case deals with an injector that is very long, so that acoustic propagation times within the injector become relevant. This case would apply to actuators where the injector nozzle is located far from the valve orifice by implementation constraints. The second case deals with an injector that has negligible acoustic delays in the injector plenum, the dynamics of the injector being determined primarily by the volume of the injector plenum.

Acoustic duct model

Figure 2-10 shows how the actuator can be modeled as an acoustic duct to investigate its unsteady dynamics. Assuming the limiting case where the ratio of plenum length to plenum volume is large, the acoustic duct analysis is appropriate. The following linearized inviscid equations relate the upstream and downstream variations in flow properties for an acoustic duct.

$$\begin{bmatrix} \tilde{p_1} \\ \rho_1 a \tilde{U_1} \end{bmatrix} = \begin{bmatrix} \cos\omega\tau & -j\sin\omega\tau \\ -j\sin\omega\tau & \cos\omega\tau \end{bmatrix} \begin{bmatrix} \tilde{p_3} \\ \rho_3 a \tilde{U_3} \end{bmatrix} \tag{2.6}$$

where

$$\tau = \frac{l}{a}$$

The variation in exit pressure $\tilde{p_3}$ can be set equal to zero since the jet exits into ambient conditions.

$$\rho_1 a\tilde{U_1} = cos(\omega\tau)\rho_3 a\tilde{U_3}$$

The following transfer function is obtained if the variation of flow density and acoustic speed is assumed to be of secondary importance.

$$\tilde{U_3} = \frac{\tilde{U_1}}{cos(\omega\tau)} \tag{2.7}$$

Figure 2-11 through Figure 2-13 show the frequency response of the acoustic duct transfer function for duct (injector) lengths of l = 50 mm, 100 mm and 150 mm respectively. Clearly, as the duct length is increased, so the high frequency response of the system deteriorates. Although the analysis is highly idealized (linearized equations, constant acoustic speed and fluid density), it does indicate at what frequencies resonance is likely to occur. Since it is undesirable to have sudden changes in phase occurring in the design frequency range of the actuator, it is best to keep the duct lengths shorter than the first critical value. Furthermore, to avoid variations in gain (say no larger than 3dB) there is a minimum duct length for any desired operating frequency. As an example, from the figures it can be deduced that a duct of length somewhere between 50 mm and 100 mm will suffice to obtain an actuator bandwidth of around 500 Hz.

Helmholtz resonator model

Figure 2-14 shows schematically how the actuator plenum can be modeled as a Helmholtz resonator. Assuming the limiting case where acoustic delays within the plenum are negligible, the Helmholtz resonator analysis is appropriate. A mass balance across the actuator can be written as

$$\dot{m}_1 - \dot{m}_3 = V_2\frac{d\rho_2}{dt} = \frac{V_2}{a_2^2}\frac{dP_{t2}}{dt} \tag{2.8}$$

If, for simplicity, it is assumed that the exit flow is incompressible and quasi-steady, the plenum pressure and the ambient exit pressure can be related by

$$P_{t2} = p_3 + \frac{1}{2}\rho_3 U_3^2 \tag{2.9}$$

Differentiating this with respect to time, and assuming the injector nozzle exit static pressure to be constant

$$\frac{dP_{t2}}{dt} = \rho_3 U_3 \frac{dU_3}{dt}$$

Combining with equation 2.8, and ignoring the effects of flow density changes, yields

$$\frac{V_2}{a_2^2} U_3 \frac{dU_3}{dt} = A_1 U_1 - A_3 U_3$$

Taking Laplace transforms leads to the following transfer function expression from the injector inlet to exit velocity.

$$\frac{U_3}{U_1} = \frac{A_1/A_3}{(1 + \frac{V_2}{A_3}\frac{U_3 s}{a_2^2})} \tag{2.10}$$

From the expression it is clear that the injector DC gain is given by the ratio of injector inlet to exit areas (A_1/A_3), while a first-order dynamic response is strongly influenced by the ratio of plenum volume to nozzle exit area(V_2/A_3). If it is assumed that the mean exit velocity is half the speed of sound (i.e. $M_j = 0.5$) and that the speed of sound is essentially constant everywhere in the system, an expression can be obtained for the first order corner frequency in terms of the ratio of plenum volume to nozzle exit area.

$$\omega_c = \frac{a_2^2}{U_3}\frac{1}{V_1/A_3} = \frac{2a_2}{V_1/A_3} \tag{2.11}$$

It is this ratio of plenum volume to nozzle exit area which will be the primary determinant of the frequency response of the injector. Figure 2-15 shows the frequency response of an injector with a plenum length of 50 mm, and a plenum diameter twice that of the nozzle exit diameter ($d_p/d_3 = 2$). This yields a plenum volume to nozzle exit area ratio of 0.4. Although the phase starts to roll off at relatively low frequen-

cies ($-45°$ at 500 Hz), the -3dB bandwidth on the magnitude plot corresponds to the corner frequency of a first order system, namely 500 Hz. To get better frequency response it is necessary to further decrease the plenum volume, or increase the nozzle exit area.

2.10 Actuator design specifications

To summarize the various elements of the jet actuator design discussed in this chapter, it is useful to consolidate all the ideas in an actuator design specification. This specification serves as a guideline for the actual actuator development discussed in Chapter 3, 4 and 5. The design specifications have been divided into those which are essential for the implementation of rotating stall control on a high speed compressor, and those which are merely desirable. The specifications are both qualitative and quantitative, and are not listed in order of importance.

2.10.1 Essential specifications

- To keep convective time delays to an acceptable level, the actuator should not be located more than 100 mm upstream of the compressor.
- The actuator should have a maximum mass flow capability of 0.1 $kg.s^{-1}$.
- The actuator mass flow modulation should be as large as possible, namely a 0.1 $kg.s^{-1}$ modulation around a mean mass flow of 0.05 $kg.s^{-1}$.
- The actuator bandwidth should be in the region of 450 Hz.
- For open loop testing of a compressor (as well as the actuator itself) the actuator phase lag is not critical, however, for closed loop testing of a compressor it would be desirable to have as small a phase lag as possible.
- The actuator should be consistent with the implementation of a continuous (continuously variable between minimum and maximum actuation as opposed to

on/off) type of control system. This is desirable since a large body of knowledge exists on the implementation of continuous (and linear) control techniques.

2.10.2 Optional specifications

- Oblique injection can be used to obtain radial and circumferential spreading of the jet, however, large injection angles should be avoided since they lead to a wake region behind the jet.
- Various degrees of radial spreading should be included in the injector development to be able to validate (or refute) the conjectures made in Section 2.8.1.
- Circumferential spreading of the jet should be maximized to mitigate the effect of undesirable higher spatial harmonics of actuation.
- Preferably no part of the actuator should protrude into the compressor flow field.
- The jet actuator should be divided into 2 modular components, namely the valve and the injector. Each component can be designed and developed separately.

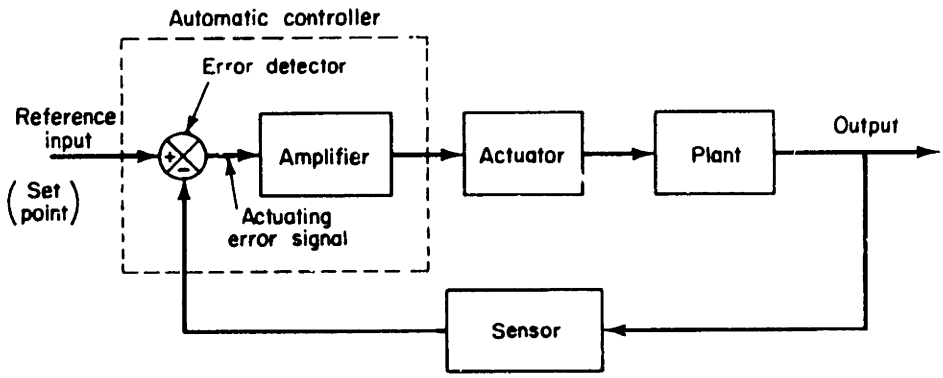

Figure 2-1: Block diagram of a control system, consisting of a plant, sensor, controller and actuator.

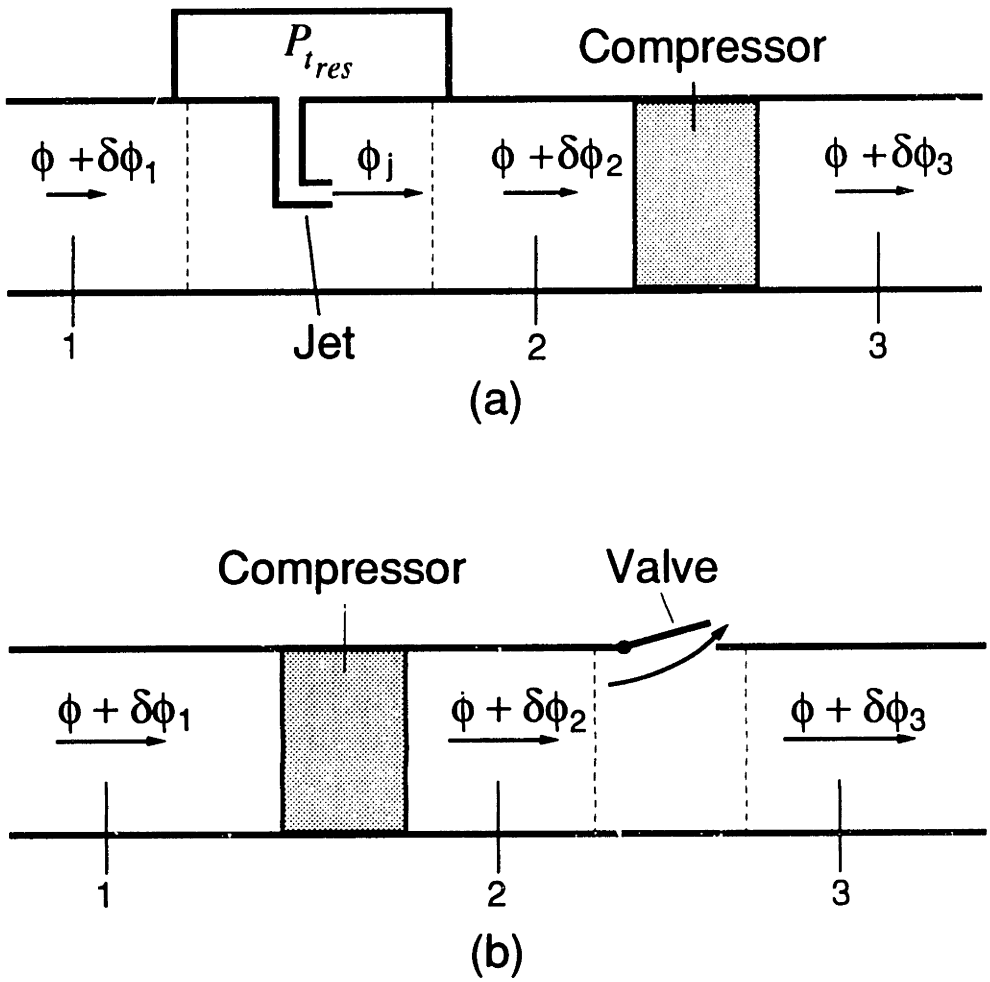

Figure 2-2: Schematic diagrams of jet injection or intake ports (a), and bleed valves (b).

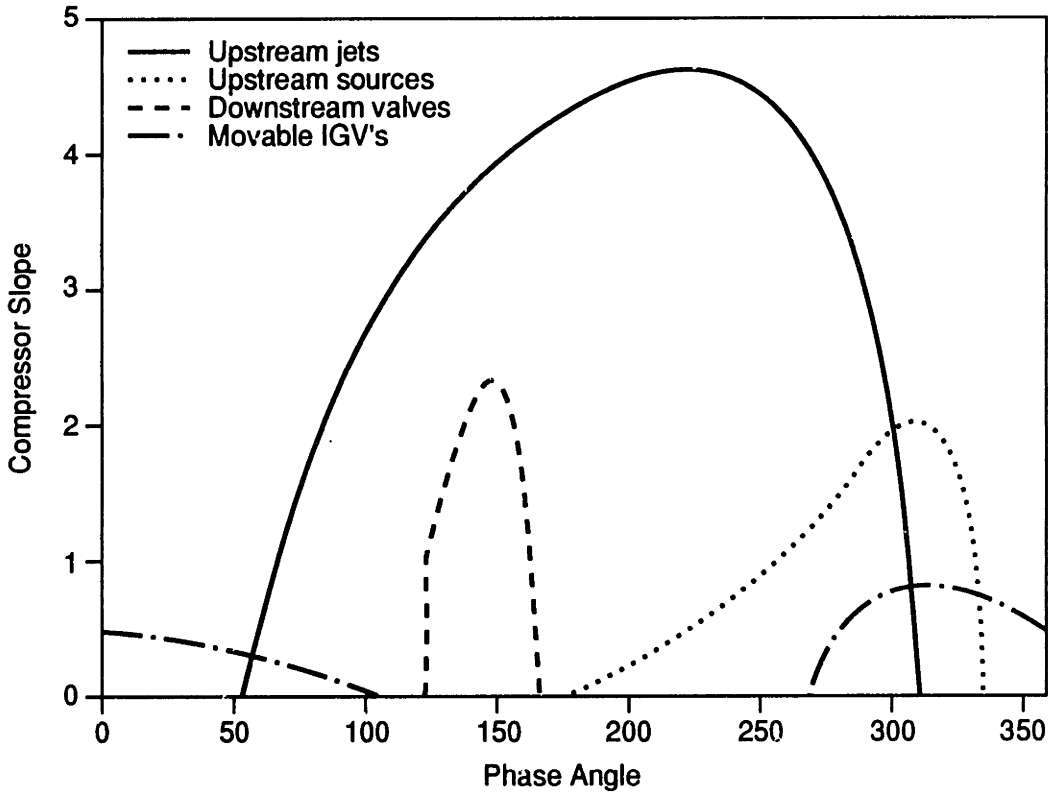

Figure 2-3: Performance comparison of the various actuation schemes. The controller gain is 4 in all cases.

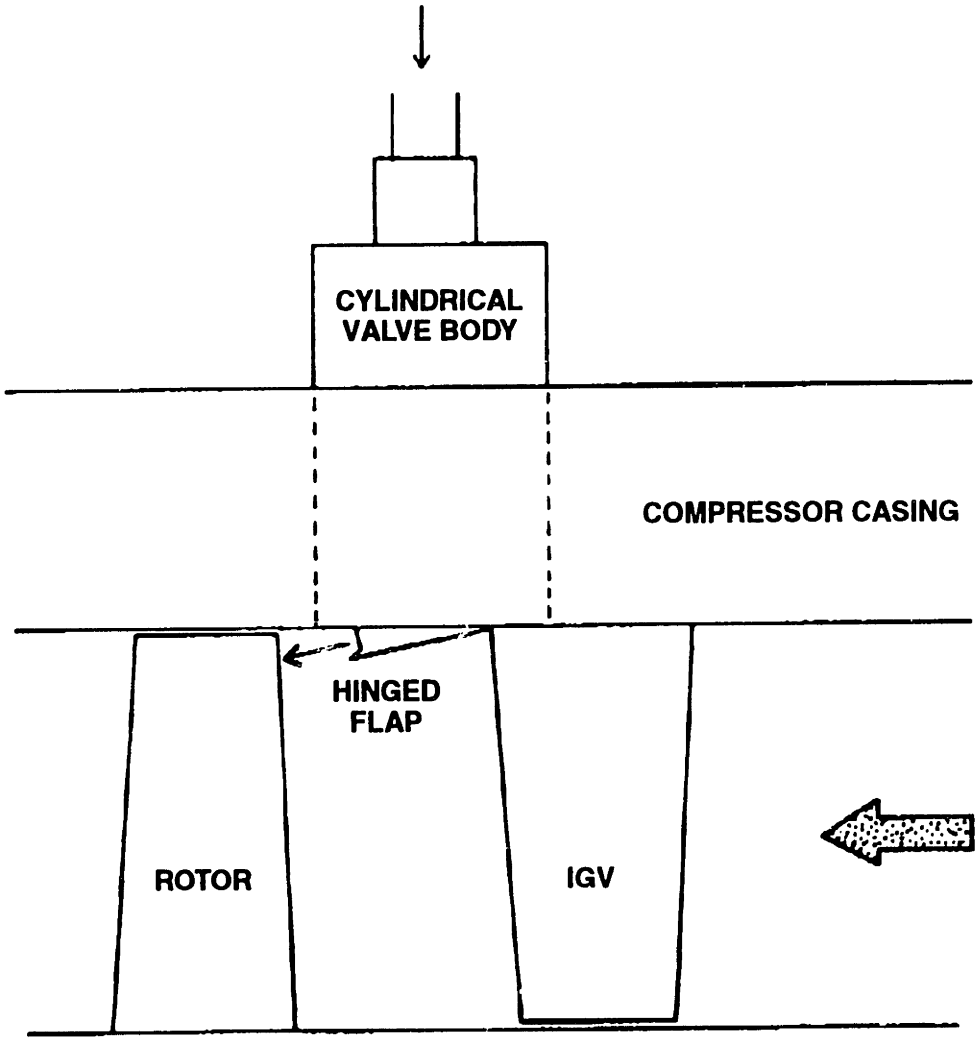

Figure 2-4: Schematic of tip injection mechanism.

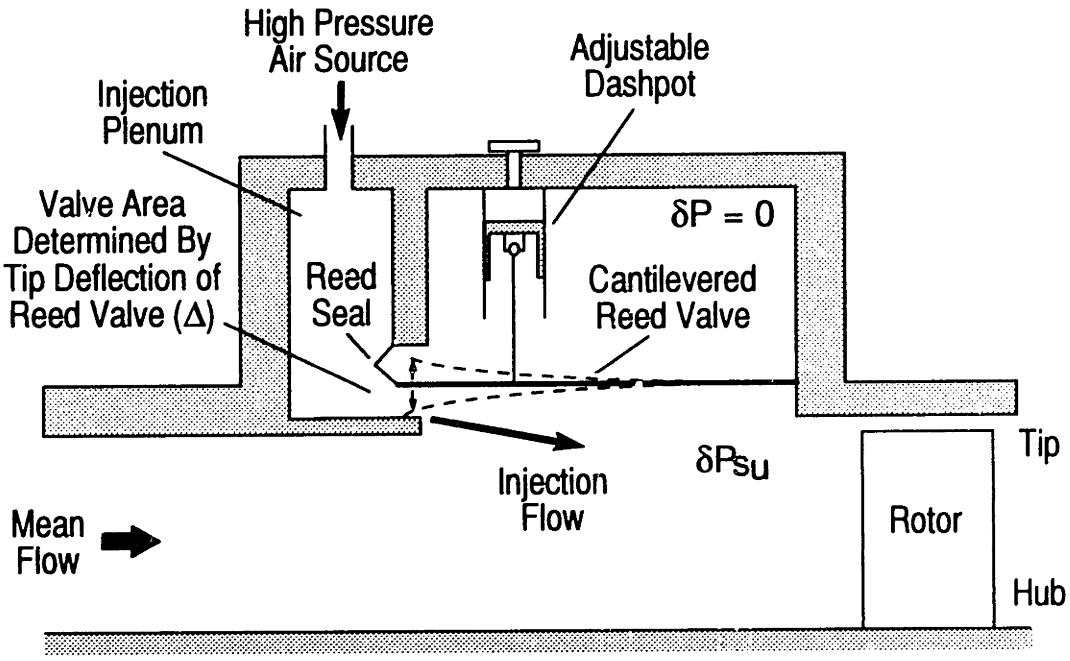

Figure 2-5: Schematic of reed valve mechanism.

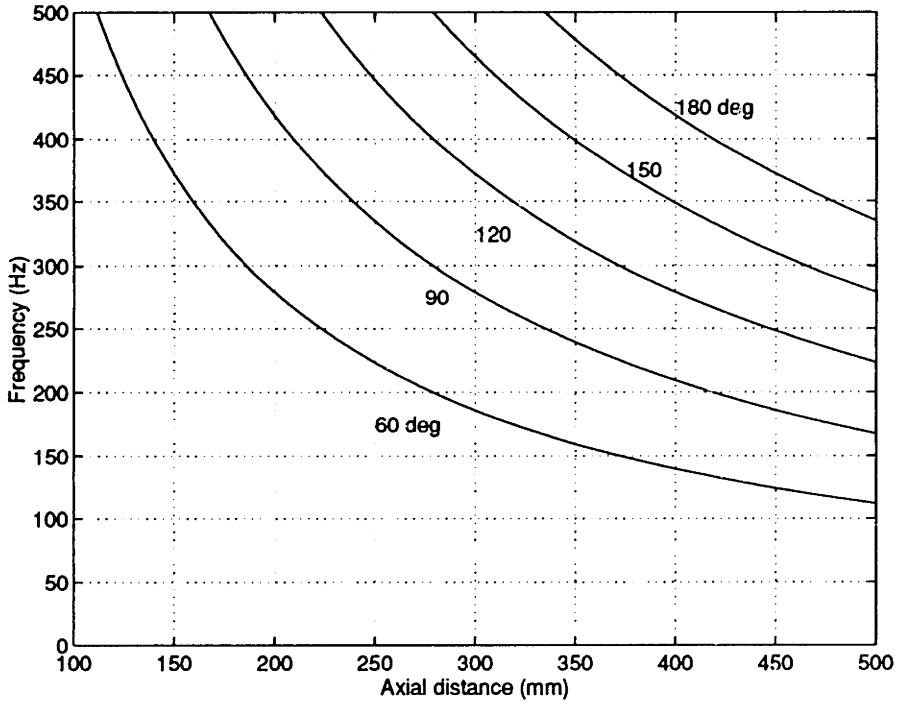

Figure 2-6: Convective delay characteristic for actuators located upstream of the compressor, $M_{f_s} = 0.5$.

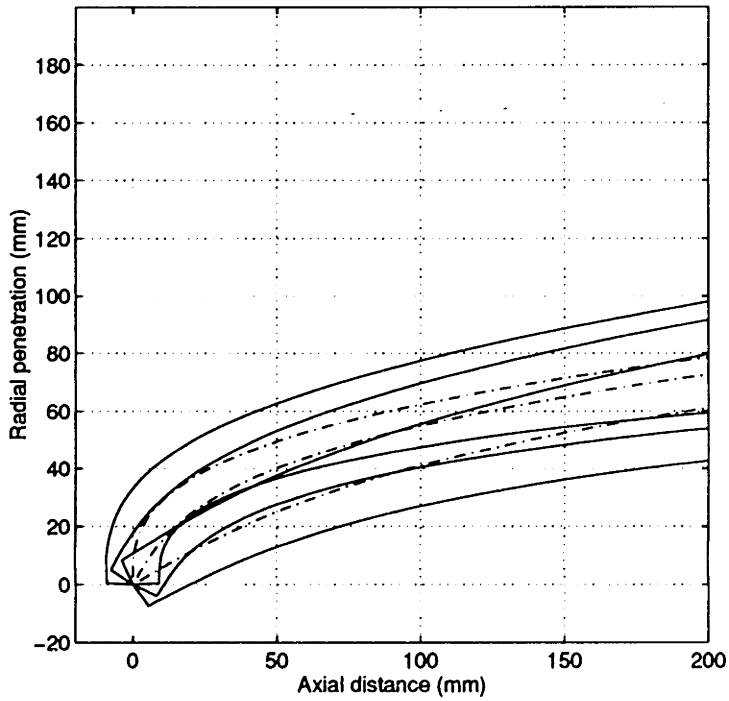

Figure 2-7: Radial penetration of an oblique jet into a freestream, $M_{f_s} = 0.5$, $M_j = 1$, $\beta = 30°, 60°$ and $90°$. Jet center-line (-.-), jet boundary (—).

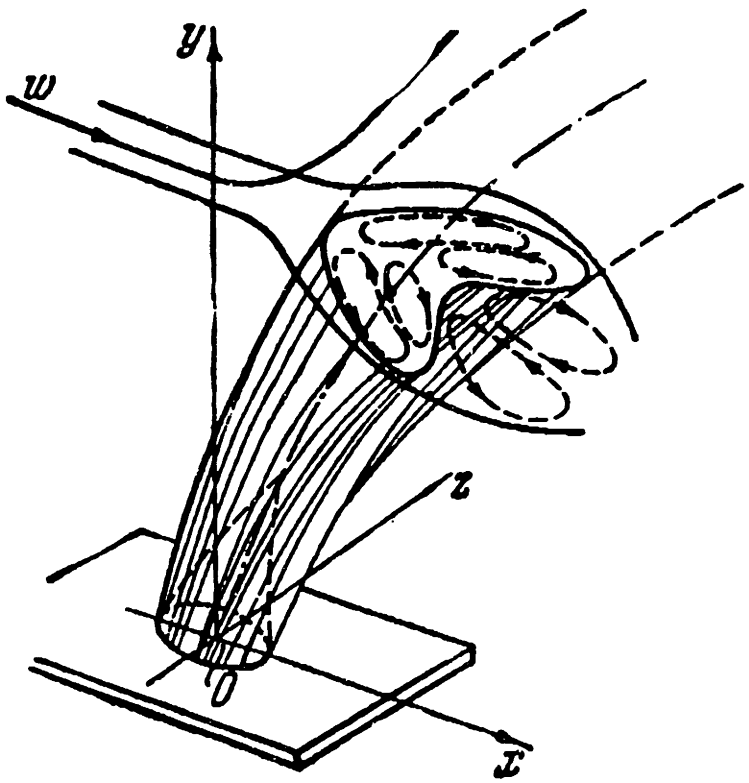

Figure 2-8: Horseshoe vortex structure of an oblique jet entering a freestream.

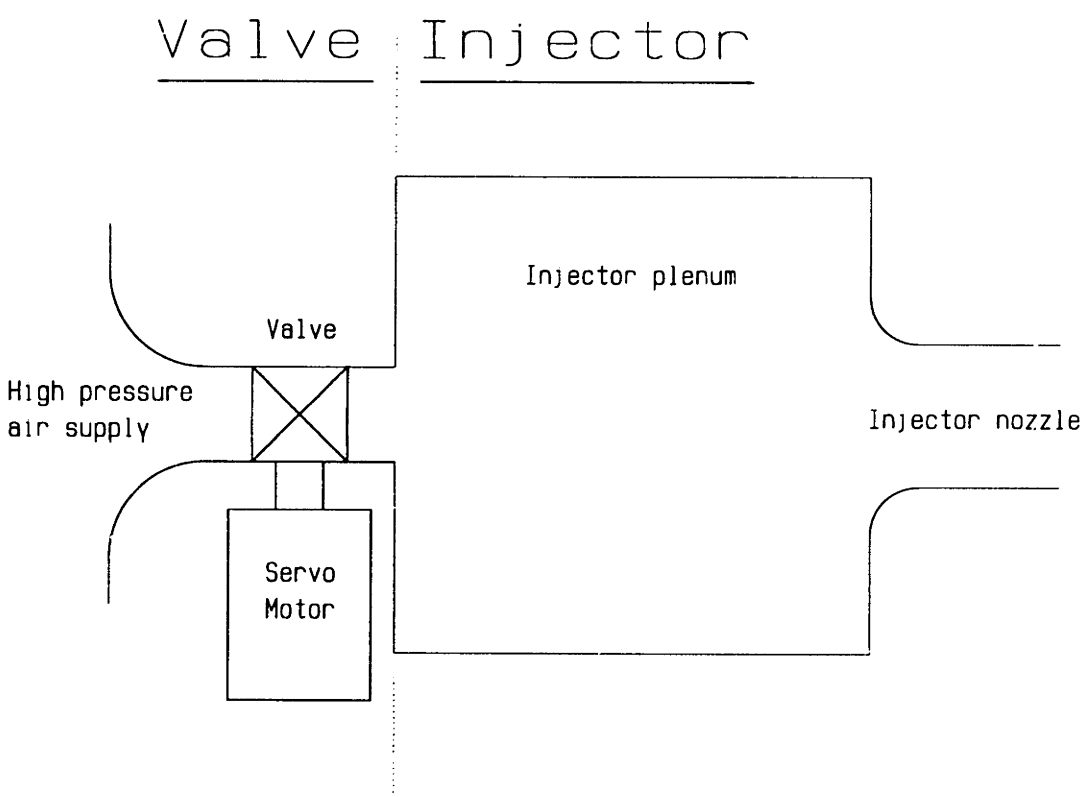

Figure 2-9: Conceptual design of the jet actuator.

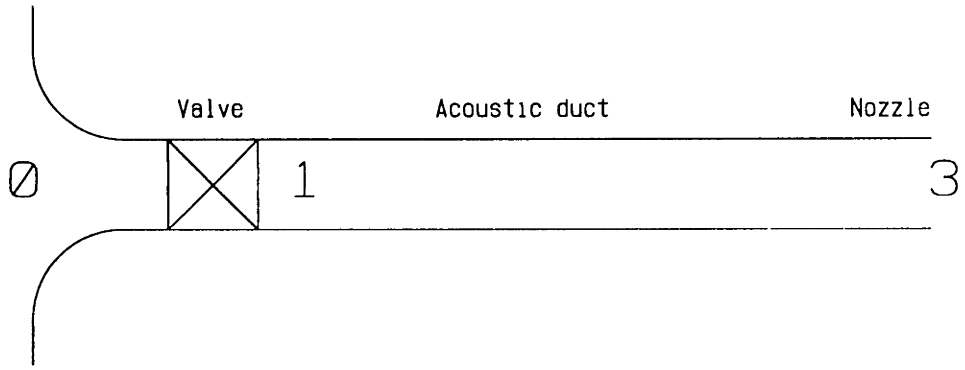

Figure 2-10: Schematic representation of an acoustic duct.

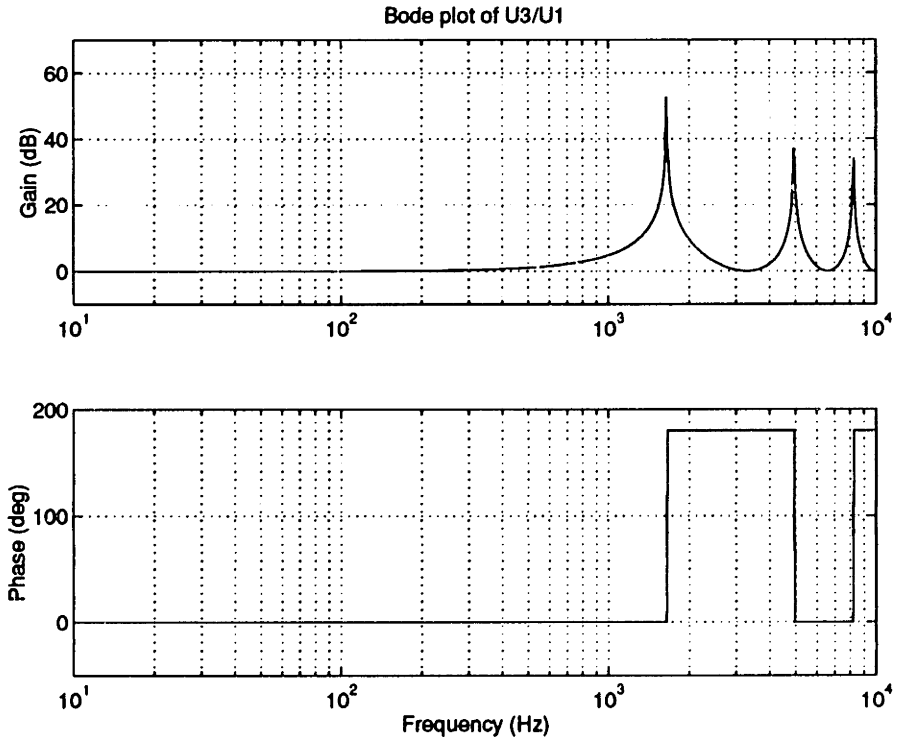

Figure 2-11: Frequency response of the acoustic duct, $l = 50$ mm.

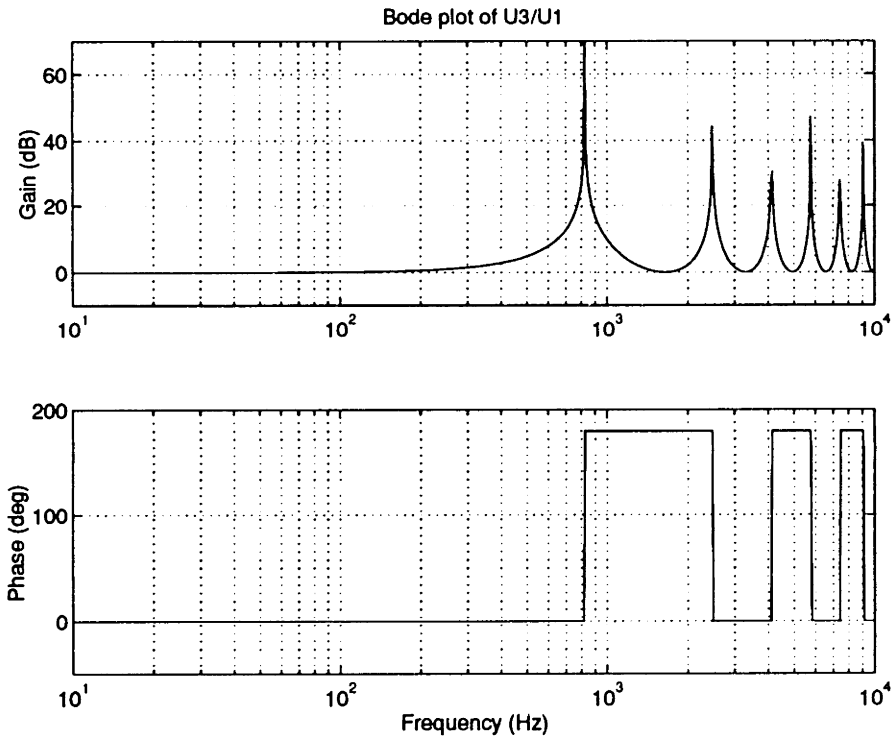

Figure 2-12: Frequency response of the acoustic duct, l = 100 mm.

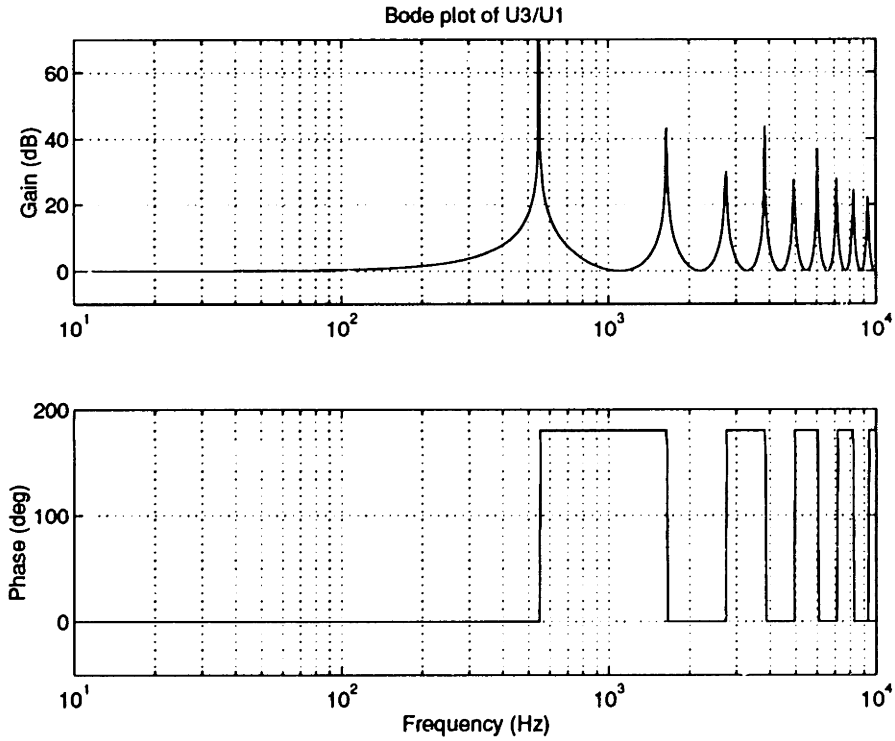

Figure 2-13: Frequency response of the acoustic duct, l = 150 mm.

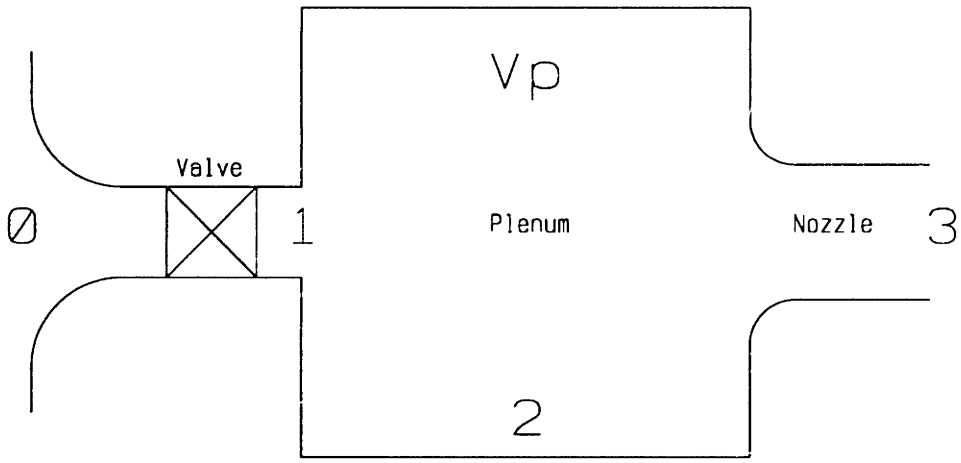

Figure 2-14: Schematic representation of a Helmholtz resonator.

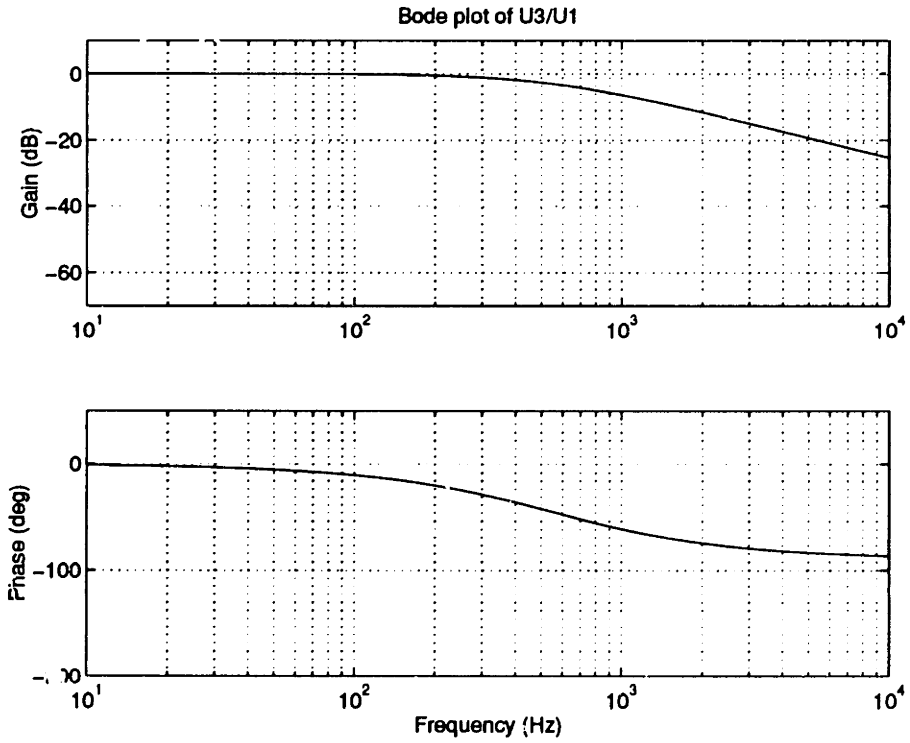

Figure 2-15: Frequency response of the Helmholtz resonator, $l_p = 50$ mm, $d_p/d_3 = 2$.

Chapter 3

Valve development

3.1 Objectives

The objective of the actuator design is to develop a device that can modulate the required injectant flow into the compressor at a sufficiently high frequency, thus converting an electrical input signal into a fluid dynamic output signal. In addition to satisfying the performance specifications, it was desirable to have an actuator which was simple in design, and that could be easily adapted to accommodate various injection schemes. In Chapter 2 the actuator was separated into two major components, namely the valve and the injector. This modular design approach was useful since it allowed various injection schemes to be tried, all using the same valve to modulate the flow into the injector. This chapter deals with the development of the valve only, while Chapter 4 and 5 deal with the development of the injection scheme. The objective of the valve development was therefore to design a device that could modulate the required mass flow into the injector at high frequency.

3.2 Electric motor selection

Before the mechanical design of the valve could be started, the prime mover that would open and close the valve had to be developed, or procured. In order to satisfy the bandwidth requirements of the actuator, electro-mechanical force motors were

investigated since these have relatively high force or torque capabilities, as well as having the required frequency response capability (up to 1 kHz). Since the overall compressor feedback system controller output is an electrical signal (assuming a computer implementaion of the controller), it makes sense to use an electro-mechanical device since this eliminates the need to convert signals, which could be a source of phase delay and system complexity. The servo motor driving the valve must be capable of producing sufficient force or torque to accelerate the mass of its own armature as well as that of the valve. Two alternatives existed in the selection of a suitable force motor, namely to use an existing motor, or to custom-build one to meet the performance requirements. Time constraints favored the former, therefore an attempt was made to find a servo motor with suitable performance.

Commercially available high frequency response servo-motors typically have a large signal bandwidth of around 100 Hz. Core-less DC motors are rotary electric motors with a bell-shaped armature containing no soft iron core, thus these motors have relatively little rotary inertia. Such motors have been used previously at the MIT GTL, but have been found to only have bandwidths in the region of 100 Hz. Printed circuit or disc DC motors are similar to core-less motors, but have a pancake shaped armature with stationary axial field magnets on either side of the armature. Again the armature has no soft iron core, keeping its inertia relatively low. Technical data obtained from commercial vendors indicated that the maximum bandwidth of such motors was also in the region of 100 Hz, significantly lower than that required for this application.

Having found no commercially available motors with the required bandwidth, the possibility of custom designing a servo motor with sufficient bandwidth was investigated. A commonly encountered linear force motor is the electro-dynamic voice-coil actuator, as found in audio loudspeakers. Although these motors can have bandwidths up to several tens of kilohertz, for the strokes envisioned (around 1 mm), 1 kHz is practically achievable. Since these motors make use of the electro-dynamic effect to produce force, with a varying electric field rather than a varying magnetic field, it is possible to obtain fairly high bandwidths compared to motors that vary a

magnetic field. As it turns out, NASA Lewis was developing a custom electro-dynamic voice-coil actuator, initial tests carried out at NASA on a simple loudspeaker motor indicating that it might be possible to use this motor in the valve application. Instead of embarking on this route, it was decided to investigate whether motors could be obtained from non-commercial vendors (e.g. military applications).

A linear force motor was obtained from Moog Inc., in the form of a electro-mechanical hydraulic valve for the flight control system of the B2 strategic bomber. The linear electro-mechanical servo motor used in this valve employs a variable reluctance magnetic flux path to generate force on the motor armature. This method of producing force is typically used in solenoid valves, albeit in an open-loop sense. The Moog force motor was attractive since the motor controller was available and did not require development. On the negative side though, the motor had limited bandwidth capability with large phase lag (more than 180° of phase lag at frequencies above 230 Hz). The variable reluctance motor is limited in frequency response mainly by the first order electrical response time (due to induction) of the coils that vary the magnetic field in the flux path. The frequency response of the motor can be increased by decreasing the reluctance of the magnetic circuit, this being most easily done by decreasing the size of the motor. In the present application, the static force produced by the motor is far greater than required, and it was therefore reasoned that a smaller motor would still be able to move the sleeve, but at higher frequency. Since Moog was working on a smaller (and less expensive) force motor, this was a realistic option. To be able to continue with the injector development at that time, however, the larger Moog force motor was used in the design of the valve, with the intent of upgrading the motor at a later stage (see Section 3.5).

Figure 3-1 shows a cutaway drawing of the Moog force motor. In the very center of the motor there are two permanent magnets that set up opposing toroidal magnetic fluxes through the circular flux gaps between the moving annular armature and the stationary outer soft iron housing. By varying the coil current, the solenoidal magnetic flux created by the electrical coils reinforces the toroidal magnetic flux (due to the permanent magnets) in one of the flux gaps, and weakens it in the other. Since the

armature is part of the soft iron magnetic flux path, with flux gaps at either end of it, an axial force is experienced due to the imbalance of magnetic flux density in the flux gaps. The armature is suspended on radial flexures, therefore it can move axially when it experiences an imbalance in axial force. The resulting 1 mm of linear motion is used to open and close the valve. The motor controller senses motor position (LDVT) and velocity (inductive sensor), and using a simple analog feedback circuit, outputs a coil current which is proportional to the sum of the position and velocity error signals.

3.3 Valve design

Having found a suitable electric motor, a valve was designed around this motor, as shown in Figure 3-1. High pressure (700 kPa or 100 psig) air enters the valve body on opposite sides (see arrows) from the outside, passes through a slotted central cylinder, and exits from the valve center. A sleeve, that is attached to the motor armature, regulates the slot orifice area, thus modulating the choked flow through the orifice. A sleeve valve design was chosen because it produces only small steady-state pressure forces that have to be balanced by the motor armature. In order to eliminate frictional damping, without producing a large leakage flow, a very small ($25\mu m$) clearance was used between the valve sleeve and cylinder. It is possible to use such close tolerances since the sleeve velocities are relatively low, the radial play of the motor is small (less than $25\mu m$), and there is significant cooling provided by air flowing through the valve. The valve body was machined in one piece to ensure concentricity of the valve cylinder and sleeve (which is attached to the servo motor armature). In subsequent tests it was found that no scuffing or abrasion occurred between the sleeve and cylinder, thus justifying the choice of such close tolerances. The valve sleeve attaches directly to the existing motor armature, thus reducing the overall inertia of the moving mass. The valve body is bolted to the existing motor housing, thus eliminating unnecessary modifications to the motor. The upstream plenum (all the volume upstream of the slot) serves two purposes, namely to provide a spatially uniform pressure supply to

Parameter	units	value
Valve stroke	mm	1
Radial clearance	μm	25
Supply pressure (gauge)	kPa	700
Maximum mass flow	$kg.s^{-1}$	0.1
Minimum mass flow	$kg.s^{-1}$	0.0
Bandwidth (-3dB)	Hz	350
Phase at -3dB	deg	360

Table 3.1: Summary of the valve design specifications

all parts of the slot, as well as to provide a large volume upstream of the valve where temporal pressure fluctuations (which may propagate upstream) are smoothed out. A pressure resistant motor cover encloses the motor and valve, with only the electrical connections passing to the outside. In this way, no special sealing arrangements are required to interface the force motor to the valve. Table 3.1 summarizes briefly some of the design specifications and constraints of the valve design.

3.4 Valve testing

The valve performance was evaluated for mechanical as well as fluid dynamic response, in both steady and dynamic tests. Testing was performed not only to obtain quantitative information about the valve, but also to investigate the reliability and robustness of the overall valve and actuator design. Since the valve portion of the actuator contains all the moving parts, it was deemed to be the most critical element of the actuator from a reliability point of view. High reliability is of some importance for the intended implementation of the actuator on a high speed compressor rig, since any downtime caused by actuator failure will be costly in terms of time lost and costs incurred in repeated tests.

3.4.1 Experimental apparatus

A brief description of the equipment used to test the valve and measure its performance is now given.

Valve command and position

A Wavetek model 166 signal generator was used to supply the ± 5V input signal to the actuator motor controller. The signal generator can be configured to provide logarithmic frequency sweeps (typically 5 - 500 Hz), or discrete frequencies. Since the signal created by the signal generator has very specific frequency content, it is not necessary to anti-alias filter the signal before sending it to the A/D system. The valve position was obtained directly from the motor controller feedback system. The ± 5V signal was anti-alias filtered by a 5 pole low pass filter set at 1 kHz corner frequency.

Computer with A/D and D/A system

A NEC 386SX personal computer was used to acquire data, using a Data Translation DT2821-G-16SE combined A/D and D/A board. This board provides 16 channels of A/D and 2 channels of D/A, the 16 single-ended A/D channels being multiplexed into a 12 bit converter. The maximum sampling rate is around 100 kHz using DMA, and around 5 kHz without DMA. The A/D was set up for a ± 10V range. The 2 D/A channels have a resolution of 12 bits and a sampling rate of about 3 kHz without DMA. The voltage range is ± 10V.

Oscilloscope and Spectrum Analyzer

A Tektronix model 2214 digital storage scope was used to look at real time data traces, and to observe output waveforms. A Hewlett Packard model 3582A spectrum analyzer was used to obtain real time transfer functions between various signals, as well as frequency spectra of signals.

Upstream valve and injector plenum pressures

The unsteady upstream valve pressure was measured by a 100 psi Kulite (XTME-190-100G) gauge pressure transducer. The injector plenum pressure was measured by a 50 psi Kulite (XTME-190-50G) gauge pressure transducer. The low level voltage signals of both transducers were amplified by an Analog Devices strain gauge bridge

amplifier. The 0-10V amplifier output was anti-alias filtered by a 5 pole low pass filter set at 1 kHz corner frequency. The filtered signals were then fed into the A/D system.

Valve mass flow

A 100 CFM Fischer and Porter rotameter was used to measure steady mass flow entering the valve. During unsteady tests, this meter measured mean mass flow.

3.4.2 Performance testing - steady tests

The valve mass flow rate versus upstream total pressure characteristic was measured, and is plotted in Figure 3-2. The relationship between mass flow rate and valve upstream pressure is linear for most of the operating pressure range of the valve, this being due to a choked valve orifice. The tests were performed with valve openings of 0%, 50% and 100%, hence the three curves of increasing mass flow rate. All three curves are linear, indicating that, for the upstream pressures typical of the valve, the valve orifice is always choked. Figure 3-3 shows a plot of mass flow rate versus valve position, for upstream supply pressures of 414, 552 and 656 kPa (60, 80 and 95 psig). At small valve openings, there is a leakage flow through the valve caused by the finite claerance (25 μm) between the valve sleeve and cylinder. The main thing to note in Figure 3-3 is that the relationship between mass flow and valve position is essentially linear between the valve operating limits of -5V and 5V (fully closed and fully open). Thus the valve acts like a linear mass flow modulator. The original valve orifice design did not have this linear relationship, as is indicated by Figure 3-4. In this case, the original mass flow characteristic at low mass flows is similar to that of the modified valve orifice design at low mass flows (Figure 3-3). However, at high mass flows, the original valve orifice caused non-linear mass flow behaviour with valve position. This can be explained by the detailed flow in the choked orifice, the geometry of which is shown in Figure 3-5. The left hand drawing shows the geometry of the original valve orifice, while the right hand drawing shows the geometry of the modified orifice. The original slot (the portion downstream of the interface between sleeve valve and valve

cylinder) has a very high aspect ratio (6:1), this being thought to cause the limiting choked area to occur in the slot region downstream of the sleeve, instead of at the interface of the sleeve and cylinder. The modified slot was made wider (aspect ratio of 3), even though the opening of the valve remained the same. This ensures that the choked area or vena-contracta occurs at the interface between the sleeve and the cylinder. In this manner a linear relationship between mass flow and valve position was obtained for the valve, as Figure 3-3 indicates.

Since most of the data in Figure 3-3 falls within the choked operation of the valve orifice, the data from all three curves can be non-dimensionalized by the following relation.

$$\dot{m}_{nd} = \frac{\dot{m}}{\dot{m}_{des}} = \frac{P_{t0}}{P_{t0,des}} \frac{\sqrt{T_{t0,des}}}{\sqrt{T_{t0}}} \frac{A_1}{A_{1,des}} \tag{3.1}$$

where $P_{t0,des}$ = 8E5 Pa, $T_{t0,des}$ = 293 K and the non-dimensional valve position is given by

$$= \alpha = \frac{A_1}{A_{1,des}}$$

Figure 3-6 shows the same information as Figure 3-3, except that the mass flow rate and valve position have been non-dimensionalized. It is observed that the non-dimensionalization works well, all of the data collapsing onto a single curve. It is also evident that the relationship between mass flow rate and valve position is linear in the region $0 < \alpha < 1$, which correspond to the fully closed and fully opened valve position. The dashed line represents the theoretical mass flow rate versus valve position if there is no leakage in the valve. Due to finite valve clearances (for mechanical reasons), there is a small leakage flow and the mass flow rate characteristic is merely shifted vertically. The valve characteristic satisfies the relation.

$$\dot{m} = b\alpha + c \tag{3.2}$$

where b = 1 and c = 0.04. This expression will be used in Chapter 4 for a simulation of the injector frequency response.

3.4.3 Performance testing - dynamic tests

The dynamic performance evaluation of the valve can be broadly divided into tests pertaining to the mechanical response of the electro-mechanical motor, and those pertaining to the fluid dynamic response of the sleeve valve. It should be noted again that Chapter 4 and 5 deal with the fluid dynamic response of the injectors, which are functionally separate from the valve itself.

Motor mechanical response

The dynamic response of the linear electro-mechanical servo motor was determined by measuring the electrical motor command and motor (valve) position signals. Figure 3-7 shows the transfer function from motor command to position for the servo motor. Because the coherence of the experimental transfer function is high throughout the frequency range of interest (0 - 500 Hz), the accuracy of the magnitude and phase plots should be high in this frequency range. High coherence also implies that the harmonic distortion (created by non-linearities in the overall motor control system) is small since a single harmonic input results in a single harmonic output. Looking first at the magnitude plot, it is observed that the motor response attenuates slightly between low frequency (50 Hz) and a motor resonance at 300 Hz. At 300 Hz the magnitude of the motor response is again at its DC value, after which it attenuates rapidly with higher frequencies (120 dB per decade). Referring to the phase plot, the motor phase rolls off fairly rapidly from low frequencies, this roll off probably being due to the finite first order inductive response time of the motor magnetic flux path. The phase lag reaches 180° at about 230 Hz. The large phase lag is highly undesirable if the actuator is to be used in the closed-loop control of a compressor, however, for the injector development, where the valve is run open-loop, there is no disadvantage in having a large phase lag. The only relevant issue in open-loop testing is that the magnitude (valve stroke) stays close to its DC value, which in this case is acceptable up to 330 Hz. The motor frequency response was found not to be altered by aerodynamic loading when the supply pressure to the valve was switched on and off. This is because the DC position gain of the motor controller is fairly high, making

the motor very 'stiff' and insensitive to external mechanical or aerodynamic loading (500 N static load capability).

Valve fluid dynamic response

To ensure that the unsteady pulsing of the valve did not produce unexpected fluid dynamic effects in the valve mass flow, the time mean mass flow rate of the valve was measured for various excitation frequencies. Figure 3-8 shows a plot of mean mass flow rate versus commanded excitation frequency. The three curves correspond to separate tests performed at 414, 552 and 656 kPa (60, 80 and 95 psig) upstream pressure. The flow rates stay virtually constant throughout the frequency range of interest (0 - 500 Hz), however, at 300 Hz there is a slight increase in the mean mass flow rate, probably due to the 'supercharging' effect of the upstream duct acoustics. It was observed during the tests that the note produced by the actuator became louder at this particular frequency, and that there was a distinct organ pipe resonance (vibration) in the air hose upstream of the valve. Since the upstream piping geometry for the valve development is not the same as for the actual compressor tests, further investigation of the upstream duct acoustics was not warranted. Figure 3-9 shows the same data as in Figure 3-8, but in non-dimensional form. The mean mass flow is slightly higher than half the design mass flow, and remains constant throughout the frequency range of interest (0 - 500 Hz).

The time scales of the flow through the valve orifice are 2 to 3 orders of magnitude lower than those in other parts of the actuator. This is because the length scale of the valve orifice is about 3 mm, while a typical velocity is the speed of sound. The characteristic time is thus on the order of 10 μs, which corresponds to a characteristic frequency of 100 kHz, much greater than the frequency range of the actuator. For this reason, the valve orifice flow has no dynamics in the frequency range of interest (0 to 500 Hz), and essentially acts quasi-steadily. Thus, the only dynamics associated with the valve portion of the actuator are those caused by the electro-mechanical servo motor driving the valve.

3.5 Second generation valve

In Section 3.2 it was mentioned that Moog Inc. was developing a smaller motor with better frequency response (higher bandwidth and less phase lag). Since this new motor was not available at the time of the valve and injector development, it was decided to proceed with these developments using the original Moog motor (referred to henceforth as the Moog I motor for clarity). Having subsequently obtained one of the smaller Moog motors (which will henceforth be referred to as the Moog II motor) after completion of the valve and injector development, a second generation valve was designed around the Moog II motor, in order to exploit the better frequency response that this motor/valve combination would offer.

In Section 3.4.3 it was shown that the frequency response of the valve portion of the actuator is essentially limited in frequency response by the frequency response of the electro-mechanical servo motor driving the valve. Section 4.4.1 will show that the injector performance is affected by the valve only in terms of the mass flow supplied to the injector by the valve. It will be shown that different valve supply pressures have no effect on the injector, as long as the same mass flow is being passed by the valve. Since the valve acts only as a modulator of mass flow into the injector, there should be no difference in the overall actuator fluid dynamic response when using the new valve with the original injectors, provided the new valve has the same fluid dynamic performance as the original valve. The design objective of the new valve was therefore to develop a device with the same fluid dynamic behavior as the original valve, but with improved frequency response due to the better frequency response of the Moog II motor.

To reduce the development risk of the new valve, the sleeve and slot geometry were kept identical to the original valve design. This was done to avoid unexpected fluid dynamic behavior of the new valve. Furthermore, the valve external dimensions had to be chosen to conform to space limitations on the NASA Stage 35 compressor test rig. Figure 3-10 shows a drawing of the second generation valve. High pressure air enters the valve from above, filling an upstream reservoir surrounding the slotted

valve cylinder. The air then passes via the choked orifice slot into the valve cylinder, flowing through the injector to be ejected into the compressor upstream flow field. A sleeve valve modulates the size of the choked orifice, thus modulating the mass flow through the valve. The sleeve is driven by the armature of the Moog II motor, the motor itself being bolted to the valve body.

3.5.1 Steady valve characteristic

The steady mass flow versus valve position characteristic of the new valve was measured using the same equipment and procedures used for the original valve. Figure 3-11 shows the valve characteristic for the 2nd generation valve. The relationship between mass flow and valve position is linear, and almost identical to that of the original valve characteristic (see Figure 3-3). This was anticipated since all the elements of the new valve orifice and sleeve are identical to those of the original valve. Since the valve fluid behavior has no dynamics in the frequency range of interest (0 to 500 Hz), it is expected that the dynamics of the new valve (ignoring the dynamics of the servo motor) will be identical to that of the original valve.

3.5.2 Motor frequency response

Figure 3-12 shows a Bode plot of the transfer function from motor command to valve position for the Moog II motor without aerodynamic loading (no air flowing through the valve). Since the Moog II motor has less force capability than the original Moog I motor (100 N static force capability as opposed to 500 N), its dynamic performance is affected somewhat by the aerodynamic loading of the valve. Whereas the original Moog I motor had a very high DC gain, and hence good steady state tracking, the Moog II motor has low DC gain (as a result of design compromise to obtain good high frequency response) and does not reject steady state disturbances (like unbalanced aerodynamic loads) very well. These loads are therfore supported mechanically by the spring flexure supporting the motor armature. Concerning high frequency behavior, the Moog II motor has significantly better frequency response than the original Moog

I motor. Not only is the bandwidth larger (430 Hz as opposed to 330 Hz), but the phase lag is substantially less than the original motor (100° at 400 Hz as opposed to 180° at 230 Hz). Figure 3-13 shows the frequency response of the Moog II motor with aerodynamic loading. The magnitude of the valve response is slightly less (1dB = 10% of stroke) than the unloaded case, however, the phase behavior is virtually identical to that of the unloaded case.

3.5.3 Summary of 2nd generation valve

It appears that the steady fluid dynamic behavior of the 2nd generation valve is very similar to that of the original valve. Since the dynamics of the valve (ignoring the dynamics of the servo motor) are essentially quasi-steady in the frequency range of interest (0 to 500 Hz), the dynamic behavior of the original and new valves is identical. The Moog II motor frequency response is substantially better than the original Moog I motor response in terms of bandwidth (450 Hz as opposed to 350 Hz), as well as phase lag (100° at 400 Hz as opposed to 180° at 230 Hz). Therefore, the overall actuator frequency response has been improved significantly. This is beneficial to the closed-loop rotating stall control that will be implemented with this actuator.

3.6 Summary: valve development

To conclude this chapter, the main findings of the valve development are reviewed. In addition, Table 3.2 gives a quantitative summary of both valves.

- Two simple modular valves, both comprising an existing electro-mechanical drive motor and a custom engineered valve component, were developed.
- The steady mass flow characteristic of both valves is linear with valve position, as a result of the choked flow at the variable orifice of the valves.
- Both valves act as mass flow modulators.

Parameter	units	Moog I	Moog II
Supply pressure (gauge)	kPa	700	700
Valve command	V	$\pm 5V$	$\pm 10V$
Maximum mass flow	$kg.s^{-1}$	0.11	0.10
Minimum mass flow	$kg.s^{-1}$	0.02	0.02
Orifice flow area	mm^2	60	60
Orifice discharge coeff		1	1
Bandwidth (-3dE)	Hz	330	400
Phase at -3dB	deg	360	100

Table 3.2: Quantitative summary of the valve development

- The fluid dynamic response of the valve orifice is unaffected by frequency, the valves (ignoring the servo motor) essentially acting quasi-steadily in the frequency range of interest (0 to 500 Hz).

- The mechanical response of both valves is limited by the frequency response of their respective drive motors, which currently have a large signal response of 330 Hz and 430 Hz, for the Moog I and Moog II motors, respectively.

- Since the valve orifice flow responds quasi-steadily and has no dynamics of its own, the overall valve frequency response could be improved by improving the frequency response of the servo motor driving the valve.

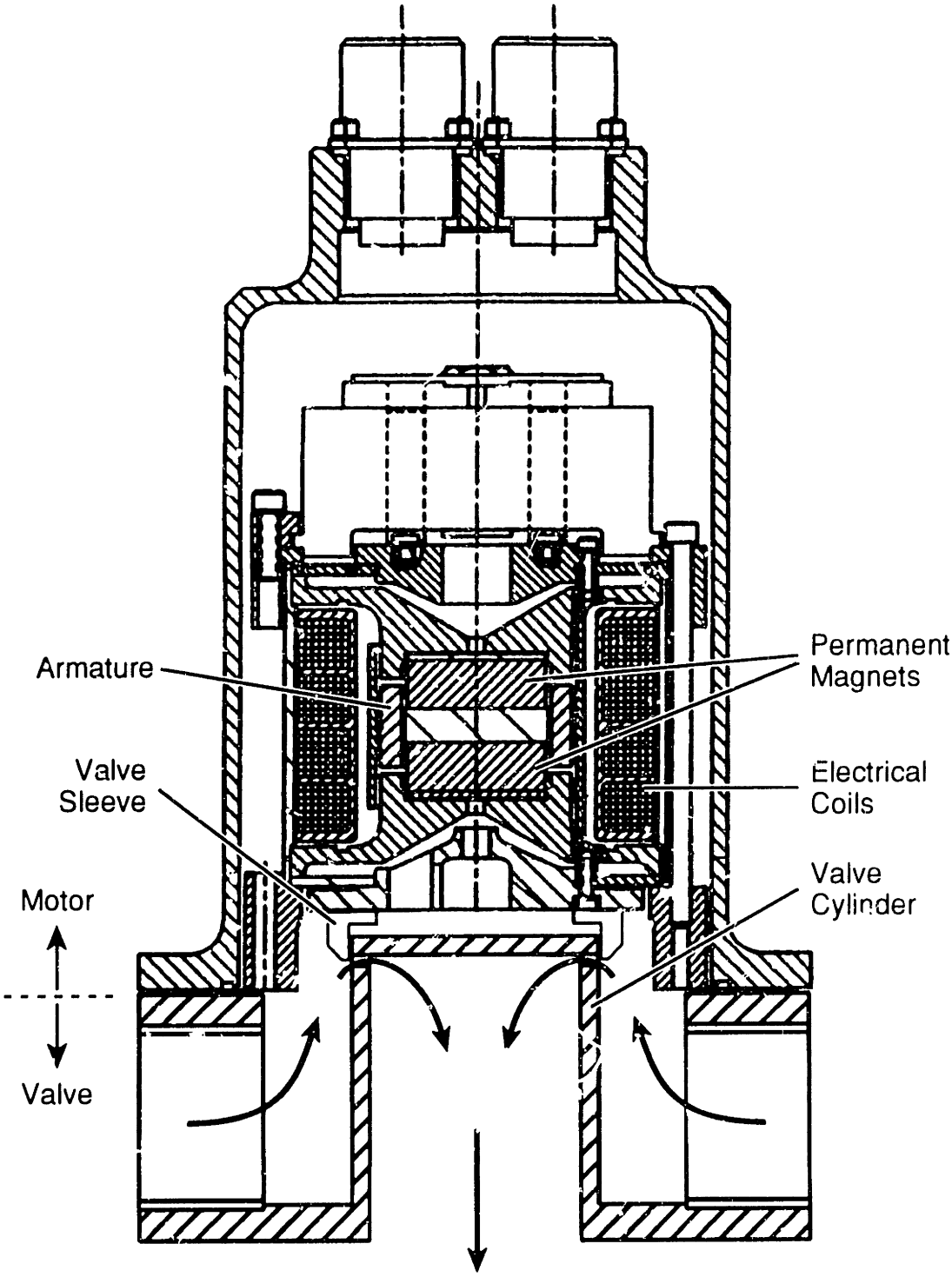

Figure 3-1: Cross-section of valve and force motor.

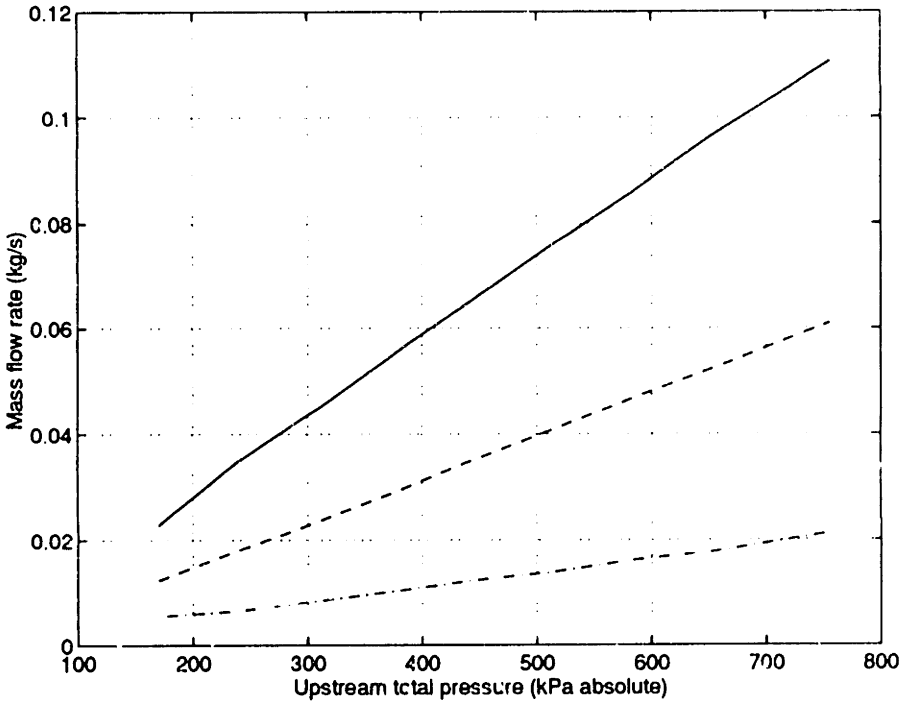

Figure 3-2: Valve characteristic, 0% (-.-), 50% (- -) and 100% (—) valve opening.

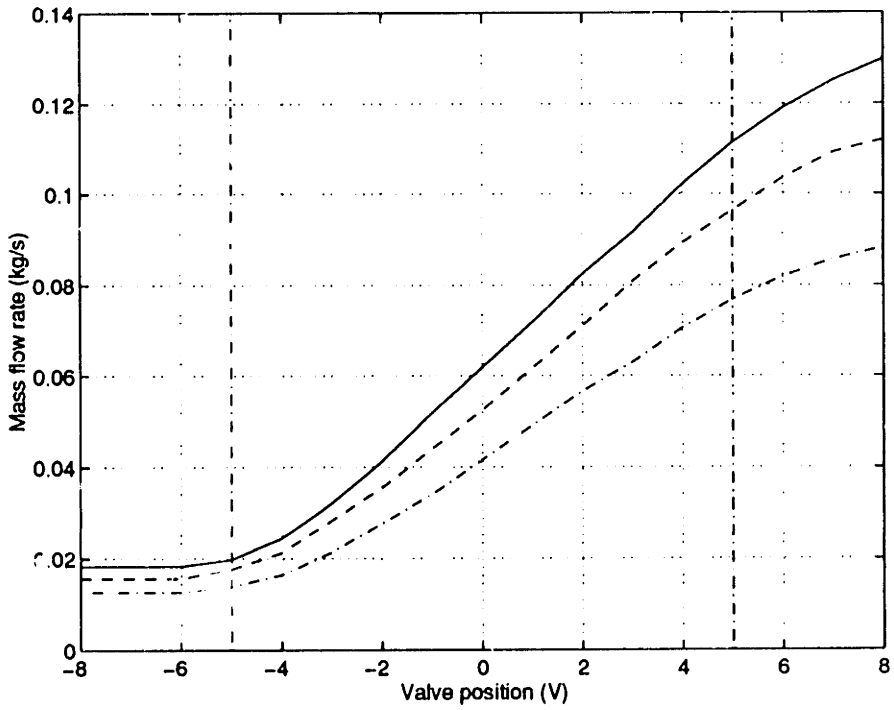

Figure 3-3: Steady valve characteristic, 414 (-.-), 552 (- -) and 656 (—) kPa (60, 80 and 95 psig) upstream pressure.

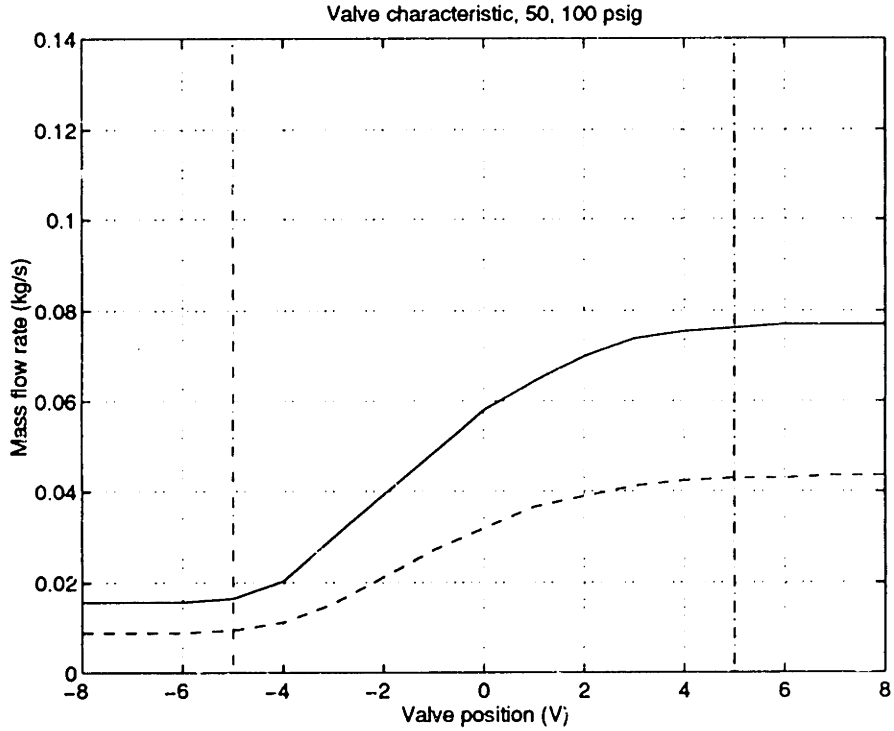

Figure 3-4: Steady valve characteristic - original valve geometry, 345 (- -) and 690 (—) kPa (50 and 100 psig) upstream pressure.

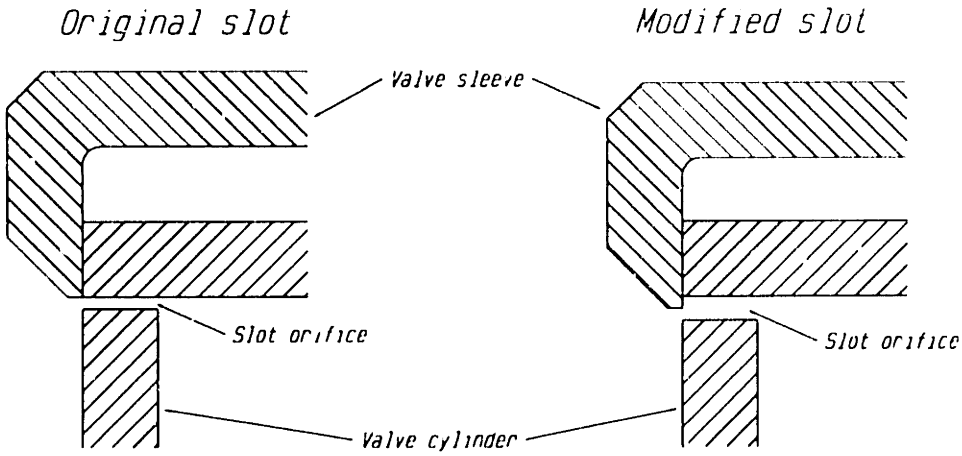

Figure 3-5: Comparison of the slot geometry for the original and modified valve orifice.

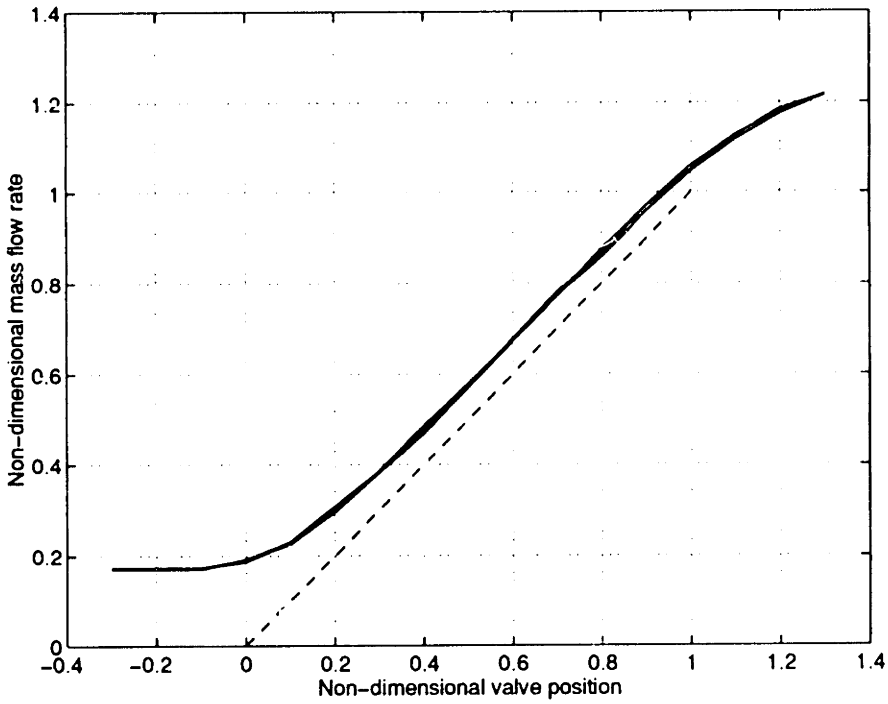

Figure 3-6: Non-dimensionalized valve characteristic, 414, 552 and 656 kPa (60, 80 and 95 psig) upstream pressure. Theoretical curve (- -).

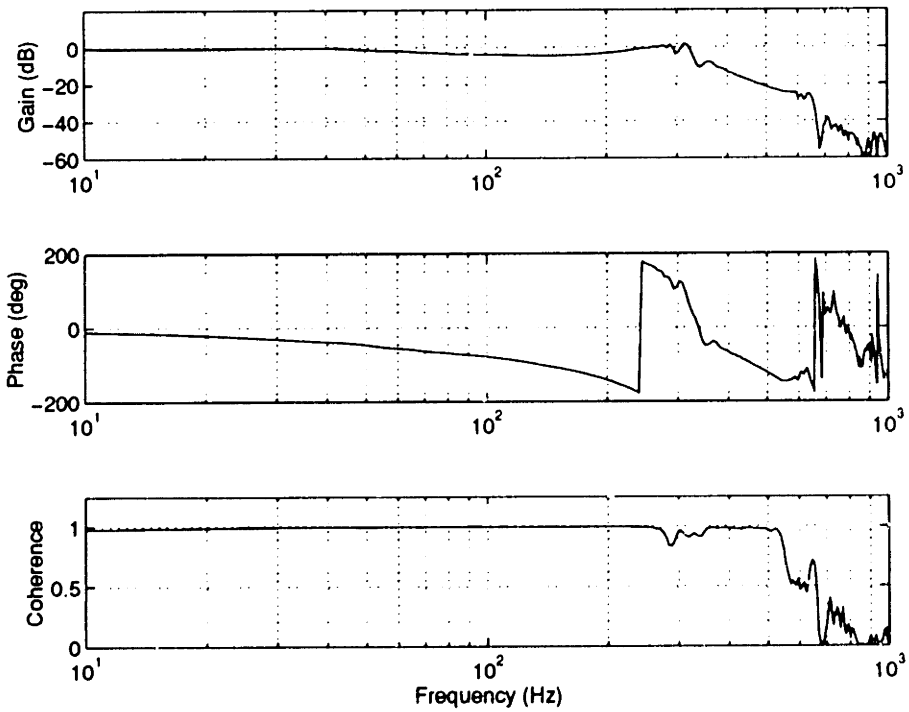

Figure 3-7: Bode plot of motor command to position transfer function.

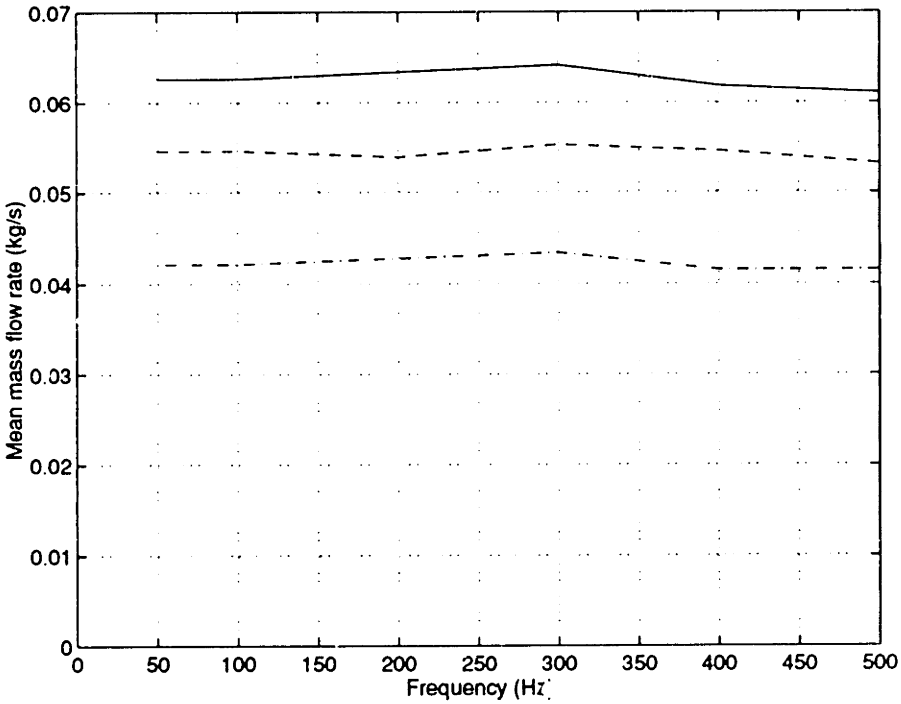

Figure 3-8: Valve dynamic mean flow characteristic, 414 (-.-), 552 (- -) and 656 (—) kPa (60, 80 and 95 psig).

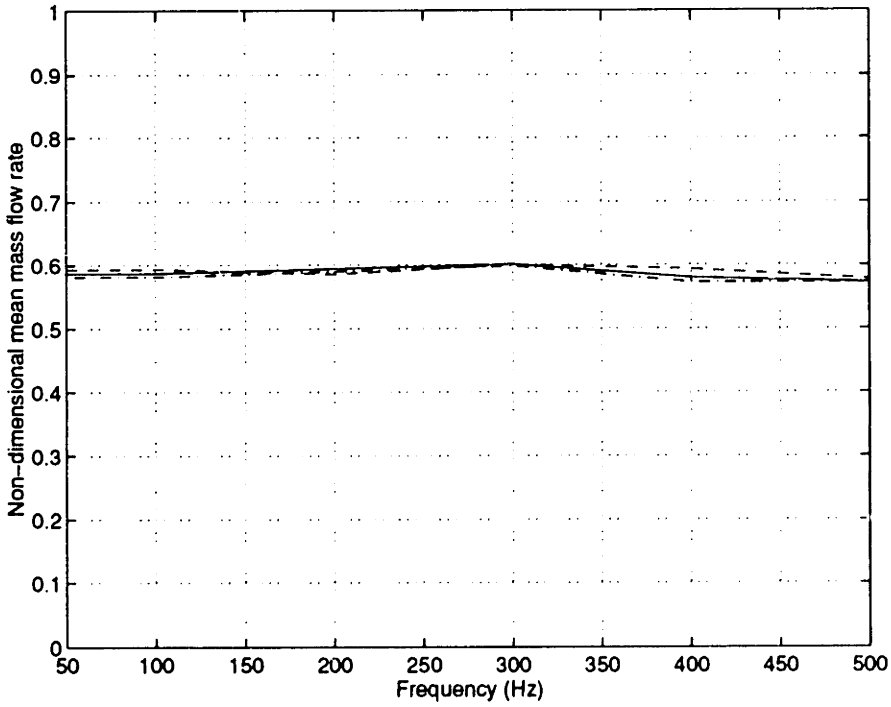

Figure 3-9: Non-dimensional valve dynamic mean flow characteristic.

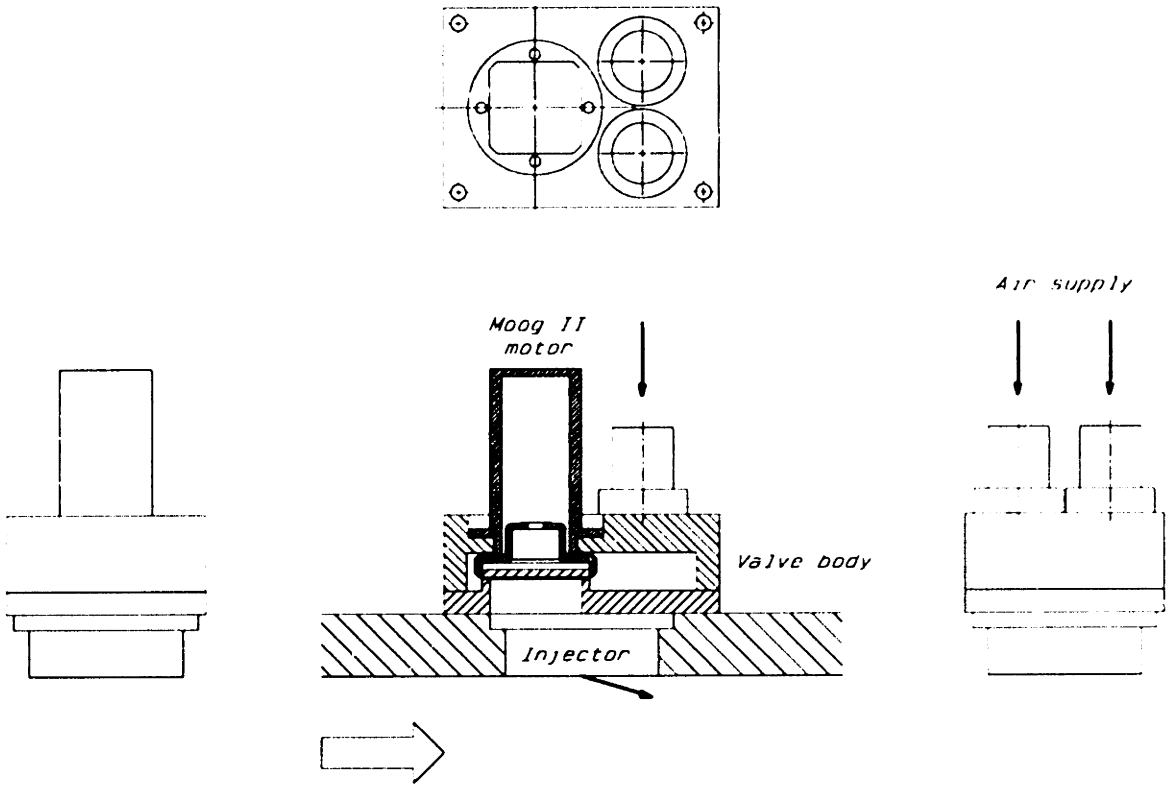

Figure 3-10: Second generation valve with Moog II motor.

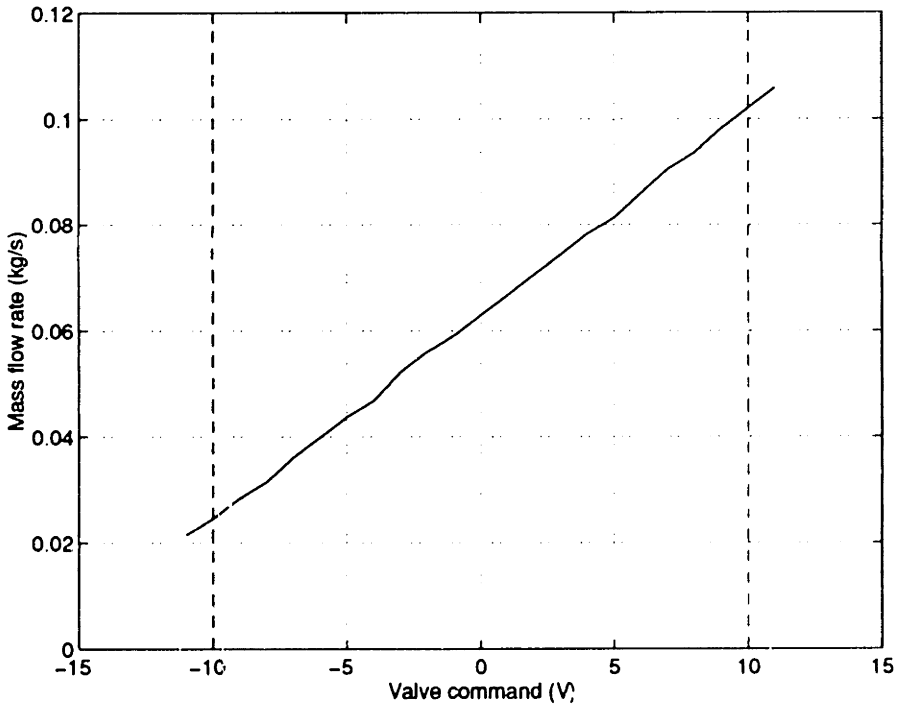

Figure 3-11: Steady valve characteristic, Moog II, 656 (—) kPa (95 psig) upstream pressure.

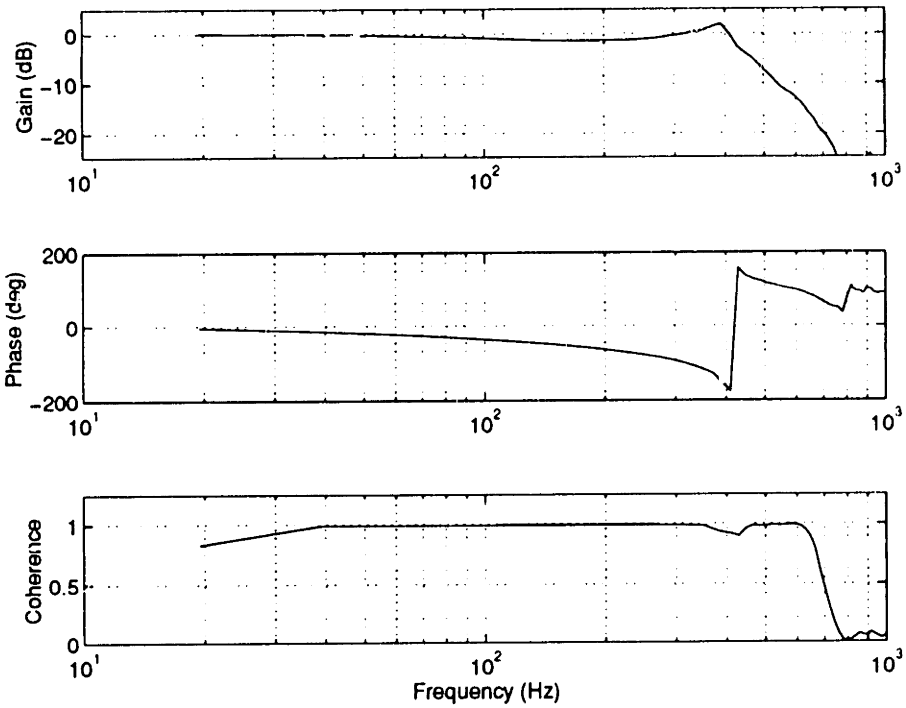

Figure 3-12: Bode plot of Moog II motor frequency response without aerodynamic loading.

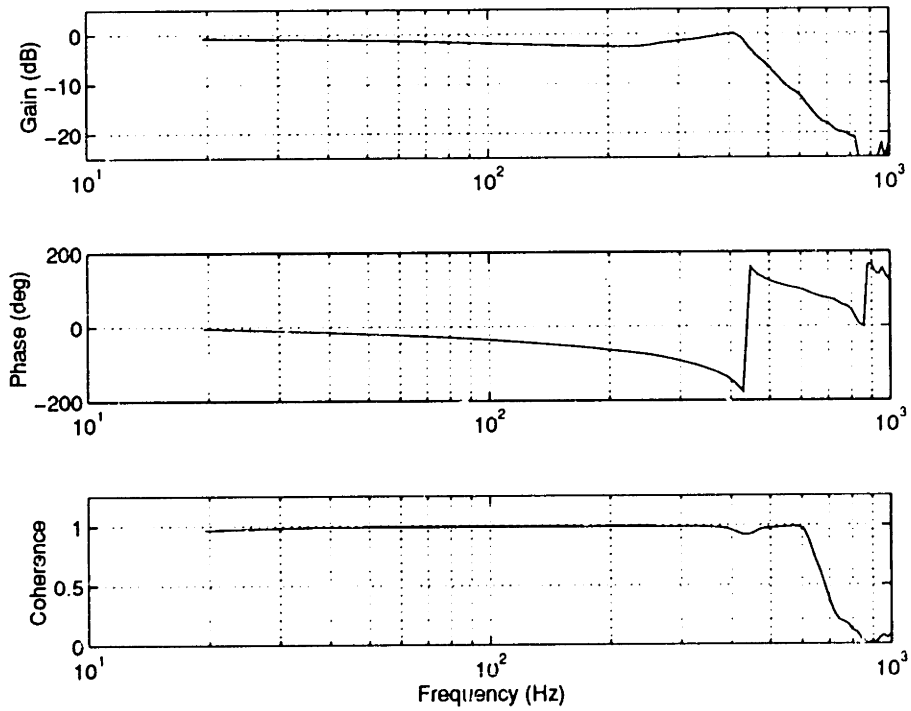

Figure 3-13: Bode plot of Moog II motor frequency response with aerodynamic loading.

Chapter 4

Initial Injector Development

From Chapter 2, the injector is defined as that part of the actuator downstream of the valve. The purpose of the injector is to impart momentum to the injectant flow, and to direct this momentum into the compressor in such a way as to achieve the maximum change in pressure rise or mass flow of the compressor. Figure 4-1 shows schematically how an upstream array of actuators would inject jets of high momentum air into the compressor face. The axial component of the jet injection translates directly into an increase in the total pressure of the upstream flow field, while the tangential component introduces swirl into the upstream flow field. Because the actuator modulates the injectant dynamically, the injector must have sufficiently high frequency response to introduce this high frequency forcing into the compressor.

4.1 Approach

The injector development consisted of several main steps to achieve the objectives stated above, and those elucidated in Chapter 2.

- Design and test some candidate injectors. These should have various degrees of radial penetration to validate the conjectures made in Section 2.8.1.
- Measure the steady spatial distribution of jet momentum of the injectors. Since jet momentum translates into a total pressure rise of the upstream flow field,

this is a useful quantity with which to characterize the injection process.

- Measure the unsteady spatial distribution and temporal nature of jet momentum.

- Compare the steady and unsteady behavior of the jet, in order to characterize the essential dynamics of the injection process (a quasi-steady description, or a simple time delay and attenuation factor, would be examples of the essential dynamics).

4.2 Design of the injectors

The design intent of the injector is to introduce high momentum fluid into the compressor flow field, upstream of the compressor. Figure 4-2 shows a drawing of the proposed actuator design. High pressure air enters the actuator, passing through the variable valve orifice into the injector where it is directed into the compressor upstream flow field (freestream) in the axial or circumferential direction. Certain constraints are imposed on the injector design by the issues discussed in Section 2.8. It is undesirable to have an injector with parts that protrude far into the freestream since such an injector will give rise to a wake when the injector is not switched on. For a given set of inlet conditions (total pressure, temperature and mass flow), the injector should impart as much momentum as possible to the injectant, since this will increase the total pressure of the compressor upstream flow the most, and could have the largest effect on the change in pressure rise of the compressor. Since one of the objectives of the actuator development is to design a device that lends itself to linear control techniques, undesirable non-linearities, such as those created by normal shock waves within the injector nozzle, are to be avoided since these would cause the momentum of the jet to be highly non-linear as the injector is modulated from minimum to maximum flow. The injectors were therefore designed with a convergent nozzle only, trading a slight decrease in potential momentum flux with the benefit of increased linearity of the jet behavior. The actuators are located 63 mm (2.5")

upstream of the compressor face to keep convective time delays small (60° at 500 Hz).

4.2.1 Sheet injector

A conjecture was made in Section 2.8.1 that the rotor tip region of the compressor would be a good location in which to inject high-momentum fluid. To be able to verify this conjecture, an injector was designed that would produce a sheet of high momentum air at the compressor tip endwall. The design goal in this case allows radial spreading to be traded for circumferential extent of the jet. Figure 4-3 E and Figure 4-4 G show a schematic of such an injector (refer to Figure 4-2 to see how the injectors fit into the overall actuator). The injector nozzles shown in E and G are both two-dimensional (2-D) and produce a jet sheet that is thin radially, yet wide circumferentially.

4.2.2 3-hole injector

In almost all the analyses of rotating stall control, it is assumed that the fluid injected by the actuator is fully mixed with the freestream flow upon reaching the compressor face. A shower-head injector, similar to the type tested by Diaz [19], was designed with the intent of spreading the jet as rapidly as possible into the freestream. There is obviously a compromise here. Rapid penetration of the jet into the freestream requires the meridional injection angle to be large, however, large meridional injection angles imply lower axial momentum flux, and the possibility of creating a wake region near the casing wall. The meridional injection angle was therefore chosen to be 30°, as a reasonable compromise between the requirements of radial penetration and axial momentum flux. Figure 4-3 D and Figure 4-4 F show schematically a 3 hole injector.

4.2.3 Summary of injector designs

A total of eight injectors were designed and tested. Some of these injectors were only bench tested, while others were wind tunnel tested to investigate their effect on a moving freestream. The first set of three injectors are simple circular hole axial

injectors as illustrated in Figure 4-3, A, B and C. These injectors were designed to get a rough estimate of the desired exit area of the injector nozzle, since discharge coefficients, as well as the behavior of the jet in unsteady conditions, were unknown. The three injectors have diameters of 12.7 mm (0.5"), 15.2 mm (0.6"), and 17.8 mm (0.7") respectively. These injectors were not used in any wind tunnel flow field tests, since the main purpose of their design was to learn more about general injector design methodologies.

A second set of two injectors are the original injectors used in the wind tunnel flow field experiments, namely a 3-hole and a sheet injector. These two injectors are shown in Figure 4-3, D and E respectively. Since the injectors are geometrically different to the circular hole injectors, it is expected that their discharge coefficients and unsteady behavior differ somewhat. However, the general trends found from the first set of circular hole injectors should be applicable to the second set of flow field injectors. The original 3 hole injector has three 7.6 mm (0.3") diameter holes, aligned in the directions indicated. The original sheet injector has a slot 57 mm (2.25") wide and 2.5 mm (0.1") thick. Both injectors have a total exit area of about 130 mm^2 (0.2 in^2), which corresponds to a single circular hole exit diameter of 12.7 mm (0.5"). It turns out that the original sheet and 3 hole injectors did not achieve the desired frequency response, as well as having some other faults, therefore they were modified to meet the design requirements.

A third set of two injectors comprises the two modified injectors, namely a 3-hole and a sheet injector, as shown in Figure 4-3, F and G. These injectors will henceforth be referred to as the modified injectors, to distinguish them from the original injectors. The development of the modified injectors, as well as their testing, is described in detail in Chapter 5. This present chapter deals only with the design methodologies and lessons learnt from the circular hole, and original sheet and 3 hole injectors.

4.3 Experimental Equipment

Before embarking on a description of the injector testing, it is necessary to give an outline of the experimental equipment developed for the purpose of injector testing.

4.3.1 Wind tunnel development

In order to be able to test the proposed actuation scheme in conditions that simulate that of a high speed compressor, a small wind tunnel test section was constructed to test a single actuator. The wind tunnel was dimensioned to represent approximately 1/12 of a compressor annulus, with freestream dynamic and static pressures equivalent to a Mach number of $M_{f_s} = 0.5$, close to that expected in an actual high speed compressor. The wind tunnel is of the 'suck-down' or open type, implying that atmospheric air is drawn into the test section by a reduced downstream pressure. A 1200 kW laboratory compressor (De Laval low pressure) was used to obtain this reduced downstream pressure, variations in tunnel speed being effected by varying the rotational speed of the drive compressor. Figure 4-5 shows a schematic of the wind tunnel and the drive compressor. Atmospheric air is drawn into the test section bellmouth inlet, passes through the test section into a pipe that feeds into the drive compressor inlet. The compressor exhaust exits to the atmosphere.

The high speed compressors on which active control is to implemented typically have an axial Mach number of around $M_{f_s} = 0.5$. A tunnel capable of a freestream Mach number of $M_{f_s} = 0.6$ was therefore designed for these injector tests. Twelve actuators evenly spaced around the annulus of the target OD 500 mm (20") compressor case (NASA Stage 35), yield an actuator spacing of about 125 mm (5"). The tunnel test section width was made slightly larger than this, namely 175 mm (7"), to keep the tunnel side wall boundary layers out of the expected region of influence of the jet injector. Figure 4-6 shows a drawing of the wind tunnel, with additional views of the actuator and a traverse mechanism. A square test section was chosen for simplicity and versatility. The bellmouth inlet of the tunnel was designed using a method outlined by Ower and Pankhurst [20]. Two elliptical sections make up

the bellmouth profile. The four sections comprising the bellmouth were cut from expanded polystyrene foam with a hot-wire profile cutter, and then covered with a layer of fiberglass cloth and epoxy for strength and surface smoothness. Twelve static pressure tappings are located 175 mm (7") downstream of the bellmouth end to measure the tunnel static pressure. The 12 tappings are averaged into a single pressure by a manifold. Since it was envisioned to use the wind tunnel for flow visualization tests, the test section walls were made of Plexiglas. The mechanical structure of the wind tunnel was stressed to resist aerodynamic pressure forces corresponding to a freestream Mach number of $M_{fs} = 1$. A bolted construction was chosen above a bonded one, thus allowing the tunnel to be modified at a later stage, should this prove necessary. Two inch (50 mm) thick aluminum honeycomb was inserted between the test section and the elbow downstream of the tunnel to minimize the effect of downstream pressure disturbances (created by the elbow) propagating upstream into the test section. The actuator was located 375 mm (15") downstream of the bellmouth end, equivalent to 2 tunnel diameters, to ensure that the freestream flow was axial at the actuator location.

Actuator air supply

Air was supplied to the actuator from a 100 psig oil-free laboratory compressed air source. The compressed air passes through a particle filter, and then through a pressure regulator. The regulated air passes through a flow meter into the actuator. Figure 4-2 shows some more detail of how the high pressure air enters the actuator valve, flowing through the injector before it is ejected into the freestream (3 hole injector in this instance).

Traverse mechanism

An X-Y traversing mechanism is located 63 mm (2.5") (or further) behind the actuator center-line. The traversing mechanism allows a full spatial flow field survey to be done at a given axial location. The entire traverse mechanism can be moved axially in 25 mm (1") increments to allow various axial locations to be traversed. The entire

traverse mechanism is housed within an aluminum pressure vessel (box), to prevent ambient air leaking into the test section via the slot through which the probe passes (the tunnel test section is at a pressure lower than ambient). The traverse mechanism is computer controlled via a serial port (RS232).

4.3.2 Wind tunnel instrumentation

Various steady and unsteady quantities were measured during a given test, to be able to build up a picture of the flow field created by the injector. For the steady tests, a pitot tube was used to traverse the flow field since it has good long term repeatability. For the unsteady tests, a hot-film probe was used since it has the required frequency response.

Valve command and position

The same equipment as described in Section 3.4.1 was used.

Computer with A/D and D/A system

The same computer as described in Section 3.4.1 was used.

Oscilloscope and spectrum Analyzer

The same equipment as described in Section 3.4.1 was used.

Tunnel total-to-static pressure

The tunnel Mach number (and hence velocity) was deduced from the tunnel total-to-static pressure ratio. The 12 upstream static pressures (manifolded) were measured relative to atmospheric pressure using a 5 psi Setra (model 239) differential pressure transducer. The 0-10V steady-state output signal was fed directly into the A/D system. In addition to the electrical pressure transducer, a precision pressure gauge was installed to show tunnel total-to-static pressure (and hence Mach number) during

a test. This gauge was used to set the tunnel speed to an accuracy within 2% at M_{f_s} = 0.45.

Pitot tube static pressure

A pitot tube was used to obtain total and static pressure measurements of the flow field, the pitot tube being positioned by the traverse mechanism. The steady static pressure distribution at the traverse location was measured using a 5 psi Setra (model 239) differential pressure transducer. The measurement was referenced to the atmosphere, therefore it is essentially the same as the tunnel static pressure (mentioned above) when there is no injection by the actuator. The 0-10V steady-state output signal was fed directly into the A/D system.

Pitot tube total-to-static pressure

The steady total-to-static pressure distribution at the traverse location was measured using a 20 psi Validyne (model CD223) differential pressure transducer. The 0-10V steady-state output signal was fed directly into the A/D system.

Hot-film anemometer

The unsteady velocity at the traverse location was measured using a TSI model 1210-20 hot-film probe. Initially, a hot-wire probe was used, but the dynamic pressure of the jet proved to be too great, destroying the probe in a matter of seconds. A TSI model 1050 constant temperature anemometer provides the feedback loop for the probe bridge. The output (typically 2-10V) of the anemometer was anti-alias filtered by a 5 pole low pass filter set at 1 kHz corner frequency, before being. fed into the A/D system.

Upstream valve and injector plenum pressures

The same equipment as described in Section 3.4.1 was used.

Valve mass flow

The same equipment as described in Section 3.4.1 was used.

4.3.3 Calibration of instrumentation

The pressure transducers were calibrated using a known pressure source. The pressure source consisted of a compressed air bottle, a needle valve throttle and a precision pressure gauge. A typical pressure transducer calibration is shown in Figure 4-7. Steady flow field tests were performed with both a pitot-static probe, as well as a hot-film probe. Since the pitot probe measurements are very repeatable (due to the repeatability of steady-state pressure transducers), it was possible to obtain accurate measurements of the flow field total-to-static pressure distribution. On later tests, only the hot-film probe was used to measure the steady flow field since a complete steady and dynamic test could be run in the course of an afternoon (recall that the unsteady flow field was measured with a hot-film probe in order to obtain the required frequency response). To maintain some level of repeatability (hot-film sensors tend to drift with time), an in-situ calibration was performed on the hot-film probe directly before and after each test. In general the calibrations differed by no more than 1 percent, therefore it seems reasonable to assume that the actual hot-film measurements do not err by more than this amount. Figure 4-8 shows a typical hot-film calibration, as well as the curve fit to the data.

4.3.4 Acquisition of data

Two computer programs were written to acquire steady and unsteady flow field data respectively. The programs, implemented by a microcomputer, perform the following tasks.

- Prompt the user for the traverse measurement grid size, the number of A/D channels, the number of data points required, and the name of the data file to which the data will be written.

- Move the traverse mechanism to map out the desired measurement grid.
- Command the desired frequencies to the signal generator via the D/A board.
- Acquire the desired data via the A/D board.
- Write the data to file.

Traversing scheme

The X-Y traverse moves the probe in the flow field to create a spatial grid of data. In both steady and unsteady tests, the same measurement grid is used. However, for different injectors, a different grid is used since the extent of radial jet penetration differs for the sheet and 3 hole injectors. The steady data acquisition follows a fairly simple procedure. At each spatial location, several hundred (750) data points are acquired and immediately averaged. The data is then written to disc for later processing. The unsteady data acquisition poses a more involved problem. Again data is taken at all X-Y spatial locations in the measurement grid, however, since it is desired to obtain temporal information about the jet as well, a whole spectrum of frequencies must be examined at each spatial location. This was implemented by exciting the actuator with eight discrete frequency sine wave inputs (50 - 400 Hz in steps of 50 Hz) at each spatial location, while simultaneously acquiring data. For each spatial location and discrete frequency, a number (typically 64) of input sine waves were commanded and measured, since it was required to ensemble average the data to separate the underlying behavior from the turbulent noise caused by mixing. In order to obtain sufficient temporal resolution of each waveform, the A/D sampling frequency was adjusted to acquire approximately 100 data points per wave.

4.3.5 Data processing

In addition to the two data acquisition programs on the microcomputer, several Matlab routines were written to process the data on a minicomputer. These routines were all fairly simple, and only the routine dealing with the ensemble averaging of

the unsteady data will be described here.

Ensemble averaging for unsteady data

In order to be able to observe the fundamental spatial and temporal behavior of the unsteadily modulating jet, the data from each spatial location and discrete frequency were ensemble averaged to conceal the effects of random turbulent fluctuations within the jet. Figure 4-9 shows a typical hot-film time trace for a spatial location in the mixing region of the jet. Such a location was chosen because it exhibits the greatest unsteadiness of the hot-film time trace. While there is a significant difference between the traces made up of the smaller number of ensemble averages, there is little difference between the traces made up the larger number of ensemble averages. Since the hot-film traces chosen for this comparison probably represents a worst case (situated in the highly turbulent mixing zone), based on the data of Figure 4-9, 64 waves were averaged to obtain the ensemble averaged waveform for all spatial locations of the measurement grid for all subsequent tests.

Since the valve position amplitude attenuated slightly between DC and frequencies up to 330 Hz (motor frequency response not perfectly flat in magnitude as shown in Figure 3-7), the valve position and jet momentum data were scaled suitably to compensate for the attenuation. This was done so that the effect of injector attenuation could be separated from the effect of valve attenuation. The data was scaled linearly in such a way so as to keep the valve position amplitude, and the mean momentum flux, constant over the entire frequency range of interest (0 - 400 Hz). This was done by finding the amplitude of the valve position (at each frequency) and increasing it by a certain factor to make it equal the DC amplitude. The same scaling factor was then used (at each frequency) to scale the amplitude of the momentum flux, without changing the mean value of the momentum flux. The scaling required in the 0 - 300 Hz frequency range did not exceed 10 percent, however, the maximum scaling required (at 400 Hz) approached 50 percent.

4.3.6 Wind tunnel checkout

Before starting the tests on the injector, it was necessary to investigate the quality of the tunnel flow field without injection, to see whether the tunnel design was adequate. Points of interest include tunnel speed stability with time, and tunnel flow uniformity.

Speed stability

The tunnel speed was observed to change no more than 2% or 3% with time, for a tunnel Mach number of $M_{fs} = 0.45$. Once the drive compressor, with its associated electrical circuitry, has reached operating temperature, the tunnel speed does not change. Tests done over an hour or two typically only required two or three small (1% or 2%) velocity adjustments. Tunnel speed was varied by simply changing the mechanical speed of the drive compressor.

Tunnel flow uniformity

To establish the inlet bellmouth performance, a steady flow field dynamic pressure survey was performed by traversing the pitot tube in the flow field (63 mm downstream of the actuator center-line). To remove the effect of any small tunnel velocity variations with time, the measured quantities were non-dimensionalized by dividing through by the tunnel dynamic pressure. Figure 4-10 shows the non-dimensionalized momentum flux (dynamic pressure) distribution in the wind tunnel test section, at an axial location 63 mm (2.5") downstream of the actuator. The large grid (175 mm by 175 mm) corresponds to the entire wind tunnel test section area, while the darker grids correspond to the portion of the test section that was actually surveyed (measurement grid). The test section flow field (dynamic pressure) is observed to be uniform to within 2%, except for a decrement in velocity at the tunnel wall due to the wall boundary layer. It was not possible to survey the entire 175 mm by 175 mm (7" x 7") test section due to probe overhang, however, that part of the flow field that would be influenced by the injector was measured and found to be uniform.

4.4 Injector testing

The tests performed on the injectors can be broadly divided into two categories, those dealing with understanding the generic behavior of the injector (bench tests on the circular hole injectors), and those dealing with the effect of the injector on the flow field (wind tunnel tests on the original sheet and 3 hole injectors).

4.4.1 Steady bench tests on the circular hole injectors

The steady tests on the circular hole injectors consisted of measuring the absolute injector plenum total pressure and the valve mass flow. Figure 4-11 shows the characteristic relationship between the injector plenum total pressure and valve mass flow for the 0.5", 0.6" and 0.7" diameter circular hole injectors. Plenum pressure increases with decreasing exit area for a given mass flow, this being expected since, in order to pass a given mass flow, the nozzle pressure drop must be larger for small exit areas, and vice versa. Furthermore, the relationship between injector plenum pressure and mass flow is linear above a certain plenum pressure corresponding to the choke point of the nozzle, the nozzle being choked above this pressure. For a fixed downstream pressure (set by the ambient atmosphere), a super-critical nozzle has a linear relationship between upstream total pressure and mass flow, while a sub-critical nozzle has an upstream total pressure that varies with the square of the mass flow. Both trends are evident from the plot, the dividing line between the two regimes occurring at approximately 190 kPa. Taking the critical pressure ratio to be 1.89 for air, it is possible to find the discharge coefficient of the choked injector nozzle since the mass flow, total temperature and total pressure of the injector plenum are known. The mass flow of a real compressible choked nozzle is given by

$$\dot{m}_3 = C_{d3}\rho_3 A_3 U_3 \tag{4.1}$$

where C_{d3} is the exit nozzle discharge coefficient,

$$\rho_3 = \frac{p_3}{RT_3}$$

and

$$U_3 = M_3\sqrt{\gamma RT_3}$$

The static pressure and temperature at the nozzle exit (assuming choked flow) are given by

$$p_3 = \frac{P_{t2}}{(1 + 0.2M_3^2)^{3.5}}$$

and

$$T_3 = \frac{T_{t2}}{(1 + 0.2M_3^2)}$$

Substituting any experimental pressure/mass flow combination above the choke point (e.g. 450 kPa, 0.1 kg/s), and assuming the exit Mach number M_3 to be unity, yields a discharge coefficient $C_{d3} = 0.75$. This is close to the value commonly used ($C_d = 0.65$) for a sharp-edged circular orifice, thus it can be used as a first guess for the discharge coefficient of the flow field injectors.

The overlapping of the three separate curves, which make up the characteristic for each of the 3 circular hole injectors, indicates that modeling the valve as a mass flow modulator simplifies the analysis of the valve/injector combination. Since the injector must pass the same mass flow as the valve (in steady operation), it will adjust its plenum pressure until this holds true, irrespective of the supply pressure to the valve. Clearly, only the mass flow supplied to the injector by the valve is relevant, not the total pressure upstream of the valve. Obviously this argument only holds if the valve remains choked. It is therefore more useful to think of the valve, not as a device which modulates total pressure of the injectant (which indeed it is doing), but rather as a device that modulates mass flow into the injector. This is because the choked valve orifice explicitly modulates mass flow, all downstream variables being set by the particular injector used.

4.5 Flow field tests - original injectors

An objective of the injector design is to add momentum to the freestream flow in a predictable and effective manner. To establish the distribution of momentum injected into the freestream flow, both steadily and unsteadily, flow field tests were performed in the wind tunnel. The tunnel freestream Mach number was taken to be $M_{fs} = 0.45$, which is equal to the upstream axial Mach number of NASA Stage 35 at stall. The steady (pitot tube) and unsteady (hot-film) probe was located 63 mm (2.5") downstream of the actuator center-line, an axial position which corresponds to the planned location of the compressor face on tests using NASA Stage 35.

4.5.1 Steady flow field tests

Figure 4-12 and Figure 4-13 show the steady momentum flux (ρV^2) distributions of the original sheet and 3 hole injector respectively. The momentum flux distributions have been normalized by the tunnel momentum flux, but the spatial coordinates have been left in dimensional form since no consistent reference length could be found. In both figures, the valve is fully open, therefore the maximum injectant mass flux is being passed.

Referring first to the sheet injector, it would appear that there are two distinct jets instead of a single jet sheet. What has happened is that the jet sheet has rolled up into two axial vortices, the vortices containing fluid with high relative dynamic pressure, while the surrounding flow has the freestream dynamic pressure. The jet sheet rolls up in this fashion because it becomes separated from the casing wall as it exits the injector. The rolling up of the jet sheet was confirmed by introducing smoke into the injector flow, thus allowing the tunnel and injector flow to be visualized. Also, the jet total pressure at the injector exit was measured to be uniform across the entire width of the sheet injector. This implies that the 2 peaks in jet momentum distribution are not present at the injector exit, but develop as the injector flow travels towards the measurement location (compressor face). The two momentum peaks (axial vortices) are undesirable since the sheet injector was supposed to inject a flat sheet of high

momentum fluid.

The original 3 hole injector, has a far more predictable momentum distribution, with three distinct peaks corresponding to the three injector nozzles. The radial penetration of the 3 hole injector is somewhat greater than that of the sheet injector, whereas the circumferential spreading is about the same. The peak momentum flux of the 3 hole injector is equal to 6, implying that the ratio of the jet to freestream Mach numbers at the measurement location is about 2.4 (momentum flux scales quadratically with velocity). For a freestream Mach number $M_{fs} = 0.45$, the peak jet Mach number is $M_j = 1.1$. The jet therefore expands to a supersonic velocity outside the convergent injector nozzle.

4.5.2 Unsteady flow field tests

Having quantified the steady spatial distribution of momentum for the original sheet and 3 hole injectors, the unsteady response of the injectors was measured next. This was done by spatially averaging the jet momentum of the entire flow field (spatial measurement grid) at each instant in time, while the jet was being modulated unsteadily at different frequencies. Figure 4-14 and 4-15 show Bode plots of the spatially averaged momentum flux (with respect to valve position), for the original sheet and 3 hole injectors respectively. The three different curves on the plots correspond to the zeroth (—), first (- -) and second (-.-) temporal harmonics of the spatially averaged momentum flux (ρV^2). For both injectors the zeroth temporal harmonic (or mean) dominates, which can be expected since the modulating jet only affects portions of the data grid in a significant way, much of the freestream flow through the grid being steady. The first temporal harmonic of momentum flux is that component of the fluid response which corresponds to the sinusoidal excitation of the valve. As such, the relative magnitude of the first temporal harmonic at different frequencies is the relevant criterion in determining the attenuation of the injector response with frequency. In this case, the response of the first temporal harmonic attenuates significantly with frequencies above 100 Hz for both injectors. This is undesirable since it implies that the injectors only have significant unsteady control power at low frequency (below

150 Hz or 200 Hz).

Referring to the phase plots for both injectors, the phase of the first temporal harmonic rolls of rapidly, and then increases again. This bending up of the phase plots is thought to be caused by low coherence between the jet momentum flux and reference valve position signals (when the magnitude of the first temporal harmonic is small). The phase of the second temporal harmonic was found to be quite random, which is expected since there is no component of this harmonic in the input excitation to the actuator. Since the magnitude of the second temporal harmonic is much smaller than that of the first, this random behavior is insignificant. For this reason, the second temporal harmonic is not shown on these, as well as subsequent, Bode phase plots.

4.6 Non-linear simulation of the injector plenum

The unsteady flow field measurements of the original sheet and 3 hole injectors indicated that their dynamic performance was unsatisfactory, the magnitude of the fluid jet modulation (first temporal harmonic) attenuating rapidly with frequencies above 100 Hz. To explain this behavior, a non-linear computer simulation of the injector performance was written. It was assumed that the mass flow entering the injector plenum is a function of the valve position only. The actual relationship between mass flow and valve position was obtained from the steady state valve characteristic described in Section 3.4.2. It was assumed that this relationship holds at the frequencies of interest (up to 500 Hz), which is justified since the time scales of the flow through the valve orifice are 2 to 3 orders of magnitude lower than those of the injector plenum, as discussed in Section 3.4.3. The injector nozzle was modeled as a quasi-steady isentropic convergent nozzle. When the nozzle pressure ratio is sub-critical the flow is subsonic, with the nozzle exit pressure matching the ambient pressure. When the nozzle pressure ratio is super-critical, the nozzle is modeled as being choked, with the nozzle exit pressure equal to the choked throat pressure. The plenum is modeled as a fixed volume with a varying density, the latter quantity being the inlet condition to the injector nozzle. The step by step implementation of the non-linear simulation

is outlined below. Figure 4-16 is a schematic of the injector geometry, showing the relevant stations for the analysis that follows.

Step 1 Quasi-steady assumption for the choked valve orifice

$$\dot{m}_1 = f(\alpha, T_{t0}, P_{t0}) \tag{4.2}$$

Step 2 Quasi-steady assumption for the injector nozzle. If $P_{t2} > 1.89 p_{at}$ we have choked flow in the injector nozzle and thus

$$\dot{m}_3 = f(T_{t0}, P_{t2}, A_3, C_{d3}) \tag{4.3}$$

If $P_{t2} < 1.89 p_{at}$ we have unchoked flow in the injector nozzle and thus

$$\dot{m}_3 = f(T_{t0}, P_{t2}, A_3, p_{at}, C_{d3}) \tag{4.4}$$

Step 3 Unsteady mass storage in the injector plenum is given by

$$\dot{m}_1 - \dot{m}_3 = \frac{d}{dt}(\rho_2 V_2) \tag{4.5}$$

$$\frac{d\rho_2}{dt} = \frac{\dot{m}_1 - \dot{m}_3}{V_2}$$

Discretizing this into finite (small) time steps using forward Euler yields

$$\rho_{2,n+1} = \rho_{2,n} + \frac{d\rho_{2,n}}{dt}\Delta t \tag{4.6}$$

Knowing $\rho_{2,n+1}$, we can calculate $P_{t2,n+1}$.

$$P_{t2,n+1} = \rho_{2,n+1} R T_{t0} \tag{4.7}$$

Step 4 Return to Step 1 until simulation is complete.

The simulation marches in time, modulating the mass flow into the plenum. The resulting injector plenum and nozzle exit quantities are calculated using the algorithm outlined above. Details of the specific equations used can be found in Appendix A.

4.6.1 Comparison of experimental and simulated results

To validate the non-linear numerical prediction, some unsteady experimental tests were performed on the 3 circular hole injectors. Since it was only desired to investigate the performance of the injector internal dynamics, it was unnecessary to perform a flow field test in the wind tunnel, a simple unsteady bench test being sufficient. The unsteady jet mass flux of the injector nozzle (ρU) was measured by placing the hot-film probe at the exit plane of the injector. Even if the nozzle underexpands the flow (as is the case with the original 3 hole injector), the pressure, density and Mach number at this location should be close to the throat values since the measurement location is well within any Mach cones that would expand the flow to ambient pressure. Since a hot-film probe directly measures the product of density and velocity, namely the mass flux (ρU), this quantity was used to plot the predicted and measured data.

Figure 4-17 shows experimental time traces of the valve position and jet mass flux at 8 different frequencies (50 to 400 Hz in steps of 50 Hz), for the 0.5" circular hole injector. The horizontal axes of both plots have been normalized by the period of a single wave at each particular frequency. On the vertical axes, valve position has been normalized, but jet mass flux ($\rho_3 V_3$) has been left in dimensional form since no obvious reference quantity could be found. The valve position traces are virtually identical since they were used as a common reference to phase lock the jet mass flux measurements. The plot of jet mass flux indicates that the modulation of the jet at low frequencies is large, but is attenuated as the frequency increases (in the figure, the highly oscillatory curves correspond to the lower frequencies). The mean jet mass flux is around 1000 $kg.m^{-2}.s^{-1}$, and remains constant with frequency. Figure 4-18 shows the simulated (using the non-linear injector simulation) time traces of valve position and jet mass flux for the same injector, also at the eight different frequencies. It is observed that the overall magnitudes and general trends of the experimental and

simulated plots are very similar. In addition, the attenuation of jet mass flux with increasing frequency is also predicted by the simulation.

To quantify the general trends more carefully, the experimental and simulated data were decomposed into their temporal Fourier harmonics. Figure 4-19 and Figure 4-20 are Bode plots of the time domain data shown in Figure 4-17 and Figure 4-18, respectively. Referring first to the experimental Bode magnitude plot, it is observed that the mean jet mass flux (—) remains essentially constant with frequency. The first temporal harmonic (- -), which corresponds in frequency to the sine wave valve excitation, attenuates rapidly at frequencies above 50 Hz. The second temporal harmonic (-.-) is small, implying that the harmonic distortion of the valve/injector combination is small. Referring now to the experimental Bode phase plot, it is observed that the phase of the first temporal harmonic of jet mass flux (- -) rolls off with frequency even at low frequencies. The bending up of the curve at higher frequencies is probably due to the small magnitude of the first temporal harmonic at high frequencies. The phase of the second temporal harmonic is not shown since it is incoherent as a result of the small magnitude of the second temporal harmonic.

The simulated injector frequency response shown in Figure 4-20 is observed to be very similar to the experimental response, even the absolute magnitudes of quantities being similar. Again, the dominant trend is that the temporal first harmonic of jet mass flux attenuates rapidly with increasing frequency. As will be shown later, this is due to the small exit area of the 0.5" circular hole injector.

Figure 4-21 through 4-24 are the same plots as Figure 4-17 through 4-20, except that they refer to the 0.7" circular hole injector. Figure 4-21 and Figure 4-23 indicate that the gross qualitative trends of the experimental and predicted data are once again similar. Figure 4-22 and Figure 4-24 show that, for this larger exit diameter, the magnitude of the first temporal harmonic of jet mass flux attenuates far less rapidly with frequency, as shown quite clearly by the experimental and simulated Bode plot magnitudes of the first temporal harmonic. Furthermore, it is observed that the magnitude of the first temporal harmonic of mass flux is large compared to the mean mass flux, and remains that way for the entire frequency measured and

predicted (0 - 400 Hz). Because the injector exit area has increased, the mean velocity and density of the jet have been reduced. This manifests itself as a decrease in the magnitude of the zeroth (mean) temporal harmonic of jet mass flux. The phase of the first temporal harmonic of jet mass flux still rolls off with frequency, but much less than with the 0.5" circular hole injector. The roll-off in phase, though reduced, is due to the first order behavior of the injector plenum. It would appear then that the one of the ways to get additional frequency response from a badly performing injector is simply to increase the injector exit area.

The good match between simulated and experimental results, as well as the simplicity of the simulation, suggest that the essential dynamics of the injector have been captured by the simulation. In Section 2.9.3 it was shown that the (much simplified) transfer function of an injector plenum (Helmholtz resonator) is given by

$$\frac{U_3}{U_1} = \frac{A_1/A_3}{(1 + \frac{V_2}{A_3}\frac{U_3 s}{a_2^2})} \tag{4.8}$$

If velocity (U) is assumed to be representative of mass flux (ρU), then this expression clearly reveals the underlying parameters that affect the frequency response of the jet mass flux for the injector. Firstly, the ratio of injector inlet to exit area (A_1/A_3) determines the DC (or mean) level of injector exit mass flux. Secondly, the ratio of injector volume to nozzle exit area (V_2/A_3) determines the corner frequency of this first order system. Thus, although the non-linear injector simulation gives more accurate quantitative results, it qualitatively predicts the same injector response as the simple transfer function model. It is interesting to note that the only 'fudge factor' used in the non-linear injector simulation was an injector nozzle discharge coefficient, which was set equal to $C_{d3} = 0.75$ (from Section 4.4.1). It therefore seems reasonable to use this simulation in a predictive fashion to optimize the design of the modified sheet and 3 hole injectors.

4.6.2 Prediction of modified injector frequency response

The non-linear injector simulation was run for various plenum volumes and exit areas. Figure 4-25 shows the baseline 3 hole injector frequency response (original injector before modification). Figure 4-26 shows the effect of halving the baseline injector plenum volume V_p, while keeping the injector exit area A_3 constant. The smaller plenum volume leads to somewhat better frequency response (less rapid magnitude and phase roll-off), but there is still too much attenuation in the first temporal harmonic. Figure 4-27 shows the effect of increasing the baseline injector nozzle exit area A_3 by a factor of two, while keeping the plenum volume V_p constant. An increase in the injector nozzle exit area improves the frequency response considerably, the temporal first harmonic of mass flux now being similar in magnitude to the mean mass flux, and remaining so for the frequency range of interest (0 - 400 Hz). The scales of the plots have been left the same as in the previous two figures so that a direct comparison can be made. Increasing the injector nozzle exit area reduces the mean jet mass flux (ρU) through the nozzle, from a value of 1000 $kg.m^{-2}.s^{-1}$ in the baseline case, to 500 $kg.m^{-2}.s^{-1}$ in the modified case. This validates the DC injector response suggested by the simple transfer function prediction (equation 4.8), since the injector exit mass flux has been halved when the ratio of injector inlet to exit areas A_1/A_3 has been halved.

Comparing the Bode plots of the three cases mentioned above, it is clear that, for the values of plenum volume and jet exit area chosen in the original baseline design, the frequency response is more sensitive to changes in jet exit area than plenum volume.

4.7 Injector modifications

Based on the preliminary tests and analysis outlined above, it was concluded that the initial injector design had too large a plenum volume relative to its exit area. Since it would be more difficult to change the plenum volume significantly in the mechanical design of the actuator, the injector exit area was modified to see whether a substantial

improvement in high frequency response could be obtained, as predicted by the non-linear simulation. Figure 4-4, F and G shows a schematic of the modified 3-hole and sheet injectors respectively, the primary difference between the original and the modified injectors being an increase (128%) of exit area from $127mm^2$ (effectively d_3 = 12.7 mm or 0.5") to 290 mm^2 (d_3 = 19 mm or 0.75"). It should be noted that the mechanical design of the modified injectors was constrained by factors other than just the required exit areas. Fitting the modified injector design, with the new desired exit areas, and the desired injection angles, into the existing actuator design proved to be quite challenging. Two practical injectors were however designed (a modified sheet and 3 hole injector), the performance of these injectors being discussed in detail in Chapter 5.

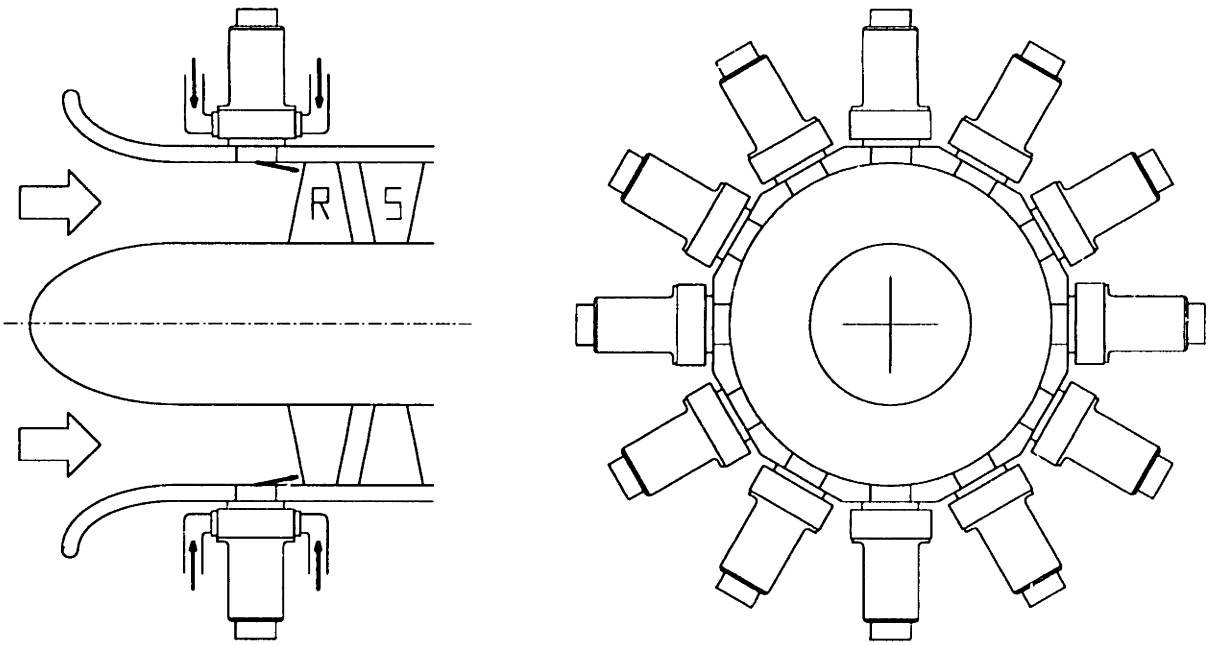

Figure 4-1: Schematic of jet actuation in a high speed axial compressor.

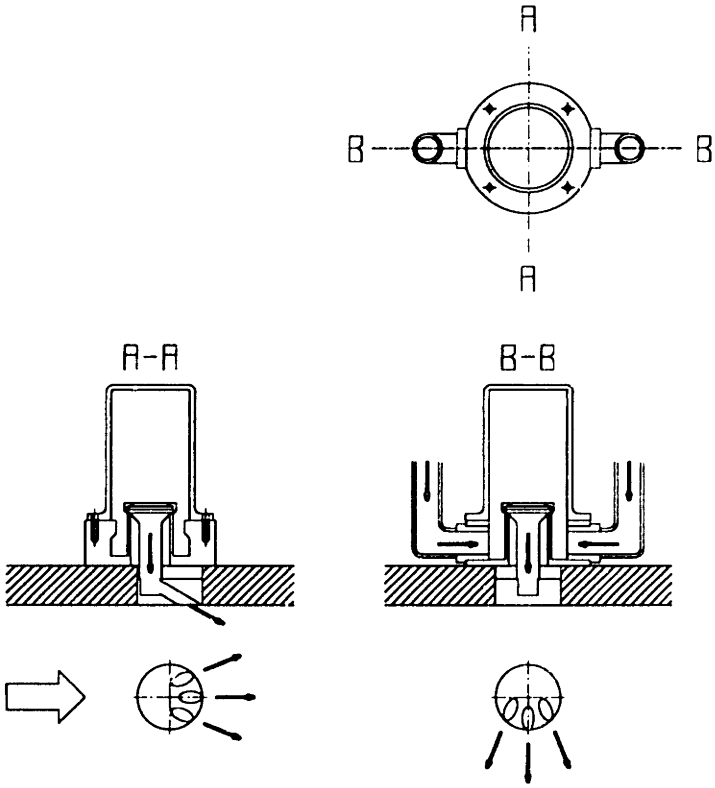

Figure 4-2: Schematic of actuator, showing valve, injector and injectant flow path.

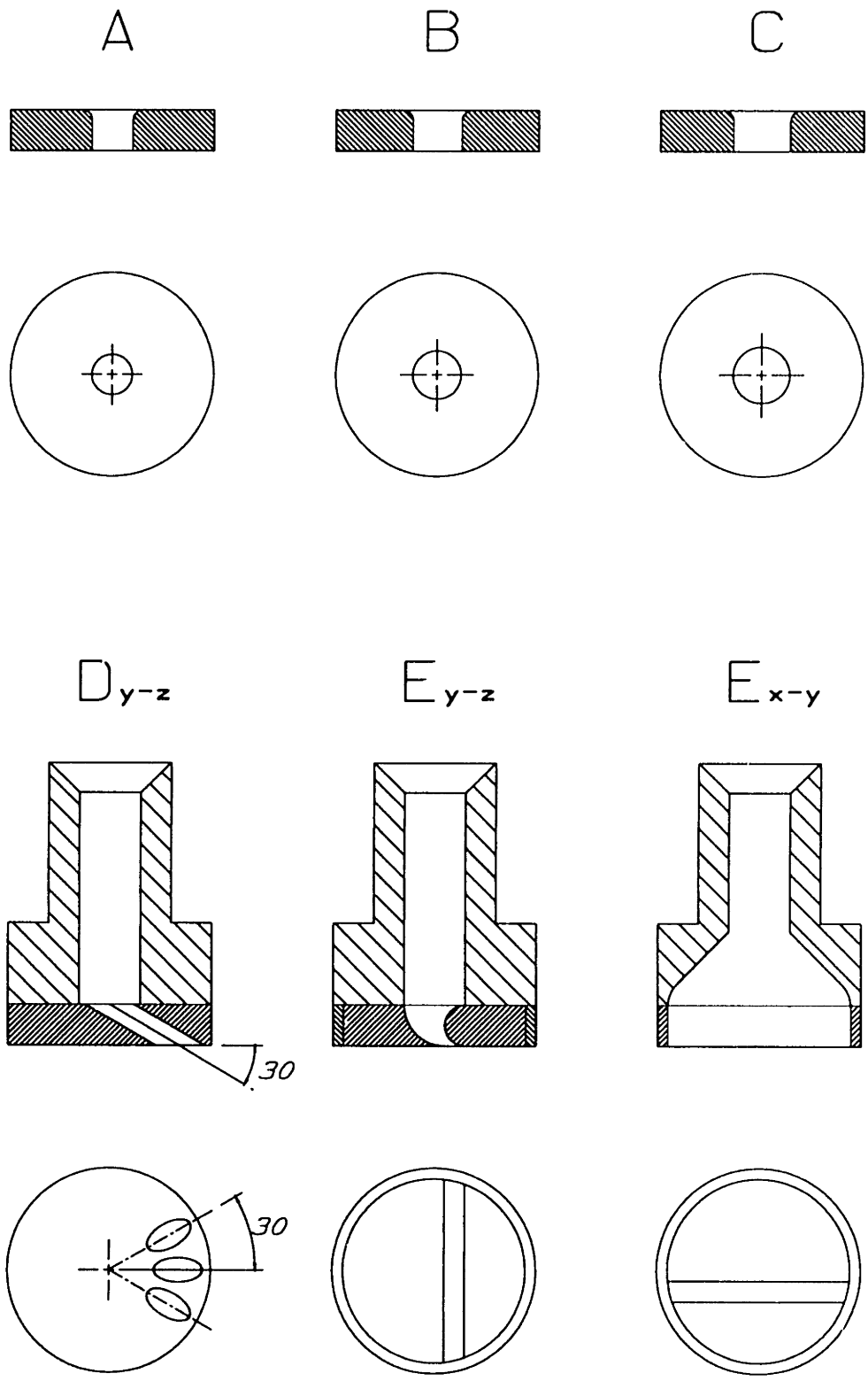

Figure 4-3: Circular hole injectors (A, B and C), and original 3 hole and sheet injectors (D and E).

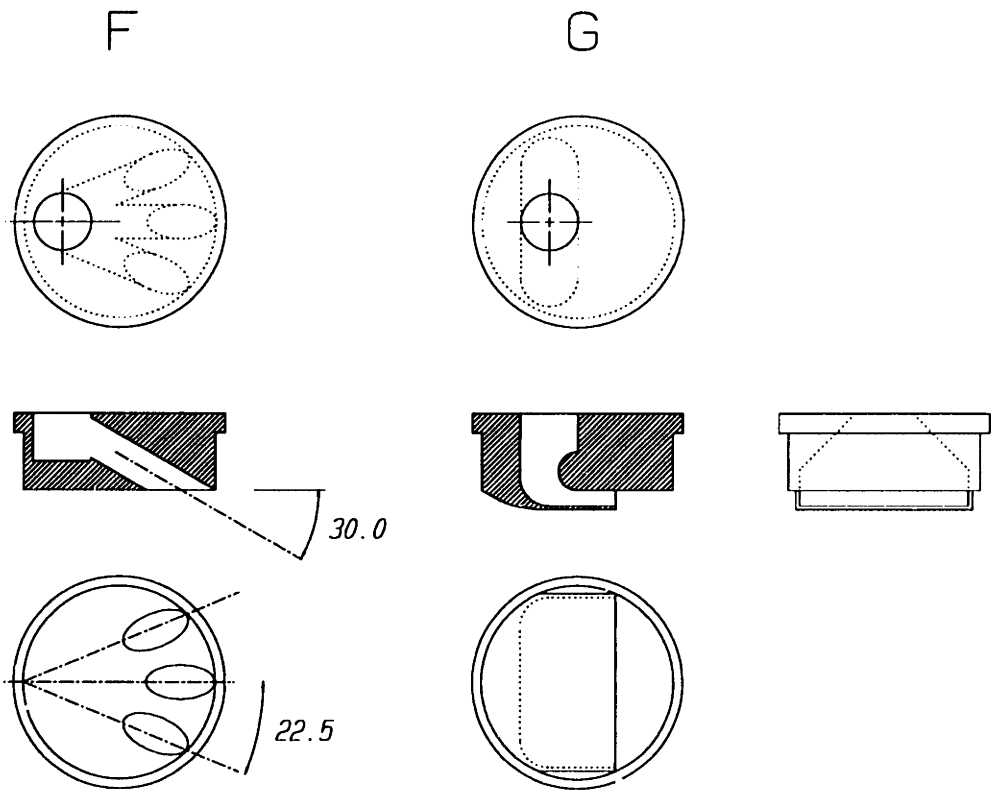

Figure 4-4: Modified 3 hole and sheet injectors (F and G).

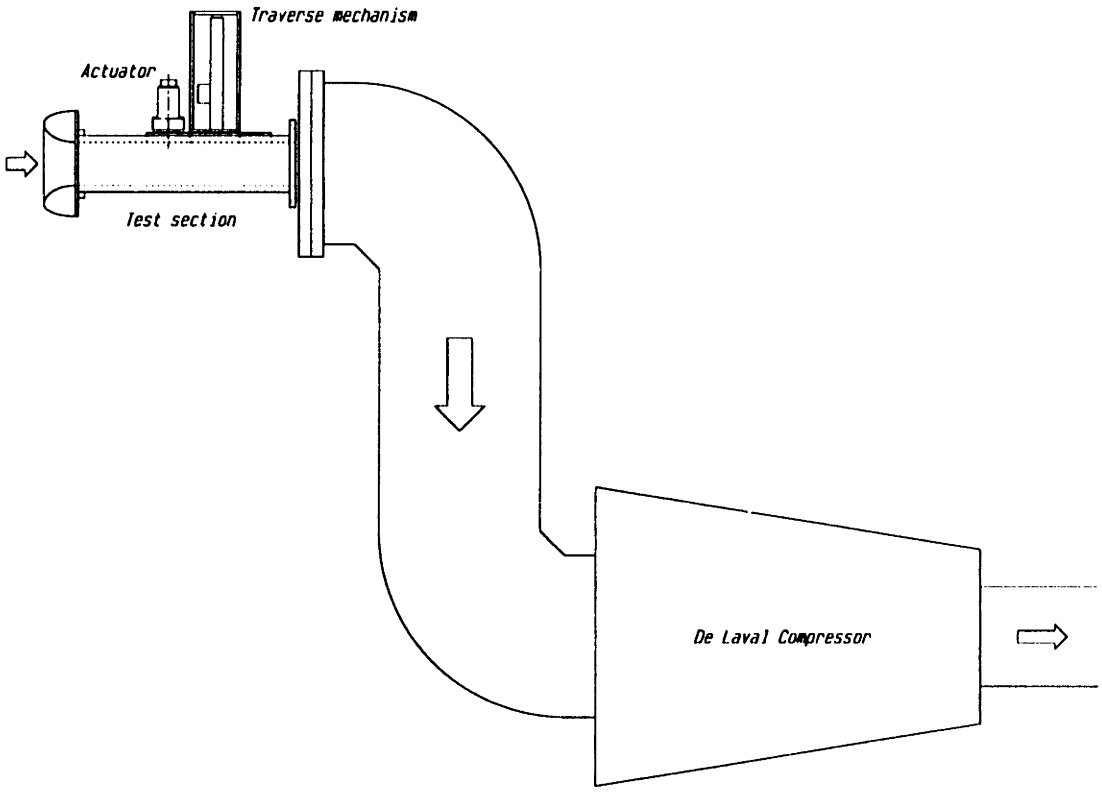

Figure 4-5: Schematic drawing of the wind tunnel and its drive compressor.

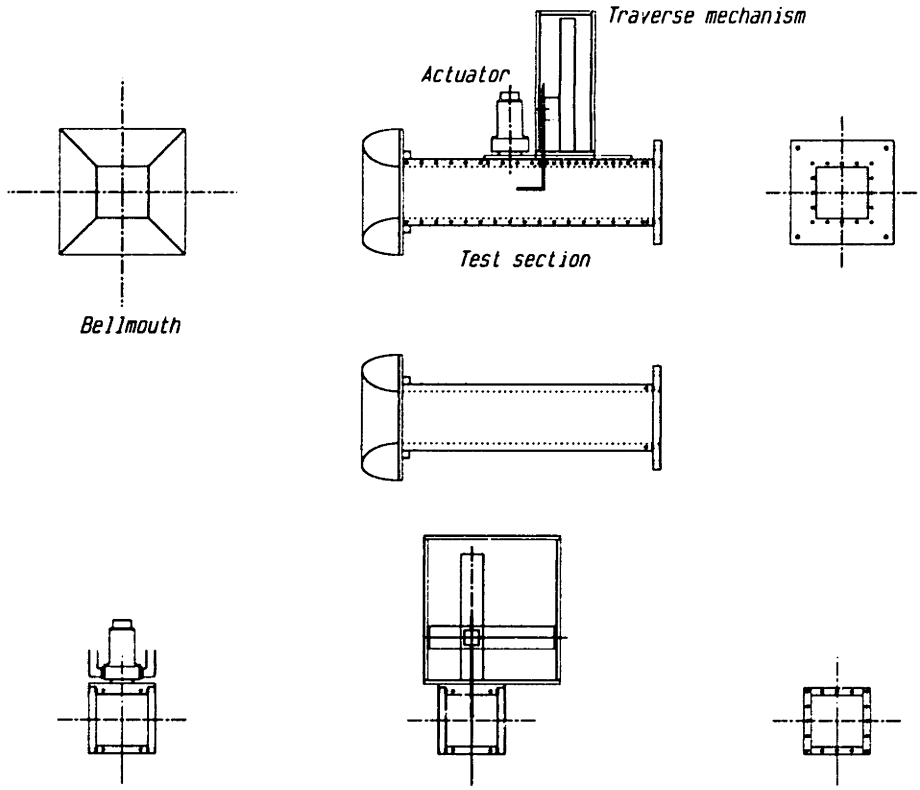

Figure 4-6: Detail of the wind tunnel used for the actuator flow field tests.

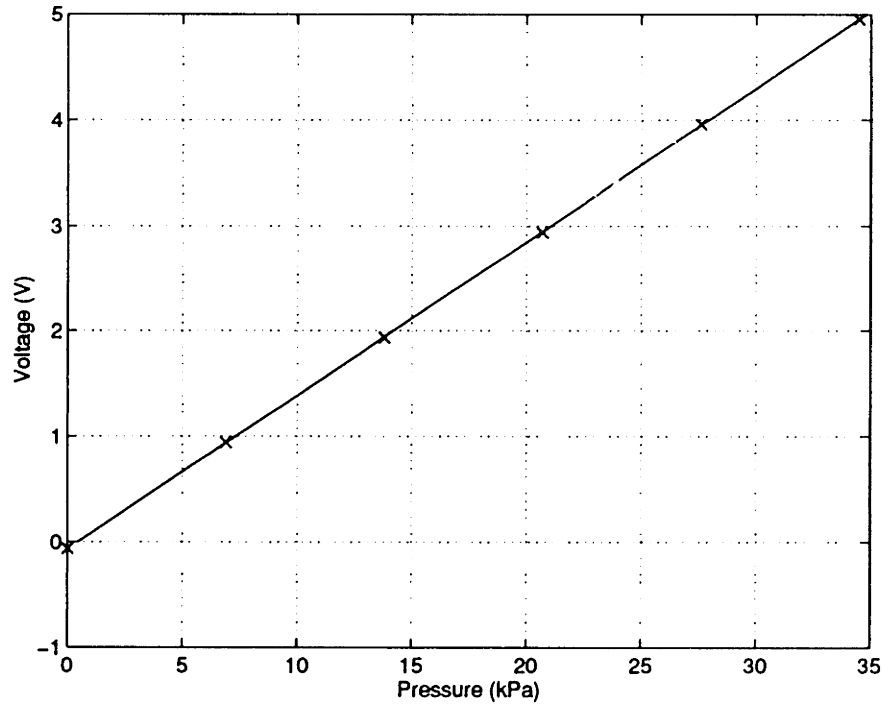

Figure 4-7: Typical pressure transducer calibration.

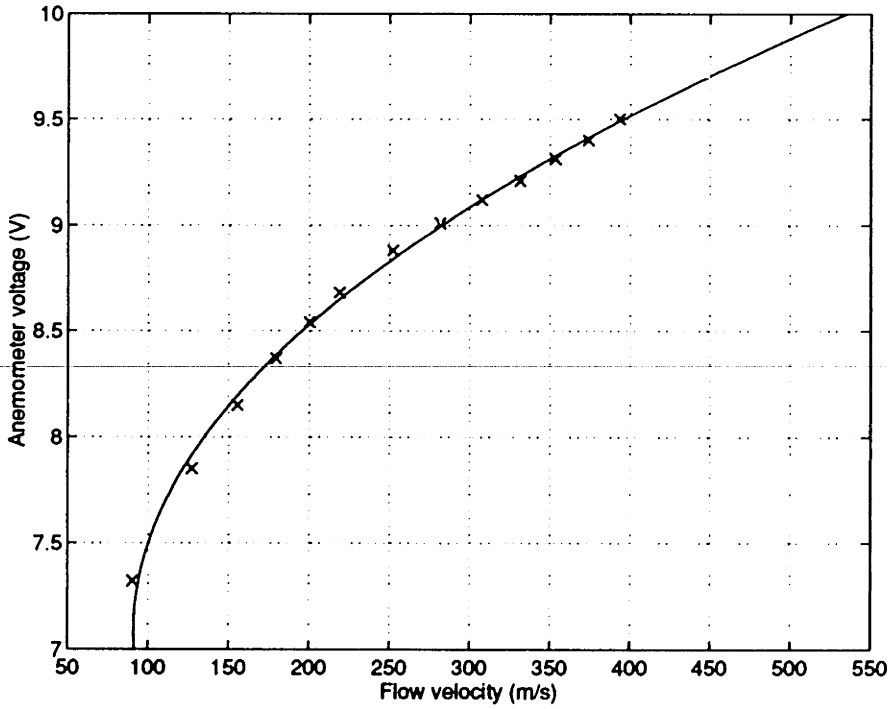

Figure 4-8: Typical hot film calibration data and curve fit.

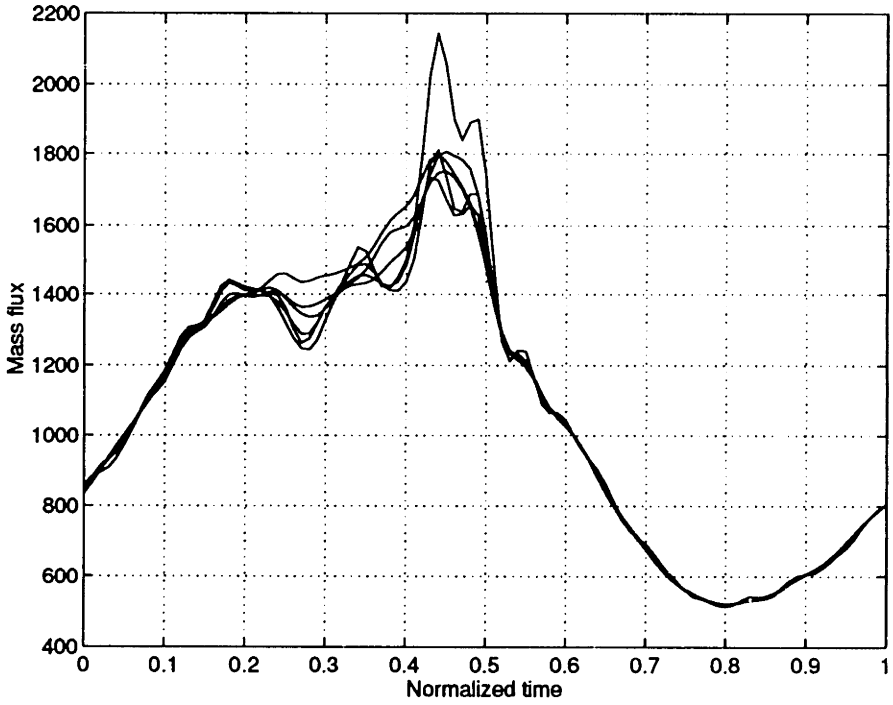

Figure 4-9: Ensemble averages of 1, 2, 4, 8, 16, 32 and 64 hot-film traces.

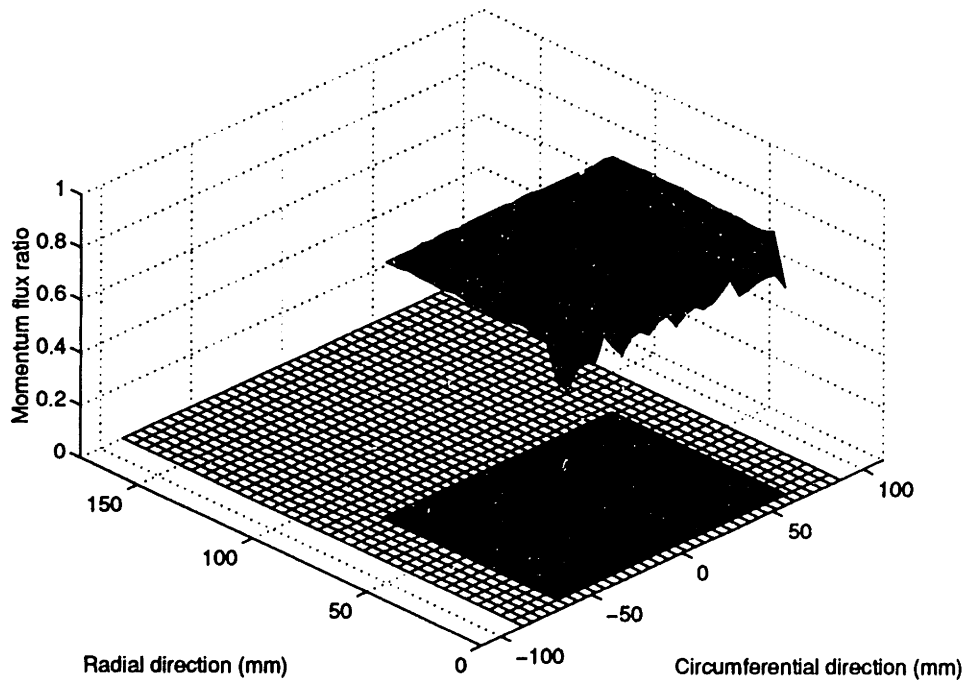

Figure 4-10: Distribution of dynamic pressure in the wind tunnel section, no injection.

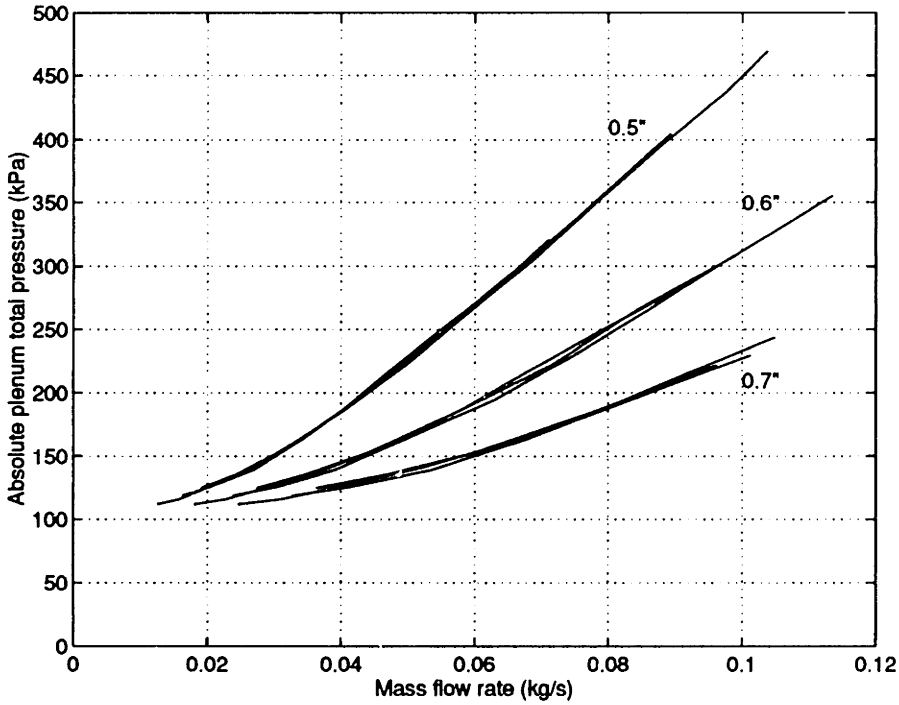

Figure 4-11: Plenum pressure versus mass flow characteristic, 0.5", 0.6" and 0.7" circular hole injectors. Overlapping curves correspond to 414, 552 and 656 kPa (60, 80 and 95 psig) valve upstream pressure.

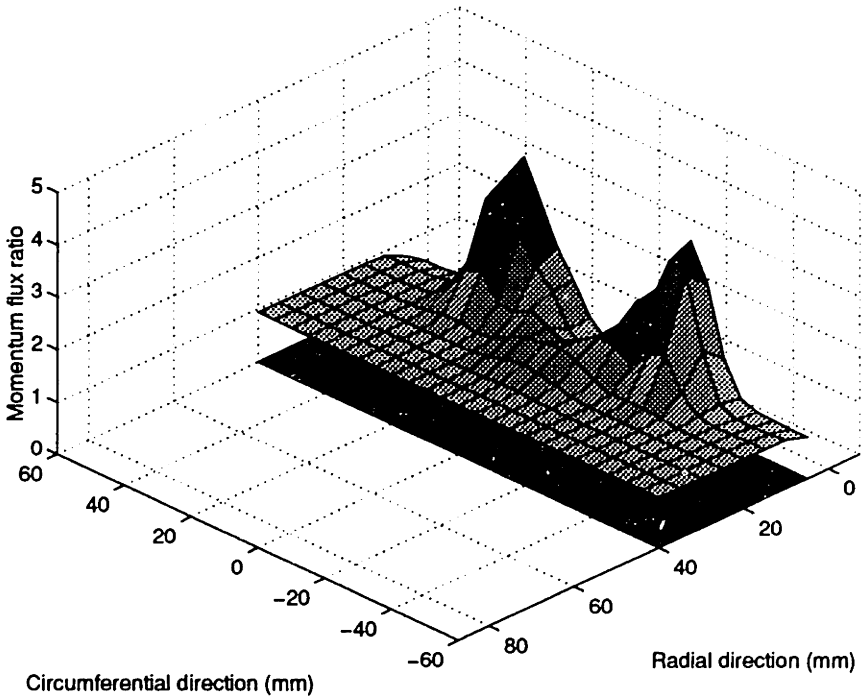

Figure 4-12: Steady momentum flux distribution of the original sheet injector, $\alpha = 1$.

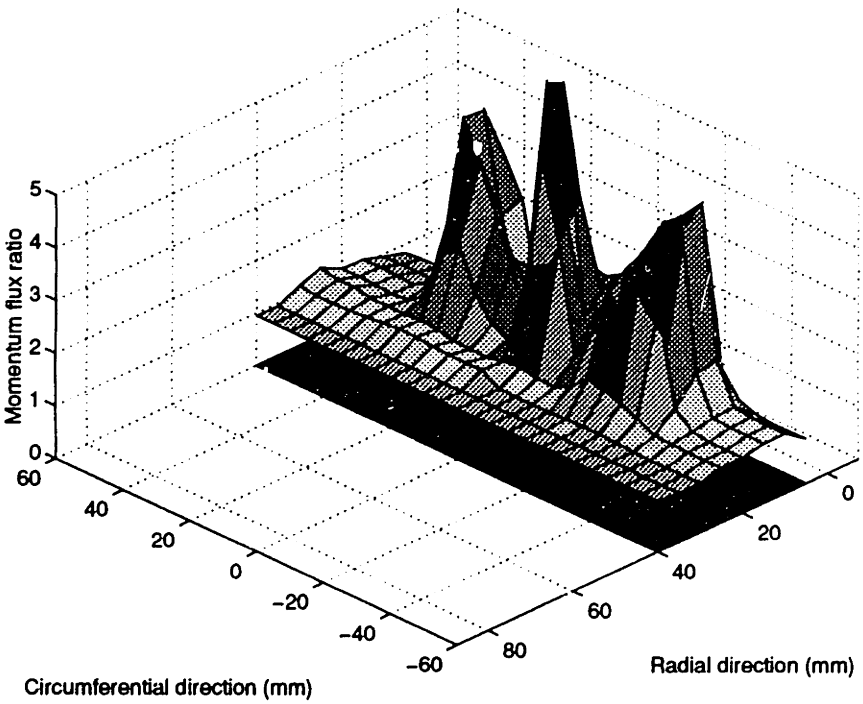

Figure 4-13: Steady momentum flux distribution of the original 3 hole injector, $\alpha = 1$.

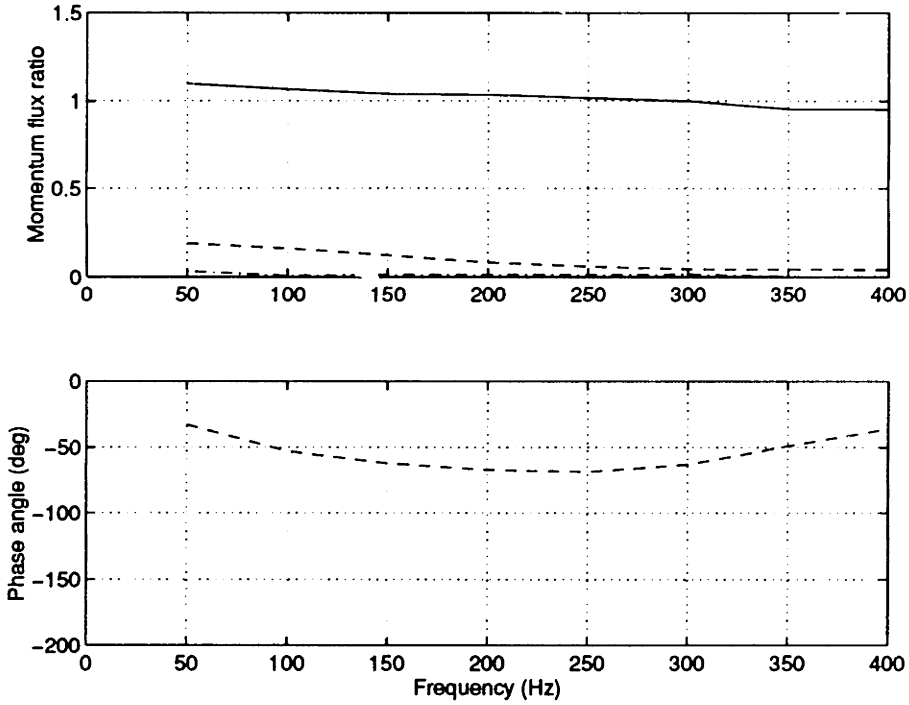

Figure 4-14: Bode plot of valve position to spatially averaged momentum flux for the original sheet injector. Zeroth (—), 1st (- -) and 2nd (-.-) temporal harmonic.

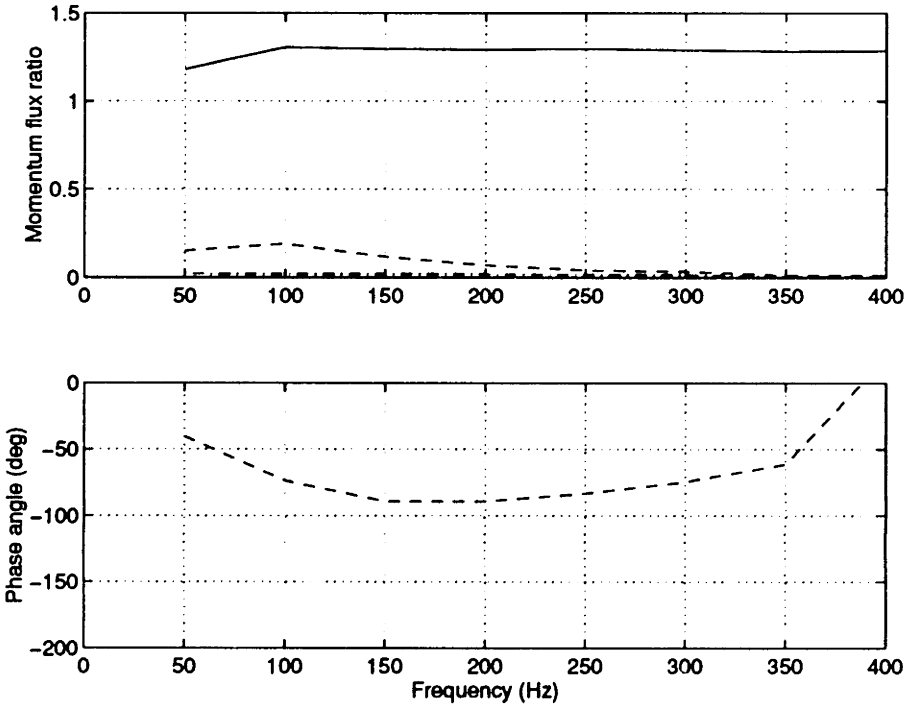

Figure 4-15: Bode plot of valve position to spatially averaged momentum flux for the original 3 hole injector. Zeroth (—), 1st (- -) and 2nd (-.-) temporal harmonic.

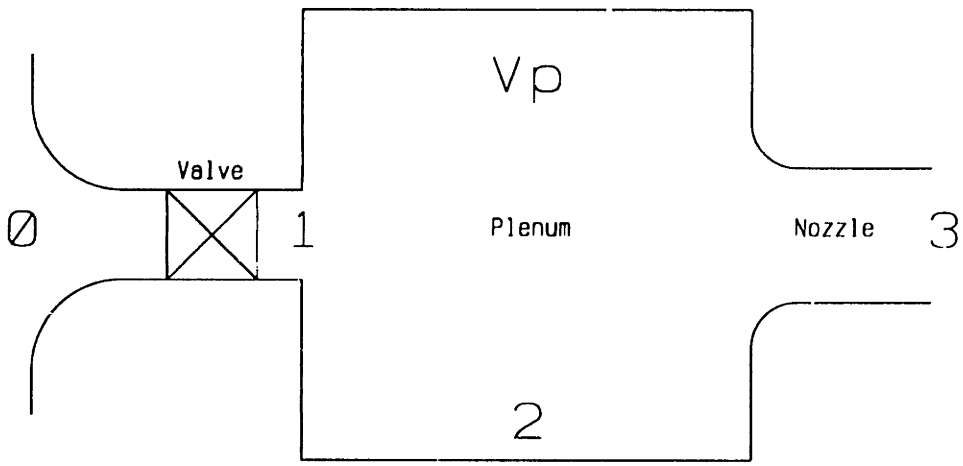

Figure 4-16: Schematic representation of the injector geometry.

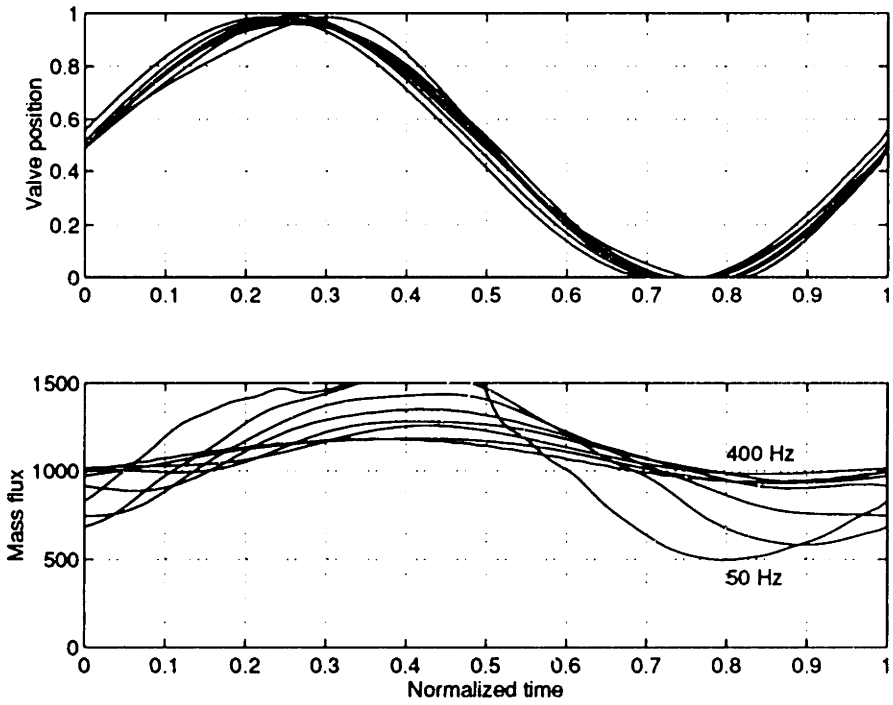

Figure 4-17: Experimental time traces of valve position and jet mass flux, 0.5" circular hole injector, 50 - 400 Hz.

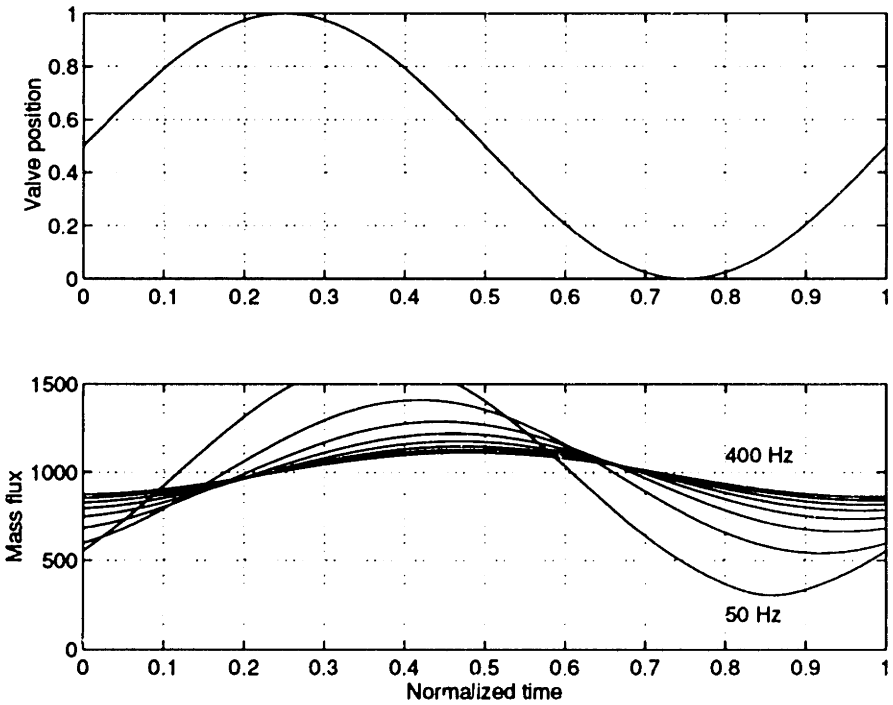

Figure 4-18: Simulated time traces of valve position and jet mass flux, 0.5" circular hole injector, 50 - 400 Hz.

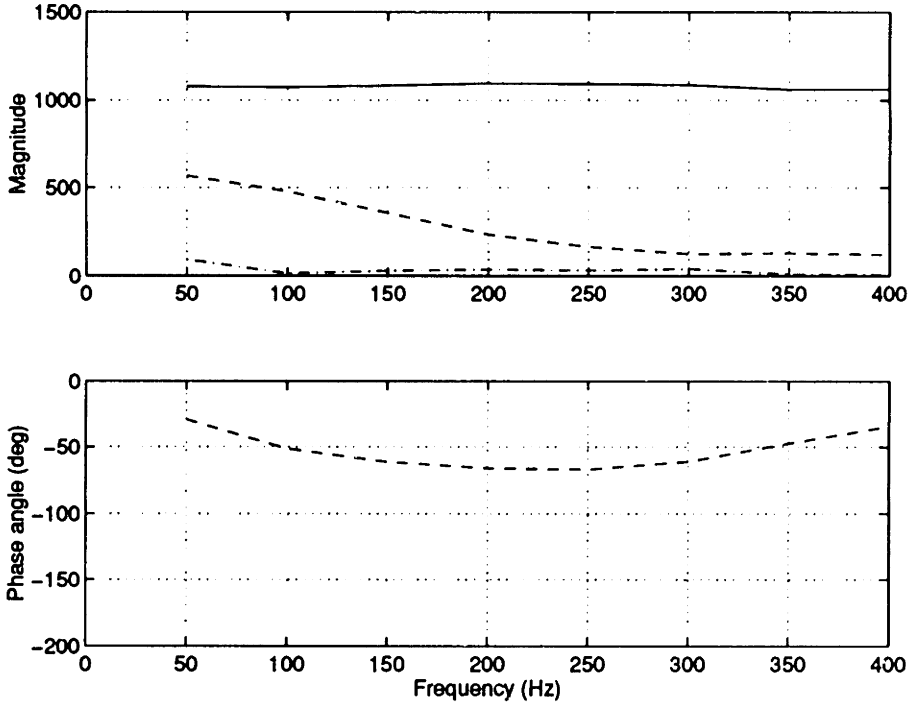

Figure 4-19: Experimental Bode plot of valve position to jet mass flux, 0.5" circular hole injector. Zeroth (—), 1st (- -) and 2nd (-.-) temporal harmonic.

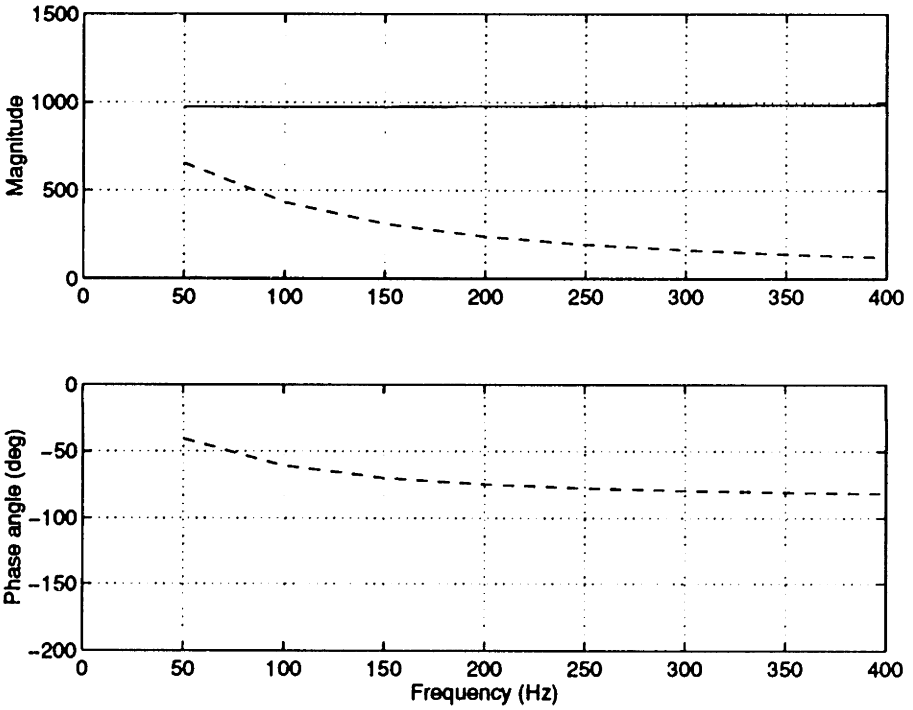

Figure 4-20: Simulated Bode plot of valve position to jet mass flux, 0.5" circular hole injector. Zeroth (—), 1st (- -) and 2nd (-.-) temporal harmonic.

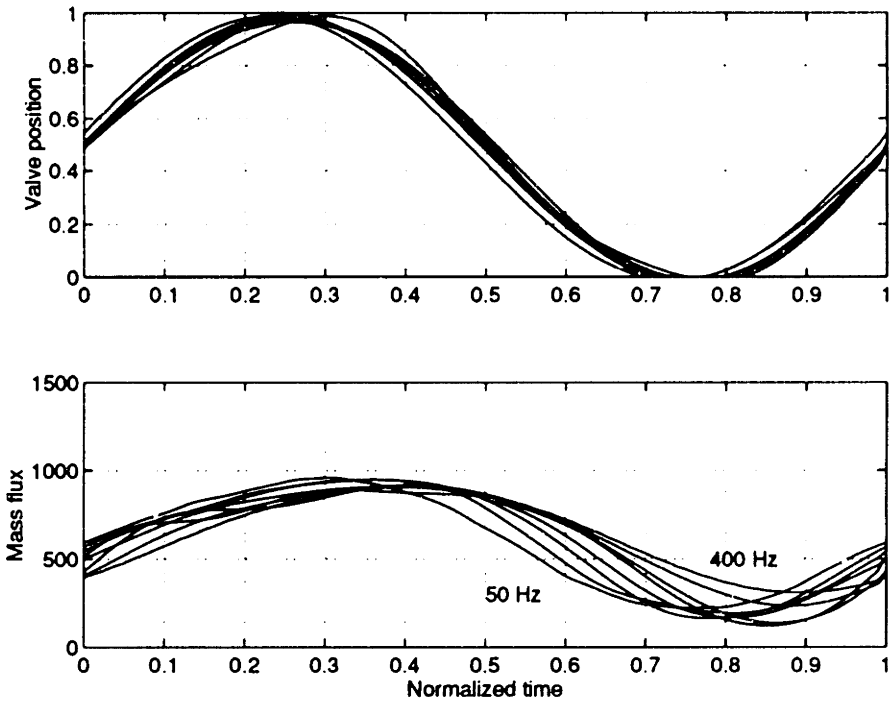

Figure 4-21: Experimental time traces of valve position and jet mass flux, 0.7" circular hole injector, 50 - 400 Hz.

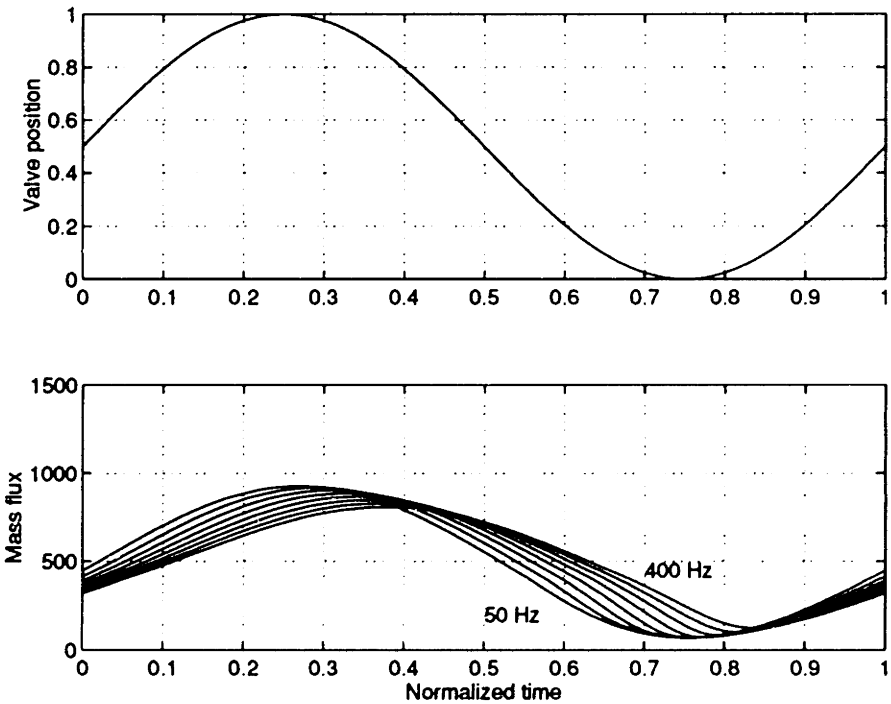

Figure 4-22: Simulated time traces of valve position and jet mass flux, 0.7" circular hole injector, 50 - 400 Hz.

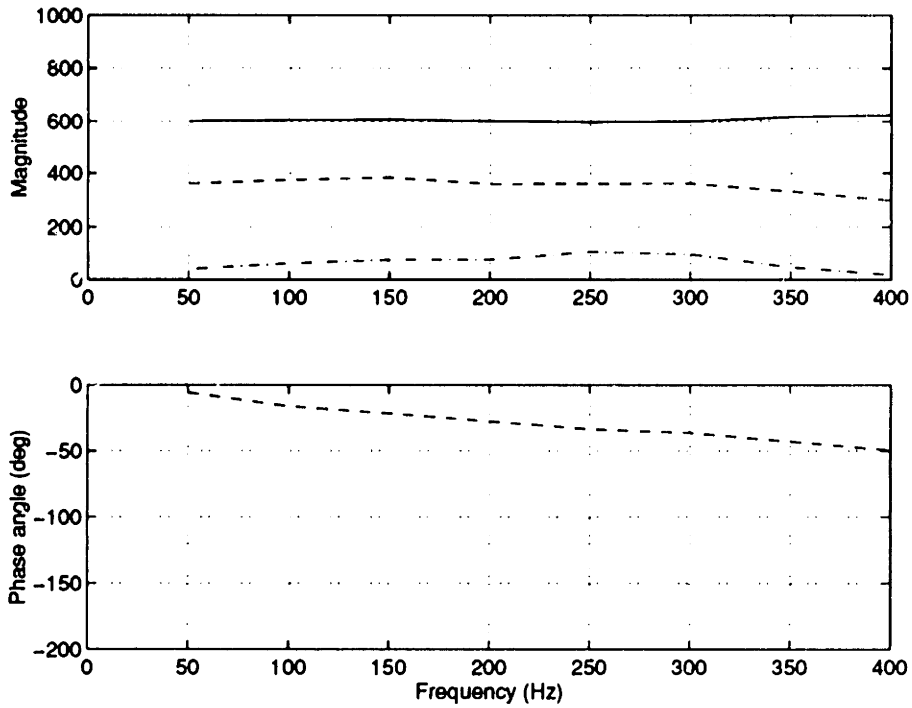

Figure 4-23: Experimental Bode plot of valve position to jet mass flux, 0.7" circular hole injector. Zeroth (—), 1st (- -) and 2nd (-.-) temporal harmonic.

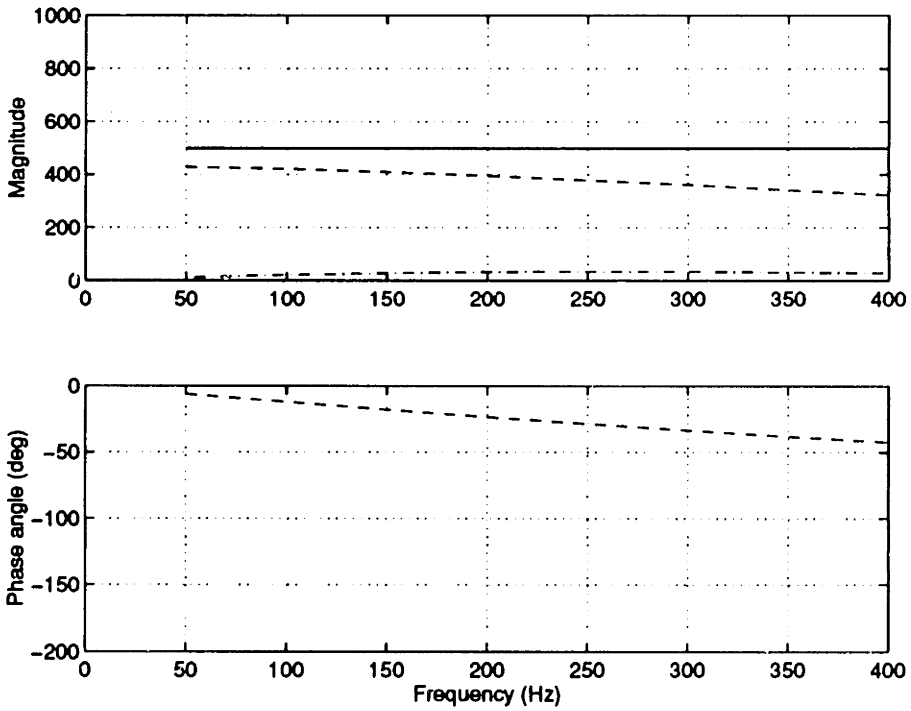

Figure 4-24: Simulated Bode plot of valve position to jet mass flux, 0.7" circular hole injector. Zeroth (—), 1st (- -) and 2nd (-.-) temporal harmonic.

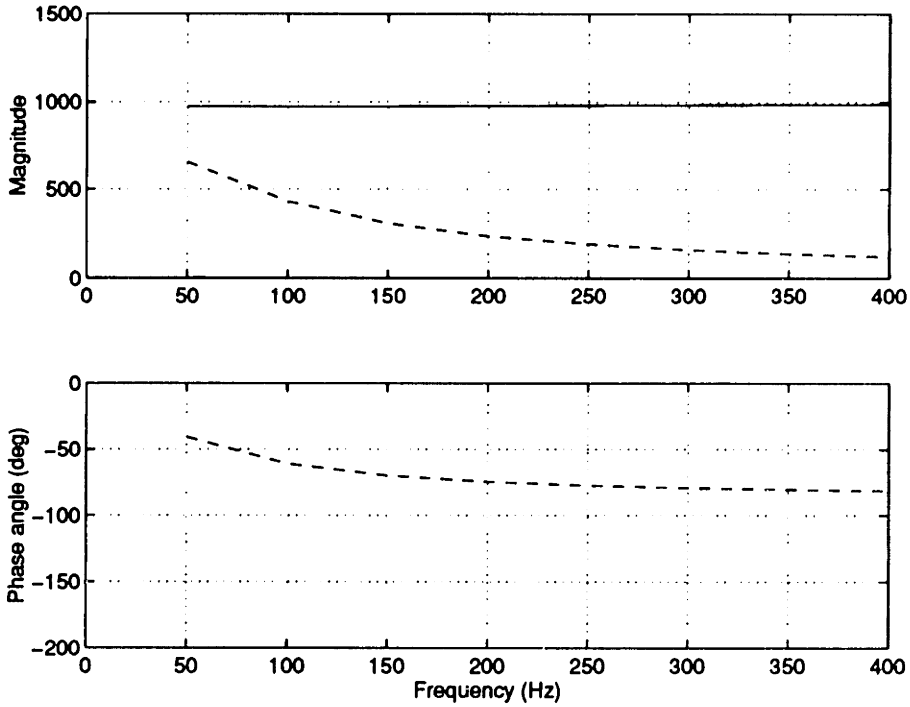

Figure 4-25: Simulated Bode plot of valve position to jet mass flux, original 3 hole injector baseline case. Zeroth (—), 1st (- -) and 2nd (-.-) temporal harmonic.

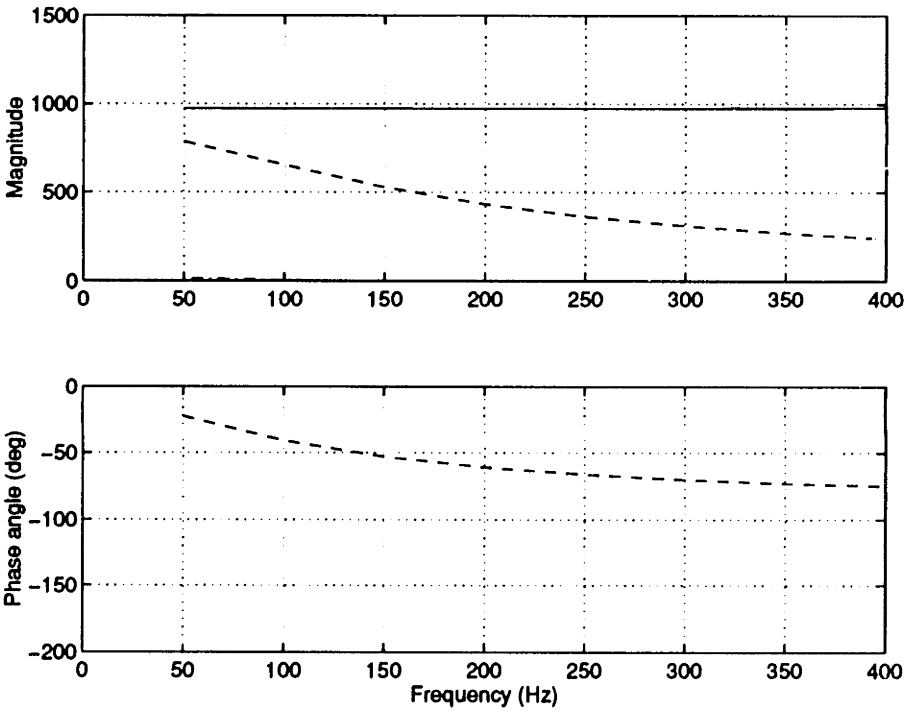

Figure 4-26: Simulated Bode plot of valve position to jet mass flux, $V_p = 0.5V_{p,baseline}$. Zeroth (—), 1st (- -) and 2nd (-.-) temporal harmonic.

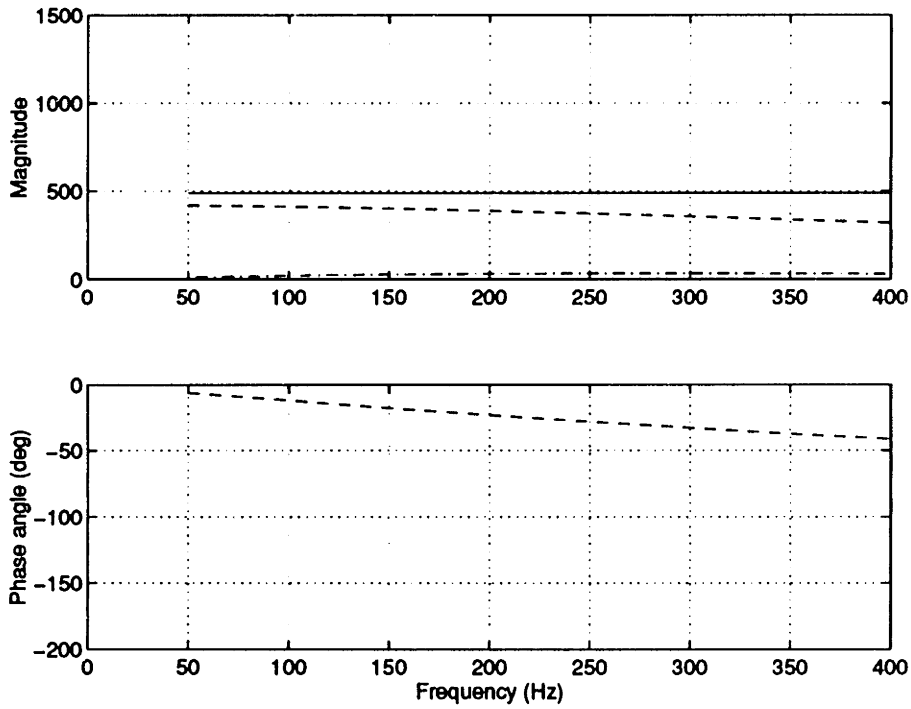

Figure 4-27: Simulated Bode plot of valve position to jet mass flux, $A_3 = 2A_{3,baseline}$. Zeroth (—), 1st (- -) and 2nd (-.-) temporal harmonic.

Chapter 5

Final Injector Development

In Chapter 4 it was shown that the original sheet and 3 hole injectors had unsatisfactory dynamic behavior and that, in addition to this, the original sheet injector produced a jet with an undesirable steady momentum flux distribution (2 momentum peaks). The remedy for the unsatisfactory dynamic behavior of the injector was to increase the exit area of the injectors. The steady performance of the sheet injector was improved by preventing the jet sheet from separating from the tunnel (casing) wall as it exited the injector. This was achieved by turning the jet sheet in the axial direction for some distance before allowing it to exit the injector. Figure 4-4, F and G show schematically the design of the modified 3 hole and sheet injectors respectively. The modified 3 hole injector has three 11.4 mm (0.45") diameter holes aligned in the directions indicated. The modified sheet injector has a slot 57 mm (2.25") wide and 5.1 mm (0.2") thick. Both modified injectors have a total exit area of about 290 mm^2 (0.45 in^2), which is just more than twice the exit area of the original flow field injectors.

5.1 Steady flow field tests

Using the same equipment and procedures as outlined in Section 4.5, the steady flow behavior of the modified sheet and 3 hole injectors was measured. Again, the freestream Mach number was taken to be $M_{f_s} = 0.45$ (NASA Stage 35 at stall). The

steady data are presented in several different forms, to show the effect of the injectors on the freestream.

5.1.1 Steady spatial distribution of momentum

Figure 5-1 through Figure 5-6 show the steady momentum flux distributions for the modified sheet injector as the injectant flow is reduced from maximum ($\alpha = 1$) to minimum ($\alpha = 0$). The spatial grid corresponds circumferentially (-60 mm to 60 mm) to the actuator spacing, and radially (0 to 80 mm) to the annulus height of NASA Stage 35. The modified sheet injector now produces a more uniform sheet of high momentum fluid, instead of two peaks as was the case with the original sheet injector. Also, the influence of the injector is confined to a small radial depth (12 mm), but considerable circumferential extent (90 mm). Referring to Figure 5-1 specifically, it is observed that the peak momentum flux ratio is 4, indicating that the maximum jet velocity is about twice the freestream velocity (momentum is proportional to the square of velocity). Since the freestream Mach number is $M_{fs} = 0.45$, the peak jet velocity at the measurement location (compressor face) is about M = 0.9. Assuming the jet Mach number at the injector exit to be $M_j = 1$, this implies that the jet core doesn't experience much mixing with the freestream in the 50 mm between the injector nozzle exit and the sensor (compressor face) location.

The sheet injector generates a wake (region of momentum less than the freestream) at valve openings less than $\alpha = 0.4$. This is because a portion of the sheet injector protrudes into the freestream, giving rise to a wake when insufficient momentum is being injected into the freestream to overcome the drag of the protruding injector. Also, purely because low momentum fluid is being introduced into the freestream, a momentum deficit will form if this fluid has less momentum than the freestream. The lack of momentum excess or deficit at the mean valve position could turn out to be quite useful for the actual high speed compressor tests since the mean injection rate may turn out not to change the baseline characteristic of the compressor at all. Recall that the purpose of dynamic feedback control using unsteady injection is to modify the unsteady performance of the compressor in such a way as to make the

effective compressor characteristic slope appear to be negative (stable). This does not imply that the steady compressor slope without feedback control needs to be altered. In fact, it would be preferable to keep the steady compressor characteristic without feedback control unchanged, since the original compressor design was optimized in some way to yield this characteristic.

Figure 5-7 through Figure 5-12 show the steady momentum flux distributions for the modified 3 hole injector as the injectant flow is reduced from maximum ($\alpha = 1$) to minimum ($\alpha = 0$). The radial influence of the 3 hole injector is about 2.5 times that of the sheet injector (30 mm compared to 12 mm), while the circumferential spreading is about the same (90 mm). The peaks of the momentum flux are not as high as those of the sheet injector, the maximum momentum flux ratio being just over 2. This is because the 3 jets are separate and have a chance to mix with the freestream (just like the edges of the sheet injector) in the 50 mm between the injector nozzle exit and the compressor face. The 3 hole injector also starts forming a wake at valve positions less than $\alpha = 0.4$, the wake being caused not by the protrusion of the injector into the freestream, but solely by the addition of low momentum fluid to the freestream at small injector flow rates. Again, this could be beneficial regarding the implementation of the actuator in an actual compressor since it may be desirable to alter the steady state characteristic of the compressor, without feedback control, as little as possible.

5.1.2 Steady spatially averaged jet momentum

To quantify the gross effect of the injector (in terms of momentum addition) on the freestream in the region bounded by the measurement grid, the jet momentum flux data was spatially averaged. Figure 5-13 and 5-14 show the variation of spatially averaged jet momentum flux with varying valve position, for the modified sheet and 3 hole injectors respectively. The relationship between cumulative jet momentum flux and valve position is quadratic. This is expected since valve mass flow rate is directly proportional to valve position, and jet momentum flux varies quadratically with jet mass flux if the flow density is close to unity. For a fully expanded jet, this

latter assumption is reasonable since the jet exit static pressure will approach ambient static pressure. Since the total temperature of the jet is close to the ambient total temperature, the jet exit density should be similar to the ambient air density, which is close to unity.

For the sheet injector, the mean jet momentum flux is close to the freestream momentum flux of unity. This is because this injector protrudes into the flow and causes a momentum deficit (wake) at low injection flow rates, even though it creates a momentum excess at high injection flow rates. The 3 hole injector does not protrude into the freestream, therefore on average its mean momentum flux is somewhat above the freestream momentum flux of unity (i.e. more of the curve is above unity). If it is required to have a linear variation of injector momentum flux with actuator command, the command to the actuator can be 'linearized' by the equation given in the plots. X is the modified command while x is the desired quantity of momentum flux (x = 0 corresponds to the minimum momentum flux and x = 1 corresponds to the maximum). Since the variation of momentum flux with valve position (mass flow) is quadratic in nature, a simple square-root relation with only one constant can be used to obtain the actual actuator command from the desired level of momentum flux. The dotted curves in both plots indicate the momentum flux which will be obtained if these actuator command modifications are employed (essentially a straight line between the minimum and maximum momentum flux).

5.1.3 Steady radially averaged jet momentum

Since the jet momentum flux distribution of the injectors have both radial as well as circumferential variations, it is useful to average the data along one of these dimensions to simplify the presentation of the data. Figure 5-15 and Figure 5-16 show the momentum flux distributions of the modified sheet and 3 hole injectors, after the data have been averaged in the radial direction. Obviously only circumferential variations are then relevant, as is shown in the figures. The six curves correspond to the six valve openings used previously.

Since the measurement grid of the sheet injector has much less radial extent than

that of the 3 hole injector, the casing (tunnel) boundary layer (momentum flux ratio lower than unity) will encompass a larger part of the data grid. For this reason, the radial averages at the edge of the sheet injector (no influence of the jet) are somewhat lower than unity, while those of the 3 hole injector are only slightly so. From the plots it is again evident that the circumferential extent of the two injectors is about the same (90 mm), however, the peak momentum flux of the 3 hole injector is much lower than that of the sheet injector. Furthermore, the 3 hole injector tends to have fairly uniform momentum flux over the entire circumferential distribution of injection, while the sheet injector tends to have a very peaky distribution.

5.1.4 Steady circumferentially averaged jet momentum

In the case of steady injection, and looking at the actuator flow field from the frame of reference of the compressor rotor, circumferential variations of the jet in the absolute frame will be smeared to a constant value in the relative frame by time averaging (since the blade rows only have relative circumferential velocity). On the other hand, radial variations of the jet in the absolute frame will remain the same in the relative frame after time averaging. It was planned to run some steady (time averaged) CFD simulations on the effects of fluid injection on a compressor rotor, therefore averaging the jet momentum flux circumferentially, but not radially, is a sensible way to obtain input data for a steady CFD simulation.

Figure 5-17 and Figure 5-18 show the average radial penetration of the modified sheet and 3 hole injectors respectively. The scales on the horizontal axes are such that they represent the entire annulus height (80 mm) of NASA Stage 35, thus the curves in the plots are correctly scaled momentum flux profiles. Whereas the radial penetration of the sheet injector does not seem to change much with the amount of injection (the curves look self similar), that of the 3 hole injector does. This is because the 3 hole injector injects fluid at a meridional angle of 30°, the depth of penetration depending on the component of jet momentum perpendicular to the freestream. For both injectors, the momentum flux profile corresponding to $\alpha = 0.5$ (between $\alpha = 0.4$ and $\alpha = 0.6$) is close to the freestream momentum flux of unity. The mean injection

flow rate has therefore effectively removed the tunnel (casing) boundary layer.

5.1.5 Steady center of action of jet

Modulation of the actuator leads to a 'wiggling' of the jet spatially. This effect may influence the aerodynamics of the compressor as the actuator is modulated, therefore it should at least be quantified. In order to characterize the spatial movement of the jet as it is modulates between minimum and maximum injection flow rate, a spatial center of action (C.O.A.) of the jet was defined. A center of action can be defined in a manner analogous to the center of gravity (C.O.G.) of a solid body. The difference in this case is that the weighting factor is taken to be the local jet momentum flux ratio, C_m, instead of infinitesimal mass as is the case with the center of gravity. The formal definition of the radial center of action is given by

$$\bar{y} = \frac{\sum y C_{mom}}{\sum C_{mom}} \tag{5.1}$$

Notice that y is taken to be zero at the casing, and positive into the flow. The formal definition of the circumferential center of action is given by

$$\bar{x} = \frac{\sum |x| C_{mom}}{\sum C_{mom}} \tag{5.2}$$

Notice that x is taken to be zero at the actuator center line, and because there is symmetry about this line, $|x|$ is used to calculate $\bar{x}$. Because of this definition, $\bar{x} \neq 0$, as would be the case if $|x|$ were not used. Figure 5-19 shows how the radial and circumferential jet C.O.A. is defined in the wind tunnel coordinate system.

Radial and circumferential variations

Figure 5-20 and Figure 5-21 show the movement of the radial and circumferential C.O.A. for the modified sheet and 3 hole injectors vary as the injection flow rate is modulated from minimum to maximum ($\alpha = 0$ to $\alpha = 1$). The spatial coordinates have been left in dimensional form so that both $\bar{x}$ (—) and $\bar{y}$ (- -) can be plotted on

the same axes. For the sheet injector, most of the jet momentum flux is at a radial depth of about 10 mm, while the circumferential 'spreading' of the jet is about 30 mm. Notice that the jet 'center' comes closer to the injector as injector flow rate is increased, which may be confusing at first. This does not imply that the jet is spreading less at higher injection flow rates, as can be verified by closer inspection of the steady momentum flux distribution plots given in Figure 5-1 through Figure 5-6. The C.O.A. simply gives a measure of where most of the momentum flux is acting spatially. For the 3 hole injector, there is virtually no movement of the jet C.O.A. as the injection flow rate is varied. The circumferential 'spreading' of the 3 hole injector is about the same as that of the sheet injector (30 mm), but that the radial penetration is about twice as much (20 mm as opposed to 10 mm).

5.2 Unsteady flow field tests

Using the same data acquisition procedures as outlined in Section 4.5, the dynamic behavior of the modified injectors was quantified. Again, the freestream Mach number was taken to be $M_{f_s} = 0.45$, which is close to the upstream axial Mach number of NASA Stage 35 at stall. The data are presented in several different forms to clarify the unsteady jet behavior.

5.2.1 Unsteady spatially averaged jet momentum

To quantify the unsteady nature of the jet, the jet momentum flux distribution was spatially averaged at each instant in time as the jet was being unsteadily modulated. Figure 5-22 and Figure 5-23 show Bode plots of the magnitude and phase of the spatially averaged momentum flux with respect to valve position, for the modified sheet and 3 hole injectors respectively. The three curves correspond to the zeroth (—), first (- -) and second (-.-) temporal harmonics of the spatially averaged momentum flux.

Concerning the magnitude plots, it is observed that the zeroth temporal harmonic dominates, which can be expected since some portions of the spatial data grid are not

influenced by the modulating jet. The zeroth temporal harmonic has a magnitude near unity, which is desirable since it implies that the mean injection of the actuator does not significantly alter the steady upstream flow field of the compressor. Referring to the magnitude of the first temporal harmonic, it is observed that the magnitude of this harmonic corresponds to a quarter of the mean momentum flux (unity) for the sheet injector, and about one eighth for the 3 hole injector. The difference is due to the different sizes of the measurement grids over which the momentum flux data were spatially averaged. In the case of the sheet injector, the measurement grid is half the size of that of the 3 hole injector. Thus, if equal measurement grid areas (or the entire annulus area) were taken to spatially average the injector momentum flux, the absolute magnitude of the momentum flux (zeroth and first temporal harmonic) would be more or less equal. This is expected since there is no significant difference between the exit areas of the injectors, and hence no significant difference between the amount of momentum ejected in the axial direction by the sheet and 3 hole injectors. Returning once more to the magnitude plots of both injectors, the most important feature of the plots is the flatness of the first temporal harmonic of jet momentum flux. Since the input to the actuator was a pure sinusoid corresponding to this harmonic, these curves show that the dynamic response of the modified injectors no longer attenuate with increasing frequency (up to 400 Hz), as the original injectors did. The frequency response improvement that was predicted by the non-linear injector simulation has therefore been realized. The second temporal harmonics are plotted to indicate that the temporal harmonic distortion of the fluid dynamic output of the actuator is relatively small (5% of the mean). Almost all of this temporal harmonic distortion comes about purely as a result of the quadratic relationship between momentum flux and valve position, as will be shown in Section 5.3.

The phase plots of both Figure 5-22 and Figure 5-23 show that the phase lag of the first temporal harmonic of jet momentum flux looks like that of a pure time delay. One possible source of time delay is the finite time taken for fluid from the injector exit to convect to the measurement (or compressor face) location. For a convection distance of about 50 mm (the distance between injector exit and compressor face),

and a convection velocity of 153 $m.s^{-1}$ ($M_{f_s} = 0.45$), a convection delay of 0.33 milliseconds is calculated. At 400 Hz, a 0.33 ms delay corresponds to a phase lag of about 45°. Figure 5-22 and Figure 5-23 indicate that the overall injector phase lag at 400 Hz is closer to 85°. The difference (about 40° at 400 Hz) comes from the first order system response of the injector plenum, as indicated by the modified injector frequency response prediction in Figure 4-27. The first temporal harmonic phase behavior of the overall actuator (not including the motor dynamics) is thus simple and intuitively consistent. It will be seen in subsequent Bode phase plots that the first temporal harmonic behavior is virtually identical for other unsteady jet quantities (210° per decade). This implies that the combination of a first order system response (injector plenum dynamic) and a pure convective time delay are the fundamental ingredients in determining the fluid dynamic phase behavior of the actuator. The phase of the second temporal harmonic is fairly random, which is expected since there is no component of this harmonic in the input wave. Since the magnitude of the second temporal harmonic is much smaller than the mean, this random behavior is not shown on these, as well as subsequent Bode phase plots.

5.2.2 Unsteady center of action of jet

Using the same definitions for the C.O.A. of the jet as in the steady case, and looking at the variation of these quantities as the actuator is modulated at different frequencies, it is possible to determine the dynamic behavior of the jet position. This is relevant since it is useful to get an idea of how much the jet is 'wiggling' around in the freestream.

For both injectors, the C.O.A. of the jet was found at each instant in time. The time domain data was then decomposed into its temporal Fourier harmonics. Figure 5-24 and Figure 5-25 show the Bode plots of the zeroth (—), first (- -) and second (-.-) temporal harmonic of the circumferential and radial location of the C.O.A. of the unsteadily modulating jet. Looking first at the zeroth temporal harmonic of both circumferential Bode magnitude plots, it is observed that the C.O.A. of both injectors spread about the same amount (30 mm). Radially, however, the 3 hole

injector penetrates the freestream about twice as much as the sheet injector (18 mm vs 9 mm). The zeroth temporal harmonic of jet momentum flux is significantly larger than the other two temporal harmonics for both injectors. This implies that the relative jet 'wiggling' is not significant in the circumferential or radial directions as the actuator is modulated between minimum and maximum flow. Comparing the relative size of the circumferential zeroth and first temporal harmonic for the sheet and 3 hole injectors, it is observed that the 3 hole injector exhibits far less 'wiggling' than the sheet injector (7% vs 15%). This same observation applies to the radial 'wiggling' of the 3 hole and sheet injectors (11% vs 20% respectively). For both injectors, the second temporal harmonic is much smaller than the first, implying that there is little (less than 2% for the sheet injector, and close to 0% for the 3 hole injector) harmonic distortion (recall that the actuator input signal corresponds to the first temporal harmonic).

Referring to the phase plots, it is observed that the first temporal harmonic has a linear relationship with frequency, rolling of at 210° per decade. This behavior is virtually identical to that seen in the Bode plots of the spatial averaged momentum flux in Section 5.2.1, and is due to the same processes discussed previously. The phase of the second temporal harmonic is not plotted since it is small and random, and has no physical significance.

5.3 Spatial spectral content of actuation

Since it is intended to use the modified injectors in a control system that uses a modal description of the compression system dynamics, it is useful to investigate the spatial spectral content of actuation. Since there are a discrete number (12) of actuators, it can be expected that some spatial harmonic distortion will occur if a single spatial harmonic is commanded.

5.3.1 Sheet injector

Figure 5-26 shows the spatial (circumferential) distribution of actuator command, and resulting jet momentum flux distribution, for a first spatial harmonic of actuation of the modified sheet injector. The jet momentum flux distribution produced has first spatial harmonic content (single-lobed sinusoid), but is also very peaky. Figure 5-27 shows the spectral content of the actuator command and jet momentum flux. Obviously the actuator command only has a first spatial harmonic, however, it is observed that the spectrum of jet momentum flux has more than one spatial harmonic. The strong 11th, 12th and 13th spatial harmonic are caused by the peakiness of the momentum flux distribution due to the 12 individual actuators contributing to the distribution. Whether these three harmonics will excite dynamic modes in the compression system will depend on the dynamics of the compression system involved. Furthermore, the only significant spatial harmonic distortion at low harmonic numbers is the 2nd spatial harmonic. This harmonic is caused primarily by the quadratic relationship between valve command (or position) and jet momentum flux. If this non-linearity is removed using the equations given in Figure 5-13, the actuator command and jet momentum flux distributions become those shown in Figure 5-28. The spectral content plots Figure 5-29 indicate that the 2nd harmonic distortion disappears, but that the higher harmonic distortions (around the 12th) grow by about 25%

Figure 5-30 and Figure 5-31 show the distribution and spectral content of jet momentum flux for a 2nd spatial harmonic actuator command. Again the spatial harmonics around the 12th harmonic are excited due to the finite number of peaky jets making up the momentum flux distribution. Figure 5-32 and Figure 5-33 show the distribution and spectral content of jet momentum flux for a 3rd spatial harmonic actuator command. From the jet momentum spectral content plot it is clear that it is difficult to command a 'clean' 3rd spatial harmonic, since there is harmonic distortion from the 6th harmonic (non-linearity of momentum flux with valve position), as well as from the 9th and 12th harmonic (12 discrete actuators).

5.3.2 3 hole injector

Figure 5-34 through Figure 5-41 are identical to Figure 5-26 through Figure 5-33, except that they refer to the modified 3 hole injector. The only difference between the sheet and 3 hole injectors is that the momentum flux distribution for the latter is less peaky than the former. This manifests itself in the spectral content plots as a decrease in the relative magnitudes of the spatial harmonics around the 12th harmonic. It can be verified that the spatial harmonic distortion at the lower harmonics (2nd harmonic distortion for a commanded 1st spatial harmonic of actuation, etc.) is unaffected by the type of injector, confirming that the primary reason for this distortion is the quadratic relationship between the jet momentum flux and the actuator command. Thus, if the equations given in Figure 5-14 are used to 'linearize' the actuator command, these lower spatial harmonic distortions can be eliminated, as shown by Figure 5-36 and Figure 5-37.

5.4 Blade mechanical excitation

Implementation of the actuation system on an actual high speed compressor introduces considerations that would not normally be relevant to low speed research machines. Due to the high mechanical (centrifugal) and aerodynamic loads on the rotor blades of a high speed machine, it is necessary to investigate the effect the actuation system will have on an existing compressor. One of the first things that can be looked at is the blade frequencies that will excited by the actuation system. These excitation frequencies may interact with the natural mechanical frequencies of the compressor rotor blades, leading to resonance and ultimate failure of the machine.

Figure 5-42 through Figure 5-44 are PSD plots of the blade excitation caused by commanding a 1st, 2nd and 3rd spatial harmonics of actuation for the sheet injector, respectively. The excitation frequencies have been normalized by the rotor frequency, while the power density is plotted in decibels. Essentially these three plots convey exactly the same data as the plots of spatial spectral content of actuation, except that in this case the magnitude represents a power (square of the momentum flux)

and is plotted on a decibel scale. The main point of the three plots is that the blade excitation caused by the 12 discrete actuators is as significant as the excitation (loading) caused by the commanded spatial harmonic.

Figure 5-45 through Figure 5-47 are PSD plots of the blade excitation caused by commanding a 1st, 2nd and 3rd spatial harmonics of actuation for the 3 hole injector, respectively. The only difference between these plots and the previous three for the sheet injector, is that the excitation caused by the 12 discrete actuators (12th harmonic) is slightly less for the 3 hole injector than for the sheet injector. This is because the momentum flux distribution of the 3 hole injector is less peaky than that of the sheet injector. Once again, however, the excitation caused by the 12 discrete actuators is similar in magnitude to that caused by the commanded spatial harmonic.

5.5 Summary: injector development

To conclude this chapter, the main findings of the injector development are reviewed. In addition, Table 5.1 gives a quantitative summary of the injector development.

- Two final candidate injectors have been developed and their performance carefully quantified.
- The first injector, a sheet injector, introduces excess axial momentum into the outer 12 mm of the compressor annulus, which corresponds to the outer 15% of the annulus for NASA Stage 35.
- The second injector, a 3 hole injector, introduces excess axial momentum into the outer 30 mm of the compressor annulus, which corresponds to the outer 40% of the annulus for NASA Stage 35.
- Both injectors create a jet that spreads a total of about 90 mm in the circumferential direction, which corresponds to 70% of the actuator spacing for NASA Stage 35

- The spatial 'wiggling' of the jets in the freestream, as the injection flow rate is modulated between minimum and maximum, was found to be about 20% of the mean penetration for the sheet injector, and 10% for the 3 hole injector. Table 5.1 gives the quantitative amounts of jet wiggling (percent wiggling over the mean jet penetration) for both injectors.

- Both injectors have good overall frequency response, with no (0 dB) attenuation in control power in the frequency range measured (0 to 400 Hz).

- Both injectors have a linear phase roll-off with frequency, the phase lag at 400 Hz being 85°. This phase lag does not include the dynamics of the valve servo motor.

- The steady response of the injectors is characterized by a spatial distribution of momentum flux as the valve is modulated between minimum and maximum flow rate.

- The dynamic response of both injectors is characterized by the steady-state momentum flux distribution modified by a phase lag. The total phase lag comprises a first order system lag due to the injector plenum dynamics, and a pure time lag due to the finite convection time taken by fluid moving from the injector to the compressor face.

- The first order frequency response of the injectors is determined by the ratio of plenum volume to exit area of the injector. A numerical simulation of the first order injector response was developed and gives good predictions of the trends observed experimentally.

5.6 Summary: overall actuator development

Since the development of the jet actuator comprised the separate development of a valve and the injectors, it is useful to combine these into a summary of the jet actuator itself. The summary of the overall actuator is best given by a quantitative summary

Parameter	units	Sheet injector	3 hole injector
Radial penetration	mm	12	30
Circumferential spread	mm	90	90
Bandwidth (min.)	Hz	400	400
Phase lag at 400 Hz	deg	85	85
Radial jet wiggling	%	20	11
Circumferential jet wiggling	%	15	7

Table 5.1: Quantitative summary of the injector development

Parameter	units	Valve	Overall actuator	
			Sheet injector	3 hole injector
Supply pressure (gauge)	kPa	700	–	–
Valve command	V	$\pm 10V$	–	–
Maximum mass flow	$kg.s^{-1}$	0.1	–	–
Minimum mass flow	$kg.s^{-1}$	0.02	–	–
Radial penetration	mm	–	12	30
Circumferential spread	mm	–	90	90
Bandwidth (-3dB)	Hz	400	400	400
Phase lag at -3dB	deg	100	185	185

Table 5.2: Quantitative summary of the overall actuator development

of the performance of the combined valve (2nd generation) and injector (sheet or 3 hole), as shown in Table 5.2.

5.7 Actuator applications

Although the actuator (valve and injectors) was developed for a particular application, namely rotating stall control on NASA Stage 35, the control power and bandwidth capabilities of the actuator make it suitable for a number of other applications in the control of compressor instabilities. Table 5.3 lists some of the compressors that could employ the actuator for either surge or rotating stall control. The table lists the compressor name, the type of instability that is expected in the machine (surge or rotating stall), the number of actuators required, the mass flow of the compressor, the highest characteristic frequency to be controlled for the compressor, the percentage

Compressor Name	Type of instability	Number of actuators	$\dot{m}_{comp}$ $kg.s^{-1}$	f_{comp} Hz	Con Pow %	Bandwidth factor
NASA S37	R/S	12	20	295	6.0	1.36
NASA S67	R/S	12	32	267	3.8	1.50
ADP	R/S	12	25	200	4.8	2.0
T55	R/S	8	12	300	6.7	1.33
Allison C250	Surge	1	4	50	2.5	8.0
Lycom L101	Surge	1	5	80	2.0	5.0

Table 5.3: Possible applications for the MIT GTL jet actuator

control power (Con. Pow.) the MIT GTL jet actuator would be able to provide, as well as the excess bandwidth factor of the actuator. The highest characteristic frequency of the machine refers to the 'compressible' rotating stall mode rotating at the rotor rotation frequency in the case of high speed axial machines, and the surge frequency in the case of high speed radial machines.

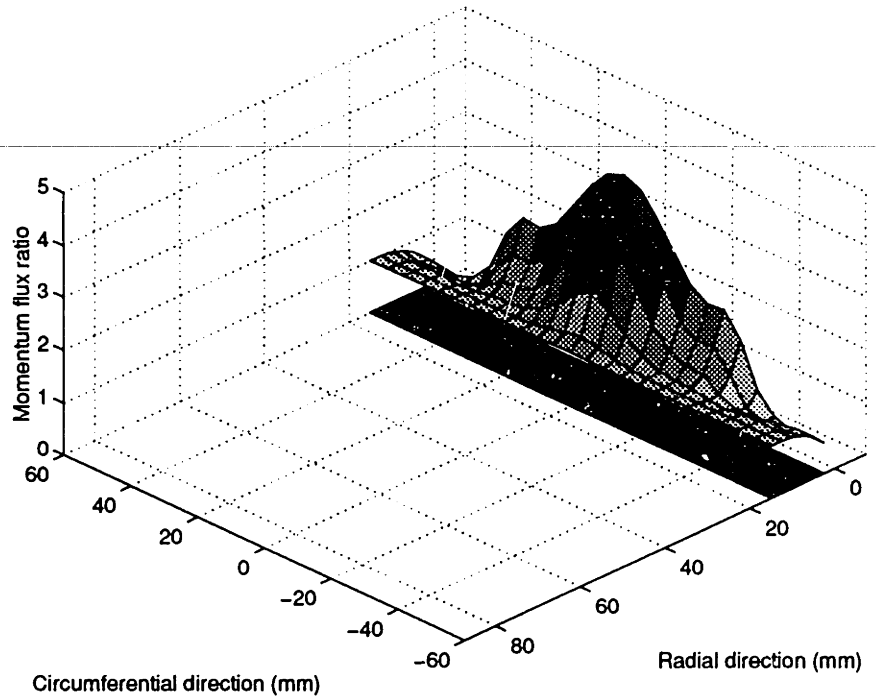

Figure 5-1: Steady momentum flux distribution of the modified sheet injector, $\alpha = 1$.

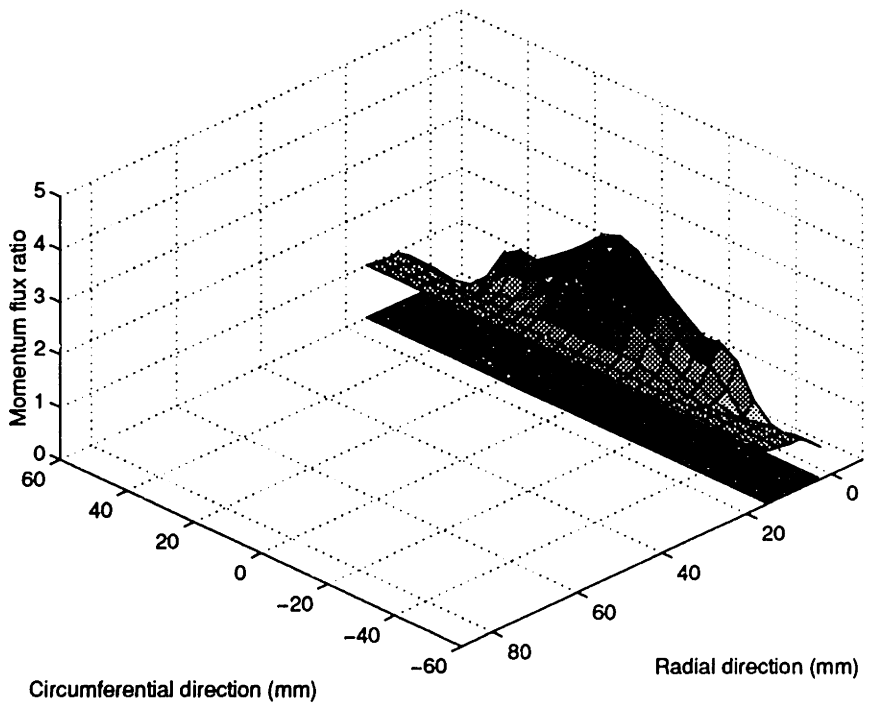

Figure 5-2: Steady momentum flux distribution of the modified sheet injector, $\alpha = 0.8$.

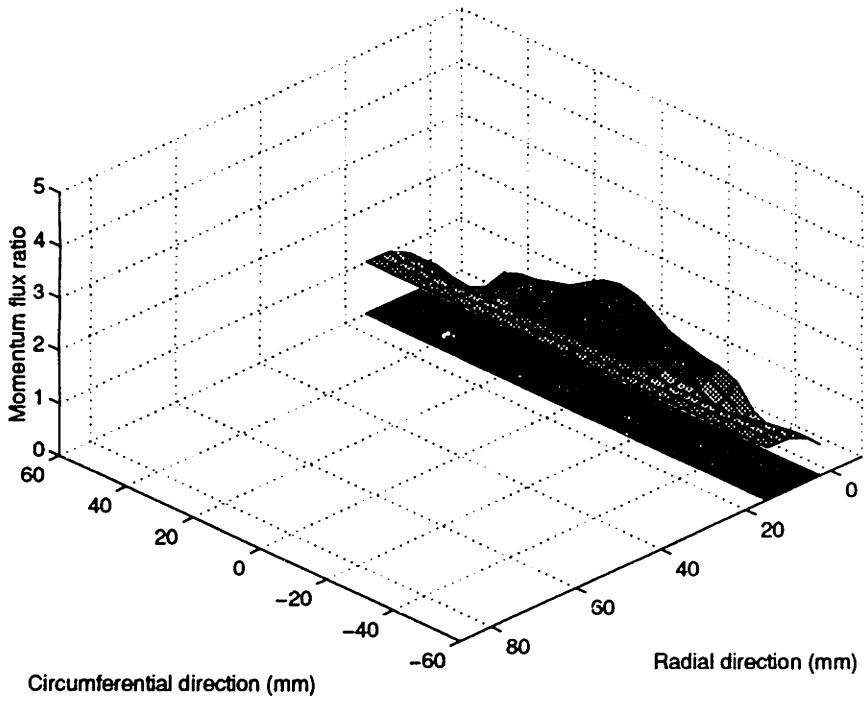

Figure 5-3: Steady momentum flux distribution of the modified sheet injector, $\alpha = 0.6$.

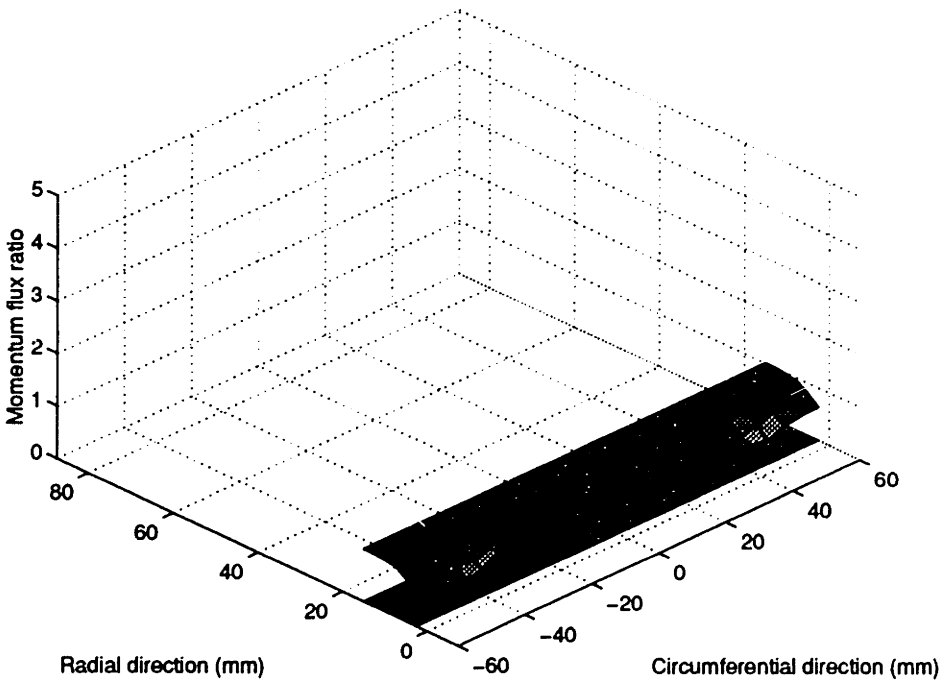

Figure 5-4: Steady momentum flux distribution of the modified sheet injector, $\alpha = 0.4$, Note: axes rotated.

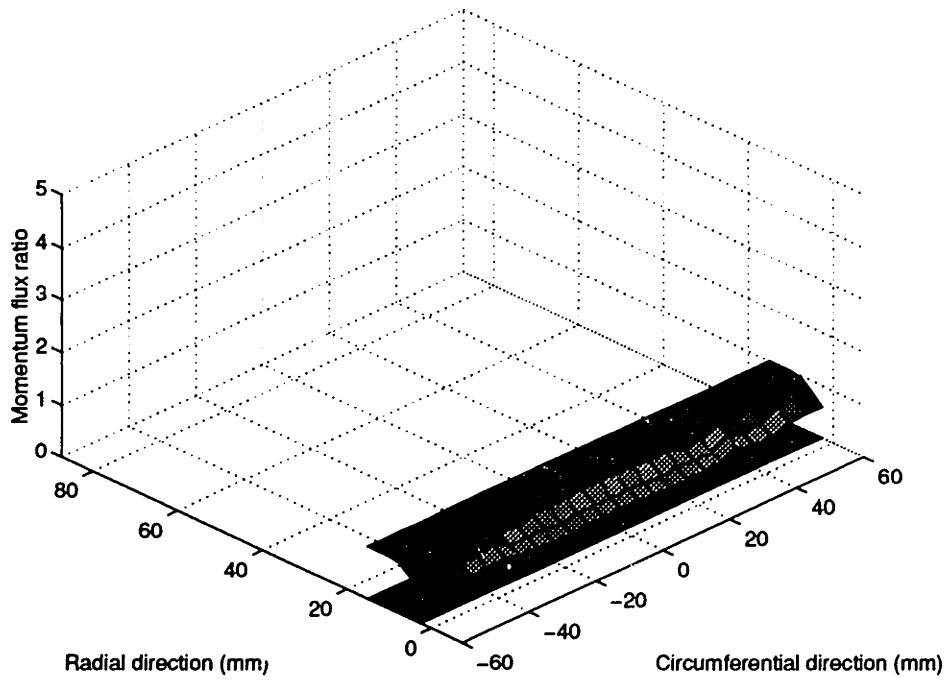

Figure 5-5: Steady momentum flux distribution of the modified sheet injector, $\alpha = 0.2$, Note: axes rotated.

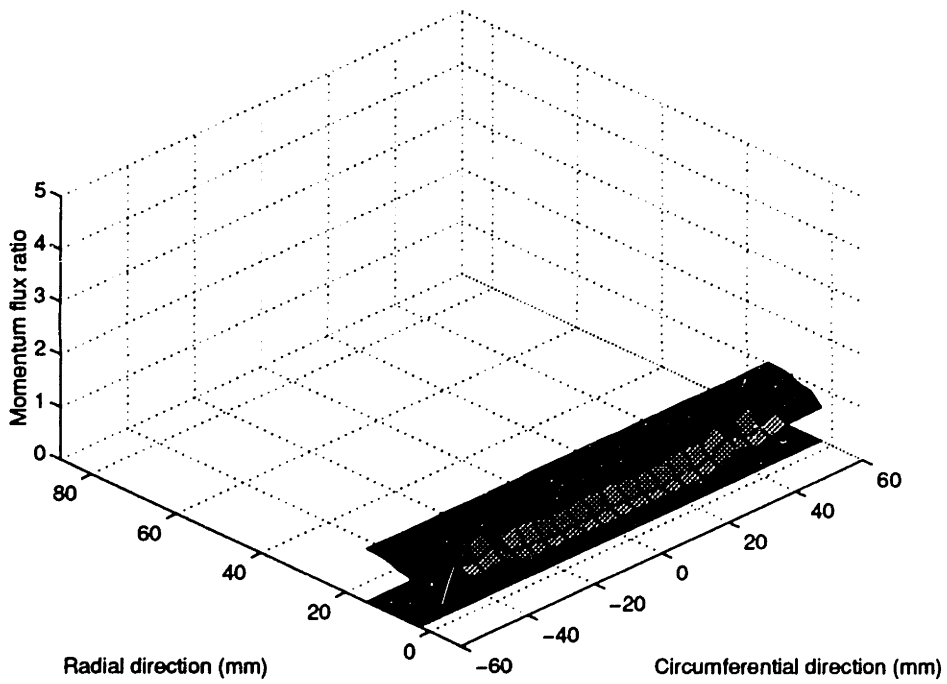

Figure 5-6: Steady momentum flux distribution of the modified sheet injector, $\alpha = 0$, Note: axes rotated.

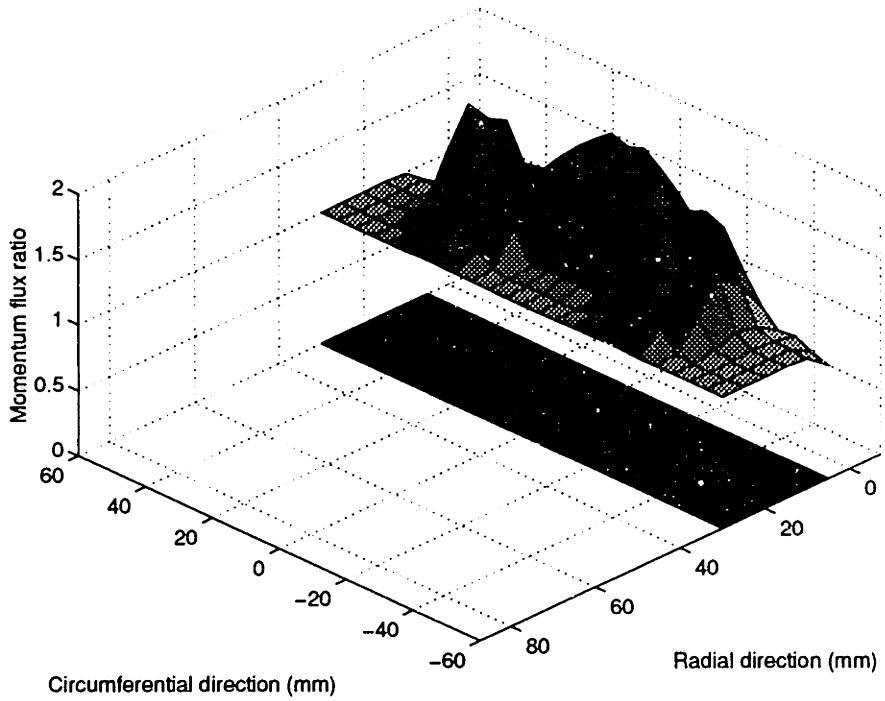

Figure 5-7: Steady momentum flux distribution of the modified 3 hole injector, $\alpha = 1$.

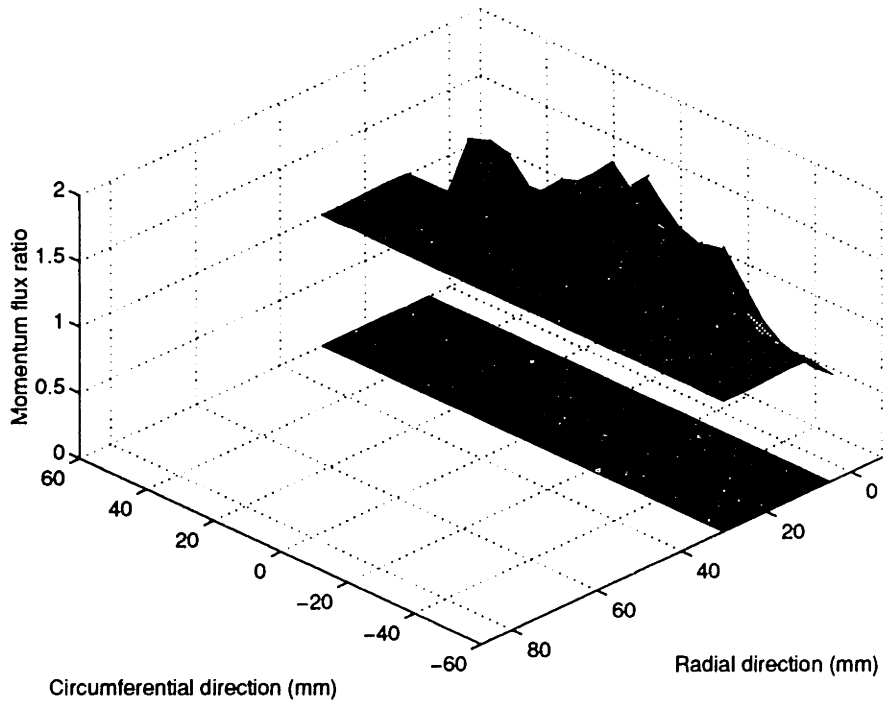

Figure 5-8: Steady momentum flux distribution of the modified 3 hole injector, $\alpha = 0.8$.

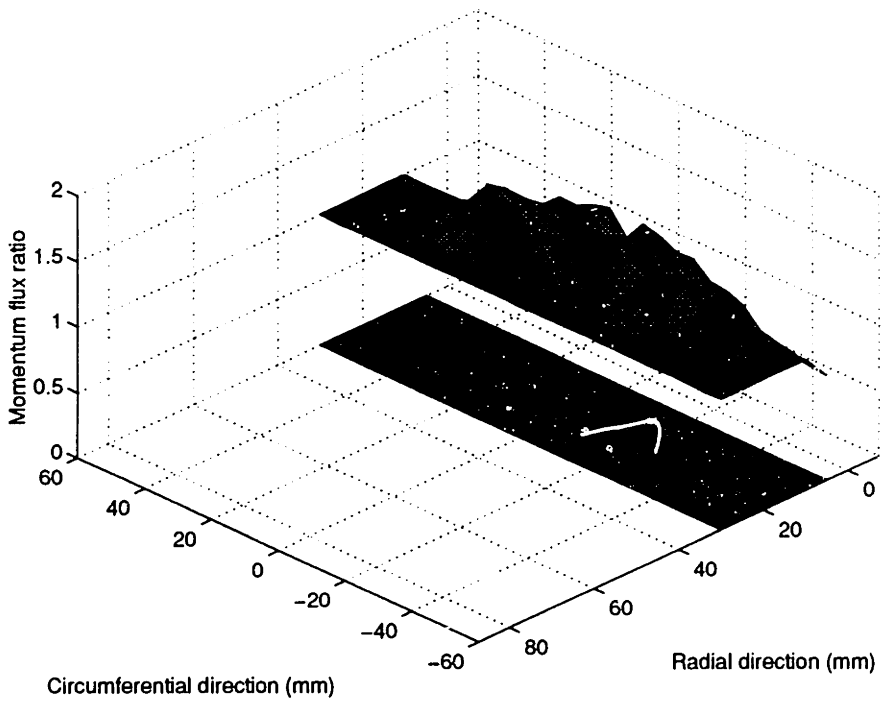

Figure 5-9: Steady momentum flux distribution of the modified 3 hole injector, $\alpha = 0.6$.

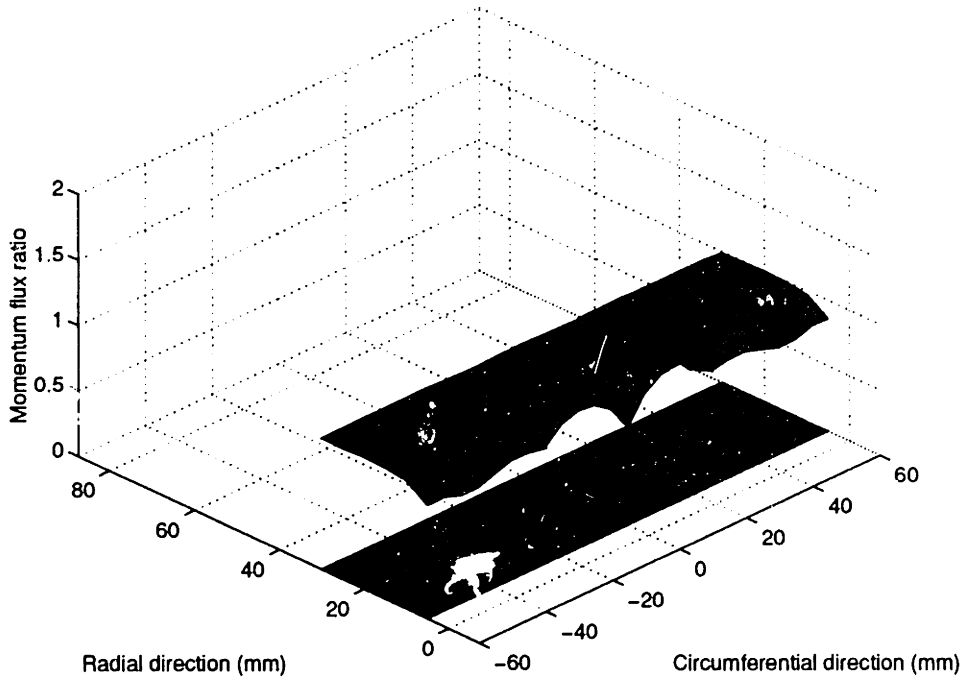

Figure 5-10: Steady momentum flux distribution of the modified 3 hole injector, $\alpha = 0.4$, Note: axes rotated.

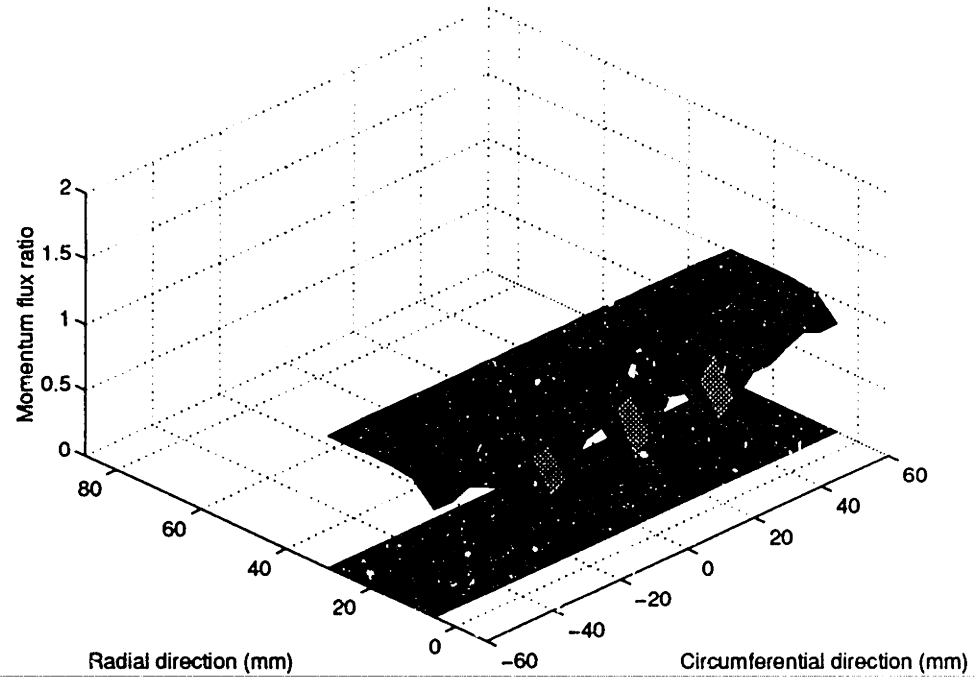

Figure 5-11: Steady momentum flux distribution of the modified 3 hole injector, $\alpha = 0.2$, Note: axes rotated.

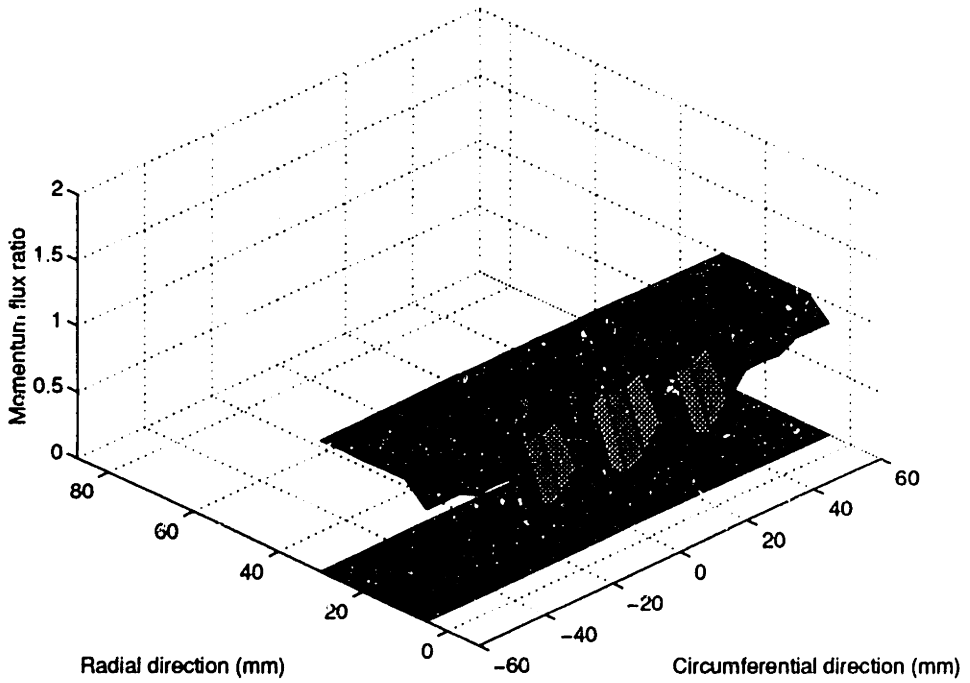

Figure 5-12: Steady momentum flux distribution of the modified 3 hole injector, $\alpha = 0$, Note: axes rotated.

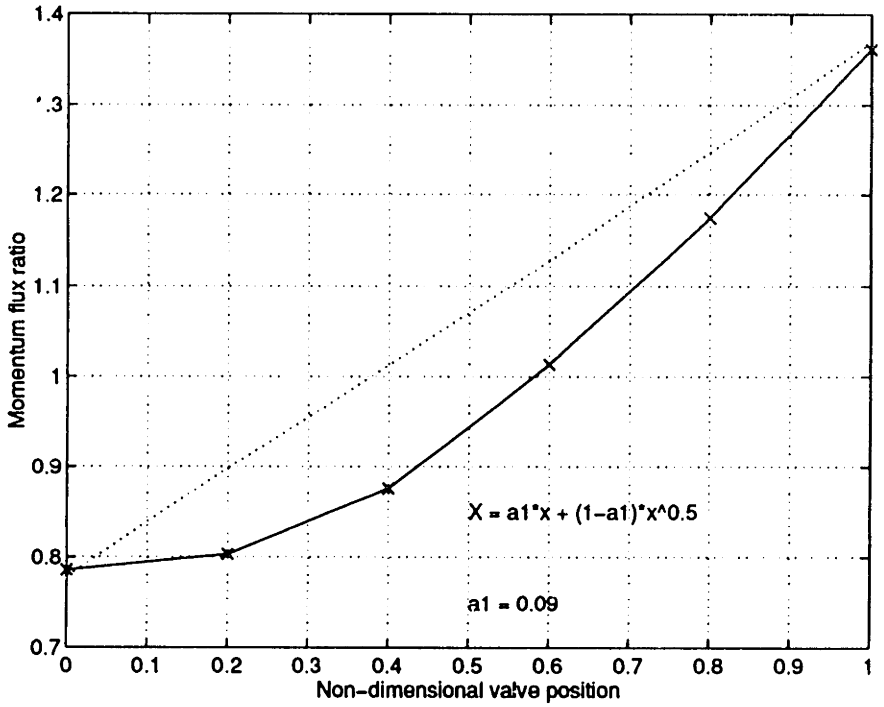

Figure 5-13: Spatially averaged momentum flux for the modified sheet injector. Measured (—) and linearized (...).

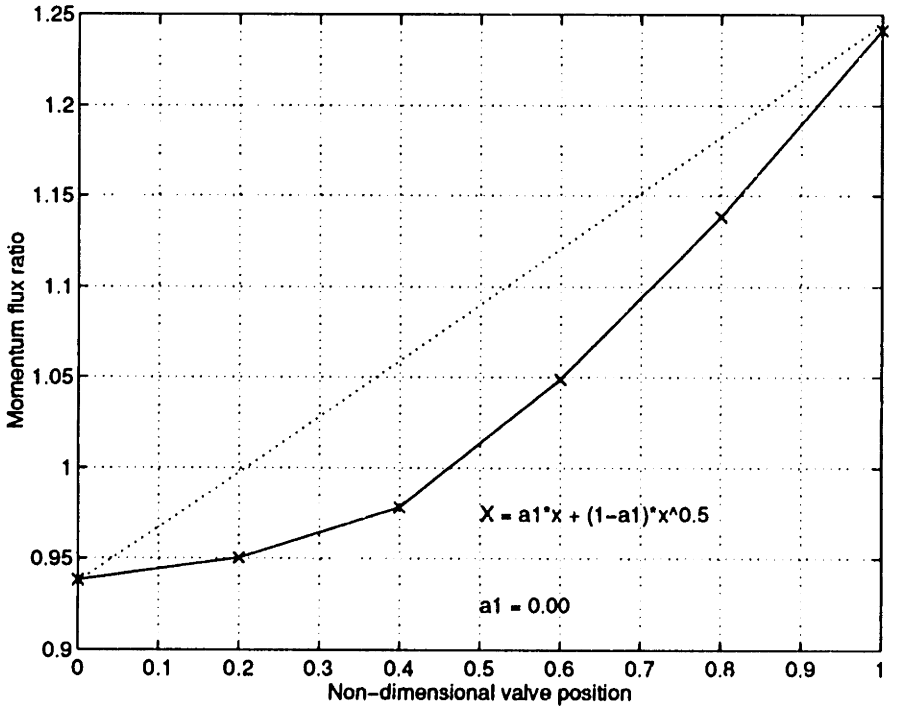

Figure 5-14: Spatially averaged momentum flux for the modified 3 hole injector. Measured (—) and linearized (...).

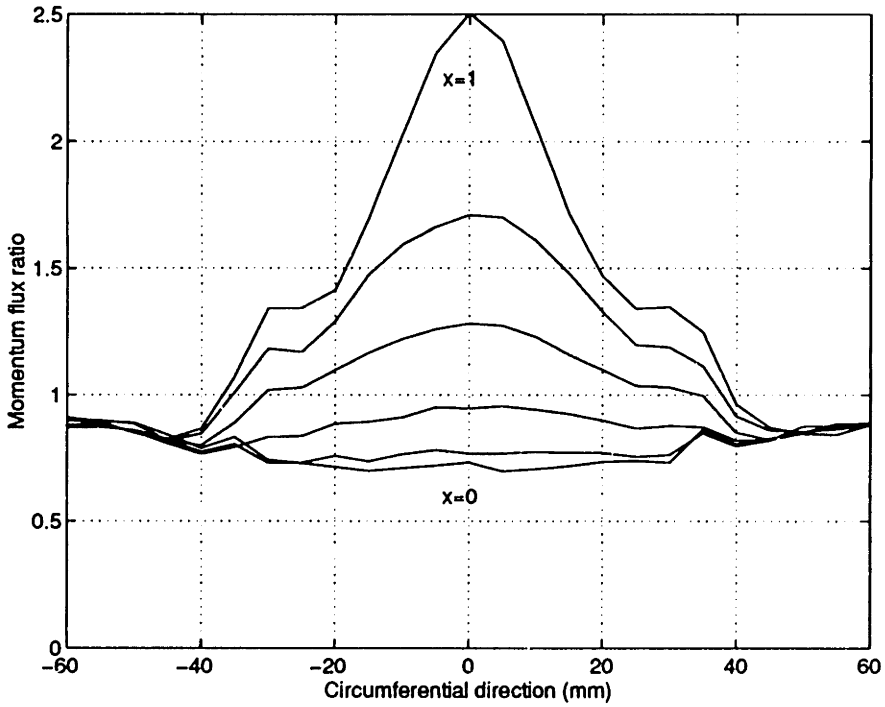

Figure 5-15: Radially averaged momentum flux distribution for the modified sheet injector, $\alpha = 0$, 0.2, 0.4, 0.6, 0.8 and 1.

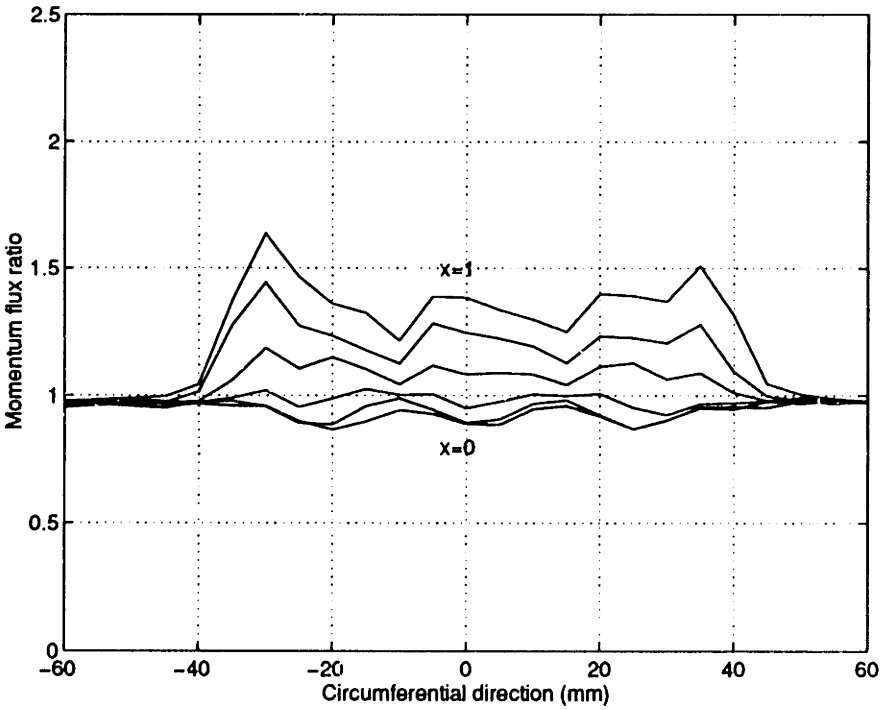

Figure 5-16: Radially averaged momentum flux distribution for the modified 3 hole injector, $\alpha = 0$, 0.2, 0.4, 0.6, 0.8 and 1.

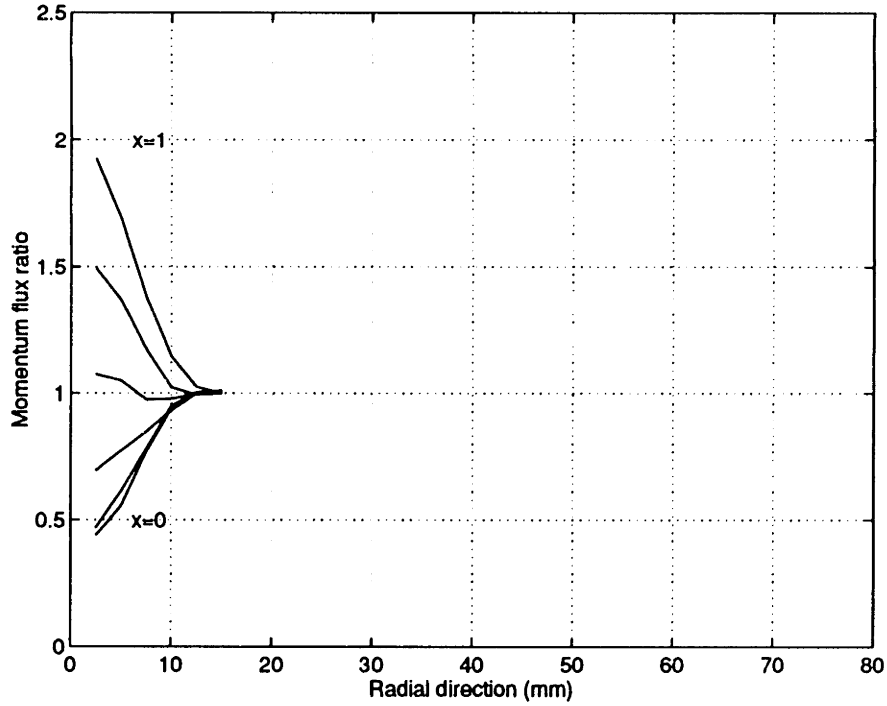

Figure 5-17: Circumferentially averaged momentum flux distribution for the modified sheet injector, $\alpha = 0$, 0.2, 0.4, 0.6, 0.8 and 1.

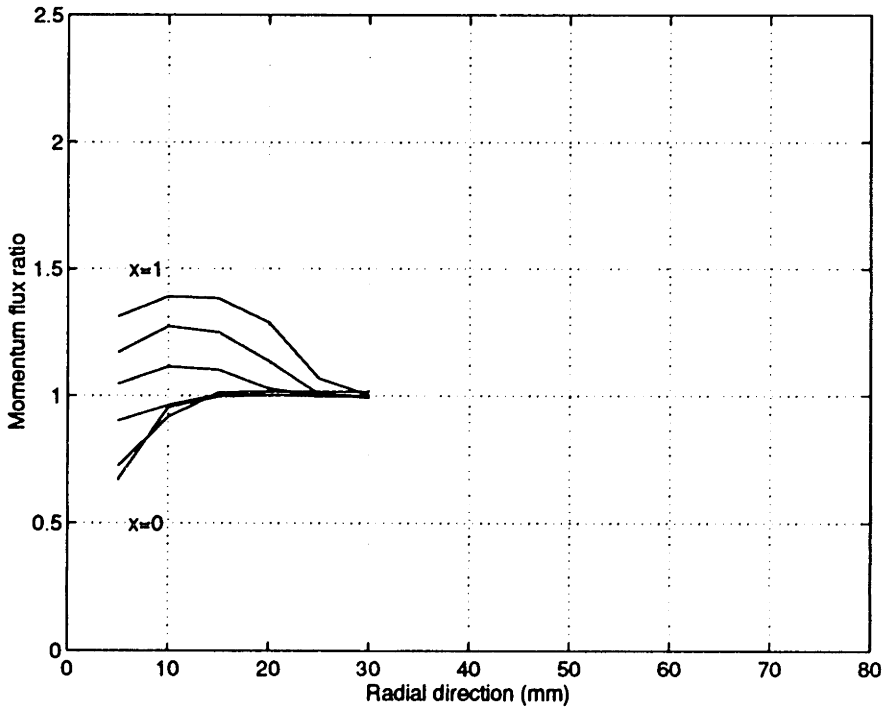

Figure 5-18: Circumferentially averaged momentum flux distribution for the modified 3 hole injector, $\alpha = 0$, 0.2, 0.4, 0.6, 0.8 and 1.

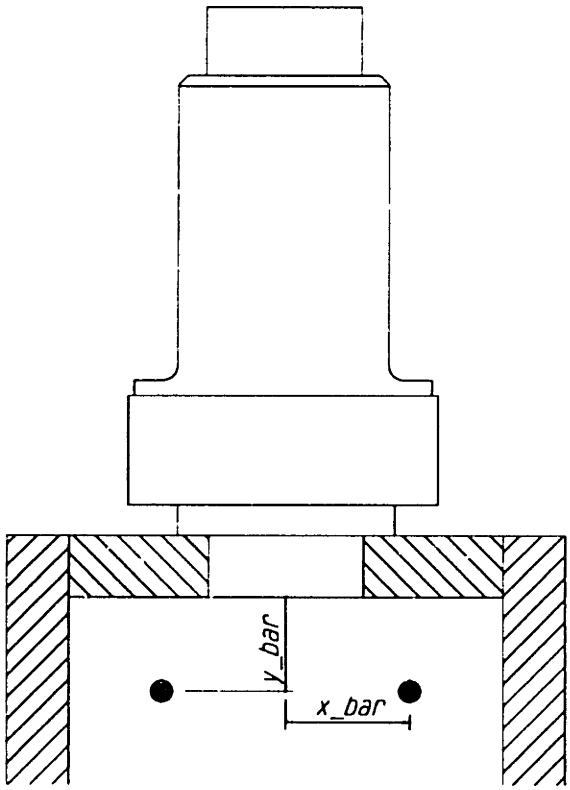

Figure 5-19: Definition of jet center of action, C.O.A.

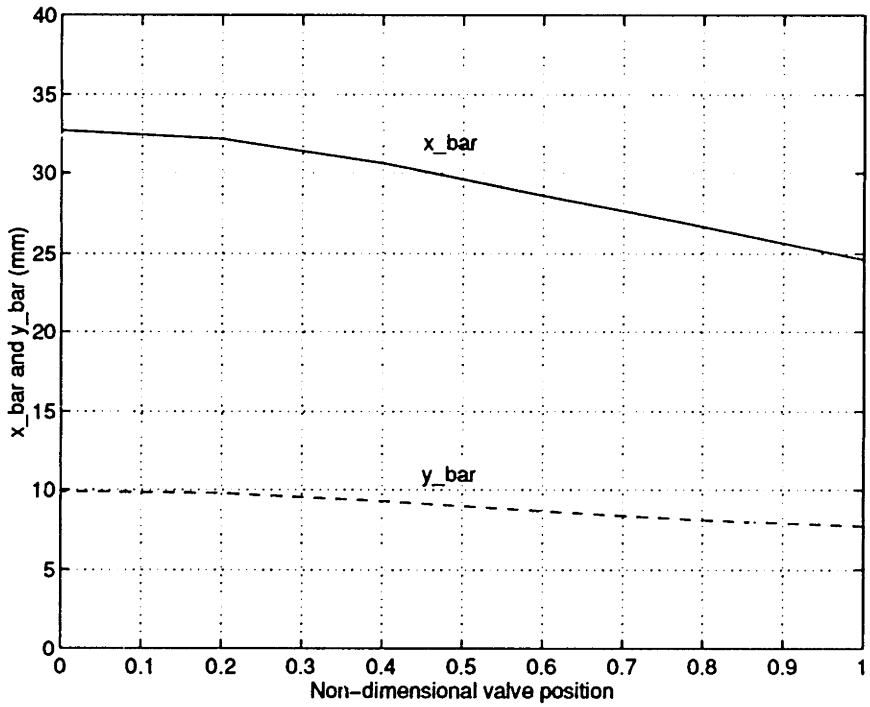

Figure 5-20: Radial and circumferential movement of the jet C.O.A. for the modified sheet injector.

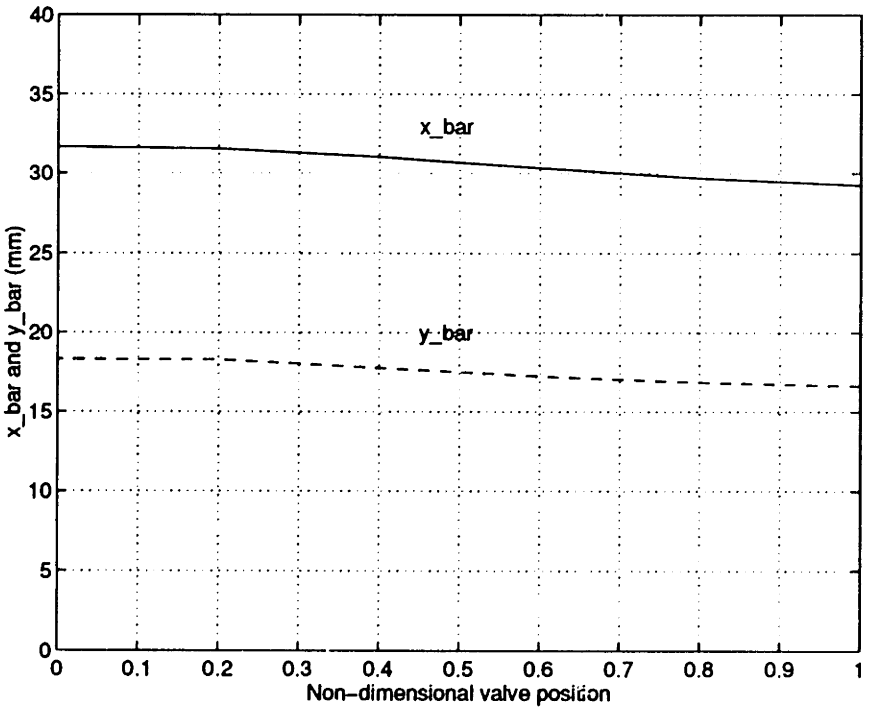

Figure 5-21: Radial and circumferential movement of the jet C.O.A. for the modified 3 hole injector.

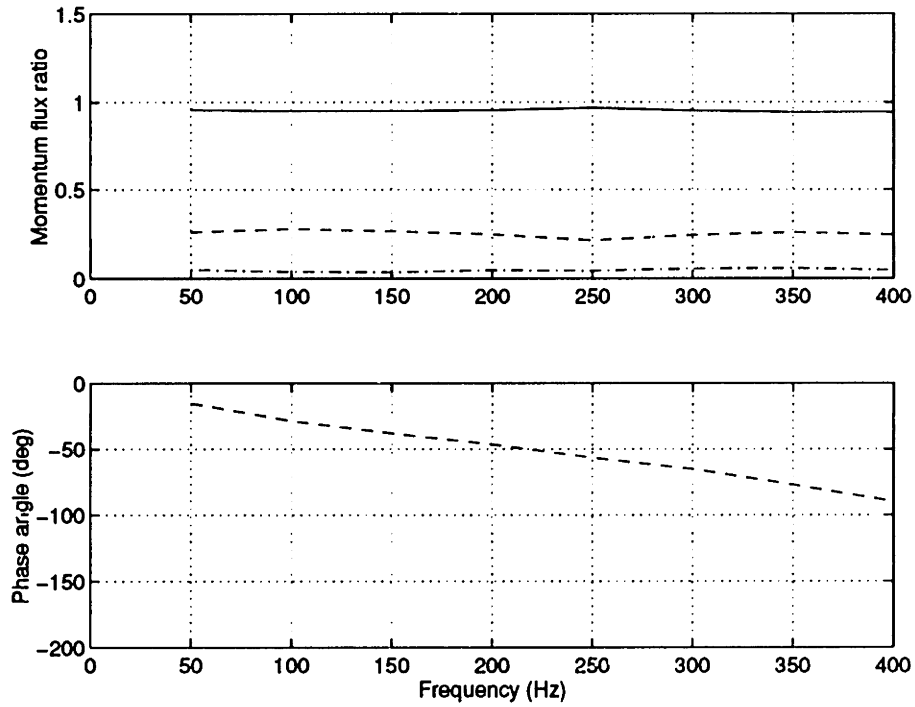

Figure 5-22: Bode plot of valve position to spatially averaged momentum flux for the modified sheet injector. Zeroth (—), 1st (- -) and 2nd (-.-) temporal harmonic.

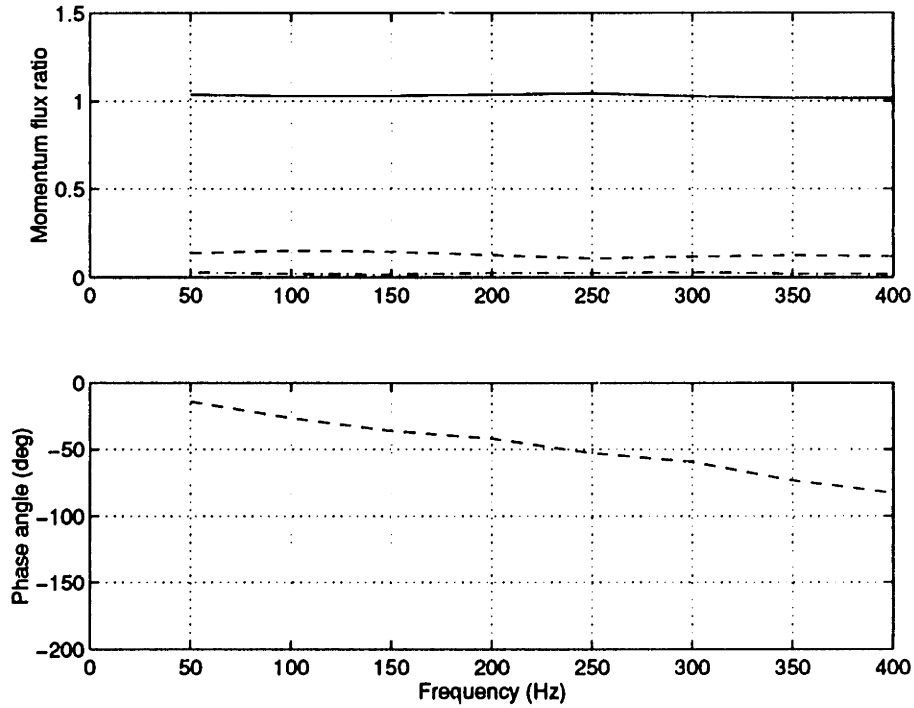

Figure 5-23: Bode plot of valve position to spatially averaged momentum flux for the modified 3 hole injector. Zeroth (—), 1st (- -) and 2nd (-.-) temporal harmonic.

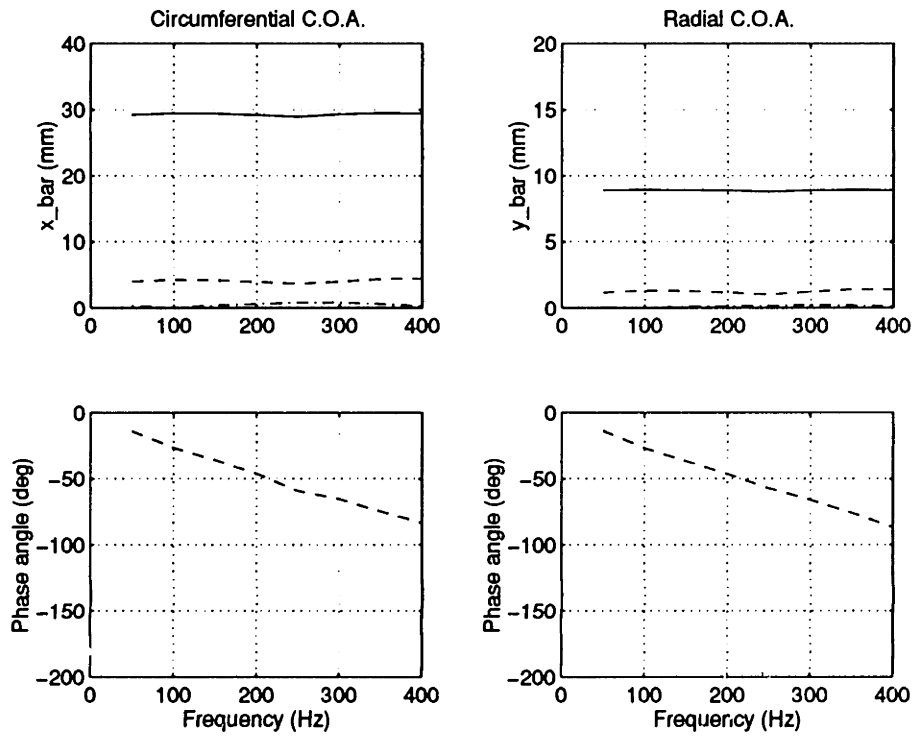

Figure 5-24: Bode plots of valve position to the jet C.O.A. for the modified sheet injector. Zeroth (—), 1st (- -) and 2nd (-.-) temporal harmonic.

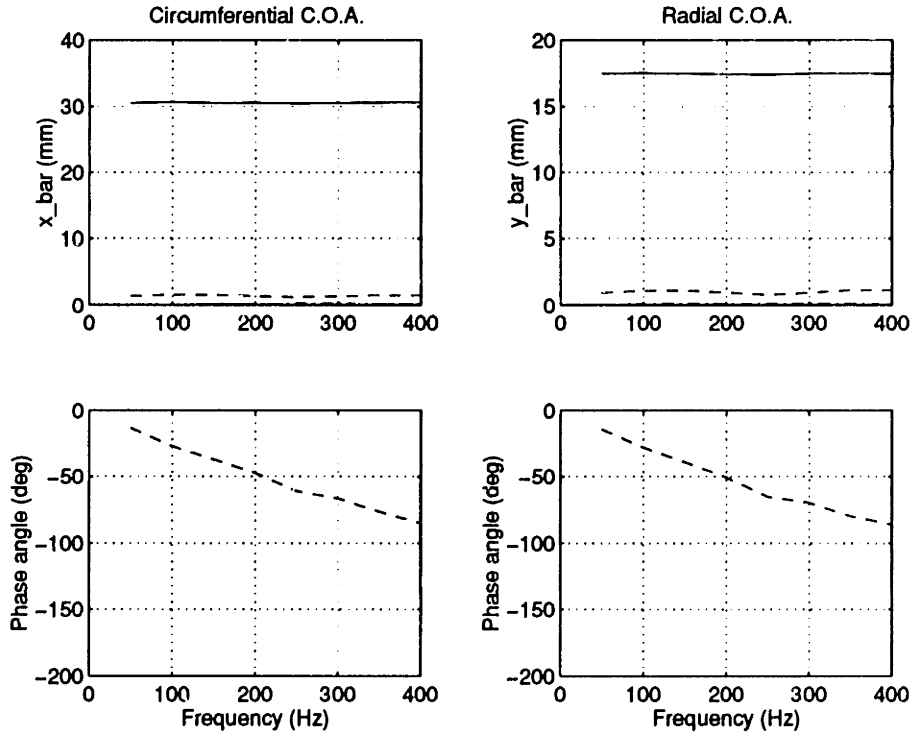

Figure 5-25: Bode plots of valve position to the jet C.O.A. for the modified 3 hole injector. Zeroth (—), 1st (- -) and 2nd (-.-) temporal harmonic.

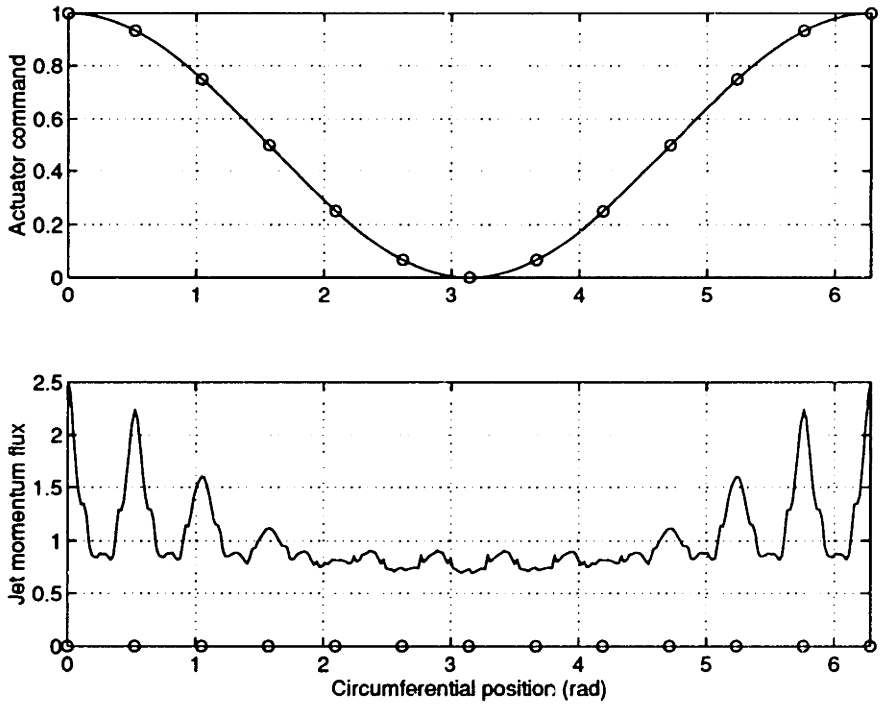

Figure 5-26: Spatial distribution of actuation for the modified sheet injector, 1st harmonic.

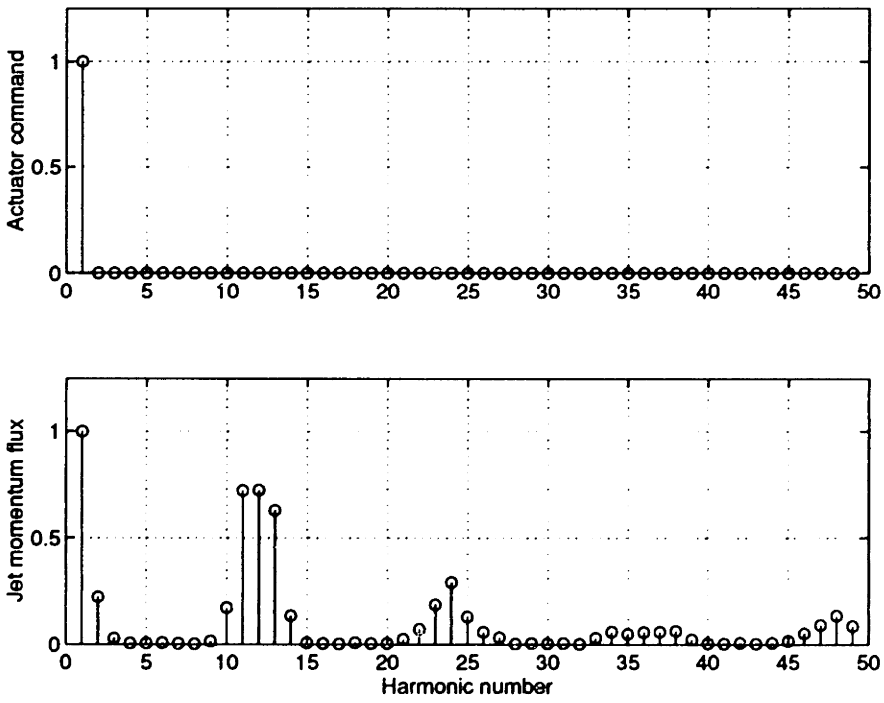

Figure 5-27: Spatial spectral content of actuation for the modified sheet injector, 1st harmonic.

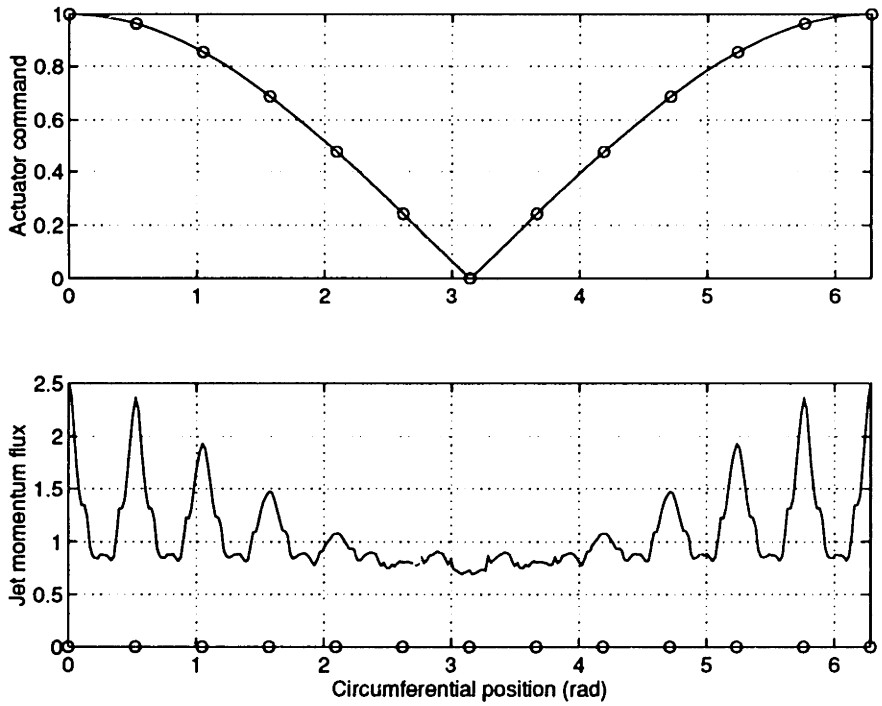

Figure 5-28: Spatial distribution of actuation (linearized) for the modified sheet injector, 1st harmonic.

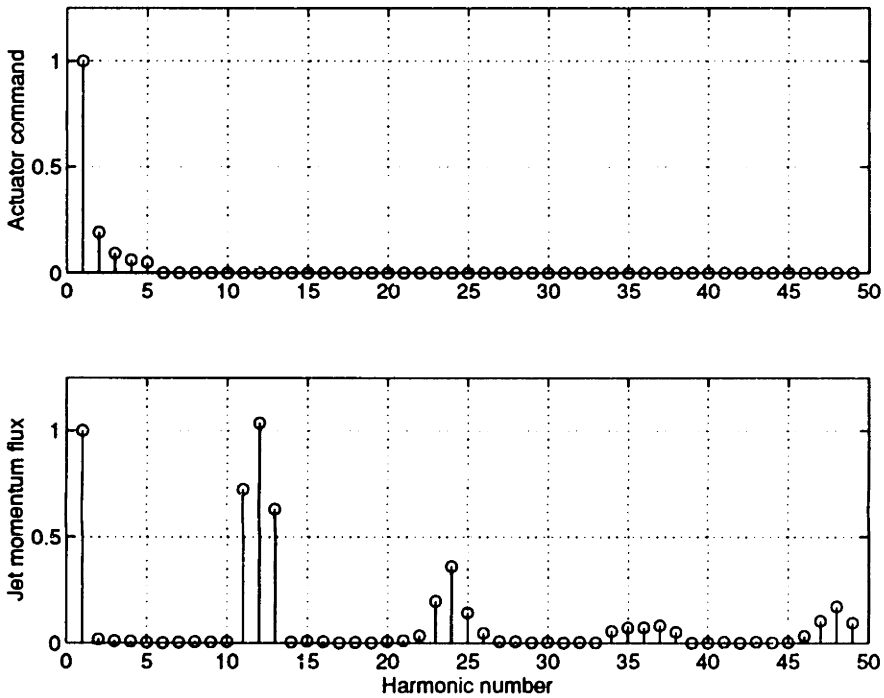

Figure 5-29: Spatial spectral content of actuation (linearized) for the modified sheet injector, 1st harmonic.

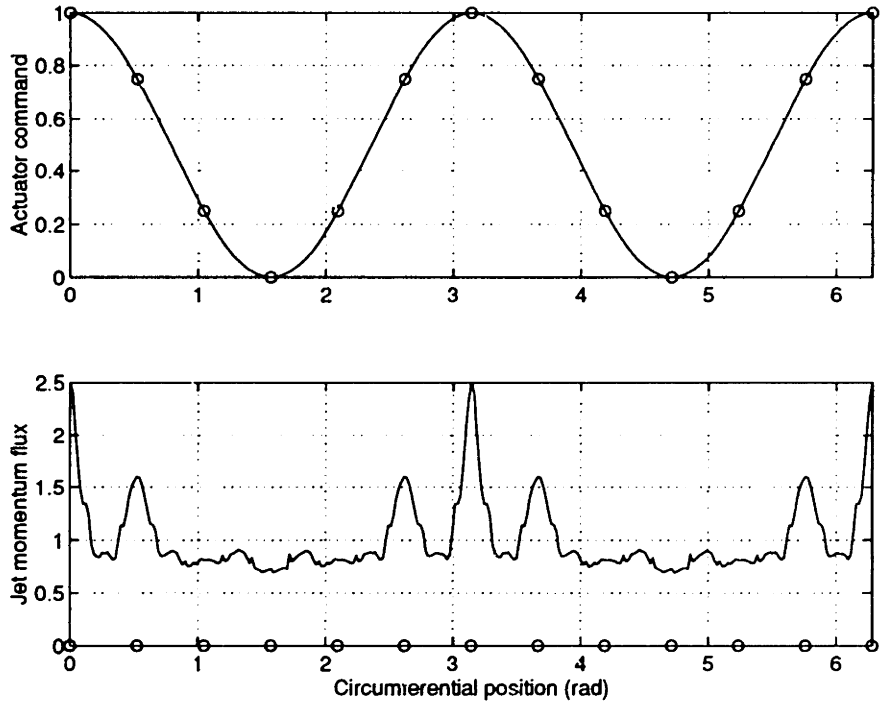

Figure 5-30: Spatial distribution of actuation for the modified sheet injector, 2nd harmonic.

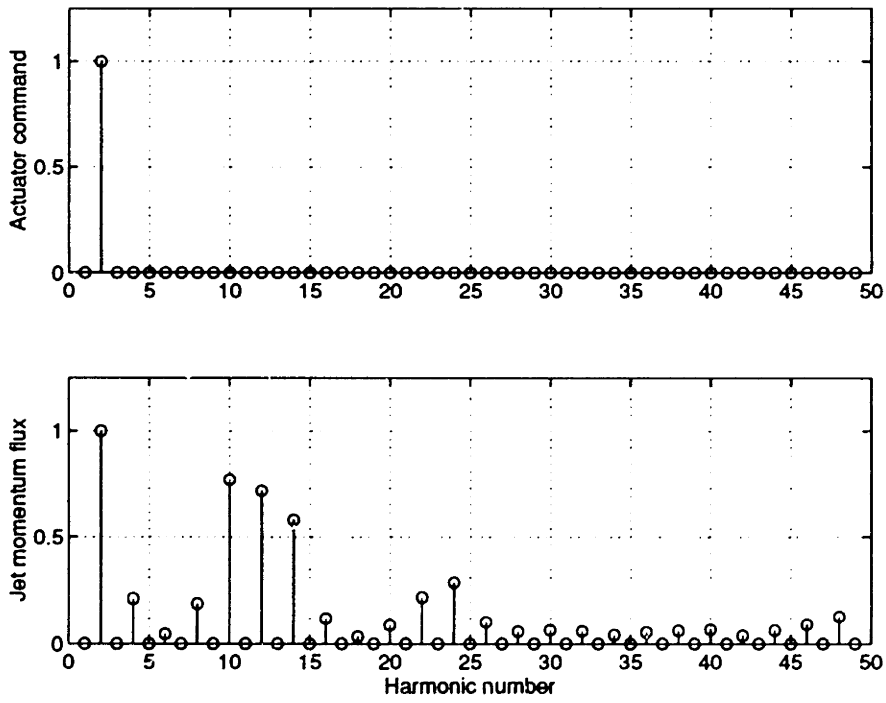

Figure 5-31: Spatial spectral content of actuation for the modified sheet injector, 2nd harmonic.

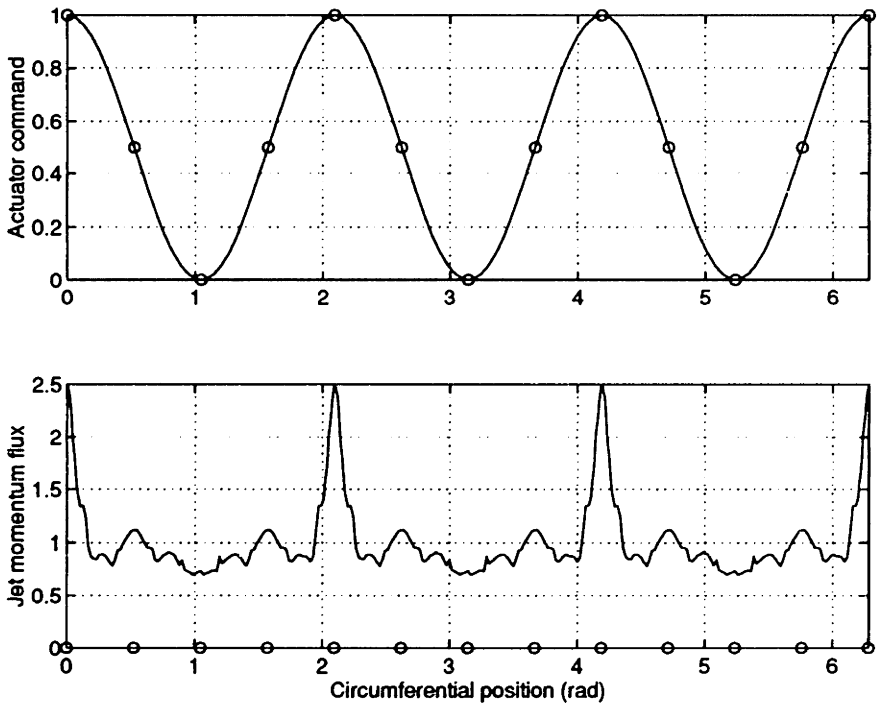

Figure 5-32: Spatial distribution of actuation for the modified sheet injector, 3rd harmonic.

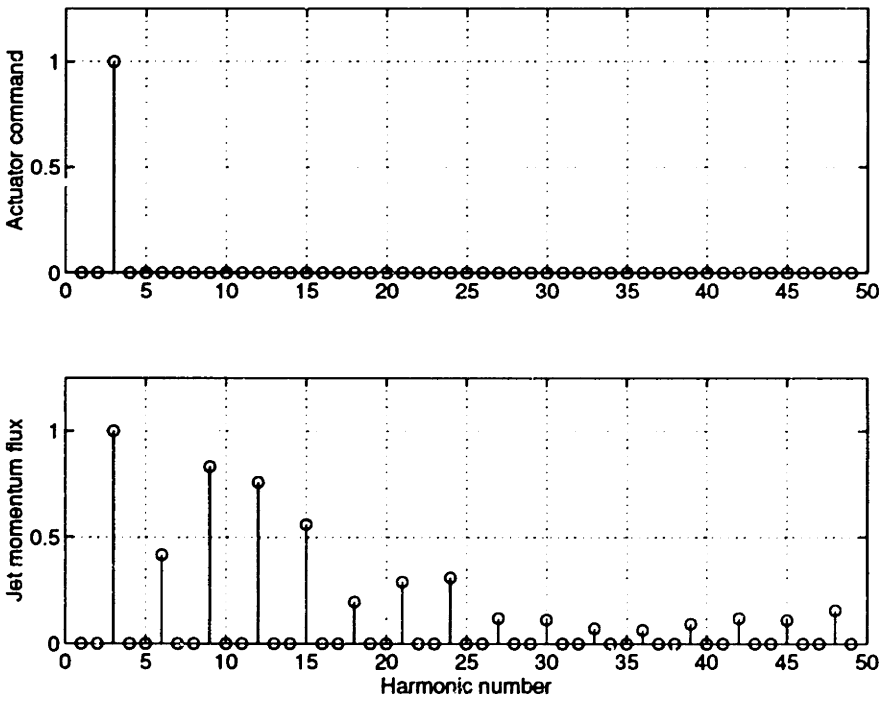

Figure 5-33: Spatial spectral content of actuation for the modified sheet injector, 3rd harmonic.

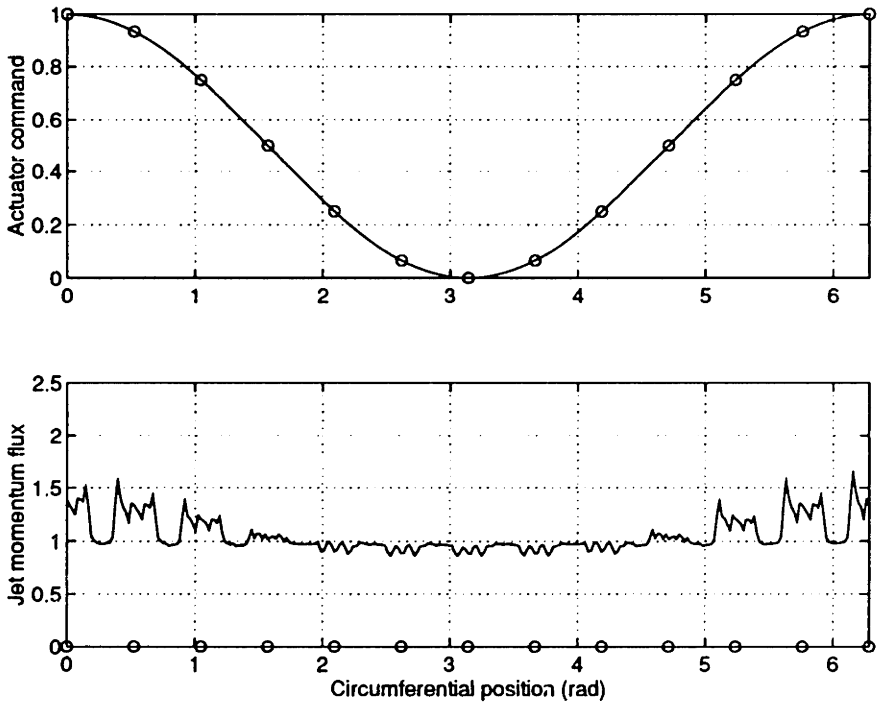

Figure 5-34: Spatial distribution of actuation for the modified 3 hole injector, 1st harmonic.

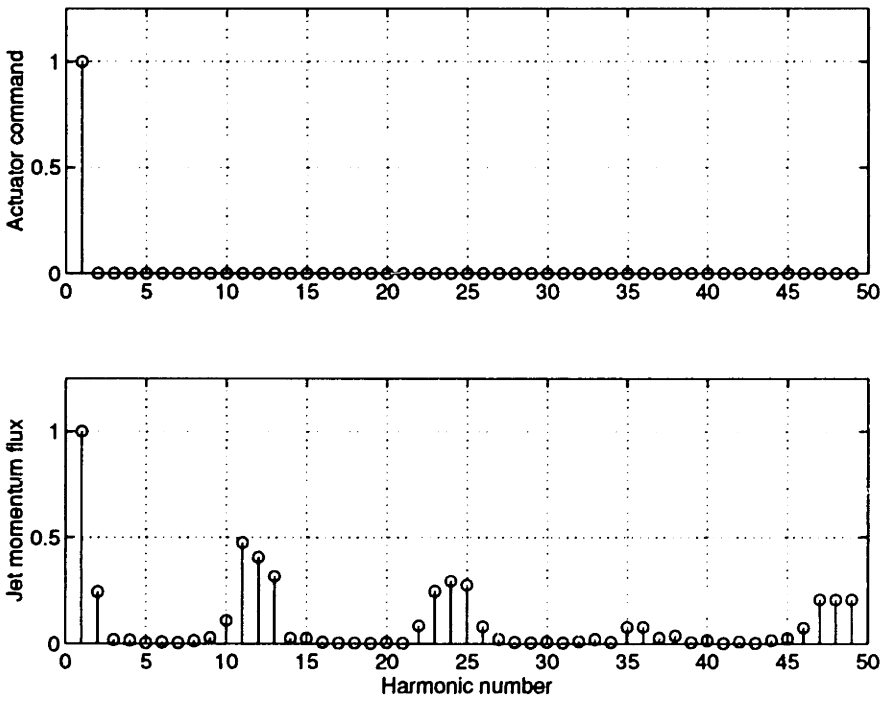

Figure 5-35: Spatial spectral content of actuation for the modified 3 hole injector, 1st harmonic.

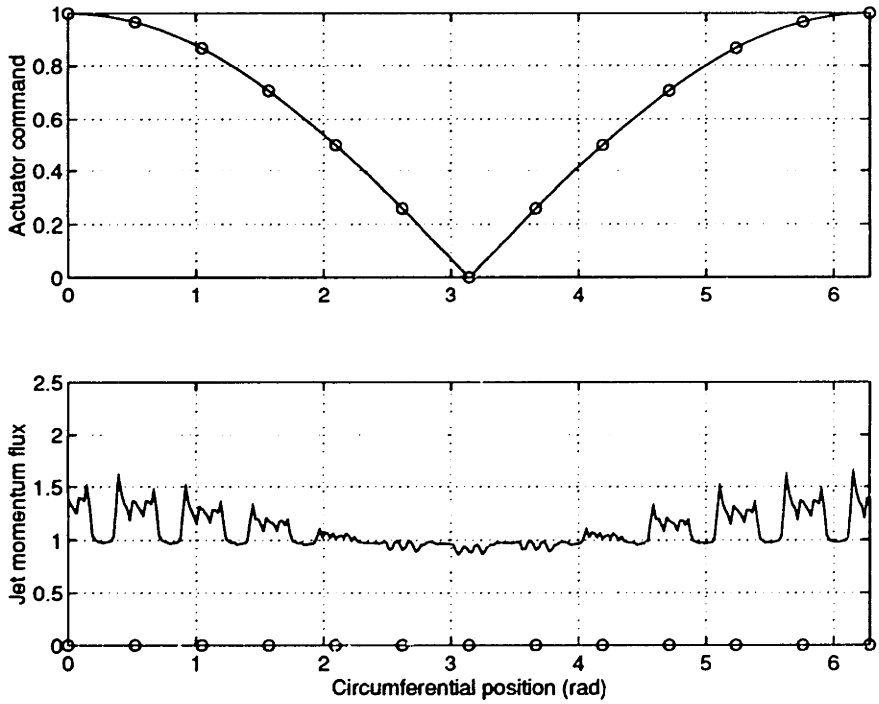

Figure 5-36: Spatial distribution of actuation (linearized) for the modified 3 hole injector, 1st harmonic.

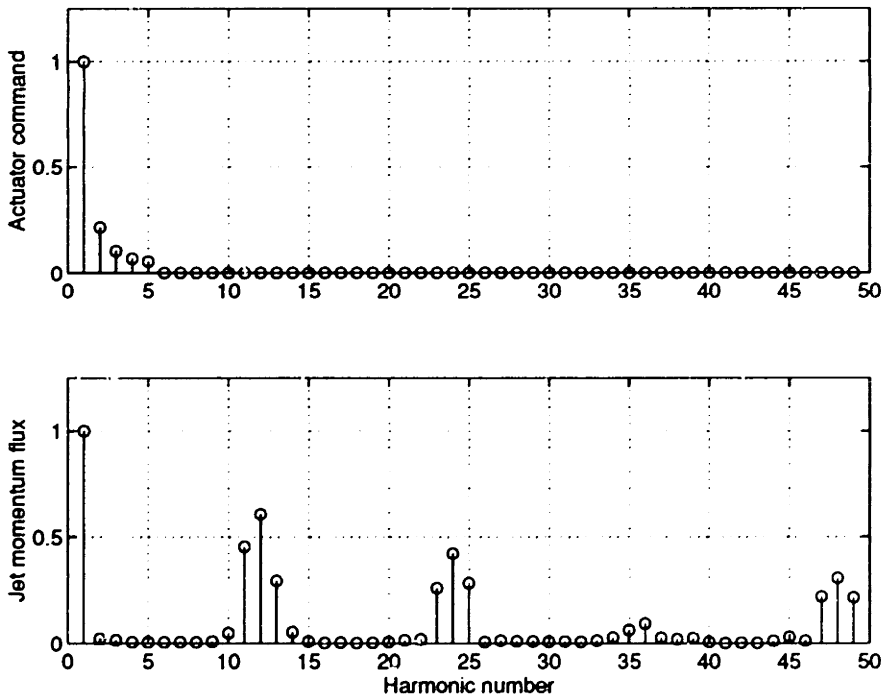

Figure 5-37: Spatial spectral content of actuation (linearized) for the modified 3 hole injector, 1st harmonic.

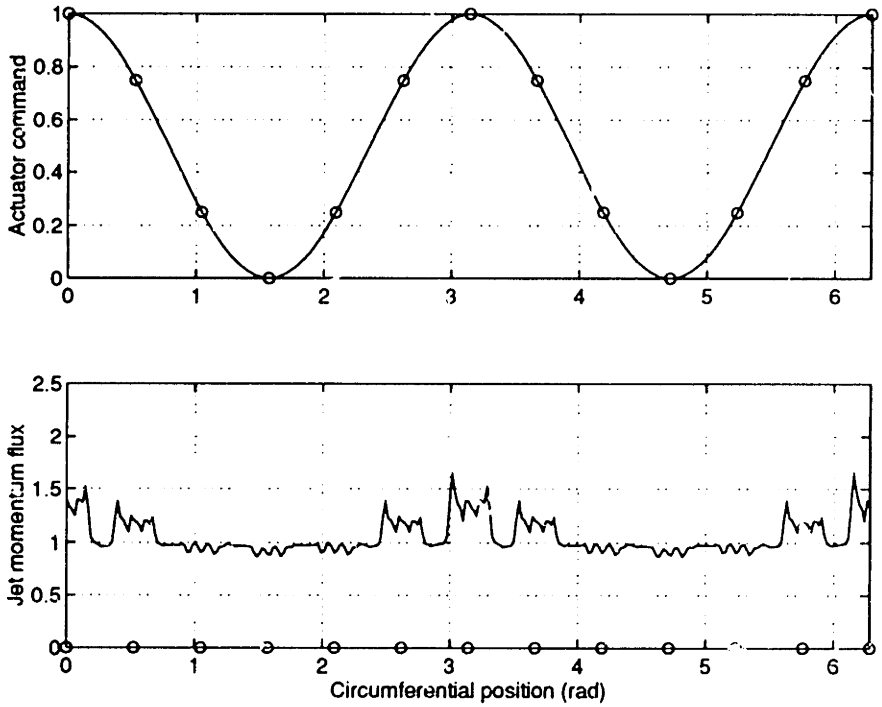

Figure 5-38: Spatial distribution of actuation for the modified 3 hole injector, 2nd harmonic.

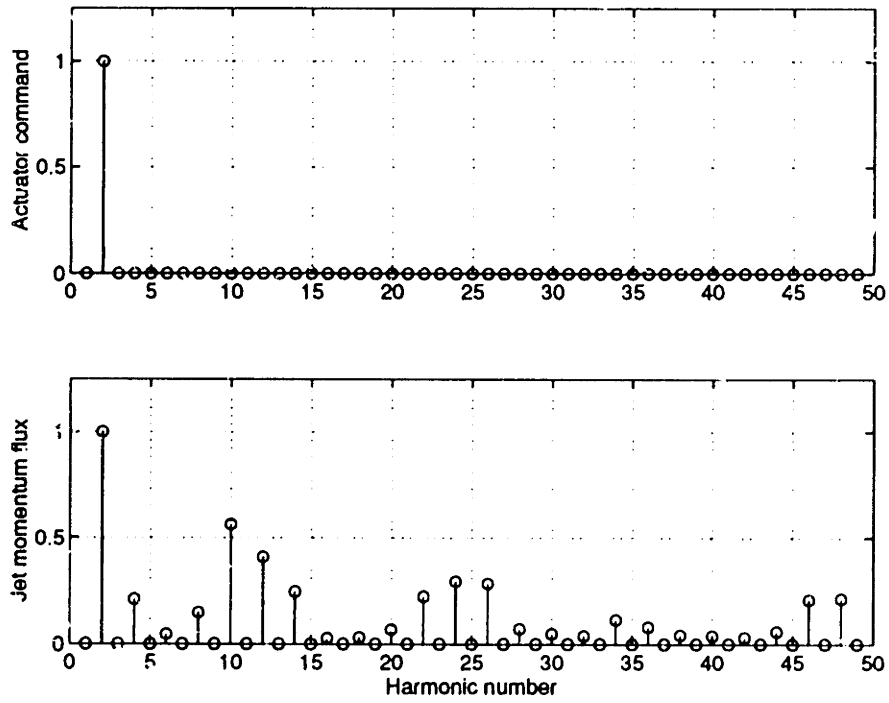

Figure 5-39: Spatial spectral content of actuation for the modified 3 hole injector, 2nd harmonic.

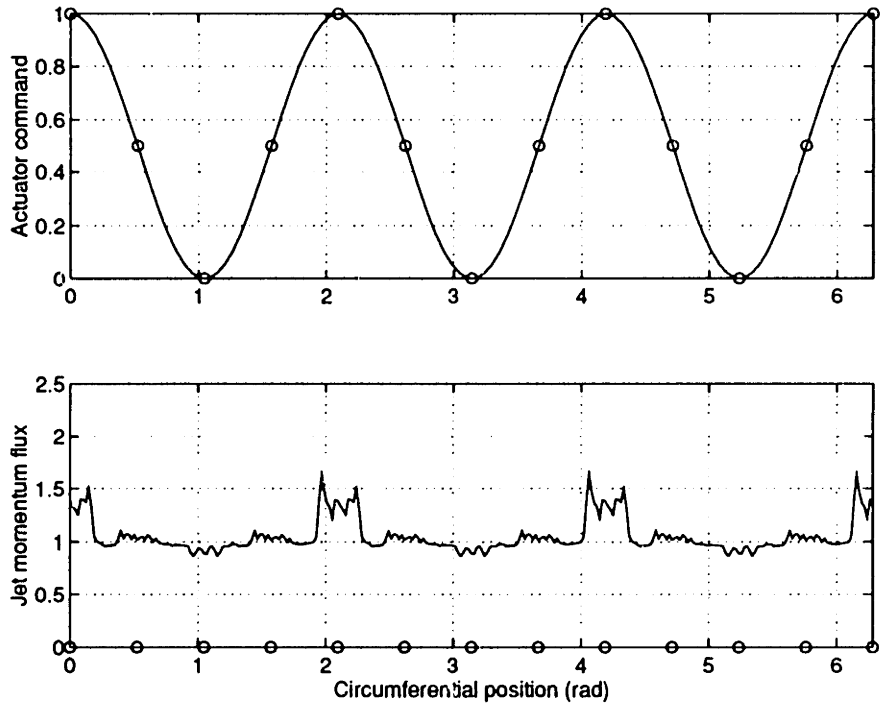

Figure 5-40: Spatial distribution of actuation for the modified 3 hole injector, 3rd harmonic.

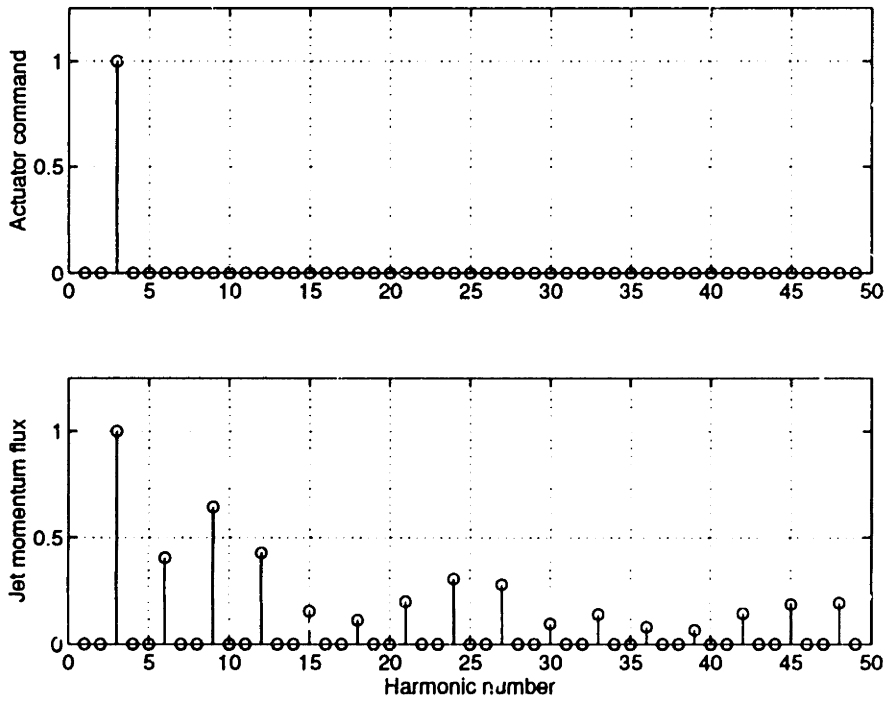

Figure 5-41: Spatial spectral content of actuation for the modified 3 hole injector, 3rd harmonic.

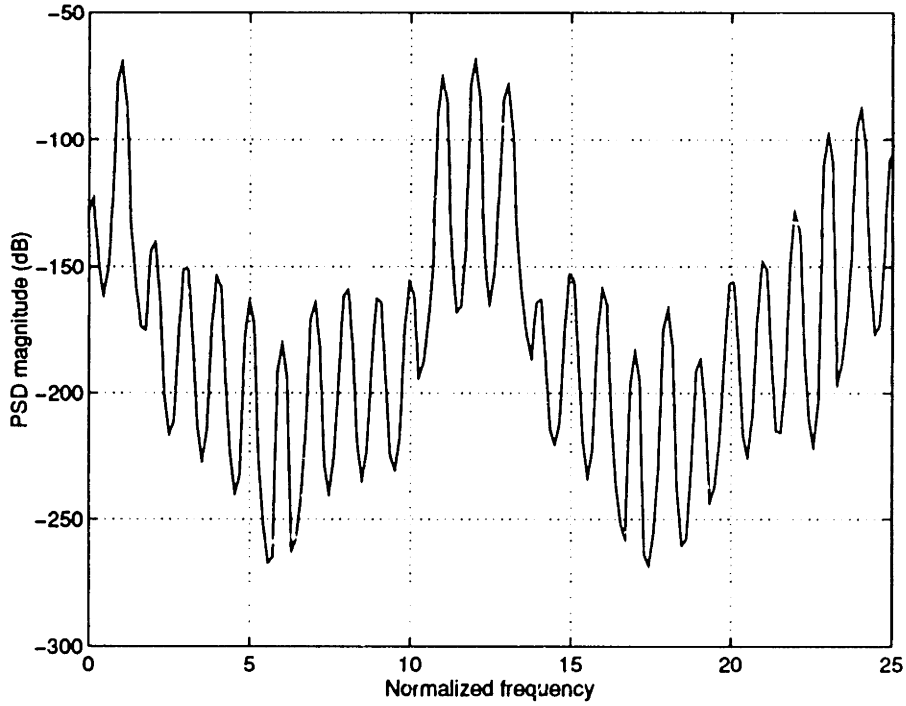

Figure 5-42: PSD of blade excitation for the modified sheet injector, 1st harmonic actuation command.

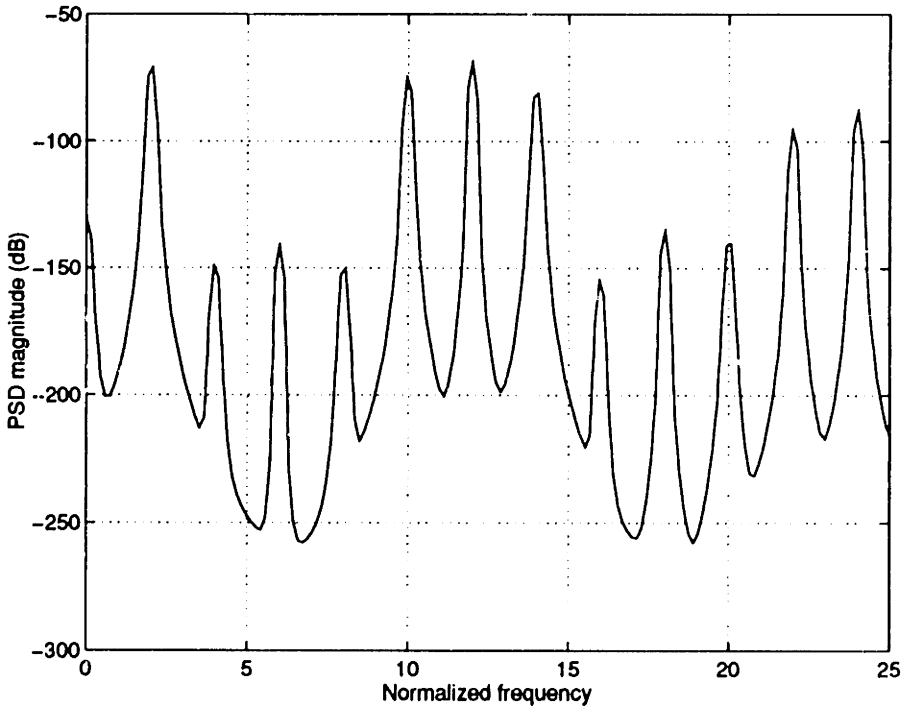

Figure 5-43: PSD of blade excitation for the modified sheet injector, 2nd harmonic actuation command.

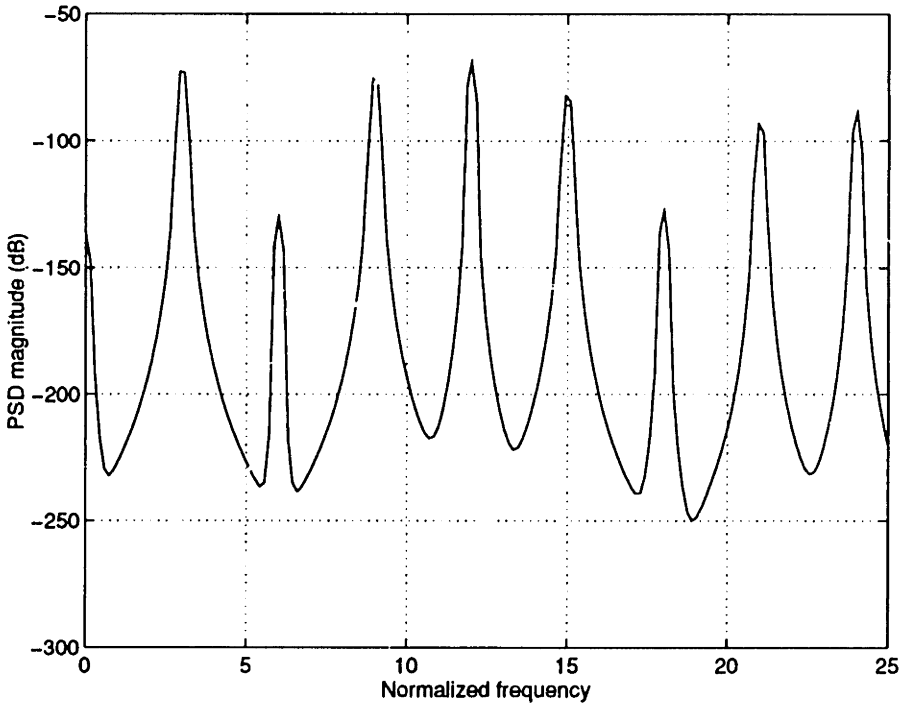

Figure 5-44: PSD of blade excitation for the modified sheet injector, 3rd harmonic actuation command.

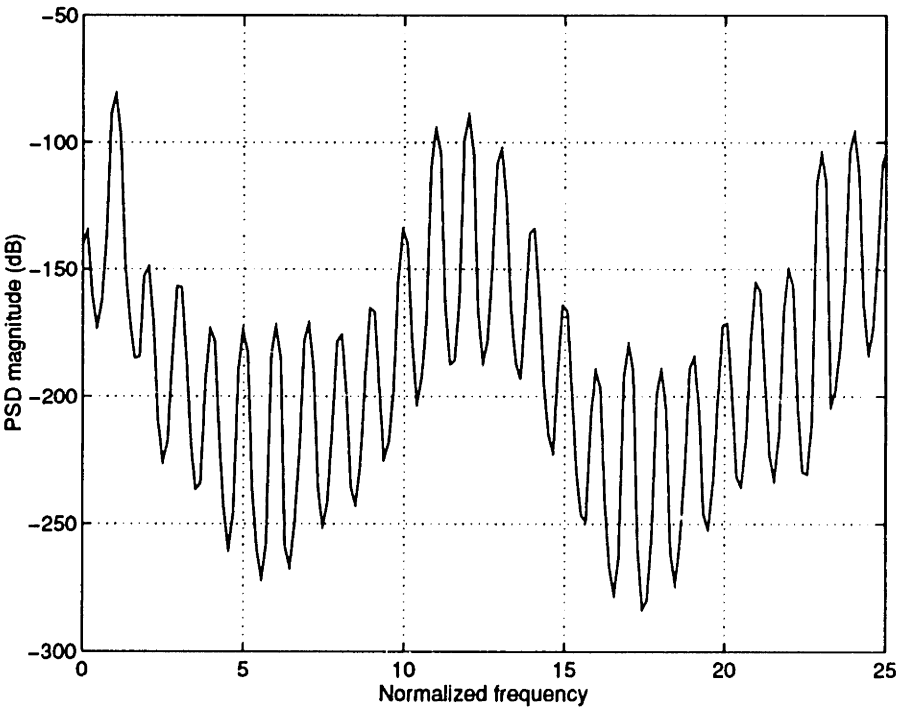

Figure 5-45: PSD of blade excitation for the modified 3 hole injector, 1st harmonic actuation command.

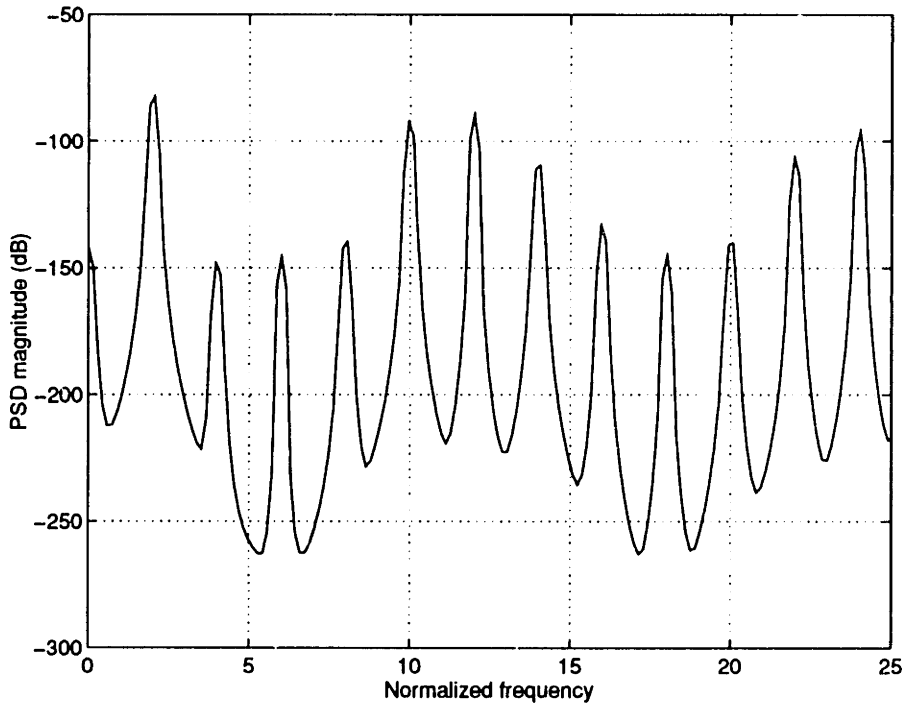

Figure 5-46: PSD of blade excitation for the modified 3 hole injector, 2nd harmonic actuation command.

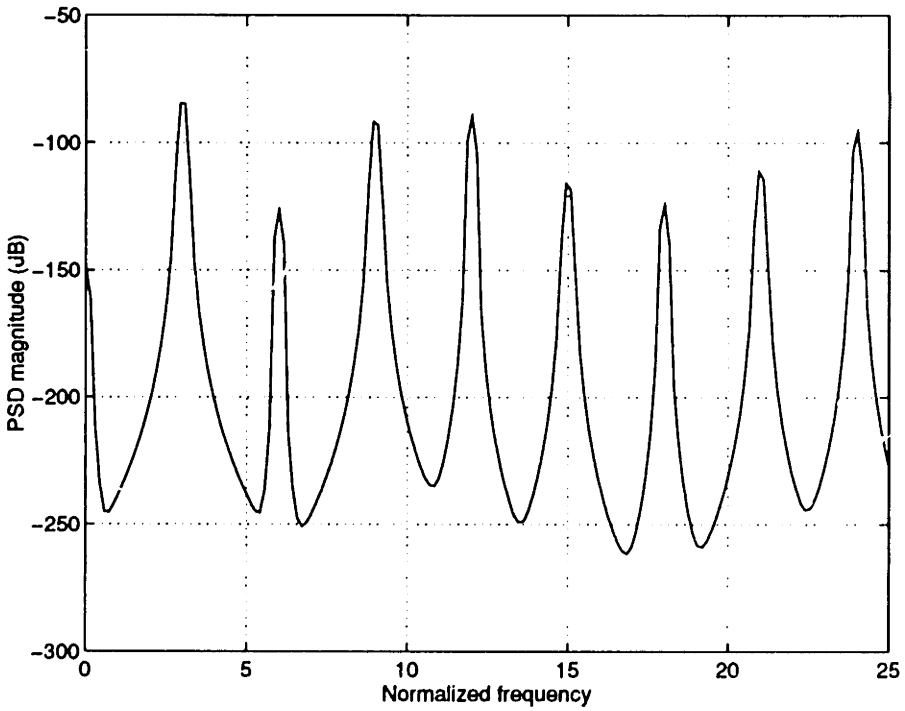

Figure 5-47: PSD of blade excitation for the modified 3 hole injector, 3rd harmonic actuation command.

Chapter 6

Sensor Development

6.1 Introduction

In addition to the actuator development, a high frequency response total pressure probe was developed. This probe allows the unsteady total pressure distribution of the flow fields upstream and downstream of a high speed compressor to be measured.

Measuring wall (casing or hub) static pressures fluctuations using high frequency response pressure transducers is routinely done in compressor tests. Since this particular type of measurement, and its associated hardware (in this case Kulite semiconductor pressure transducers), posed no significant developmental problems, it is not discussed further. High frequency response pressure measurements of the flow field away from the compressor endwalls, however, can be somewhat more challenging. Often a single probe is traversed radially and circumferentially to obtain spatial distributions of steady pressure in the flow field. If the flow is unsteady, but with some coherent temporal pattern, a picture of the flow field can be built up over time using techniques such as ensemble averaging with phase-locked measurements. To reduce the overall measurement time, several probes can be mounted in a rake that is traversed circumferentially. This approach has the advantage of allowing several radial stations to be measured simultaneously.

In the interests of high frequency response of the sensor, it is usually necessary to locate the pressure transducers at, or very close to, the actual sense point. If this is

not possible, some means must be devised whereby the pressure signals at the sense point are transmitted to a remote pressure transducer. Mounting transducers directly into the probe heads of a rake has operational limitations since it is inconvenient to replace individual transducers should they become defective. From a mechanical point of view, locating the transducers in an environment with high vibration levels or high temperatures is undesirable. Mounting the transducers remote from the probe appears attractive, but has serious performance limitations if not implemented correctly. Reflections of pressure waves between the sense location and the pressure transducer limit the frequency response of the sensor, thus for a given bandwidth requirement, an upper limit is set for the distance between the sense location and the transducer location.

6.2 The ITPS concept

The bandwidth limitations of the remotely located transducer can be overcome by making use of the so-called 'infinite tube pressure sensor' or ITPS, as described by Englund and Richards [21] and illustrated schematically in Figure 6-1. In this device, a very long ('infinite') length of tubing (0 - 3) is attached to the pressure sensing point (station 0). Pressure waves propagate down the tube, and because there is no change in acoustic impedance of the duct, there are no reflections of the wave. The waves are eventually damped out in the infinite tube by viscous dissipation. A small high-response pressure transducer is mounted flush to the inner wall of the ITPS at some location (station 4) close to the sense point, allowing pressure fluctuations passing down the tube to be sensed without causing reflections. In this manner, high frequency pressure signals can be remotely sensed, the only differences between the actual sense point pressure and the measured transducer pressure being a time delay and some attenuation. The time delay corresponds to the finite acoustic propagation time, while the attenuation is the result of viscous damping of the fluid within the infinite tube. It will be shown that for short tube lengths (l = 125 mm, L/D = 125) between the sense point and the transducer location, the signal attenuation is

typically small. If the ITPS is used for open-loop identification purposes only, the time delay associated with the finite acoustic speed can be tolerated. However, if the measurements are used for closed-loop control purposes, the time delay is undesirable and can only be reduced by shortening the distance between the sense point and the transducer location. There is thus a fundamental trade-off between time delay, and distance between the transducer and the sense point.

6.3 Theoretical analysis of the ITPS

In order to quantify the trade-off mentioned in the previous section, a simple acoustic model of the ITPS was developed to examine the effect of physical dimensions on the frequency response of the device. Referring again to Figure 6-1, the tube between 0 and 1 is called the sense tube, the tube between 2 and 3 is called the infinite tube, the volume between 5 and 6 is called the plenum, and the duct between the plenum and the infinite tube is called the plenum tube. The sense tube (0-1), infinite tube (2-3), and plenum tube (4-5) can be modeled as simple inviscid acoustic ducts, while the plenum volume V_p can be modeled as a Helmholtz resonator. A transfer function of sensed pressure (station 0) to transducer pressure (station 6) can be found by combining these simple models with a mass balance at their junction (1-2-4). Details of the transfer function derivation can be found in Appendix B. Although the final ITPS transfer function is algebraically cumbersome, it comprises two main components. The first component is the sense tube dynamic, which is given by

$$G_{0-1}(s) = \frac{p_1}{p_0} = cos\omega\tau_1 - jsin\omega\tau_1$$

where

$$\tau_1 = \frac{l_1}{a}$$

This is the transfer function of a pure time delay, with a constant magnitude (unity) for the entire frequency range, and a phase lag that increases linearly with frequency. The phase lag is also increased if the sense tube length is increased. This component

of the overall transfer function accounts for the acoustic propagation delay between the sense point and the transducer plenum. The second component of the overall ITPS transfer function is that of the plenum dynamic, given by

$$G_p(s) = \frac{p_6}{p_4} = \frac{1}{(1 - s^2 \frac{V_p}{A_3 a} \frac{l_3}{a})}$$

From the expression it is clear that the plenum transfer function is second order in nature, and can therefore lead to oscillatory behavior. Also, the ratio of plenum volume to plenum duct area (V_p/A_3) and the plenum duct length (l_3) determine the frequency response of the Helmholtz resonator. Increasing either V_p/A_3 or l_3 deteriorates the high frequency response of the plenum.

Figure 6-2 shows a Bode plot of the overall ITPS transfer function, and in particular the effect on frequency response when the sense tube length l_1 is varied from 125 mm to 250 mm (L/D = 125 to 250). The better frequency response (least phase lag) corresponds to the shorter sense tube length l_1, this length determining the frequency at which resonance in the magnitude plot commences, as well as having the greatest influence on the phase lag of the ITPS. Due to practical installation constraints in this application, the shortest sense tube length is about 125 mm (5"), therefore this was taken to be the lower limit in the theoretical prediction. The plenum tube diameter d_3 has very little effect on the frequency response of the system, therefore it is set to 0.75 mm (which corresponds to the 0.03" diameter pressure sensitive area of the particular Kulite pressure transducer used). The plenum tube length l_3 also has only a small effect on the frequency response, therefore it was made 0.5 mm to keep the machining of the ITPS simple. The plenum volume has a large effect on the frequency response of the ITPS, it being desirable to keep this volume as small as possible. Assuming that the plenum diameter is set at 1.7 mm (the 0.068" diameter hole size necessary to accommodate this particular Kulite pressure transducer), a plenum length l_p of 25 μm gives excellent results. Figure 6-3 shows the effect of varying the plenum length from 25 μm to 500 μm, the shorter plenum length corresponding to the flatter magnitude plot. Since it is possible to mechanically implement a plenum

volume with $l_p = 25\ \mu m$, this was made a design constraint. Figure 6-4 shows the ITPS frequency response with $l_1 = 125$ mm and $l_p = 25\ \mu m$, these values being selected to be the design values. The response approaches that of a pure time delay, the best possible response given the finite speed of information propagation, namely the acoustic speed.

6.4 ITPS design and fabrication

The mechanical design of the ITPS probe is an attempt to approach the ideal case of an infinite tube with a pressure sensitive inner wall at some downstream location. Any discontinuities or sharp bends in the tube will violate the condition of constant acoustical impedance, thus these must be avoided. For this reason, all joints in the infinite tube must be flush and burr-free. Also, the intersection of the pressure transducer and the infinite tube should be as unobtrusive as possible. A 1/16" Swage-lok bulkhead fitting was used to house the intersection between sense tube, infinite tube and Kulite transducer. Figure 6-5 shows the mechanical details of the modified fitting. It should be noted that only a single joint is made in the infinite tube, thus providing only one opportunity for a step in the tubing inner wall. Since the two pieces of tubing on either side of the joint are radially constrained by the modified Swage-lok fitting, it was hoped that the radial misalignment would be small compared to the tube inner diameter. This was verified to be true by sectioning a prototype fitting using a grinding machine. The Kulite is epoxied into the modified Swage-lok fitting, the 'dead volume' being kept to a minimum by seating the Kulite flush against the bottom of hole ($l_p < 25\mu m$). Figure 6-5 also shows that two versions of the ITPS were fabricated, namely a wall static pressure probe and a total pressure probe.

6.5 Performance testing

Having used a theoretical model to predict the design performance of the probe, the prediction was verified by experiment. Since the steady response of the sensor would

be identical to that of a Kulite subjected to the same pressure (provided there are no leaks in the Swage-lok fitting and 'infinite' tube), no steady tests were performed. The dynamic response of the ITPS is the important issue here, and this was to be investigated. A fluctuating pressure source was created by the apparatus shown in Figure 6-6. A high speed (1250 Hz) rotating valve modulates high pressure airflow into a small plenum volume (V = 15 cc). The plenum discharges the pulsating airflow to the atmosphere via a small nozzle (d = 6 mm). A reference Kulite pressure transducer, as well as the ITPS wall static probe, are mounted flush to an inner wall of the plenum, very close (8 mm) to one another. In this way, it is possible to measure the same static pressure fluctuation with two different sensors. Since the frequency response of the flush mounted reference Kulite pressure transducer is known (on the order of 100 kHz), it was assumed to be a good reference of the actual plenum pressure since it has essentially no dynamics in the frequency range of interest (0 to 1 kHz).Downstream of the nozzle is a hot-film sensor mounted directly next to the total pressure ITPS probe. Since the hot-film sensor has very high frequency response, it can be used as a reference measure of flow velocity (and hence total pressure) since it has no dynamics in the frequency range of interest (0 to 1 kHz). The arrangement of reference transducers (reference Kulite and hot-film probe) allows the frequency response of the wall static and total pressure ITPS probes to be measured. Notice that both ITPS probes have a sense tube length of 125 mm.

The high pressure air supply was adjusted to yield a plenum pressure fluctuation of about 6.9 kPa (1 psi) when the valve was rotating. The valve was spun at frequencies between 0 and 1250 Hz to yield frequency sweeps that could be analyzed by the usual frequency response methods.

6.5.1 Tests on the wall static probe

Figure 6-7 shows the experimental transfer function (—) from the wall static ITPS probe signal to the actual plenum static pressure signal (reference Kulite), as well as the theoretical prediction (- -). The coherence of the experimental transfer function is essentially equal to unity from DC to 1250 Hz but falls off beyond 1250 Hz. This

is expected since the rotating valve was only able to spin up to frequencies of 1250 Hz, thus there is little coherent pressure information at higher frequencies. The magnitude plot of the experimental transfer function is relatively flat, as predicted by the theoretical model. The experimental phase behavior is that of a pure time delay, and corresponds almost exactly to that predicted by the theoretical model. It appears then that the theoretical prediction matches the experimental data well for the wall static ITPS probe.

6.5.2 Tests on the total pressure probe

Figure 6-8 shows the experimental transfer function (—) from the total pressure ITPS probe signal to the jet total pressure signal as calculated from the reference hot-film anemometer data. The theoretically predicted ITPS transfer function (- -) is also shown. The reference hot-film velocity was squared to yield a quantity which is directly related to the total pressure of the flow. Since the static pressure outside the nozzle is nominally constant at the mean Mach number (M = 0.5), variations of dynamic pressure correspond to variations of total pressure. The coherence of the experimental transfer function is not as high as that of the wall static ITPS probe, due to the random turbulent fluctuations of the jet sensed by the total pressure ITPS probe and the hot-film probe. It is, however, evident that there is a significant decrease in the coherence above 1250 Hz, this frequency corresponding to the upper frequency level of the frequency sweeps. The magnitude plot of the experimental transfer function is flat, as predicted by the theoretical model. The phase behavior also corresponds almost exactly to that of the pure time delay prediction of the theoretical model. It would therefore appear that the theoretical prediction also matches the experimental data well for the total pressure ITPS probe.

6.6 Design of the ITPS module

Rig testing of the prototype ITPS on the NASA Lewis W-8 compressor test facility showed that the probe was susceptible to damage by being in an exposed position

on the rig. To overcome this, the ITPS probe was packaged in a robust module to prevent damage to the probe during the actual compressor tests. Figure 6-9 shows the design of the ITPS module, indicating that it is made up of three parts, namely a total pressure rake, an extension piece (housing the modified Swage-lok fittings and Kulites) and a coil housing. There are rake pads both upstream and downstream of the compressor (NASA Stage 35), and because the annulus height is different upstream and downstream, it was necessary to design an upstream as well as a downstream rake. Each rake has 4 total pressure heads that are spaced on the basis of equal annular areas. The extension piece is split longitudinally so that the modified Swage-lok fittings can be fastened or loosened if a change of rakes (the upstream and downstream rakes are different) is required. The entire ITPS module is bolted to the compressor casing by four bolts.

6.7 Summary

A prototype infinite tube pressure sensor was designed and tested. A simple acoustic model of the ITPS was developed to predict the frequency response of the probe. The predicted and experimental results indicate that the theoretical model captures the essential dynamics of the probe. The frequency response of the probe is essentially characterized by a pure time delay, which is due to the finite time taken to propagate information, at the speed of sound, from the sense location to the transducer location. A rugged modular version of the ITPS was developed for the actual compressor tests to be performed on NASA Stage 35. The ITPS module houses 4 ITPS probes, which are connected to a 4 head total pressure rake.

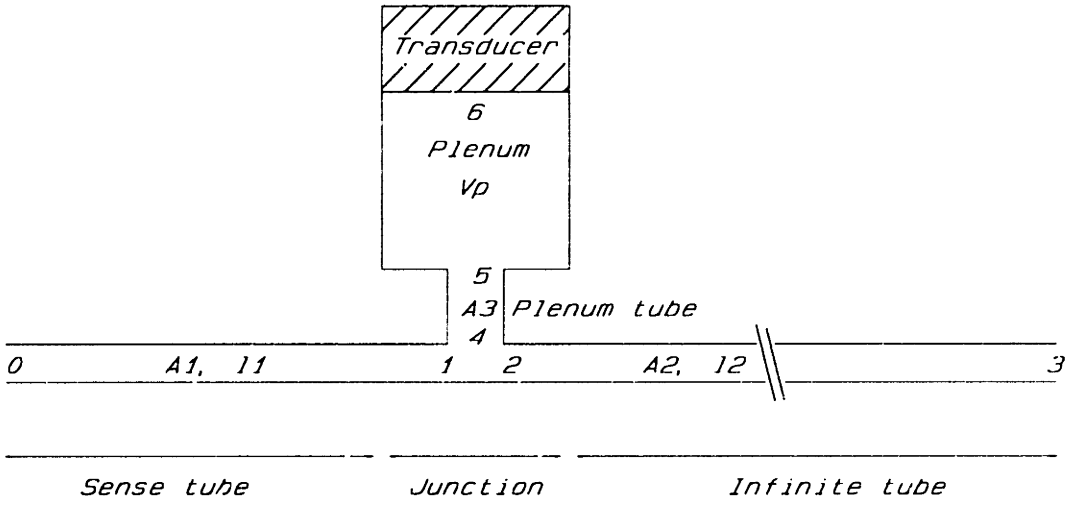

Figure 6-1: Schematic diagram of the ITPS concept.

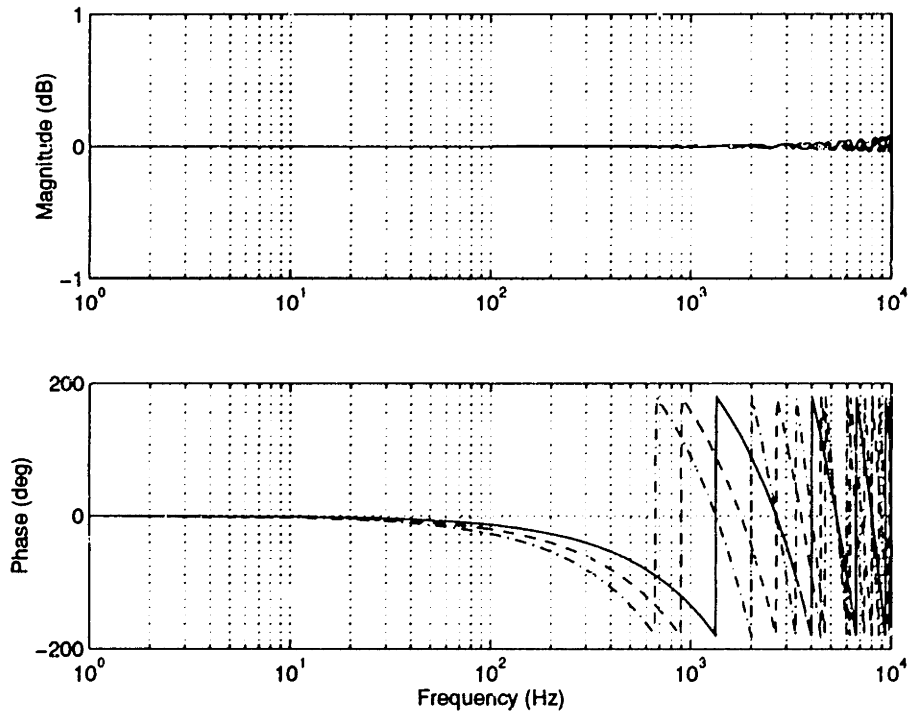

Figure 6-2: Bode plot of the predicted frequency response for the ITPS with varying sense tube length, l_1 = 125 mm (—), 188 mm (- -) and 250 mm (-.-), l_p = 25 μm.

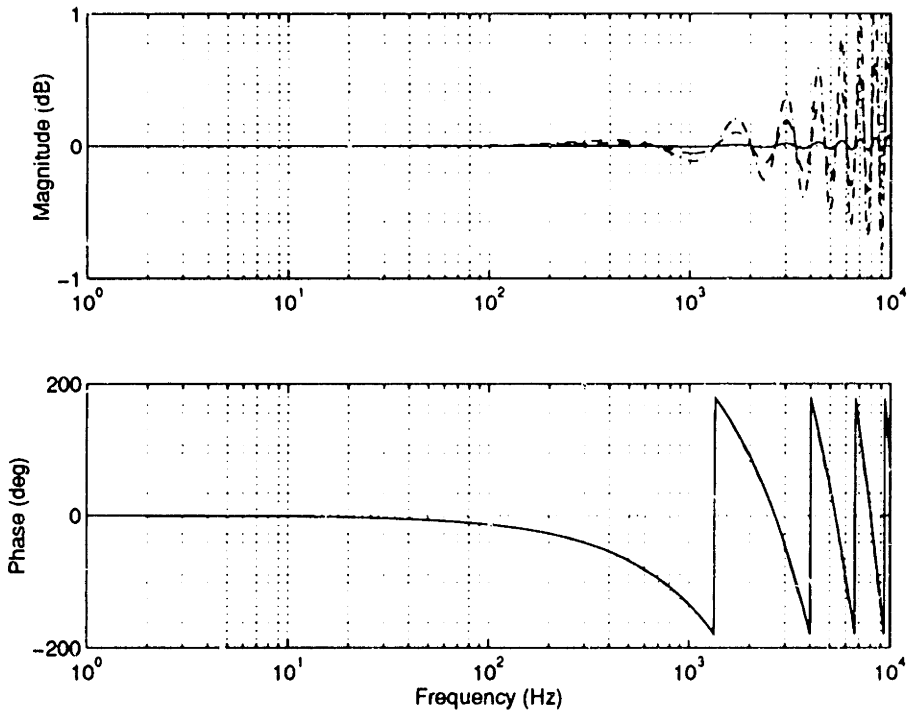

Figure 6-3: Bode plot of the predicted frequency response for the ITPS with varying plenum length, l_p = 25 μm (—), 250 μm (- -) and 500 μm (-.-), l_1 = 125 mm.

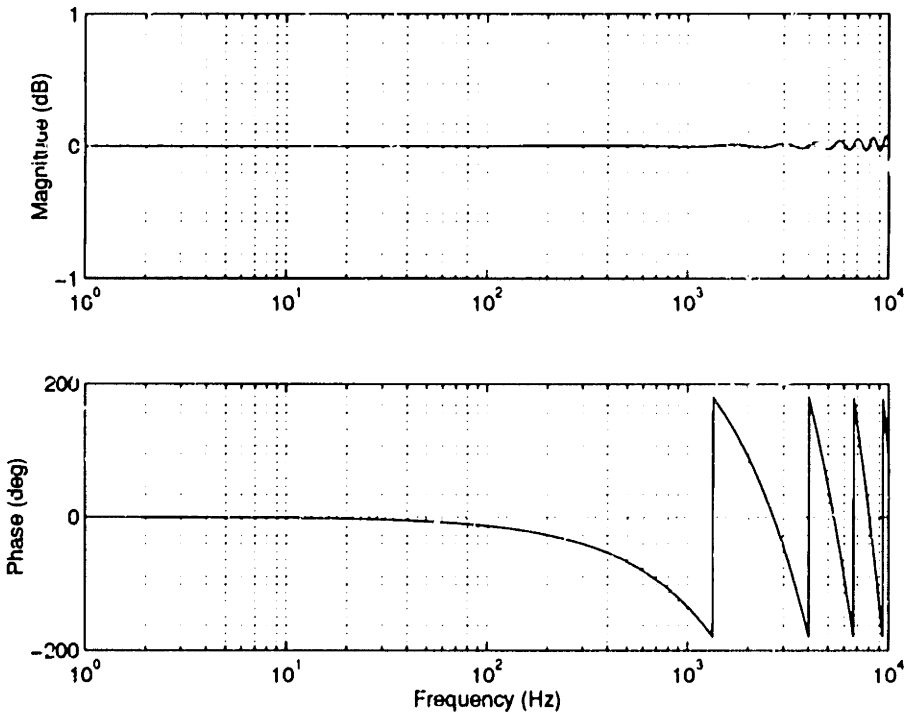

Figure 6-4: Bode plot of predicted frequency response for the final ITPS design, l_1 = 125 mm, l_p = 0.025 mm.

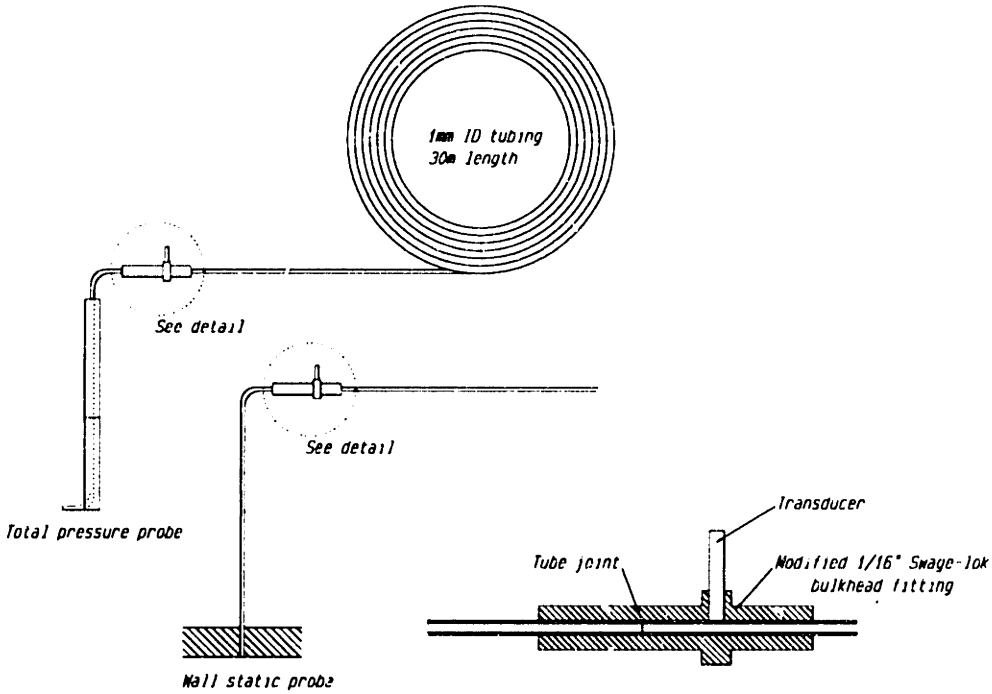

Figure 6-5: Prototype total pressure and wall static pressure ITPS probes.

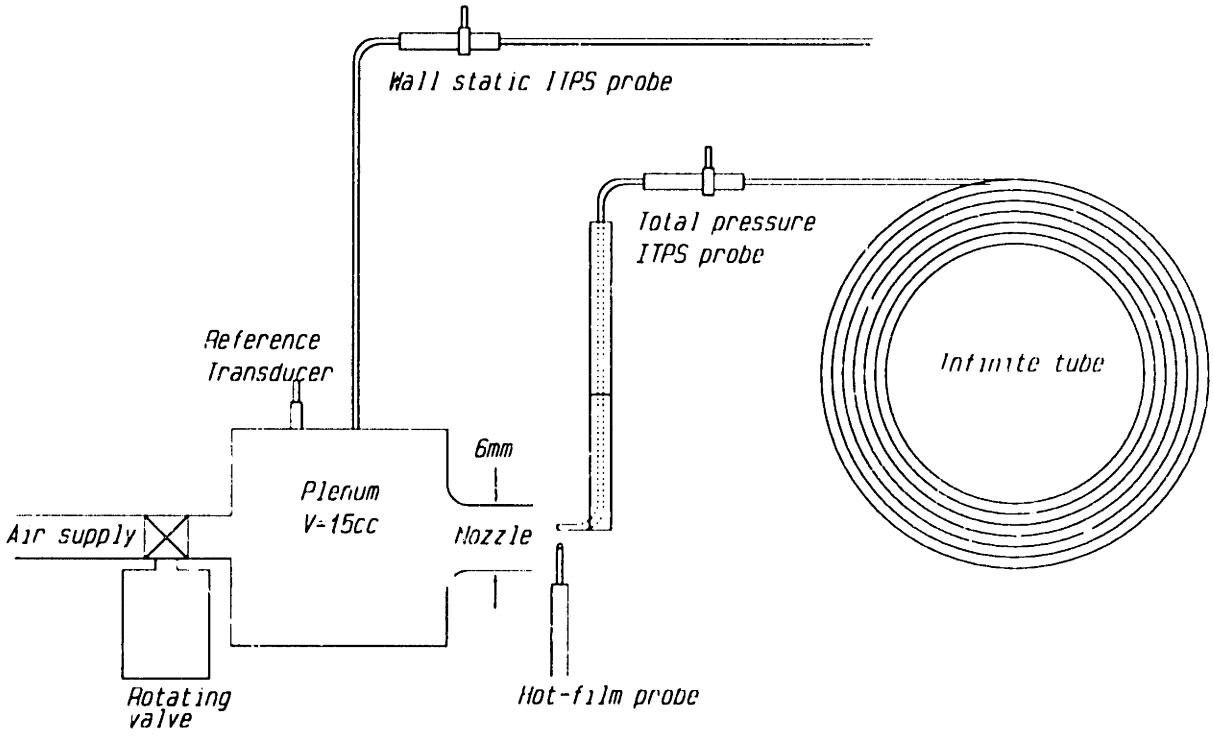

Figure 6-6: Experimental rig for testing the ITPS.

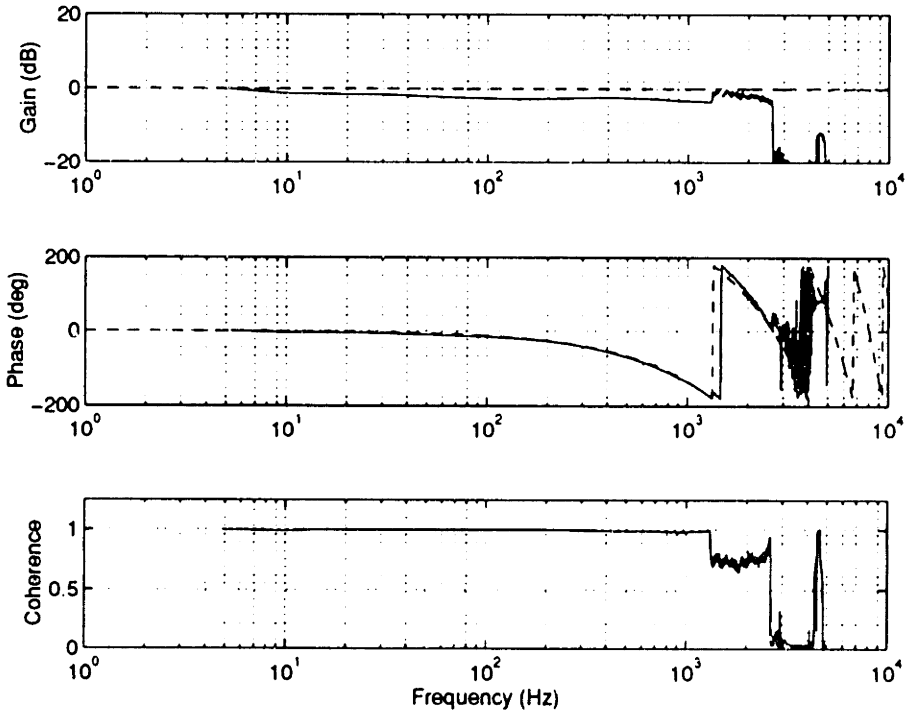

Figure 6-7: Bode plot of measured (—) and predicted (- -) frequency response for the wall static ITPS probe.

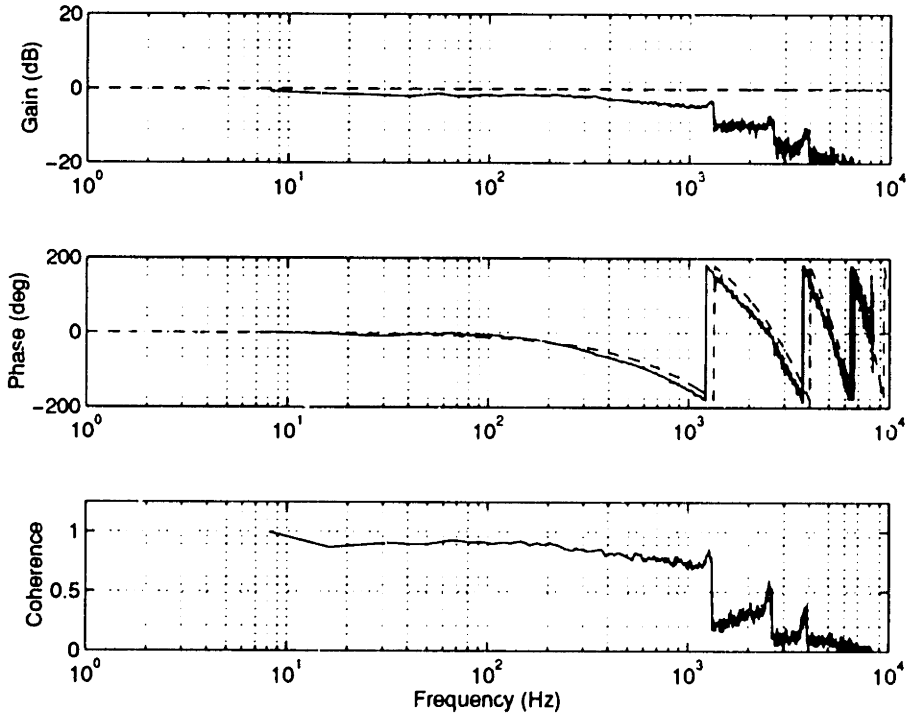

Figure 6-8: Bode plot of measured (—) and predicted (- -) frequency response for the total pressure ITPS probe.

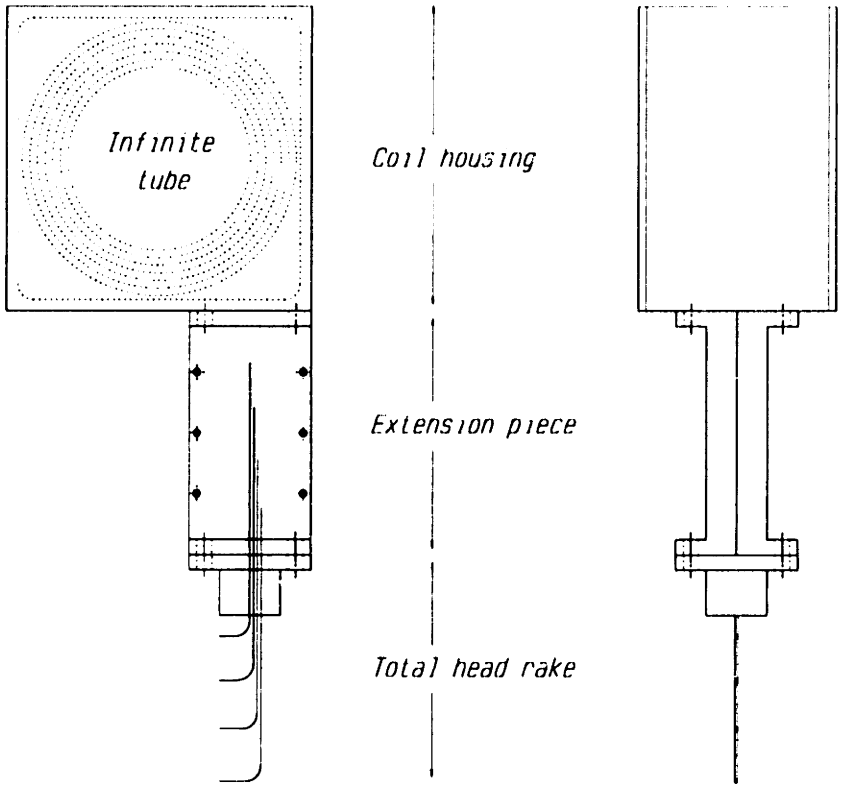

Figure 6-9: Drawing of the ITPS module designed for NASA Stage 35.

Chapter 7

Conclusions and Recommendations

7.1 Conclusions

The goal of this research was to develop an actuator with sufficient control power, temporal bandwidth and spatial (circumferential) resolution to introduce fluid dynamic forcing into the flow field of a high speed axial compressor, for the purpose of active rotating stall control. Specifically, the findings of this research are the following.

1. A high bandwidth jet actuator, for use in the active control of rotating stall on high speed axial compressors, was developed. The actuator development was divided broadly into the development of the valve, and the injector portion, of the actuator.

2. The steady fluid dynamic response (mass flow rate) of the valve was found to be linear with actuator command, the valve essentially acting as a mass flow modulator. This is due to the linearly varying choked orifice area of the valve.

3. The unsteady dynamics of the valve are governed entirely by the dynamics of the electro-mechanical servo motor driving the valve. The final valve (2nd generation) design has a -3dB bandwidth of 400 Hz, with a phase lag of 100°.

4. Two candidate jet injection schemes were developed, namely a sheet injector with fluid dynamic influence limited radially to the outer 12 mm of the compressor annulus (affecting mainly the tip clearance region of the compressor), and a 3 hole injector with influence extending radially to the outer 30 mm of the annulus. Applied to NASA Stage 35, the radial influence of the sheet injector is 15% of the annulus height, and 40% for the 3 hole injector.

5. Both the sheet and 3 hole injectors have approximately equal amounts of circumferential spreading, namely 90 mm or 70% of the circumferential actuator spacing for NASA Stage 35.

6. The fluid dynamic response of the injector was found to be characterized by a quasi-steady spatial distribution of momentum, modified temporally by a first order lag due to the internal dynamics of the injector itself, as well as a pure time delay accounting for the convective lag of fluid traveling from the actuator to the compressor face.

7. The cumulative (spatially averaged) injector momentum flux was shown to be quadratically related to commanded valve position.

8. The injector momentum distribution was shown to be 3-dimensional in nature, however the spatial 'wiggling' of the injection pattern with varying amounts of injection was found to be less than 20% of the mean penetration for the sheet injector, and 10% for the 3 hole injector.

9. The internal injector dynamics were modeled by a simple non-linear simulation, which was verified by experiment to capture the essential dynamics occurring within the injector.

10. The overall njector dynamics are not attenuated in magnitude in the frequency range measured (0 to 400 Hz), however, the combined first order (plenum dynamic) and pure time (convection) delays account for 85° of phase lag at 400 Hz.

11. The overall actuator (using the 2nd generation valve) has a bandwidth of 400 Hz with a phase lag of 185° (100° from the Moog II servo motor, and 85° from either injector).

12. The spatial spectral content of actuation was investigated and found to exhibit large harmonic content near the 12th spatial harmonic. This is due to the 12 individual jet actuators contributing to the spatial distribution of fluid injection.

13. The temporal blade excitation frequency caused by the actuation schemes was investigated. It was shown that the excitation frequency corresponding to the 12 distinct actuators was in all cases of the same magnitude as any commanded spatial harmonic of actuation.

14. As part of this research, a high bandwidth total pressure probe was developed. The ITPS probe has a pure time delay behavior (130° at 1 kHz), which was predicted by a simple acoustic model and verified by experiment. A robust version of the probe was designed for the actual compressor tests on NASA Stage 35.

The research is deemed successful since a jet actuator with significant control power (5% of the overall compressor mass flow), bandwidth (400 Hz) and spatial resolution (70% of the annulus circumference) was developed.

7.2 Recommendations

1. The conjectures relating to the effectiveness of fluid injection into the tip clearance region of the compressor should be tested by actual compressor experiments, as well as numerical simulation.

2. The effect of varying the azimuthal angle of injection should be investigated by numerical simulation, or by experiment.

Bibliography

[1] Greitzer E. M., "The Stability of Pumping Systems - The 1980 Freeman Scholar Lecture", *ASME Journal of Fluid Engineering*, Vol. 103, pp 193-242.

[2] Epstein, A. H., Ffowcs-Williams, J. E., Greitzer, E. M., "Active Suppression of Compressor Instabilities", *Journal of Propulsion and Power*, Vol.5, pp.204-211, 1989.

[3] Day, I. J., "Active Suppression of Rotating Stall and Surge in Axial Compressors", *Journal of Turbomachinery*, Vol.115, January 1993, pp.40-47.

[4] Paduano J. D., "Active Control of Rotating Stall in Axial Compressors", Ph.D. Thesis, Massachusetts Institute of Technology, Department of Aeronautics and Astronautics, November, 1991.

[5] Moore F. K., "A Theory of Rotating Stall of Multistage Axial Compressors: Part1 - Small Disturbances", *Journal of Engineering for Gas Turbines and Power*, Vol. 106, April 1984, pp.313-320.

[6] Moore, F. K., Greitzer, E. M., "A Theory of Post-Stall Transients in Axial Compression Systems, Parts I, II", *ASME Journal of Engineering for Gas Turbines and Power*, Vol 108, 1985, pp. 68-76 (Jan), pp. 231-239 (April).

[7] Haynes, J. M., Hendricks, G. J., Epstein, A. H., "Active Stabilization of Rotating Stall in a Three-Stage Axial Compressor", Presented at *The IGTI Gas Turbine Conference*, Cincinatti, OH, June 1993.

[8] Gysling, D. L., "Dynamic Control of Rotating Stall in Axial Flow Compressors Using Aeromechanical Feedback", Ph.D Thesis, Department of Aeronautics and Astronautics, MIT, August 1993.

[9] Tryfonidis, M., Etchevers, O., Paduano, J. D., Epstein, A. H., Hendricks, G. J., "Pre-Stall Behavior of Several High-Speed Compressors", *ASME Gas Turbine and Aeroengine Congress and Exposition*, The Hague, Netherlands, June 1994.

[10] Hendricks, G. J., and Gysling, D. L., "A Theoretical Study of Sensor-Actuator Schemes for Rotating Stall Control", *AIAA 92-3486, ASME Joint Propulsion Conference and Exhibit*, Nashville TN, July 1992.

[11] Hendricks, G. J., Bonnaure, L. P., Longley, J. P., Greitzer, E. M., Epstein, A. H., "Analysis of Rotating Stall Onset in High speed Axial Flow Compressors", *AIAA 93-2233, ASME Joint Propulsion Conference and Exhibit*, Monterey CA, June 1993.

[12] Bonnaure, L. P., "Modeling High Speed Multistage Compressor Stability", M.S. Thesis, Massachusetts Institute of Technology, Department of Aeronautics and Astronautics, May, 1991.

[13] Feulner, M. R., "Modeling and Control of Rotating Stall in High Speed Multi-Stage Compressors", Ph.D. Thesis, Massachusetts Institute of Technology, Department of Aeronautics and Astronautics, May, 1994.

[14] Crook, A., "Numerical Investigation of Endwall/Casing Treatment Flow Phenomena", M.S. Thesis, Massachusetts Institute of Technology, Department of Aeronautics and Astronautics, May, 1989.

[15] Crook, A. J., Greitzer, E. M., Tan, C. S., Adamczyk, J.J., "Numerical Simulation of Compressor Endwall and Casing Treatment Flow Phenomena", *ASME Journal of Turbomachinery*, Vol 115, pp.501-512, July 1993.

[16] Adamczyk, J. J., Celestina, M. L., Greitzer, E. M., "The Role of Tip Clearance in High-Speed fan Stall", *ASME Journal of Turbomachinery*, Vol 155, pp.28-39.

[17] Suder, K. L., Celestina, M.L., "An Experimental and Computational Investigation of Tip Clearance Flows in a Transonic Axial Compressor Rotor", *ASME Journal of Turbomachinery.*

[18] Abramovich M., "The Theory of Turbulent Jets", *MIT Press*, 1963.

[19] Diaz, D. S., "Design of a Jet Actuator for Active Control of Rotating Stall", M.S. Thesis, Massachusetts Institute of Technology, Department of Aeronautics and Astronautics, May, 1994.

[20] Ower, E., Pankhurst, R. C., "The Measurement of Airflow", 5th edition, Pergamon 1977.

[21] Englund, D. R., Richards, W. B., "The Infinite Line Pressure Probe", ISBN 0-87664-806-5/84/0115-10/0.

[22] Gysling, D. L., Dugundji, J., Greitzer, E. M., Epstein, A. H., "Dynamic Control of Centrifugal Compressor Surge using Tailored Structures", Journal of Turbomachinery, Vol. 113, pp. 710-722, April 1991.

[23] Simon, J. S., Valavani, L., Epstein, A. H., Greitzer, E. M., "Evaluation of Approaches to Active Compressor Surge Stabilization", Journal of Turbomachinery, Vol. 115, pp. 57-67, January, 1993.

[24] Lee, N. K. W., 1990, "Effects of Compressor Endwall Suction and Blowing on Stability Enhancement", MIT GTL Report no.192 Jan 1988, *ASME Journal of Turbomachinery*, Vol 112, pp.133-144.

[25] Schuder, C. B., Binder, R. C., "The Response of Pneumatic Transmission Lines to Step Inputs", *ASME Journal of Basic Engineering*, Dec 1959.

[26] Kerrebrock, J. L., "1981 Dryden Lecture – Flow in Transonic Compressors", *AIAA Journal*, Vol 19, No.1, Jan 1981.

[27] Wisler, D. C., "Shock Wave and Flow Velocity Measurements in a High Speed Fan Rotor Using the Laser Velocimeter", *ASME*, Paper 76-GT-49, 1976.

[28] Strazisar, A. J., Powell, J. A., "Laser Anemometry Measurements in a Transonic Axial-Flow Compressor Rotor", *ASME*, New Orleans, La, March 5-13 1980.

Appendix A

Non-linear Simulation

The simulation starts by setting a step size Δt (usually chosen such that about 100 time steps occur in the highest frequency wave required). A WHILE loop increments the counter n, and implements the simulation algorithm, until the simulation is done.

Step 1 Quasi-steady assumption for the valve orifice

$$\dot{m}_1 = b\alpha + c \tag{A.1}$$

where b = 1, c = 0.04, $\alpha = \sin(\omega\ t)$ and t = n Δt.

Step 2 Quasi-steady assumption for the exit nozzle. If $P_{t2} > 1.89P_{at}$ we have choked flow in the exit nozzle and thus

$$\dot{m}_3 = C_{d3}\rho_3 A_3\sqrt{\gamma RT_3} \tag{A.2}$$

where

$$\rho_3 = \frac{p_3}{RT_3} \quad p_3 = \frac{P_{t2}}{1.89} \quad T_3 = \frac{T_{t0}}{1.2} \tag{A.3}$$

If $P_{t2} < 1.89P_{at}$ we have unchoked flow in the exit nozzle and thus

$$\dot{m}_3 = C_{d3}\rho_3 A_3 M_3\sqrt{\gamma RT_3} \tag{A.4}$$

where

$$\rho_3 = \frac{p_3}{RT_3} \quad p_3 = p_{at} \quad T_3 = \frac{T_{t0}}{1+0.2M_3^2} \tag{A.5}$$

M_3 is obtained iteratively from the following

$$M_3 = \frac{U_3}{\sqrt{\gamma RT_3}} \quad U_3 = \frac{\dot{m}_3}{C_{d3}\rho_3 A_3} \tag{A.6}$$

Step 3 Unsteady mass storage in the injector plenum is given by

$$\dot{m}_1 - \dot{m}_3 = \frac{d}{dt}(\rho_2 V_2) \tag{A.7}$$

$$\frac{d\rho_2}{dt} = \frac{\dot{m}_1 - \dot{m}_3}{V_2}$$

Discretizing this into finite (small) time steps using forward Euler yields

$$\rho_{2,n+1} = \rho_{2,n} + \frac{d\rho_{2,n}}{dt}\Delta t \tag{A.8}$$

Knowing $\rho_{2,n+1}$, we can calculate $P_{t2,n+1}$.

$$P_{t2,n+1} = \rho_{2,n+1} RT_{t0} \tag{A.9}$$

Step 4 Return to Step 1 until simulation is complete.

Appendix B

ITPS Analysis

Acoustic ducts

The transfer matrix of an inviscid acoustic duct is given by

$$\begin{bmatrix} p_l \\ \rho a u_l \end{bmatrix} = \begin{bmatrix} \cos\omega\tau & -j\sin\omega\tau \\ -j\sin\omega\tau & \cos\omega\tau \end{bmatrix} \begin{bmatrix} p_0 \\ \rho a u_0 \end{bmatrix} \tag{B.1}$$

where

$$\tau = \frac{l}{a} \quad a = 340 m.s^{-1} \quad \rho = 1.225 kg.m^{-3} \tag{B.2}$$

Sense tube 0-1

$$p_1 = \cos(\omega\tau_1)p_0 - j\sin(\omega\tau_1)\rho a u_0 \tag{B.3}$$

$$\rho a u_1 = -j\sin(\omega\tau_1)p_0 + \cos(\omega\tau_1)\rho a u_0 \tag{B.4}$$

Infinite tube 2-3

The impedance condition for an infinite duct is given by

$$p_2 = Zu_2 \quad Z = \rho a \tag{B.5}$$

Junction 1-2-4

$$p_1 = p_2 = p_4 \tag{B.6}$$

$$\rho a u_1 A_1 = \rho a u_2 A_2 + \rho a u_4 A_3 \tag{B.7}$$

Helmholtz resonator 4-5-6

The resonator duct can be modeled as a lumped duct, the transfer matrix being

$$\begin{bmatrix} p_4 \\ \rho a u_4 \end{bmatrix} = \begin{bmatrix} 1 & -j\omega \frac{l_3}{a} \\ 0 & 1 \end{bmatrix} \begin{bmatrix} p_5 \\ \rho a u_5 \end{bmatrix} \tag{B.8}$$

The compliance of plenum volume can be modeled as an isentropic process

$$\rho a u_5 = \frac{s V_p}{A_3 a} p_5 \tag{B.9}$$

The overall plenum transfer function can then be written as

$$\rho a u_4 = G_p(s) p_4 \tag{B.10}$$

where

$$G_p(s) = \frac{\frac{s V_p}{A_3 a}}{(1 + \frac{s^2 V_p l_3}{A_3 a^2})} \tag{B.11}$$

Solving the set

The equations for the sense duct, extension duct and Helmholtz resonator can be combined to give

$$\rho a u_0 = G_0(s) p_0 \tag{B.12}$$

where

$$G_0(s) = \frac{A_1 j \sin(\omega\tau_1) + (A_2 + A_3 G_p)\cos(\omega\tau_1)}{A_1 \cos(\omega\tau_1) + (A_2 + A_3 G_p) j \sin(\omega\tau_1)} \tag{B.13}$$

The transfer function from sense location (station 0) to transducer location (station 6) can be written as

$$p_6 = \frac{A_3 a}{s V_p} \rho a u_4 \tag{B.14}$$

$$G_{itps}(s) = \frac{p_6}{p_0} = \frac{A_3 a}{s V_p} G_p(\cos(\omega\tau_1) - j \sin(\omega\tau_1) G_0) \tag{B.15}$$